A Practical MEMS Gravimeter

Richard Paul Middlemiss

Schools of Physics & Astronomy and Engineering
University of Glasgow

Presented as a thesis for the degree of Ph.D. in the University of Glasgow,
University Avenue, Glasgow, G12 8QQ

November 2016

Summary

The ability to measure tiny variations in the local gravitational acceleration allows – amongst other applications – the detection of hidden hydrocarbon reserves, magma build-up before volcanic eruptions, and subterranean tunnels. Several technologies are available that achieve the sensitivities required (tens of $\mu\text{Gal}/\sqrt{Hz}$), and stabilities required (periods of days to weeks) for such applications: free-fall gravimeters, spring-based gravimeters, superconducting gravimeters, and atom interferometers. All of these devices can observe the Earth tides; the elastic deformation of the Earth's crust as a result of tidal forces. This is a universally predictable gravitational signal that requires both high sensitivity and high stability over timescales of several days to measure. All present gravimeters, however, have limitations of excessive cost (£70 k) and high mass (>8 kg).

In this thesis, the building of a microelectromechanical system (MEMS) gravimeter with a sensitivity of 40 $\mu\text{Gal}/\sqrt{Hz}$ in a package size of only a few cubic centimetres is discussed. MEMS accelerometers – found in most smart phones – can be mass-produced remarkably cheaply, but most are not sensitive enough, and none have been stable enough to be called a 'gravimeter'. The remarkable stability and sensitivity of the device is demonstrated with a measurement of the Earth tides. Such a measurement has never been undertaken with a MEMS device, and proves the long term stability of the instrument compared to any other MEMS device, making it the first MEMS accelerometer that can be classed as a gravimeter. This heralds a transformative step in MEMS accelerometer technology. Due to their small size and low cost, MEMS gravimeters could create a new paradigm in gravity mapping: exploration surveys could be carried out with drones instead of low-flying aircraft; they could be used for distributed land surveys in exploration settings, for the monitoring of volcanoes; or built into multi-pixel density contrast imaging arrays.

Acknowledgements

Firstly, I would like to thank Prof. Giles Hammond for his patient support and supervision during this project. Like a well tuned PID controller, he kept me on track and made sure I both enjoyed and made the most of my time as a PhD student. I aspire to one day fit in half as much productive output as he manages to squeeze into a day. I would also like to thank my second supervisor, Prof. Douglas Paul, for an introduction to – and continuous lessons in – the fascinating world of nanofabrication (and for many good restaurant recommendations). To the innumerable technicians and colleagues (both in the Kelvin Building and the JWNC), I couldn't have completed this PhD without your help - thank you all.

To my office mates: thanks for all the good times (the Office Olympics, the practical jokes, the weekly trivia and all the good conversations about everything and [more often] nothing) - you've all kept me sane. I apologise for talking too much, but thanks for listening and/or buying decent headphones. Please also accept my sincere congratulations for when you all win the Nobel prize for the gravitational wave detection, allow me to buy you a celebratory drink sometime with only a hint of envy.

My wife, Aliyssa, has been my constant companion and has made life outside of academia both happy and complete. Thanks for sharing the good times and the bad with me, I also promise to never again subject you to another three minute presentation practise. Another heartfelt thank you goes to my parents, David and Liz, and the rest of my family for giving me a thirst for knowledge and for supporting me through the resultant 23 years of full time education. I literally wouldn't be here without you.

Preface

In this thesis the development of the microelectromechanical system (MEMS) gravimeter is discussed in detail. Chapter 1 is an outline of the long history of gravimeter development, the resultant range of commercially available gravimeters, an discussion of MEMS technology, some theoretical background about harmonic oscillators, and a short synopsis of some of the potential applications for gravimetry.

The following chapter focuses upon the geometry of the MEMS device developed during this project – an asymmetric geometrical anti-spring – and why this geometry is enables the proof mass to oscillate stably at a very low frequency. Contribution to the design of the geometrical anti-spring came from the author, Giles Hammond and Paul Campsie. The experimental/computer modelling results on the asymmetric design were obtained by the author. Valuable suggestions were made by Liam Cunningham on the running of complex finite element analysis models using the ANSYS software package. In this chapter some early abandoned designs are also discussed, the experimental results for these designs were obtained by Paul Campsie.

Chapter 3 contains a description of the fabrication processes used to make the MEMS device. All of the fabrication was carried out by the author. The fabrication processes were originally built around standard procedures, but to meet the needs of the design many of these procedures were augmented and optimised, and several original processes were developed by the author. Invaluable guidance and advice on the building blocks mirco-fabrication was given by Douglas Paul, and other users of the clean room.

The development of an optical shadow sensor is discussed in chapter 4. This optical sensor was used to measure the displacement of the MEMS proof mass. Significant optimisation was required to allow this sensor to reach both the sensitivity and stability required to measure slowly varying gravitational signals. The initial design for this sensor was suggested by Giles Hammond. The experimental work was also carried out by the author in partnership with Giles Hammond. The process of optimising systems to maintain stabilities over week time-scales is a laborious one. Daily meetings were held to discuss the night's data, and what

to change to improve the system. Suggestions of what to change (and crucially what not to change) came from both parties. The labview script used to run the PID controller was put together by Giles Hammond.

Chapter 5 contains a discussion of the main experiment so far carried out with the MEMS device - a measurement of the Earth tides. This chapter expands upon a recent first-name publication by the author [1]. The experimental results were obtained by the author, with the exception of the data included in figure 5.1, which was taken by Giles Hammond. The analysis of the data in this chapter was carried out by the author, under the supervision of Giles Hammond, and with suggestions from Matt Pitkin and Mark Fletcher. The use of the Allan Variation analysis technique was suggested by a reviewer of the initial manuscript of the paper referenced above.

In chapter 6 the results of this thesis are summarised, and plans for future development of the MEMS gravimeter are outlined.

There are also three appendices in this thesis. Appendix A contains a conversion chart for the various units that are commonly used to describe gravitational acceleration. Appendix B is a description of the basic operation of the ANSYS finite element analysis software. Appendix C contains the MATLAB code used to carry the analysis described in chapter 5. The first iterations of this code were developed from a regression analysis program, used by Chris Bell. Innumerous alterations were made to this script by both the author and Giles Hammond, until it arrived at the state presented.

Table of contents

List of figures

List of tables

Chapter 1

Gravimetry

Since the gravitational pull of an object is directly proportional to its mass, measuring the gravitational acceleration, g, caused by the Earth can reveal density changes of the ground below us. Since the gravitational force is so weak (roughly forty orders of magnitude weaker than the electromagnetic force), instruments used to detect it – gravimeters – must therefore be highly sensitive.

Since gravimetry was first performed in the 1700s, academic research has been performed continuously on the applications of gravimetry, and the tools used to conduct it. Gravimetry has also been applied successfully outside of academia in numerous industrial, civic, environmental and defence projects. To place into context the research that is summarised in this thesis, it is necessary to first consider the field as a whole. This chapter will highlight the technological developments of gravimeters, and the diverse applications for which they are used.

1.1 Gravimetry and Gravimeters

Arguably, the birth of modern gravimetry can be placed at the moment when Galileo Galilei observed that the acceleration of an object is independent of its mass. This break from the Aristotlean tradition was the paradigm shift that would allow those who followed to formulate a scientific description of gravity and its measurement. This classical description of gravity would not be surpassed until the advent of general relativity at the start of the 20^{th} Century, and it is still all that is needed to describe modern geophysical applications of gravimetry. Galileo's free fall law and his further observation that the period of a pendulum was only dependent on its length (and the acceleration due to gravity) formed the basis of gravimetry.

It was not until 1687 that Newton applied a mathematical rigour to gravity with the derivation from Kepler's laws of a universal law of gravitation [2]:

$$F = G\frac{M_1 M_2}{r^2}\hat{r} \tag{1.1}$$

where F is the force between the two masses, M_1 and M_2 that are separated by radius r, G is the gravitational constant, and $\hat{r}$ is the unit vector of radius. A further step in the field was made in 1656, when Christian Huygens took advantage of the pendulum law to develop the pendulum clock [3]. At the time, the pendulum clock was so accurate that it was used to define the foot length standard. One foot was defined as the length of pendulum that would result in a two second period of oscillation. Pendulum clocks quickly spread around the world given their use as a navigation tool and in 1672/1673 Jean Richter observed a Paris-calibrated pendulum clock run slow when it was used in French Guiana. This was the first indirect observation of gravitational acceleration variance across different locations; he had essentially used the device as a pendulum gravimeter. It would be pendulum gravimeters that would be the only tool used for measuring gravity for the next two and a half centuries.

Throughout the centuries after Richter's first observation, gravimeters were being developed with ever greater accuracy. Figure 1.1 shows the increasing accuracy of gravimeters over the past three hundred years. This figure divides the instruments of this period into six separate categories: wire pendulum gravimeters, reversible pendulum gravimeters, relative pendulum gravimeters, relative gravimeters, rise and fall gravimeters, and free-fall gravimeters. This categorisation could be further simplified into three basic technologies; pendulum gravimeters (encompasing wire pendulum, reversible pendulum, and relative pendulum designs), relative gravimeters, and absolute gravimeters (encompasing rise and fall and free-fall gravimeters):

- Pendulum gravimeters - that were operated from the field's inception until around 1970 [4, 5] - are used by measuring the period of oscillation of a pendulum (or pendula) of a set length. Gravitational acceleration, g, is then given by equation 1.2:

$$g = \frac{4\pi^2 L}{T^2} \tag{1.2}$$

  where L is the length of the pendulum and T is the period of oscillation. The two most accurate pendulum gravimeters reached sensitivities of ± 400 μGal[1] [6] and 300

[1] Appendix A has been included to disseminate the various units that are used throughout the literature for describing g.

μGal [4]. The unit 'Gal' is named after Galileo, and is commonly used in the field of gravimetry. 1 Gal is equivalent to 1 cm/s^2. Although beautiful in their simplicity, the accuracy of pendulum gravimeters was ultimately limited by three parameters: the timing accuracy with which one could measure the oscillation period; the ability to maintain a constant pendulum length in the face of environmental variations; and the mechanical wear of the pivot from which the pendulum hung. One could decrease the timing accuracy limitation by lengthening the pendulum, but this would increase the impact of thermal variations on the length as well as making the tool more bulky.

- The second broad category is the relative gravimeter. Relative gravimeters measure gravitational acceleration by monitoring the displacement of a test mass on a spring. Spring-based gravimeters were first proposed by William Herschel in 1833 [7] but were not built until the 1930s [8, 9]. In a spring-based gravimeter the gravitational acceleration is given by equating Hooke's Law and Newton's Second Law, then rearranging for g:

$$g = \frac{kx}{m} \tag{1.3}$$

where k is the spring constant, x is the displacement of the mass, and m is the mass itself. Most gravimeters use a mechanical spring of varying design, the main exception being the superconducting gravimeter, in which the mechanical spring and proof mass is replaced by a magnetically levitated superconducting sphere [10, 11][2]. Relative gravimeters have moved significantly beyond the most accurate pendulum gravimeters. The *Scintrex CG5* relative gravimeter, for example, can measure gravity variations down to 2 μGal [12, 13]. There are three parameters that can be tuned to improve the sensitivity of a relative gravimeter whilst maintaining a small size[3]. To increase sensitivity the spring can be made softer, the mass heavier, or the displacement measurement more accurate. The spring, however, is also the main drawback for relative gravimeters; springs are highly susceptible to thermal variations. As the temperature changes, the thermal expansion coefficient and Young's modulus of the material will change, thus altering the spring constant. Since the measurement of gravitational acceleration in these devices is directly proportional to its spring constant, it is imperative that relative

[2] Superconducting relative gravimeters achieve sub-μGal sensitivities [11], they also have better stabilities than their mechanical counterparts, but they are not as mobile or cheap because of the need for them to be cryogenically cooled to liquid helium temperatures.

[3] This is in contrast to the pendulum design, where once the timing limit was reached, the only way that sensitivity could be increased was to make the pendulum impractically longer.

gravimeters are temperature controlled - something that can be technologically difficult to achieve outside of the lab. This is a challenge, but one that has been overcome by many manufacturers. Relative gravimeters are sold in large volumes to users in many different fields. They are desirable due to their mobility and comparatively low cost, when compared to the third and final category of gravimeter: the absolute gravimeter.

- Absolute gravimeters were first proposed in 1938 by Guillet [14]. All absolute gravimeters simply measure the time of flight of a test mass over a set distance. Like relative gravimeters, there are variations in their design, but most importantly they make an absolute measurement of gravity. Starting with Volet in 1946 [15], these devices have been developed over the second half of the last century and now achieve very high sensitivity. The *Micro-g Lacoste FG5* [16], for example, achieves acceleration sensitivities of 1.6 μGal/$\sqrt{Hz}$ [16]. Absolute gravimeters, however, are costly (generally over \$100 k) and heavy (over 100 kg)[4]. For this reason relative gravimeters are often used as survey instruments in preference. Atom interferometers can also be used as absolute gravimeters [17–19]. These devices also achieve μGal sensitivities but are similarly encumbered by their high cost, large size and a need for seismic isolation from ground vibrations[5].

Towards the end of the 17$^{\text{th}}$ century and into the 18$^{\text{th}}$ century various scientists (including Newton, Huygens, Euler, MacLaurin, Bouguer and Clairaut) were able to develop the science of gravimetry and geodesy (the temporal and spacial variations of the Earth and its corresponding gravitational field). The gravitational acceleration, g, was found to be the summation of two major components: the Earth's gravitation and its centrifugal acceleration. The Earth's gravitation is found by equating Newton's 2nd law and the universal law of gravitation:

$$g = G\frac{M_E}{r^2} \tag{1.4}$$

The magnitude of centrifugal acceleration is given by equation 1.5 [22]:

$$z = \omega^2 r \cos\bar{\phi} \tag{1.5}$$

where ω is angular velocity of the earth about its axis, r is again the radius of the Earth, and $\bar{\phi}$ is the geocentric latitude - the angle between the polar axis and the observation latitude, as

[4]The Micro-g Lacoste A-10, for example, is classed as a 'portable' absolute gravimeter, but it weighs 105 kg.

[5]Typical ground vibrations in a quiet seismic location would be of order 20 nm at 1 Hz [20].

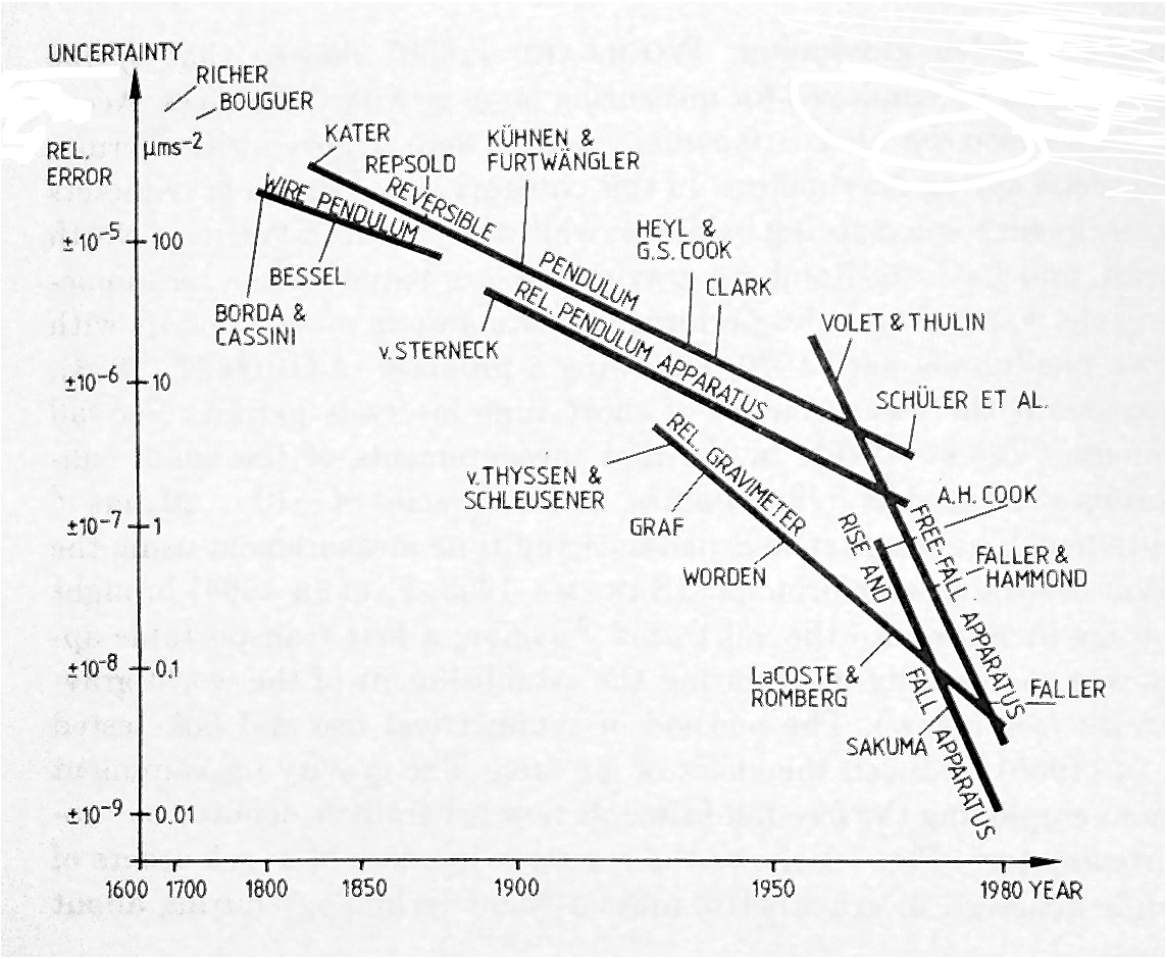

Fig. 1.1 The increase of gravimeter accuracy through time (image reproduced from [21]). This graph outlines six categories of gravimeters: wire pendulum gravimeters, reversible pendulum gravimeters, relative pendulum gravimeters, relative gravimeters, rise and fall gravimeters, and free-fall gravimeters. It also shows the inventors responsible for them. Rise and fall gravimeters, and relative gravimeters are the two main types of sensor that are still used today, both now achieve sensitivities of around μGal.

measured from the centre of the Earth. The gravitational field equipotential (defined at sea level) that encompasses both the Earth's gravitation and the centrifugal acceleration is known as the 'geoid'. The geoid, however, is not a simple sphere. In order to conduct successful gravity surveys - where underground features are observed - it is therefore important to understand where departures occur in the geoid's shape. Latitude is the first major factor. The Earth is slightly oblate, it is flattened by about 0.3% at the poles. Since the polar radius is different to the equatorial radius, the Earth's gravitation differs at sea level between these locations. At the equator centrifugal acceleration is observed, but at the poles there is no such acceleration. These latitude variations in centrifugal acceleration account for a variation of 4 Gal, a change of 0.4 % in the observed gravitational acceleration at sea level (9.78 ms^{-2} at the equator and 9.83 ms^{-2} at the poles).

When conducting a gravity survey, other factors must also be taken into account that will affect the gravity readings. The first of these is the effect of elevation. Elevation variations can be further split into two categories: the Free-Air Effect and the Bouguer Effect. The Free-Air Effect takes account of the fact that when a reading station is located above sea-level, the radius from the Earth's centre of mass is increased. By equation 1.4 this means that the measurement of gravitational acceleration will be smaller. The Free-Air gravitational acceleration anomaly is given by [23]:

$$\Delta g_{FA} = \frac{-2GM_E\Delta Z}{R_E^3} \ \text{ms}^{-2} \tag{1.6}$$

where M_E is the mass of the Earth, R_E is the radius of the Earth, and ΔZ is the variation in altitude. This means that the Free-Air variation per metre gained in altitude, in units of μGal, is:

$$\Delta g_{FA} = -309 \ \ \mu\text{Gal/m} \tag{1.7}$$

The Bouguer Effect works to counter to the Free-Air Effect – increased elevation normally implies that the observation location is on top of a large land mass. This land mass will create a local downward acceleration that will increase the net gravitational acceleration measured at the site. When calculating the Bouguer Effect, it is assumed that the land mass is an infinitely wide slab of material [23]. It is given by [24]:

$$\Delta g_B = 2\pi\rho GH \ \ \text{ms}^{-2} \tag{1.8}$$

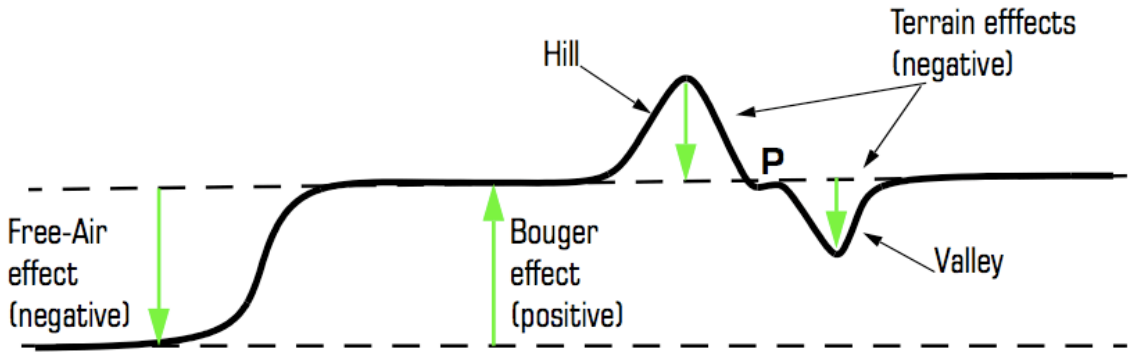

Fig. 1.2 The Free Air, Bouguer and Terrain Effects, reproduced from [23]. The Free-Air effect makes the gravitational signal smaller with increasing altitude, the Bouguer effect makes the gravitational signal larger with increasing altitude, and the Terrain effects always make the gravitational signal smaller (regardless of whether they are hills or valleys).

where ρ is the density of the infinite slab of rock, and H is the thickness of the infinitely wide slab of rock. This means that the Bouguer variation per metre gained in altitude, in units of μGal, is:

$$\Delta g_B = +42 \ \ \mu\text{Gal/m} \tag{1.9}$$

In an underground measurement location the Bouguer and Free-Air Effects swap signs: the centre of mass radius is reduced so the Free-Air Effect is positive, whereas the land mass that is now above the observation site will induce a negative Bouguer Effect. Regardless of elevation, the surrounding terrain of a observation location will also alter the measurement. In fact all terrain variations will cause a negative effect on the total acceleration. Valleys near the observation location will reduce the Bouguer Effect because there will be less mass below the instrument to pull downwards. Mountains on either side of the survey location, however, will create a negative Bouguer Effect, providing a small upwards component of acceleration. Figure 1.2 summarises the Bouguer, Free-Air and Terrain Effects.

Sometimes gravity surveys are carried out in the same location over a period of time. These are known as 'time-lapse surveys'. Time-lapse surveys are used to monitor oil reservoirs as they are drained [25], and to observe the intrusion of magma under active volcanoes to forewarn of eruptions [26]. For time-lapse surveys the spatial variations in gravity discussed above are less important, but there are temporally varying signals that are significant. The first of these signals is the effect of the gravitation of nearby celestial bodies: the Earth tides. The Earth tides are an elastic distortion of the Earth's crust caused by the changing relative phase of the Sun, the Earth and the Moon [27]. This is the same

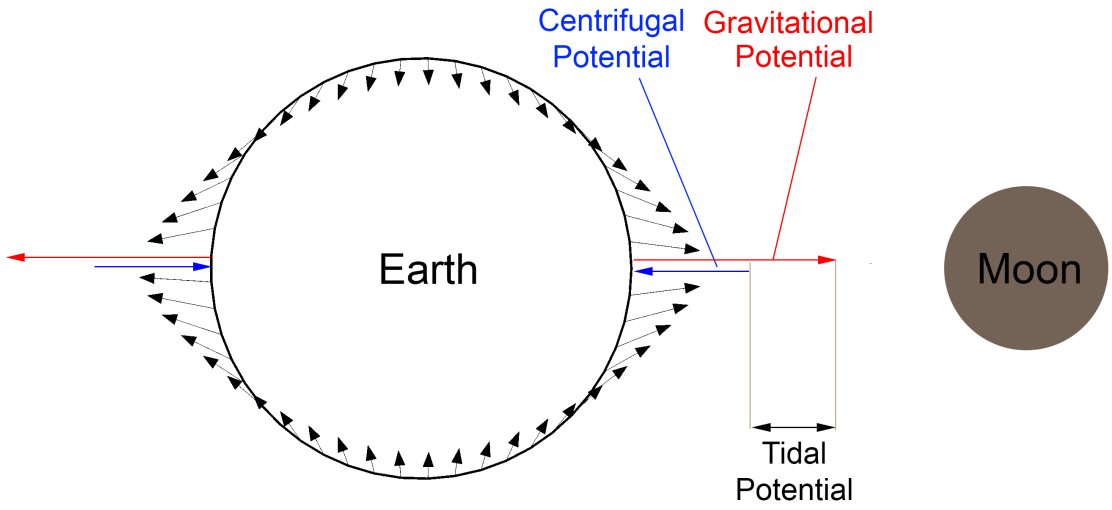

Fig. 1.3 A force diagram demonstrating tidal potential generated by the presence of the Moon. The tide raising potential is the net difference between the centrifugal acceleration and the gravitational acceleration caused by the Moon's presence. The Sun also generates a tidal potential, but the magnitude of this signal is about half of that caused by the Moon.

effect that causes the ocean tides. A diagram of how tidal forces arise is displayed in figure 1.3. They produce a small variation in the local gravitational acceleration, the size of which depends also on the latitude and elevation of the measurement location, but they have a peak signal strength of less than 400 μGal [13]. Depending on the time of the lunar month, the Earth tides vary in amplitude and frequency, moving between diurnal (2×10^{-5} Hz) and semi-diurnal (1×10^{-5} Hz) peaks. Figure 1.4 is a plot of the Earth tide signal as would have been observed from Glasgow in January 2015. This plot is the net signal due to both the Moon and the Sun. The Lunar signal is about twice the magnitude of the Sun's. A beat signal can be observed as the Sun and the Moon pull in either orthogonal or parallel directions.

Another temporally varying signal that must be accounted for in gravity surveys is that of atmospheric pressure. Changes in atmospheric pressure in the region within 50 km of the survey location can cause changes in gravity readings of up to 30 μGal [28]. The final means by which gravity surveys can be altered temporally is by the effect of precipitation. Porous rocks can absorb rain or snow melt and change the density of the ground, thus changing the result given by equation 1.9. The changing level of nearby oceans and lakes can also have a loading effect that must be considered [29]. Ocean loading can have an effect as large as 20 μGal/m [23].

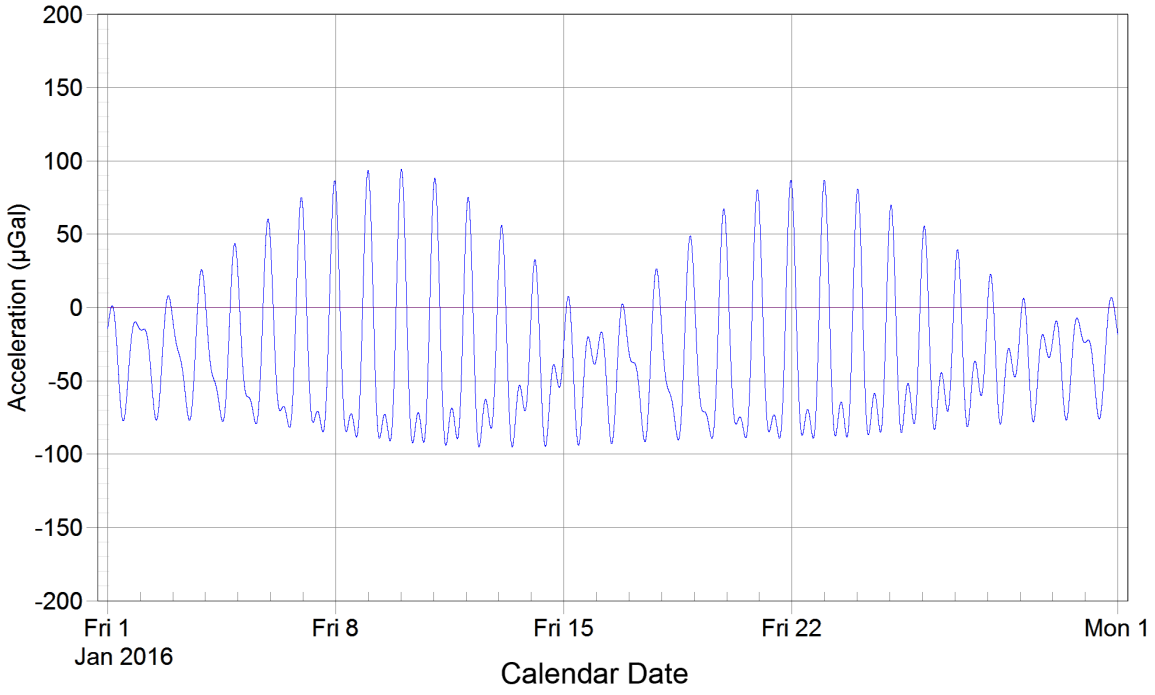

Fig. 1.4 A plot of the tidal signal as would have been observed from Glasgow in the month of January 2015. This data was generated using the software package TSOFT [30]. There is a daily variation in the tidal signal caused by the Earth's rotation – the Earth tides. There is also a longer term variation caused by the changing phase of the Sun/Earth/Moon system. The points in the graph where the pull of the Sun and Moon align to give maximal amplitude, are known as spring sides (around the 10^{th} and 21^{st} of January). The points in the graph where the pulls sum constructively are known as the neap tides (around the 2^{nd}, 16^{th} and 30^{th} of January).

1.1.1 Gradiometry

Einstein's Equivalance Principle states that gravitational accelerations cannot be distinguished from inertial accelerations [31]. A single gravimeter can therefore not distinguish an acceleration of the test mass caused by inertial acceleration of the device housing from a gravitational acceleration. One such source of inertial acceleration may be simply the vibration of the ground – seismic noise, or the vibration of the vehicle from which a survey is being performed. To overcome this issue, gravity gradiometry can be utilised [32].

Gradiometry is the study of the spatial rate of change of gravitational acceleration. Gravimeters are operated in gradiometer configuration by grouping them into sets of two or more, separated by a finite distance. This allows the differential accelerations – or gravity gradient – to be measured by comparing the signals. To do this the Common Mode Rejection Ratio (CMRR) is used, i.e signals measured in both of the instruments are rejected, thus reducing the sensitivity to inertial accelerations and leaving behind a measurement of the gravitational gradient. Gradiometry reduces the power of the total signal but produces less noise due to the inertial motion of the instrumentation. Gradiometry also increases the spacial resolution of sub-surface features because gradiometers are able to distinguish between small, close objects from those that are massive and far away. Like gravimeters, gradiometers are still susceptible to spurious signals caused by the tilting of the ground. Since $F = mg\sin\theta$, a gradiometer cannot distinguish between a changing force caused by a change in g, and one caused by a change in the tilt of the instrument.

If aligned with the axes of the local gravitational field, the gravitational field of the Earth (or any planet) can be characterised by the gravity gradient tensor [21, 33]:

$$\mathbf{W} = \text{grad}\,\mathbf{g} = \text{grad} = \begin{pmatrix} \mathrm{W}_{xx} & \mathrm{W}_{xy} & \mathrm{W}_{xz} \\ \mathrm{W}_{yx} & \mathrm{W}_{yy} & \mathrm{W}_{yz} \\ \mathrm{W}_{zx} & \mathrm{W}_{zy} & \mathrm{W}_{zz} \end{pmatrix} \tag{1.10}$$

where each matrix element of W describes how the components of gravity vary with direction. If the system is not rotating with the Earth then this tensor simplifies to the *gravitational* gradient tensor, of which only five elements are mutually independent of the *gravity* gradient tensor [34]. This is due to the fact that in this situation, Laplace's equation applies [35, 36]; the diagonal components are equal to zero in an inertial frame of reference:

$$\begin{aligned} \mathrm{W}_{xx} + \mathrm{W}_{yy} + \mathrm{W}_{zz} &= 0 \\ \mathrm{W}_{xy} &= \mathrm{W}_{yx} \\ \mathrm{W}_{xz} &= \mathrm{W}_{zx} \\ \mathrm{W}_{zy} &= \mathrm{W}_{yz} \end{aligned} \tag{1.11}$$

The gravitational gradient tensor is also known as the Eötvös tensor, and gravity gradients are often measured in units of the same name, where 1 Eötvös = 10^{-9} s^{-2}.

In a gradiometer, two or more sensors are separated by a baseline and these sensors are optimised to respond in the same way to an identical external force. A schematic representing this concept can be seen in figure 1.5. In this image - where two sensors are separated by a baseline in the x-axis - the level of optimisation of the system is characterised by the scaling factors α and β. The more similar the values of α and β are, the higher the CMRR. The resulting signal is given by:

$$s = (g_{x+dx} - g_x) + (\beta\ddot{x} - \alpha\ddot{x}) \tag{1.12}$$

Inertial accelerations are therefore removed when $\alpha = \beta$.

The acceleration differences between the two masses of the sensors are characterised by differential translations or rotational translations. The differential translations arise from the acceleration of the test masses over its three axes. The rotational translations are due to the pitch, yaw, and roll of the test masses. Depending on the configuration of a gradiometer, different parts of the gravitational gradient tensor can be found using alternative device configurations. Figure 1.6 demonstrates three different examples of possible configurations. The translational components of the tensor required for reconstructing the gravity field are given by the difference between the forces on each of the test masses, divided by the distance between them. For example, in the vertical system shown in figure 1.6A, the W_{ZX} tensor component could be found by:

$$W_{ZX} = \frac{F_2 - F_1}{\Delta x} = \frac{m_2 g_2(z) - m_1 g_1(z)}{\Delta x} \tag{1.13}$$

Similarly, components W_{ZZ} and W_{XX} could be found using the configurations shown in figures 1.6B and 1.6C respectively:

$$W_{ZZ} = \frac{m_2 g_2(z) - m_1 g_1(z)}{\Delta z} \tag{1.14}$$

$$W_{XX} = \frac{m_2 g_2(x) - m_1 g_1(x)}{\Delta x} \tag{1.15}$$

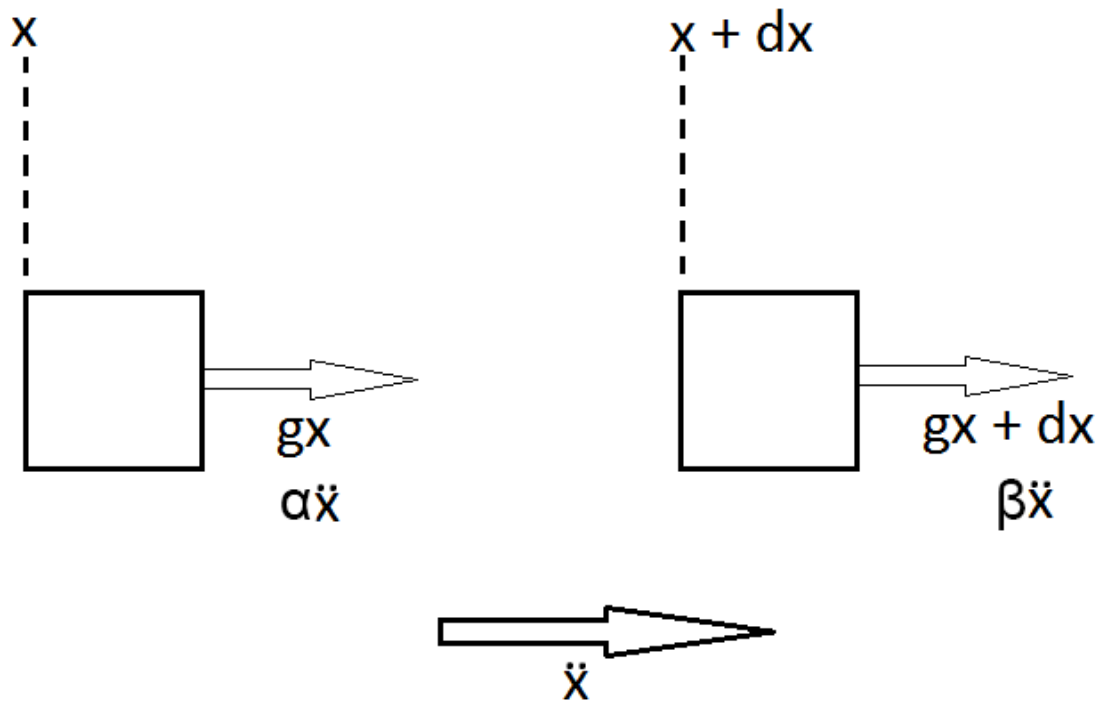

Fig. 1.5 A schematic diagram of a gradiometer configuration indicating the different responses of two sensors separated by a baseline in the x-axis. The two blocks represent the two sensors, each of which would respond to a gravitational acceleration in the x-axis from a hidden object. If these devices were mounted on a platform that was also prone to inertial acceleration, the gravitational acceleration signal would likely be swamped by this inertial signal. If both devices are designed to respond to a given acceleration in the same way, however, then the difference in acceleration between the two devices can be measured, thus nullifying the effect of the inertial signal. This will give a measure of the gravity gradient over the baseline. It is not possible to make two perfectly identical sensors, therefore their similarity is judged by their common mode rejection ratio (CMRR).

1.2 Micro-electro-mechanical Systems (MEMS)

The aim of this PhD project was to develop a microelectromechanical system or 'MEMS' gravimeter, but what are MEMS? The term MEMS is used to describe many different microscopic sensors made from silicon. The field can be traced to around 1960 when multiple universities, particularly Stanford, started to conduct research into micro-fabricated sensors [37]. The field has since split into several more sub-disciplines: RF-MEMS, optical-MEMS (MOEMS), bio-MEMS, microfluidic-MEMS and inertial-MEMS [38]. The complexity of some of the MEMS now designed is impressive, an example of this complexity is shown in figure 1.7. A multi layer system with 240 process steps is used as a safety mechanism

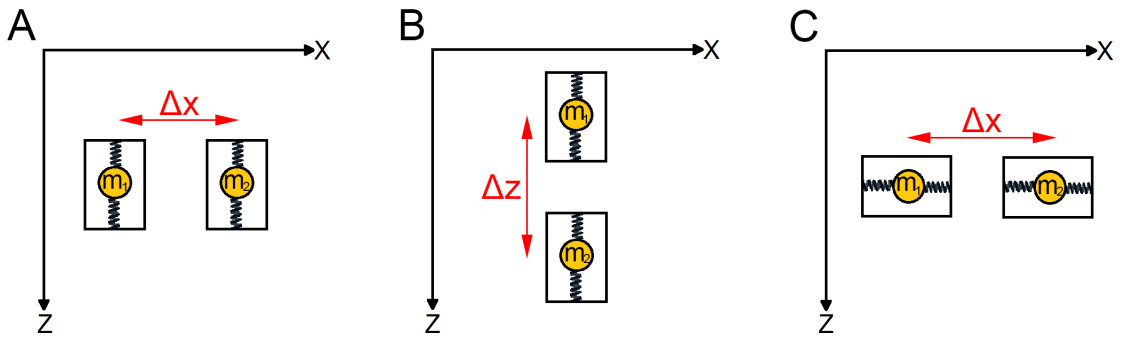

Fig. 1.6 By utilising different constellations of gravimeter it is possible to measure all five independent components of the gravitational gradient tensor. A gives W_{ZX}, B gives W_{ZZ} and C gives W_{XX}.

to prevent accidental arming of nuclear weapons [39]. Figure 1.8 shows the progression of MEMS development, and the subsequent diversification of the field. This figure only covers the U.S.A, but it is a good proxy for the global expansion of MEMS.

The first MEMS based accelerometer was developed by Vaganov in 1975 [37], shortly followed by Roylance and Angell in 1979 [41]. The Roylance and Angell device is pictured in figure 1.9, it had a sensitivity of 1 Gal, and a resonant frequency of over 1 kHz. The displacement of the device was measured piezoelectrically. The development of MEMS accelerometers took a huge leap in the 1990s when car air bags started to be introduced. Air bags required a cheap accelerometer that could detect the sharp deceleration indicative of a car crash - MEMS were the perfect solution to this market need. In 1990 a device built by Allen et al. [42] was first fitted in a car. By 2007 over 100 million MEMS accelerometers were sold per year [37].

More recently, another large market has opened up for MEMS accelerometers and gyroscopes: smart phones. Every smart phone produced now contains a three-axis MEMS accelerometer. The iPhone 5, for example, uses an accelerometer with a sensitivity of 234 mGal [43]. Although MEMS accelerometers are now ubiquitous, few achieve sensitivities that could be considered useful for gravity surveys, and none have achieved a sufficient stability to compete with commercial gravimeters. 'Stability' is used very broadly here. As will be discussed in chapter 4, all electronic devices suffer from low frequency noise (also known as '1/f' or 'pink' noise), where the noise floor of a device increases with the acquisition time. The causes for low frequency noise are many and various, and it takes effort to minimise its effects. No evidence is available in the literature to suggest that this effort has been applied to the reduction of low frequency noise in MEMS accelerometers below 10^{-2}

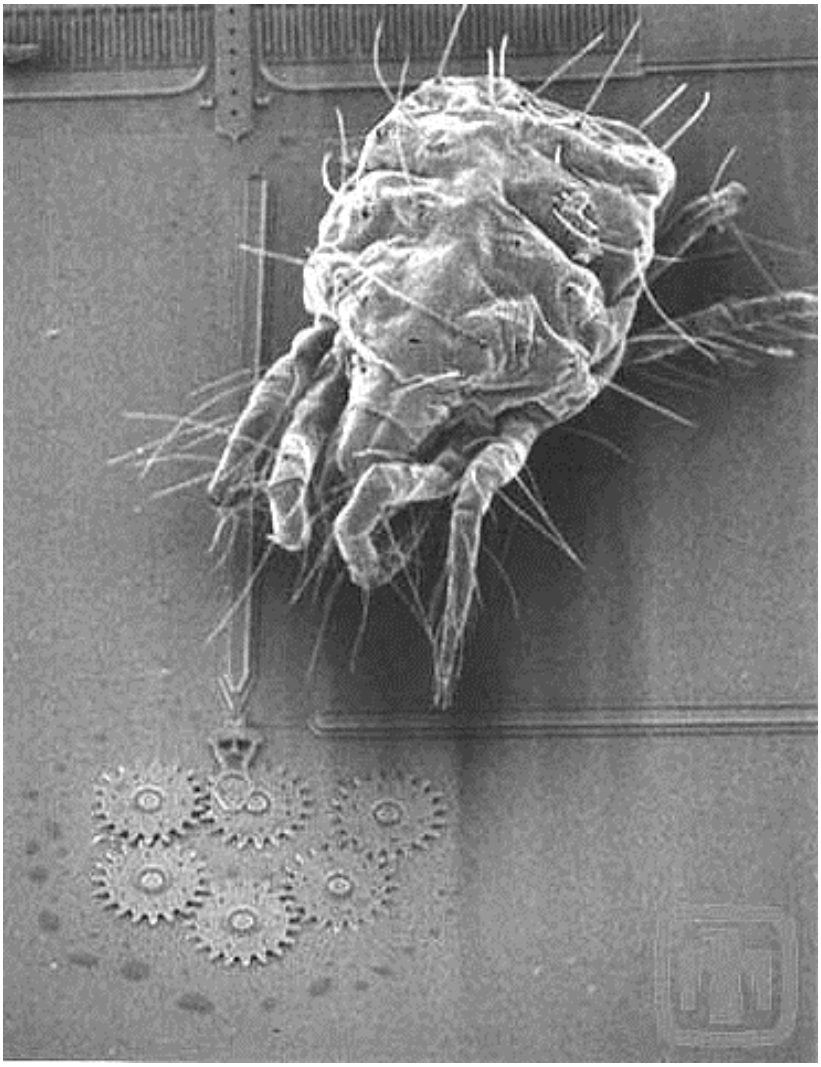

Fig. 1.7 Micro-electromechanical systems, or 'MEMS' are used in many different fields. This is an image of a mite approaching a tiny MEMS ratchet developed by Sandia Ltd [40]. It demonstrates the complexity of structures that can be built at microscopic scales.

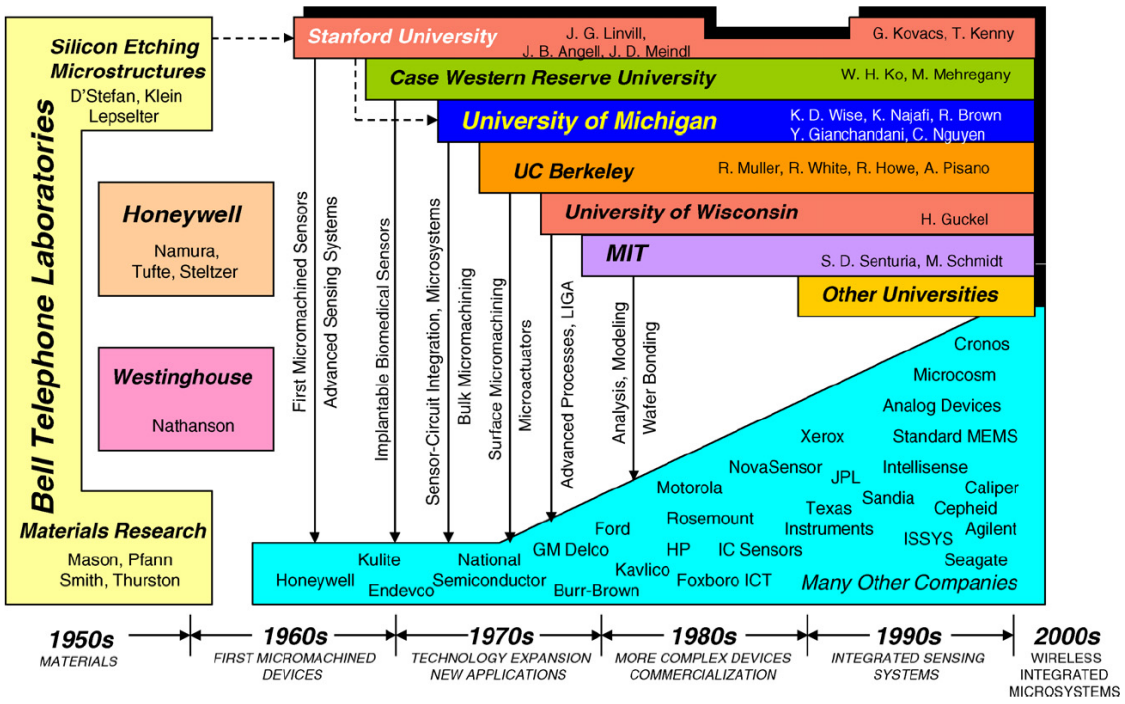

Fig. 1.8 The development of MEMS and microsystems in the U.S.A. Image reproduced from [38].

Hz. There is therefore no published data for MEMS accelerometers that achieve comparable noise floors to those of commercial gravimeters in the frequency regime below 10^{-2} Hz. This topic will be discussed in more detail later in this thesis: firstly later in this chapter, and then again in chapters 4, 5 and 6. In 2009 Sandia National Laboratories anticipated that within ten years, MEMS accelerometers may expand into 'long period' stability, which they define as 0.01 Hz [44]. As of this year, no MEMS accelerometers have demonstrated a stability that can be maintained for more than 100 seconds. This is with the the exception of the device outlined in this thesis. There is, however, a desire for instruments that achieve this criterion [45, 44, 46].

1.3 Applications of Gravimetry

As early as 1825 Sabine suggested using gravity data to look at mass variations in the Earth's crust. It was not until the 20$^{\text{th}}$ century, however, that gravimetry became a widely applied field. In 1918 Schweydar was the first person to use gravimetry to look at a salt dome [21], a geological feature that often contains trapped oil. Since this time gravimetry has grown into

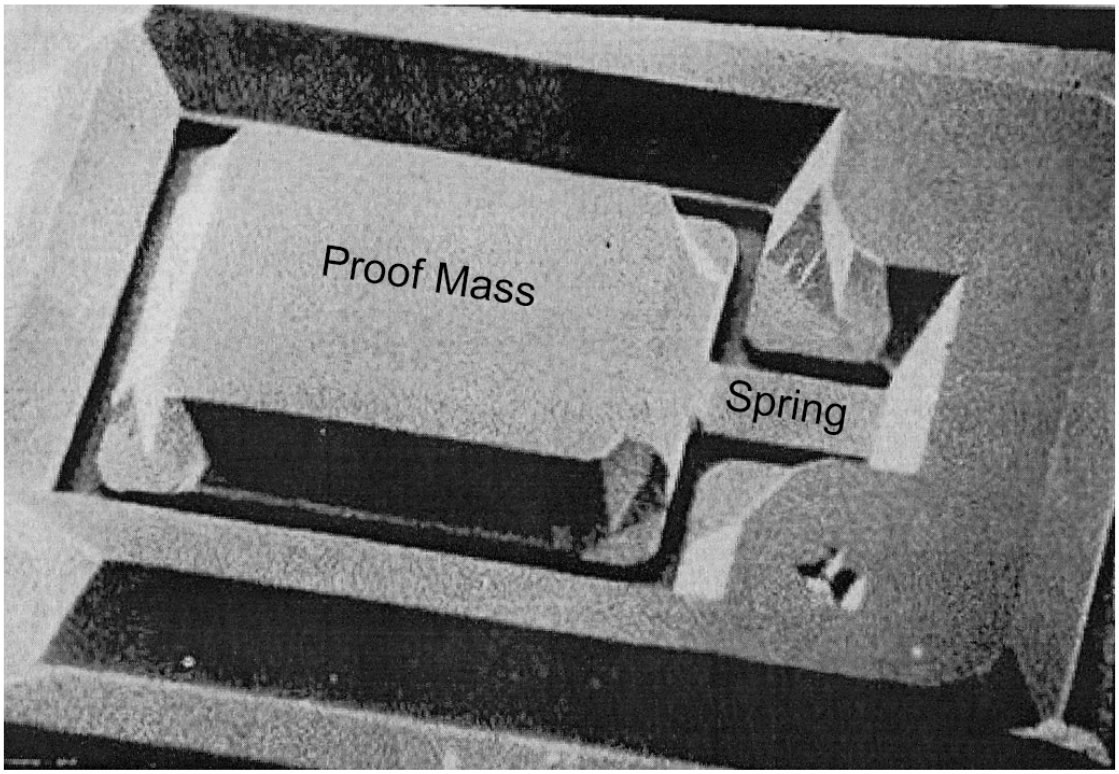

Fig. 1.9 One of the first MEMS accelerometers, developed by Roylance and Angell in 1979 [41]. Here a proof mass is suspended from a cantilever spring; its motion being measured piezoelectrically. This device had a resonant resonant frequency of over 1 kHz, and a sensitivity of only 1 Gal.

a global industry. The gravimeter instrument market is now estimated to be worth around $25 M worldwide, and the gravity survey market about the same again [47]. Gravimetry is extensively used for mineral exploration, and to a lesser extent in other fields. The gravimetry market, however, is limited by the expense of the tools used to carry out the surveys. Typical gravimeters weigh upwards of 8 kg and cost over £70 K [47]. If these devices were cheaper (and smaller) there would be scope to expand the gravimetry market greatly. In contrast, the seismic survey market for the oil and gas industry alone is worth over $1 B. This is in no small part due to the fact that seismometers are small and cheap. MEMS seismometers are quickly becoming the dominant technology in this field. Due to their small size and low cost, MEMS gravimeters could create a new paradigm in gravity mapping.

MEMS gravimeters have the potential to be used for many significant industrial applications. Given their small size and low cost, they could be used for down borehole exploration in the oil and gas industry [48] and utilised to monitor well drainage. Airbourne gravity surveys are often used by oil and gas companies but they require dangerously low altitude aeroplane flights. Commercially available gravimeters are too heavy to be carried by anything other than an aeroplane or helicopter. A MEMS-based gravimeter would be small and lightweight enough to be carried by a drone. Many types of remote sensing are already carried out using a drone platform [49] but the technology has not been previously available to include gravity sensing. Drone based gravity surveys could revolutionise the geophysical exploration industry, but many technological barriers would still need to be overcome to make this possible. MEMS gravimeters could also be utilised for environmental monitoring, where networks of sensor arrays could monitor groundwater levels [50], or to determine the location of historic landfill sites. The security industry is an area for which low cost/small form-factor gravimeters would also be a transformative technology. They could be used to detect subterranean tunnels [51, 52], or to image the inside of cargo containers where high spatial resolution via numerous sensors would be an advantage [53]. Such devices could also be used in civil engineering. At present in many of the UK Victorian cities the placement of utilities is only accurate on maps to within 15 m of land marks such as trees, fences or buildings. There have already been trials of the *Scintrex CG5* gravimeter for these civil engineering applications, and MEMS based arrays would offer an exciting opportunity to expand the use of gravity data in this field. Gravimetry is already used in volcanology and can be used to help predict eruptions. A change of 45 μGal was a 'clear precursor' to a volcanic eruption in the Canary Islands in 2011 [54]. It is accepted that intrusion of new magma into a reservoir precedes volcanic eruptions [26]; continuous micro gravity measurements around volcanoes are a useful tool in monitoring such events [55]. The ratio

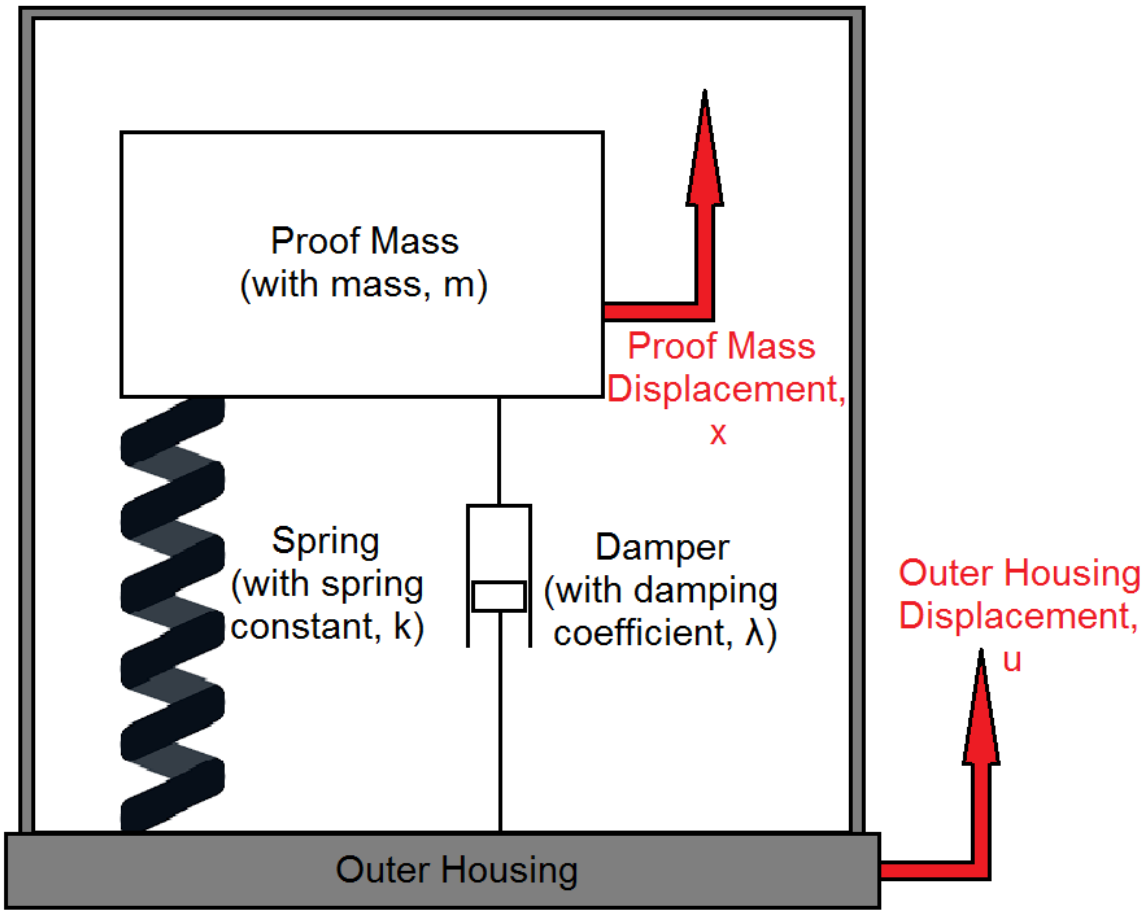

Fig. 1.10 A proof mass suspended from a damped spring, within an outer housing. Under the influence of external motion, the outer housing will move with a displacement, u, and the proof mass will move with a displacement, x.

of ground deformation to change in gravity can be used to monitor magma chambers at depths of several km [56]. Networks of small, low-cost gravimeter arrays could revolutionize the way volcano gravimetry is carried out [54, 56, 55], improving the spatial and temporal resolution of subsurface density changes. This would allow improved hazard forecasting and the reduction of occupational risk to monitoring personnel [56, 57].

1.4 Relative Gravimeter Background Theory

Since this project concerns the development of a new relative gravimeter, it is worth considering the physics behind their operation in more detail. All of the relative gravimeters and MEMS seismometers characterised in figure 1.14 utilise the same basic mechanical

system: a mass on a spring. However, the resonant frequency of the system and the means of measuring the mass displacement vary from instrument to instrument. A mass on a spring behaves as a harmonic oscillator. Such a system is pictured in figure 1.10. This figure shows a proof mass m, suspended by a spring (with a spring constant, k) from the inside of an outer casing. The proof mass will respond dynamically when the outer casing is itself acted upon by an external motion. Let us define x as the displacement of the proof mass, and u as the displacement of the outer casing. The equation of motion for the system can therefore be defined by balancing the external and internal forces that act upon the proof mass [58, 59]:

$$m\frac{\delta^2}{\delta t^2}(x+u) = -kx \tag{1.16}$$

Dividing equation 1.16 through by m gives:

$$\frac{\delta^2}{\delta t^2}(x+u) = -\frac{k}{m}x \tag{1.17}$$

Since the ratio of k/m is equal to the angular resonant frequency of an oscillator, ω_0^2, equation 1.17 can therefore be written as:

$$\frac{\delta^2 x}{\delta t^2} + \omega_0^2 = -\frac{\delta^2 u}{\delta t^2} \tag{1.18}$$

If the oscillating system is damped, then a further term needs to be included in equation 1.18. Damping is carried out by applying a force that is proportional to the velocity of proof mass relative to the outer housing. The equation of motion becomes:

$$\frac{\delta^2 x}{\delta t^2} + 2\lambda\omega_0\frac{\delta x}{\delta t} + \omega_0^2 = -\frac{\delta^2 u}{\delta t^2} \tag{1.19}$$

where λ is the damping ratio. A system with a damping ratio of 1 would be critically damped. To simplify this partial differential equation, $\delta/\delta t$ can be replaced with $i\omega$ (by taking the Fourier Transform):

$$-\omega^2 x + 2i\lambda\omega_0\omega x + \omega_0^2 x = \omega^2 u \tag{1.20}$$

Equation 1.20 describes the motion of the proof mass, x, relative to the motion of the outer housing, u. It can be expressed in the form of a transfer function if the output of the system is divided by the input. Let us consider how the system will behave depending on how the measured ground frequency compares to the resonant frequency of the device. Leaving the left hand side of equation 1.20 as a displacement output, the right hand side can be expressed in three three ways:

Equation 1.20 can be written in terms of the acceleration of the outer housing:

$$-\omega^2 x + 2i\lambda\omega_0\omega x + \omega_0^2 x = -\frac{\delta^2 u}{\delta t^2} \tag{1.21}$$

and the transfer function (output over input) is given by:

$$\frac{x}{\frac{\delta^2 u}{\delta t^2}} = \frac{-1}{-\omega^2 + 2i\lambda\omega_0\omega + \omega_0^2} \tag{1.22}$$

Equation 1.20 can be written in terms of the velocity of the outer housing:

$$-\omega^2 x + 2i\lambda\omega_0\omega x + \omega_0^2 x = i\omega\frac{\delta u}{\delta t} \tag{1.23}$$

and the transfer function is given by:

$$\frac{x}{\frac{\delta u}{\delta t}} = \frac{i\omega}{-\omega^2 + 2i\lambda\omega_0\omega + \omega_0^2} \tag{1.24}$$

Equation 1.20 can be written in terms of the displacement of the outer housing:

$$-\omega^2 x + 2i\lambda\omega_0\omega x + \omega_0^2 x = i\omega^2 u \tag{1.25}$$

and the transfer function is given by:

$$\frac{x}{u} = \frac{-\omega^2}{-\omega^2 + 2i\lambda\omega_0\omega + \omega_0^2} \tag{1.26}$$

The transfer functions characterised by equations 1.22, 1.24, and 1.26 have been plotted in figures 1.11, 1.13, and 1.12 respectively.

In the centre of the plot in figure 1.11 a resonance peak can be seen. In the sub-resonance region of this figure (the left hand side of the plot) there is a constant relationship between the acceleration of the housing, $\delta^2 u/\delta t^2$, and the displacement of the proof mass, x. This is

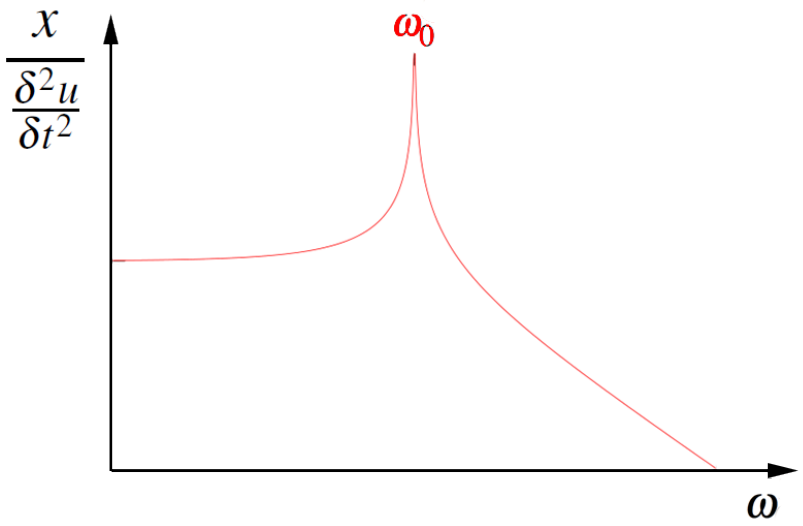

Fig. 1.11 The acceleration transfer function of an ideal harmonic oscillator in a box. In the region below the resonance peak there is a constant relationship between acceleration of the outer housing, and the displacement of the mass. The size of the resonance peak decreases with damping.

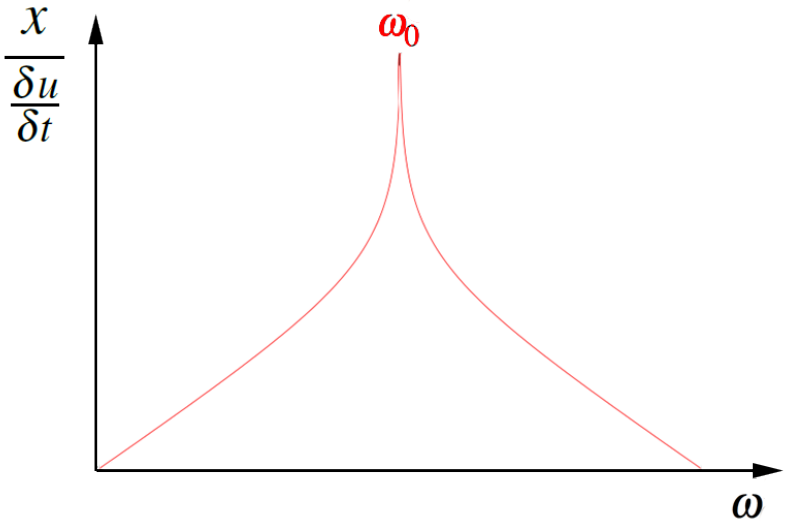

Fig. 1.12 The velocity transfer function of an ideal harmonic oscillator. The size of the resonance peak decreases with damping.

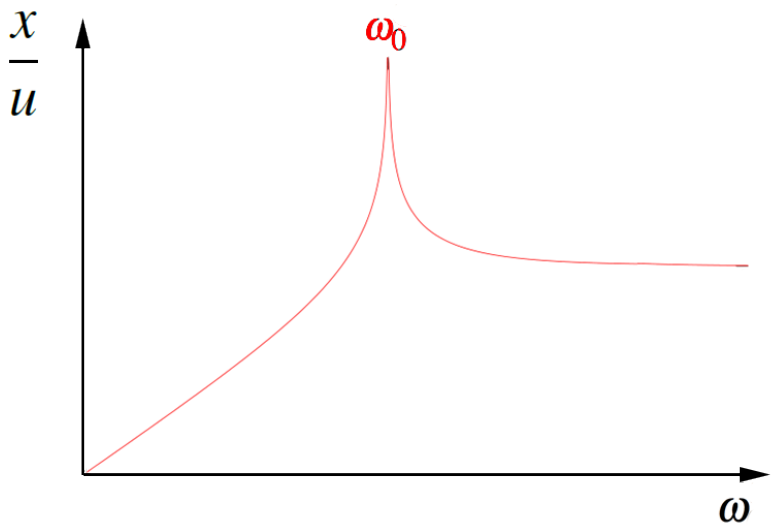

Fig. 1.13 The displacement transfer function of an ideal harmonic oscillator. In the region above the resonance peak there is a constant relationship between displacement of the outer housing, and the displacement of the mass. The size of the resonance peak decreases with damping.

the region where the system can be used as an accelerometer because a simple reading of the displacement of the proof mass relative to the housing will provide a measurement of the acceleration of the whole instrument. At frequencies higher than the resonance, the device acts as a displacement sensor and the sensitivity to accelerations of the outer housing is diminished. The device will therefore be isolated from acceleration signals above its resonant frequency but be sensitive to those below.

The resonant frequency of a relative gravimeter can therefore be selected in order to isolate from different areas of the seismic spectrum. As mentioned earlier, a low resonant frequency is an advantage to a gravimeter because it implies that the ratio of k/m has been minimised. For a given external acceleration, the proof mass of a device with a low resonant frequency will be displaced further than one with a higher resonant frequency. This either means that the acceleration sensitivity is improved, or that the acceleration sensitivity can be maintained but with a displacement sensor that does not need to be so accurate.

1.5 Other Gravimeters and Seismometers

The distinction between seismometers and gravimeters is a subtle one. Seismometers are used to measure inertial acceleration caused by vibrations within the Earth's crust; and like gravimeters, high acceleration sensitivity is also essential. They are even applied in

similar geophysical applications to gravimeters. The distinction can be muddied further by considering Einstein's equivalence principle, which states that inertial and gravitational accelerations are fundamentally indistinguishable. So what, one may ask, is the difference between these instruments? The answer can be found by observing the frequency ranges within which useful seismic signals, and useful gravimetric signals can be observed. For spatial or temporal gravity surveys it is important that gravimeters remain stable for days, weeks or months. Seismic surveys, however, are not designed to measure the long term acceleration changes that gravimeters are capable of recording. Most seismometers are designed to operate in the 10 Hz - 100 Hz range, where surface seismic signals are typically dominant [60]. Seismic data below this range are referred to as 'low frequency' [61]. The 'long period seismic band' occurs at frequencies below this, and includes signals down to 10^{-4} Hz [62, 63]. Below 10^{-4} Hz is the regime of the gravimeter. The Earth tides – which occur at around 10^{-5} Hz – are often used as a calibration of gravimeter precision for continuous recordings [64]. An ability to measure the Earth tides is therefore a useful bench-mark for a practical gravimeter. Until now, no MEMS accelerometer has been reported that can operate as a gravimeter. Several can operate with sufficient sensitivity, but none with a stability to monitor gravitational signals below 10^{-2} Hz [44], let alone 10^{-4} Hz.

In this chapter multiple kinds of acceleration measuring devices have been described, and their advantages/disadvantages discussed. A useful method of viewing how these devices compare with one another is by graphing their acceleration sensitivities in frequency space. Such a graph – known as a spectral density plot – is displayed in figure 1.14. The acceleration sensitivities form the y-axis of the graph and are plotted in units of power: $\mu\text{Gal}^2/\text{Hz}$ (as opposed to amplitude [$\mu\text{Gal}/\sqrt{\text{Hz}}$]). The lower x-axis is in units of frequency, but a useful conversions to temporal space have been highlighted at the top of the graph. The power spectral densities for eight different instruments are displayed in this graph. It is clear that different instruments operate over a range of frequencies, and with varying sensitivities.

Let us first consider the instruments in figure 1.14 that are classed as seismometers. To the far right hand side of the plot are two MEMS seismometers: the pink series is a MEMS seismometer by Pike et al. [65] and the dark blue series is a commercial MEMS seismometer by *Microseis* [66]. It can be observed that although these devices achieve exceptional acceleration sensitivity in the short term, they do not operate for long timescales: no data for either has been published in the frequency range below 10^{-2} Hz. It is likely that the acceleration sensitivities of both of these instruments would rise sharply below this point in frequency space because neither are temperature controlled.

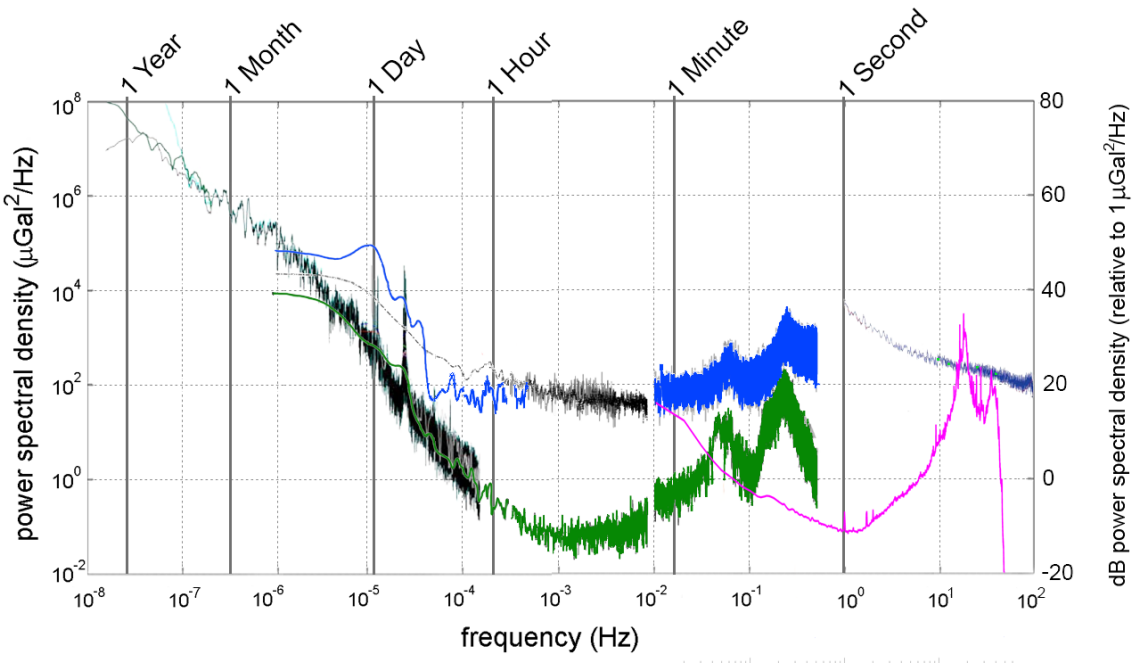

Fig. 1.14 A power spectral density plot displaying data for a selection of commercial gravimeters, and two MEMS seismometers. The power spectral density demonstrates the acceleration sensitivity of these devices as a function of frequency. From left to right the series are as follows: the green series is the *GWR Instruments SG-C026* superconducting gravimeter, the black series is the *GWR Instruments SG-C021* superconducting gravimeter, the cyan series is also the *GWR Instruments SG-C021* superconducting gravimeter but with a polynomial drift removed, the royal blue series is the *Micro-g Lacoste gPhone-054* gravimeter, the black dashed series is the *Scintrex CG5* gravimeter, the racing green series is the the *Micro-g Lacoste FG5* gravimeter, the pink series is a MEMS seismometer by Pike et al., and the dark blue series is a commercial MEMS seismometer by *Microseis*.

All of the other instruments in figure 1.14 are classed as gravimeters[6]. They are all commercial products used to monitor variations in gravitational acceleration over long time scales. All of these devices are designed with the aim of keeping their acceleration noise floor as low as possible, as far down the frequency range as possible. It is clear, however, that the different gravimeters are themselves divided into groups that occupy different frequency band widths. These groupings are broadly dependent on the technology used to construct the instrument.

Consider the instruments that occupy the far left hand side of the plot: the devices that can operate over the longest timescales/down to the lowest frequencies (over timescales of more than a year!). There are three series here: the green series is the *GWR Instruments SG-C026* superconducting gravimeter [67], and the black and cyan series are the *GWR Instruments SG-C021* superconducting gravimeter with and without a polynomial drift respectively [16].

Let us now turn our attention to the grouping of gravimeters that lie between 10^0 Hz and 10^{-6} Hz. There are two different technologies represented by the series in this region. The blue and black series are data acquired from spring-based relative gravimeters. The royal blue series is the *Micro-g Lacoste gPhone-054* gravimeter, and the black dashed series is the *Scintrex CG5* gravimeter [16]. The dark green series is that of an absolute free-fall gravimeter, the *FG5* [16]. It can be observed that the absolute free-fall device achieves a lower acceleration noise floor than the two relative spring-based devices.

Since the aim of this PhD project was to create a relative MEMS *gravimeter*, some of the series in figure 1.14 are more important to consider than others. A MEMS device will never achieve the sensitivity of an absolute device, or the stability of a superconducting gravimeter. An ideal result would be a device that achieved a noise floor similar to the spring-based relative gravimeters, and over a similar frequency range. A companion graph to figure 1.14 is displayed in figure 6.1. Figure 6.1 shows the same data as figure 1.14, with the addition of data acquired from the device developed during this PhD project. Table 1.1 contains further specifications of some of the devices from figure 1.14 that are relevant comparisons for a MEMS gravimeter. Drift values are not provided for MEMS seismometers because no data is available for these devices below 10^{-2} Hz.

[6]It is worth noting that there is an overlap in frequency space between the seismometers and the gravimeters; hence the ambiguity in the distinction of these two classes of instrument that can both measure acceleration.

Table 1.1 A comparison of a relative spring-based gravimeter, and three MEMS seismometers.

Device	Technology	Sensitivity at 1 Hz	Inherent Drift	Resonant Frequency	Use
Scintrex CG5 [12, 13]	Fused Quartz	2 μGal	0.5 mGal/day	3 Hz	Gravimetry
Krishnamoorthy [68]	MEMS	17μGal	N/A	36 Hz	Seismology
Quietseis [66]	MEMS	15 μGal	N/A	800 Hz	Seismology
Pike [65]	MEMS	0.3 μGal	N/A	6 Hz	Seismology

Chapter 2

Geometrical Anti-Springs for Low Frequency Gravity Sensors

As discussed in the previous chapter, MEMS accelerometers are ubiquitous across the automotive and smart phone industries. These accelerometers have resonant frequencies in the kHz range. One way to maximise the sensitivity to gravitational acceleration is to minimise the ratio of k/m, or in other words: reduce the resonant frequency. The design specification for the MEMS gravimeter developed through the course of this PhD project was governed by this principle. A resonant frequency target for the device was set at 4 Hz or lower. For accurate displacement measurement of the mass, it was also important that the geometry allowed motion only in one dimension (or as close to one dimension as practically possible). This was the second major design specification. The final design target was that the device would be capable of measuring in all three dimensions: g_x, g_y and g_z. The geometry of the MEMS device was crucial to achieving all of these targets, and several designs were considered before ultimately settling on a geometrical anti-spring geometry. The finite element analysis (FEA) software, ANSYS, was used to test the efficacy of the three designs that were considered. Appendix B gives greater details about the ANSYS software package.

2.1 Early Designs

2.1.1 Serpentine

The first design considered utilised a design seen in other MEMS accelerometers [68]. A proof mass was suspended between two serpentine springs (as seen in figure 2.1). ANSYS

models suggested that the device had a maximum stress in the flexures of only 50 MPa. This level of stress was well inside the 2 GPa breaking stress of pristine crystalline silicon [69]. Etched silicon, however, will have micro-cracks in the surface which can reduce the breaking stress to hundreds of MPa [70]. By increasing the length of the springs in the *y*-direction to over 10 mm, and decreasing their profile to 15 μm, an optimal resonant frequency of 6 Hz could be reached. Secondary modes were also measured of about 90 Hz in both the y and x dimensions (as displayed in figure 2.1). This information was ascertained using ANSYS. This design, however, was highly susceptible to out-of-plane bending. The out of plane bending can be modelled by assuming that the mass is placed at the end of two flexures, each the length of one of the unfolded serpentine springs (about 80 mm each). The out of plane displacement of the proof mass when placed horizontally is therefore given by:

$$\delta_{\max} = \frac{FL^3}{48EI} \tag{2.1}$$

where F is the force of the proof mass due to gravity, L is the total length of the two flexures, E is the Young's modulus of silicon (150 GPa) and I is the moment of the beam. I is given by $wt^3/12$ where w is the width of the beam and t is the thickness of the beam. If the serpentine springs were the only mechanical support for the proof mass, then when turned horizontal it could sag as much as 13 mm. Any multidimensional movement of the mass makes optical displacement measurements much more difficult because it is hard to decouple motion in more than one dimension in these measurements. In an effort to reduce this effect, stabilising ribbons were added to the sides of the proof mass. These can be observed in figure 2.1, connecting the proof mass to the outer frame. The ribbons, however, had the effect of increasing the resonant frequency. Ultimately it was impossible to model a structure with this geometry that had both a low enough resonant frequency, and little out-of-plane (x-axis) motion. For these reasons it was decided to model other designs before progressing to the fabrication stage.

2.1.2 Inverted Pendulum

The next design considered can be seen in figure 2.2. This design utilised the tensile strength of silicon. By suspending the test mass from silicon pendula, flexures within these pendula could be reduced in width to reduce the resonant frequency of the sensor. This design was inspired by historical pendulum gravimeters, and more recently the development of a pendulum gravimeter by Micro-g Lacoste [71, 72]. To stop the mass swinging in an arc, an inverted pendulum was added to the bottom of the test mass to provide a negative restoring

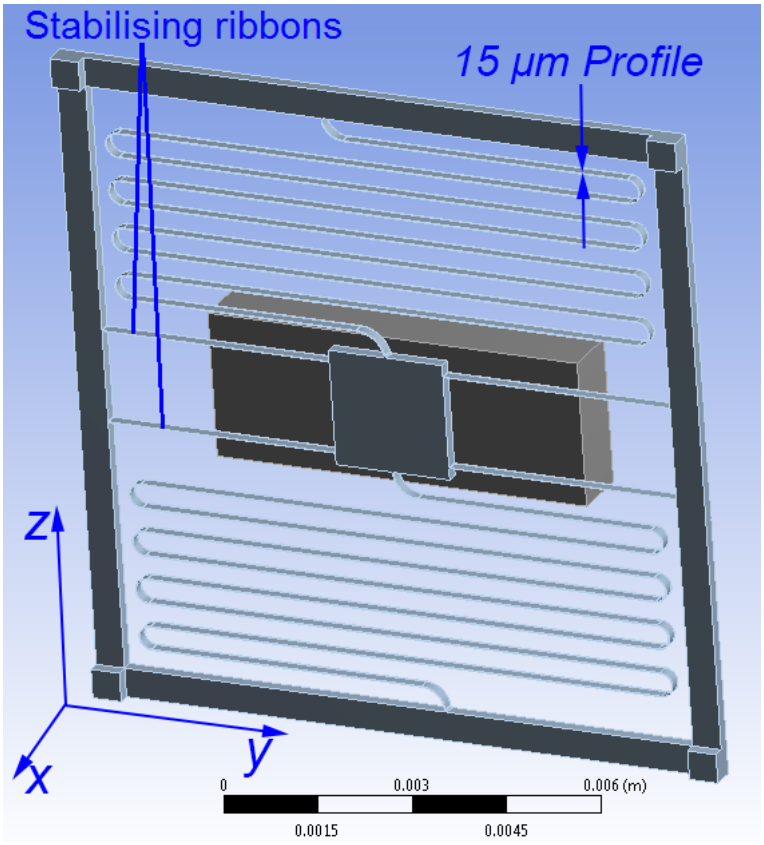

Fig. 2.1 A schematic of the serpentine flexure design. Although reaching a favourable resonant frequency of 6 Hz, this design was shelved due to to significant out-of-plane bending.

force. This aided stability and ensured parallel transport of the mass in the horizontal plane. Unlike the serpentine spring design, multidimensional motion of the mass was minimal, making displacement measurements easier. Using ANSYS, careful tuning of the length of the pendula/inverted pendula (and the mass of the proof mass[1]), demonstrated that the horizontal resonant frequency could be reduced to 1.4 Hz. A plot of this optimisation process can be seen in figure 2.3. The maximum stress in this design was modelled in ANSYS to be 200 MPa. This figure is an order of magnitude smaller than the breaking stress of perfect crystalline silicon [69]. The value was chosen as a safety factor [73] because it was expected that micro-cracks in the surface of silicon would significantly reduce the strength of the material. Micro-cracks would inevitably develop through the process of etching the silicon [74–77]. The likelihood of a flexure breaking follows a cumulative distribution function [75], with the risk of failure increasing as the stress in the system rises. A safety factor of 10% was deemed as appropriate to mitigate against regular breakages of the MEMS devices. The stress in the system, however, would have been substantially greater if the device were tilted onto its side. In this situation, the stresses would move away from being mostly tensile, and breakages would be very likely. Fabrication problems were also an issue for this design: adding the mass in two halves on each side of the mass plate would have increased the number of process steps and therefore increased the chance of material failure. The two halves would also have had to be aligned prohibitively accurately (to less than 1 μm where 10 μm was the fabrication tolerance) in order to avoid an increase in the primary resonant frequency, and the introduction and lowering of other unwanted resonant modes. Ultimately, however, it was this sensor's inability to provide readings of the horizontal components of gravity (g_x and g_y) that caused it to be abandoned.

2.2 Geometrical Anti-Springs

In the pursuit of a sensor capable of measurement of the g_z component of the gravity tensor, a geometrical anti-spring design was considered. An anti-spring can be characterised as having a negative or at least partially negative restoring force. As an anti-spring moves away from its nominal position, the spring constant lowers. This is in contrast to classical springs

[1] Obviously, the frequency of a pendulum is not a function of the suspended mass. So increasing the mass of the proof mass would not decrease the frequency of the system. This system, however, is not a perfect mathematical pendulum: it will also behave with a spring-like behaviour. As the system oscillates side to side, the flexures will stretch, inducing a restoring force. Also, the flexures are not perfect pivots, instead they include very thin sections of silicon that will bend easily. Despite being very soft, these thin sections will still have a spring constant.

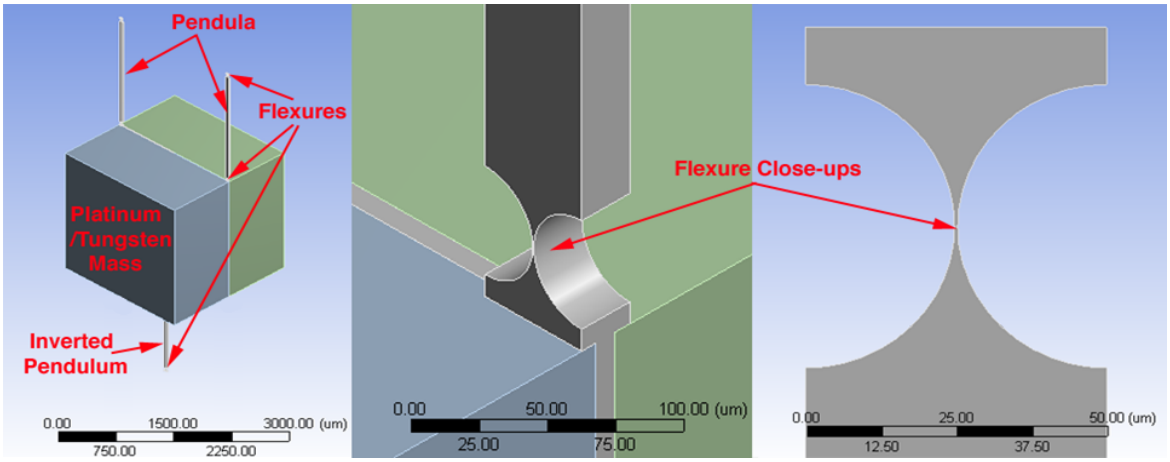

Fig. 2.2 A schematic of the horizontal flexure design. Despite a resonant frequency of 1.4Hz and favourable 1D motion, this design does not allow measurement of the g_x and g_y (horizontal) components of the gravity tensor.

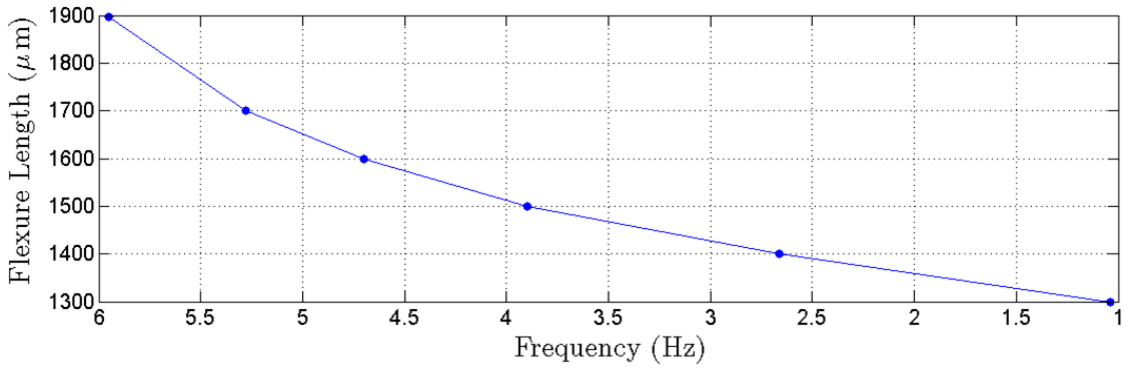

Fig. 2.3 A plot of the optimisation of the flexure length (see figure 2.2) that allowed a resonant frequency of 1.4 Hz to be reached. This data was acquired by Paul Campsie using ANSYS. From equation 1.2, it would be expected that as the flexure length increases, the resonant frequency would decrease.

for which the spring constant remains the same during stretching, assuming the absence of mechanical hysteresis or environmental changes. This non-linear behaviour of force versus displacement can be induced in a classical spring by means of magnetic actuation [78]. Here, however, geometrical means of achieving anti-spring behaviour will be focussed upon. Euler buckling springs [79], for example, are comprised of a pair of vertical ribbon springs, under compression they buckle in opposite lateral directions. The force required to buckle the springs further reduces as the vertical displacement increases – an anti-spring behaviour. The torsion crank linkage is another example of a geometrical anti-spring [80, 81]. In this configuration a non-linear restoring force is achieved by linking a pair of torsion-sprung crank arms with a linkage from which a mass is suspended vertically. The linkage constrains the motion of the crank arms along a vertical line. A third way to design an anti-spring is using curved monolithic cantilevers, again connected at a central point to constrain the motion vertically. Monolithic geometrical anti-springs are used as low frequency seismic isolators in the Virgo Gravitational Wave Detector [82–84].

With the aim of achieving better acceleration sensitivity for the MEMS gravimeter, a monolithic geometrical anti-spring configuration was opted for that would give the MEMS a low resonant frequency of under 10 Hz. A monolithic geometry was important so the device could be fabricated from a single silicon chip (see next chapter on fabrication). The geometry of the MEMS was based on the isolation system of the Virgo gravitational wave detector.

The initial design consisted of two pairs of arched flexures like the pair seen in the left hand image of figure 2.4. Each pair is centrally constrained on a proof mass[2]. This created an axis along which the motion was constrained, allowing the geometrical antispring effect to occur. The geometry can be seen in the upper schematic of figure 2.4. The flexures are ribbon-like, they are only 5 μm wide but are 200 μm deep (into the page) and are each about 7 mm long from the outer frame to the centre. The flexures have a radius of curvature of about 6 mm. The high aspect ratio of the flexures was chosen to minimise the resonant frequency of the vertical primary mode, whilst maximising the frequencies of of other mechanical modes[3]. Initially due to an accidental breakage of one of the four flexures, a configuration of three flexures was also investigated. A schematic diagram of this configuration is displayed right hand side of figure 2.4. This 'broken' device, however, turned out to be a remarkably effective

[2]The proof mass in figure 2.4 is an oblong of dimensions 4.5 mm $\times$ 10 mm. Originally, this had been designed as a square but it was realised that if the square was used then the proof mass would touch the lower flexures as it was displaced vertically. The square proof mass design is pictured in figure 3.12 in the following chapter.

[3]On closer inspection of the flexure profile in a scanning electron microscope (SEM), it was observed that the flexures were not rectangular. Due to the fabrication process, they tapered from 7 μm at the top, down to about 5 μm at the bottom of the 220 μm wafer, creating a trapezoidal profile.

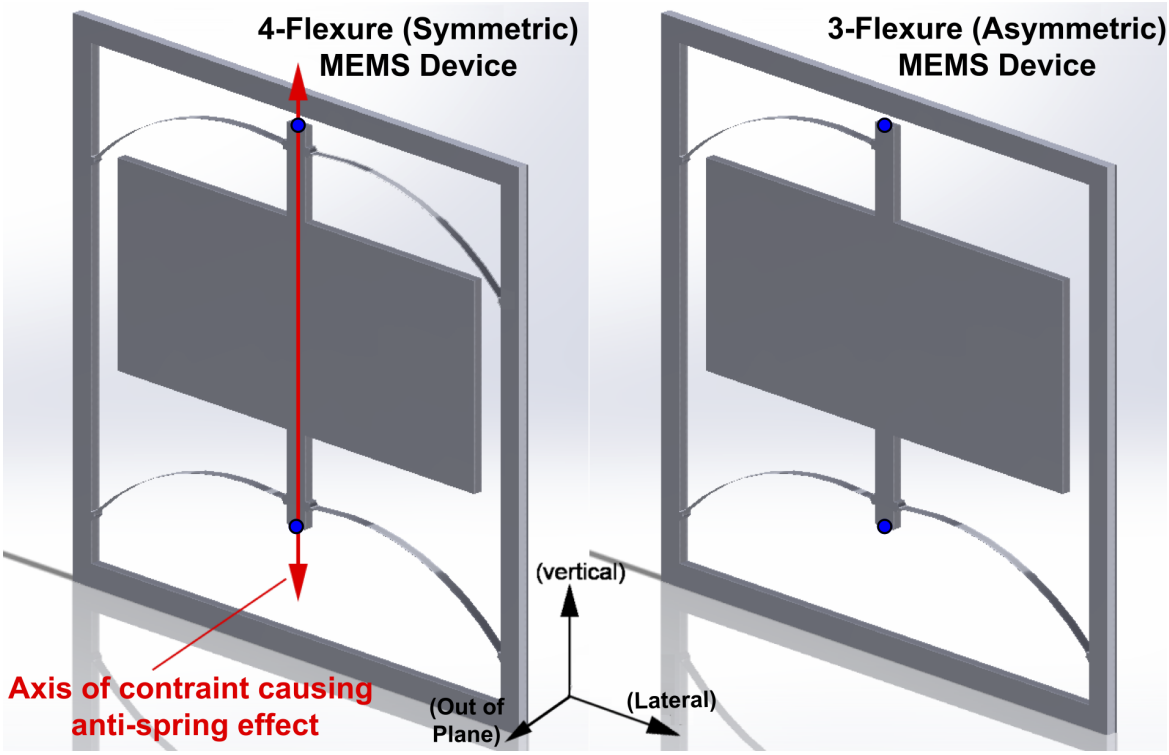

Fig. 2.4 The two different anti-spring geometries. The left hand image is the initial design consisting of four flexures. The right hand image is the asymmetric variation in which the top right flexure has been removed. The flexures have a high aspect ratio, they are 220 μm deep but only 5 μm wide. The proof masses are 10 mm $\times$ 4.5 mm $\times$ 220 μm, and therefore weigh 23.1 mg. The anti-spring effect is caused by the constraint of the motion of the proof mass in the vertical dimension (this axis is highlighted in red). This effect is observed in both the four and the three flexure designs, although the two do behave differently. The blue dots are the vertex points used to calculate the tilt of the proof mass discussed later in this chapter.

design, with many characteristics that were an improvement on a four-flexure system. These characteristics will be the topic of the rest of this chapter.

2.2.1 Are Three Flexures Better Than Four Flexures?

To better understand the characteristics of an anti-spring MEMS geometry with differing numbers of flexures, it is worth working through how a mass on spring system would behave with differing numbers of flexures and different shapes of flexures. Figure 2.5 provides a summary of the force versus displacement behaviour for 5 different geometries. All of the plots in figure 2.5 were created using ANSYS finite element analysis models. In the models the geometries were placed vertically in a gravitational field of 9.8 m/s^2, the proof masses were then released and allowed to displace under the influence of gravity. The model tracked

the displacement of the device from 0% to 100% of the gravitational force. A more detailed discussion of the way in which ANSYS was used to analyse the MEMS device can be found in Appendix B.

Let us first consider a very simple situation: a cantilever, clamped at one end, and free to move at the other. A proof mass mounted on the moving end will oscillate with a frequency that depends on the profile of the cantilever, and the Young's modulus of the material from which it is made. The proof mass will oscillate along an arc, defined by the length of the flexure. The system will behave as a Hooke's Law spring, with a linear relationship between force and displacement. This behaviour can be observed in figure 2.5a. The next plot shows the same behaviour for a single cantilever with a curved profile.

To create an anti-spring, one can take two such curved cantilevers and attach them at a central pivot point. A proof mass mounted at this point will no longer be able to trace out an arc as it oscillates. Instead – because of the symmetrical forces applied by the two identical cantilevers – its motion will be constrained along a vertical axis (as presented in figure 2.4). It is this constraint that forces the spring constant to change as the displacement increases. Instead of observing a linear relationship between force and displacement, a non-linear behaviour is found. This behaviour can be observed in figure 2.5c. This now means that the spring gets softer with increasing displacement.

A four flexure anti-spring system is a simple extension of a two-flexure system. Here, a second pair of cantilevers are placed below the first pair, this allows a non-point source proof mass to be suspended. The behaviour of the spring is still non-linear, and is displayed in figure 2.5d. The behaviour is identical to that of a two flexure system, except the system can support twice the mass.

Both the two and four anti-spring systems can be used to create oscillators that have low resonant frequencies. When the limits of k/m are pushed to create the lowest resonant frequency possible, however, these systems become unstable. They become unstable because the motion is so well constrained along its vertical axis, the spring gets softer and softer until it can no longer support the weight of the proof mass. This behaviour can be observed in figures 2.5c and 2.5d: as the force increases, the displacement increases rapidly. A stable resonant frequency is imperative for a useful relative gravimeter, therefore this instability would create problems if used for the design of a MEMS gravimeter. It would require the use of a closed-loop feedback system.

Now consider a three-flexure anti-spring system, with one flexure of the upper pair of cantilevers removed. In the first instance, the device behaves as a four-flexure anti-spring: it gets rapidly softer as the displacement of the proof mass increases. The anti-spring

behaviour is maintained while the proof mass moves along its vertically constrained axis. The asymmetry of the system, however, means that the device does not stay constrained along the anti-spring constraining axis. The single upper flexure ultimately tilts the proof mass marginally away from the constraining axis. As the motion is pulled from this axis, the anti-spring trend is halted and the device regains a Hooke's Law behaviour, where dF/dz = constant. This behaviour can be observed in figure 2.5e where the gradient of force vs displacement reaches a minimum at Displacement = 0.6.

To further understand the system, ANSYS models were run to investigate the resonant frequencies of the three and four flexure systems. ANSYS is capable of finding all of the resonant modes of the structure, for which an analytical solution would be extremely challenging to calculate. Figure 2.6 demonstrates the strength of ANSYS for finding higher order modes of oscillation. In this figure the first six modes of the 3-flexure system are shown. An ideal system would have a low frequency in one sensitive axis, and infinitely high frequencies for all higher modes. This would mean that the device would only move in 1D, making the measurement of its displacement much simpler. This 3-flexure system achieves a ratio of 1:27 between the first and second modes, meaning that there will be little motion of the device outside of its sensitive axis.

2.2.2 Modelling and Experimental Results of a 4-Flexure System

To investigate the behaviour of the 4-flexure anti-spring design, a MEMS device was gravitationally loaded by increasing its mass. Pieces of 50 μm thick indium foil were placed on the MEMS proof mass and melted into position by heating radiatively with a halogen bulb. Each time mass was added the resonant frequency was recorded. This was carried out by clamping the MEMS vertically in a rotation stage (see figure 2.7). This rotation stage could be turned through 360°. A micrometer was mounted on the stage and used as a clamp to hold the MEMS device. Two strips of rubber were glued to the mouth of the clamp to avoid breaking the silicon whilst maintaining a good grip on the sample. A spectrum analyser could have been used for the purpose of measuring the resonant frequency, in fact, this could have provided a more accurate measurement. Given the delicacy of the samples it was thought that using a mode of measurement that could be carried out remotely (i.e the camera) would be preferable to avoid breaking the MEMS device.

The device was tilted from horizonal to vertical, and excited by tapping the table with a fist. The amplitude of the primary mode of oscillation ranged from around 100 μm to 1 mm. This amplitude depended on the impulse of the tap and the current resonance of the device.

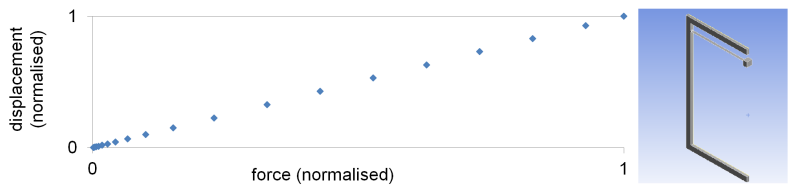

(a)

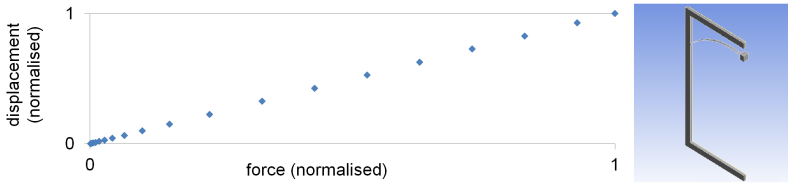

(b)

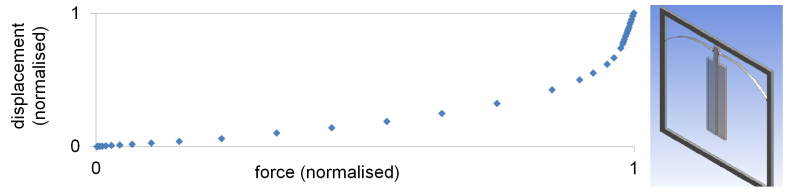

(c)

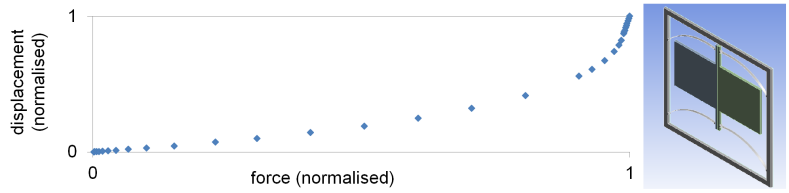

(d)

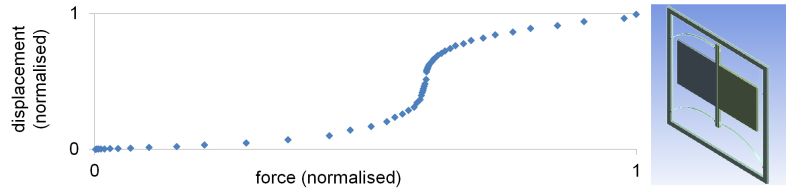

(e)

Fig. 2.5 . Figures 2.5a and 2.5b demonstrate the Hooke's Law behaviour of a straight and curved cantilever respectively. Figures 2.5c and 2.5d demonstrate the unstable anti-spring characteristics of a 2 and 4 flexure MEMS device respectively. Figure 2.5e demonstrates behaviour of a 3 flexure MEMS device (see the right hand image of figure 2.4). Whilst a 2 or 4 flexure system reaches an instability with increasing load, a 3 flexure system regains a Hooke's Law behaviour. The 3-flexure system behaves as such because it is pushed off its constrained axis by the asymmetry of the design. All of these plots were produced using ANSYS finite element analysis software.

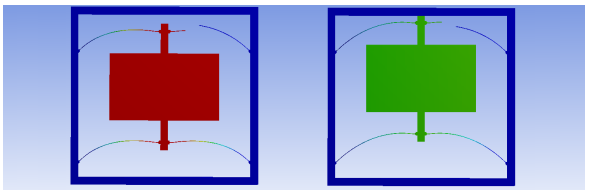

(a)

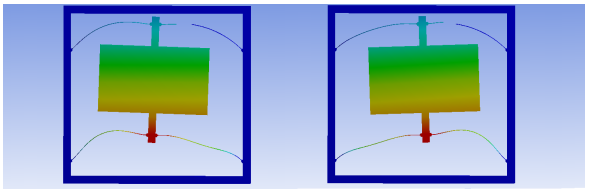

(b)

(c)

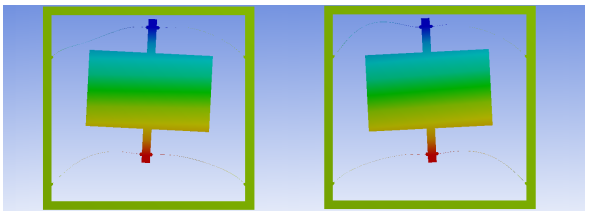

(d)

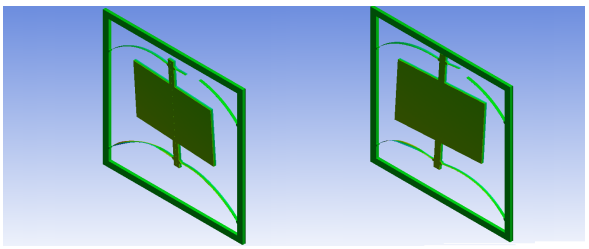

(e)

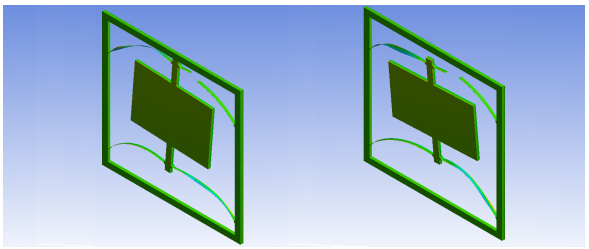

(f)

Fig. 2.6 . This figure demonstrates the first 6 modes of the 3-flexure system, calculated using ANSYS. From top to bottom the modes have frequencies of 2.3 Hz, 62.3 Hz, 107.7 Hz, 110.2 Hz, 204.4 Hz and 350.3 Hz.

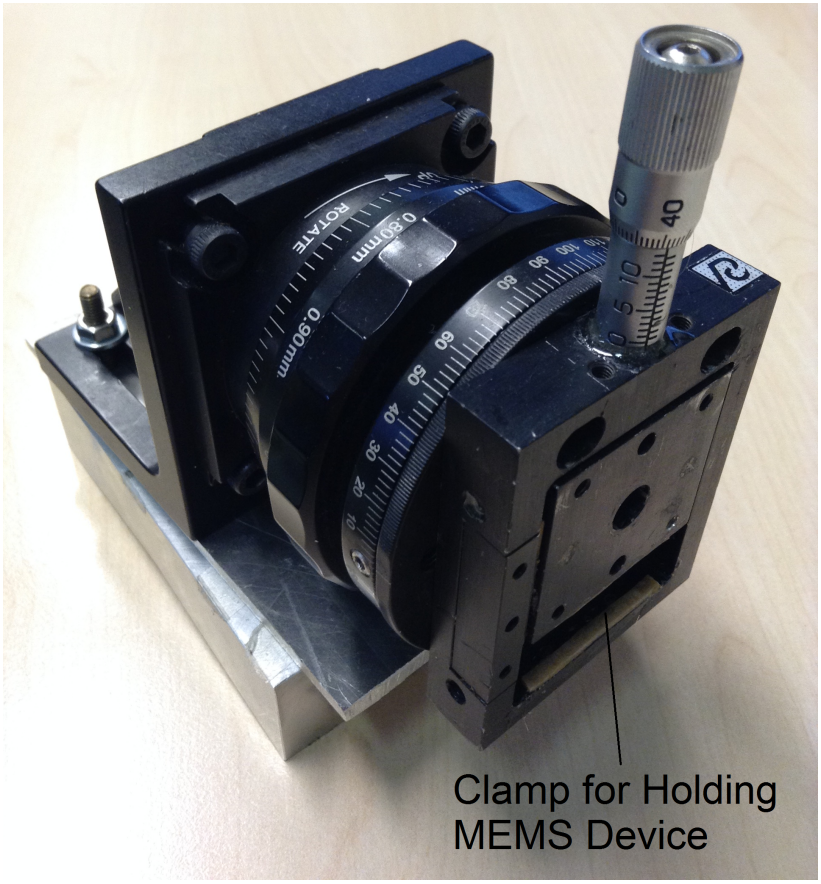

Fig. 2.7 The rotation stage used to measure the resonant frequency of the MEMS devices. MEMS devices were placed in the clamp and tilted to 90°, they were then excited and filmed with a fast frame rate camera to measure the resonant frequency.

To measure the frequency, at least ten oscillations were filmed with a 210 frame/second camera. As more mass was added the resonant frequency decreased, as would be expected in a geometrical anti-spring. With greater mass, this resonant frequency started to drop quickly, ultimately reaching a point at which the slightest acceleration shock would make the oscillator unstable. At this point the proof mass would drop onto the bottom frame. Recovery was only possible by manually pushing the device upwards. The blue trend in Fig. 2.8 shows this data, the error represents the precision with which the indium foil could be measured and cut with a scalpel.

This experimental test was also modelled using ANSYS. This model was designed to match the experimental design as closely as possible: a trapezoidal structure was included with a taper from 7 μm down to 5 μm, but the scalloping caused by the Bosch Process[85] (see chapter 3) was not modelled. The red series in Fig. 2.8 demonstrates the results of this model. The trend of rapidly decreasing resonant frequency was again observed as mass was added. The model would fail to give a result if further mass was added to the system beyond the final data point in this series. The small discrepancy between the experimental and modelled series is easily explained by subtle variations between the modelled flexures, and the physical flexures which have scalloping (ridges) caused by the etch process and an etch mask still in place.

2.2.3 Modelling and Experimental Results of a 3-Flexure System

After a breakage during the fabrication process, one sample only had three flexures (right hand image, Fig. 2.4). This device was observed to have a resonant frequency of 2.3 Hz when vertical. Figure 2.9 is a graph of the resonant frequency as the MEMS was tilted from 80° to vertical, and beyond to 100°. It was observed that the frequency dropped to a 1.85 Hz minimum at 88°, increased to 2.2 Hz at 90°, then displayed a symmetric trend when tilted beyond vertical. Crucially the device reached a minimum frequency without becoming unstable like the 4-flexure system. Instead of rapidly decreasing to zero frequency, it gained a Hooke's Law behaviour (to second order) at the minimum. The error bars in the tilt measurement are $\pm 0.25°$: half the smallest unit on the analogue scale of the tilting stage upon which the MEMS device was mounted.

As mentioned earlier, an accidental breakage during the fabrication process meant that one MEMS device only had three flexures. Since this sample was designed with the same thickness of flexures, the resonant frequency of the device was lower than an equivalent device with four flexures. This sample was also placed in the rotation stage, orientated

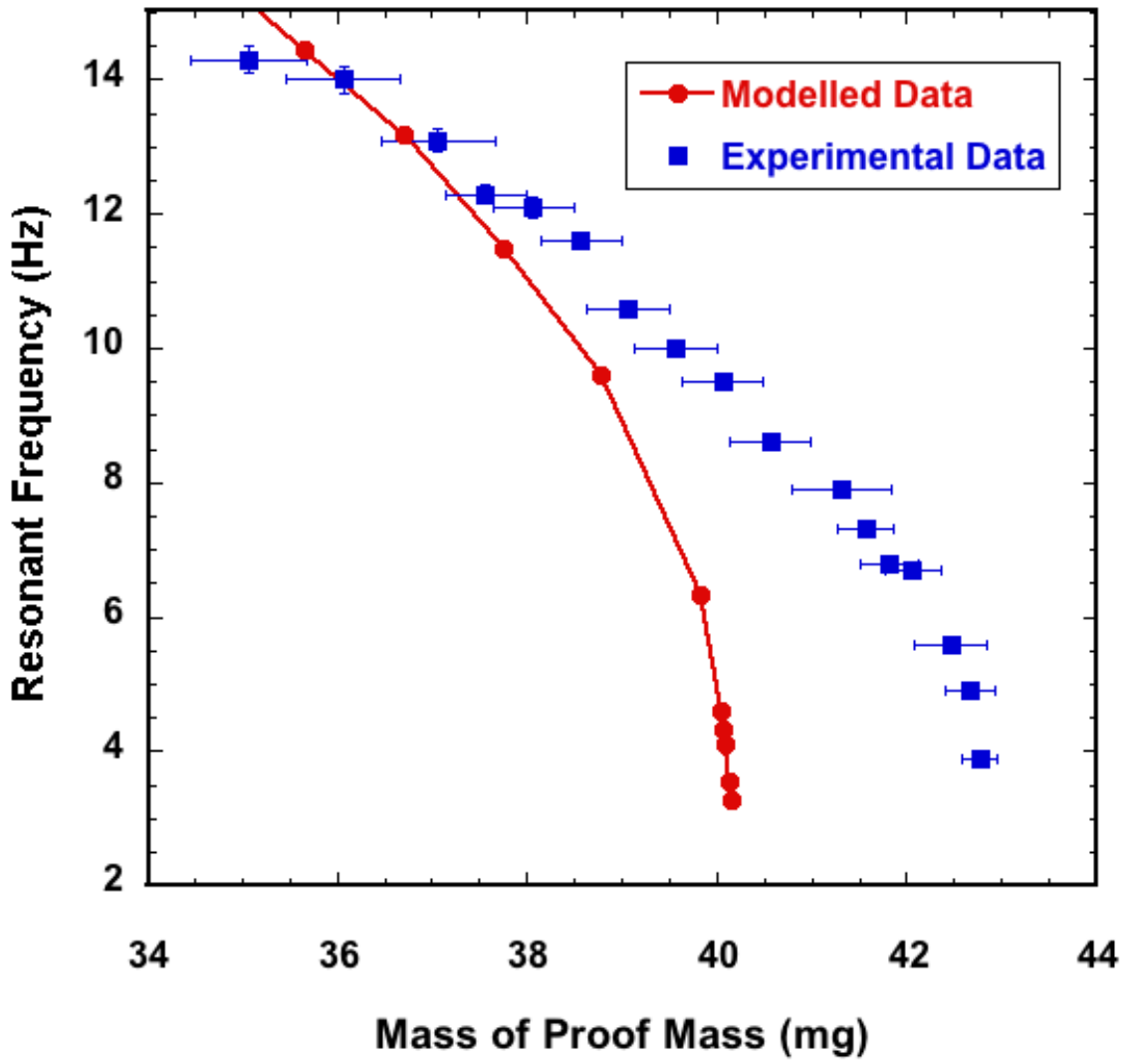

Fig. 2.8 This figure demonstrates the effect of adding mass to the 4-flexure (symmetric) MEMS device. The blue series is the experimental data achieved by increasing the mass of the proof mass using additional indium foil. The red series is the data for an equivalent ANSYS model. As more mass is added the resonant frequency tends to zero, ultimately reaching an instability.

vertically, and filmed with the fast frame rate camera. The footage was then used to calculate that the resonant frequency of the device was 2.3 Hz at 90°[4]. Since a low frequency in the vertical orientation was essential for an Earth tide measurement[1], it was not desirable to potentially break the sample by adding further mass. Instead, the device was tilted from horizontal to vertical to observe how the resonant frequency changed. The data from this experiment is plotted in figure 2.9. The error bars in the tilt measurement are $\pm 0.25°$: half the smallest unit on the analogue scale of the tilting stage upon which the MEMS device was mounted. It was observed that this asymmetric system did not become unstable. As it approached maximal gravitational loading the resonant frequency decrease slowed, reached a minimum and then rose again (see figure 2.9, inset plot A). At this minimum – that occurred at 88° – the oscillator has a Hooke's Law behaviour to second order. Since these measurements were taken by tilting the device (rather than adding mass), we could observe the trend as the device was tilted beyond vertical. The trend was symmetric on the other side of 90°, with a second minimum at 92°, demonstrating that the first minimum was not just a symptom of incorrectly measuring the vertical. It was further observed that the system would even recover from large excitations where the proof mass bounced off both the top and bottom of the frame.

To assess why this miniumum occured, a series of 3-flexure FEA models were constructed. FEA models were used for this process because it was possible to rapidly scan through multiple parameters such as flexure profile and the mass of the proof mass. To iteratively change the design of a physical MEMS in such a way would have been a prohibatively lengthy process. It was observed using these models that 3-flexure systems did not become unstable, with the resonant frequency going through a minimum as the gravitational loading changed. Figure 2.10 is a demonstration of how changing the proof mass alters the angle at which the minimum frequency occurs. The greater the mass, the shallower the angle at which the minimum was found, but the models never became unstable, unlike the 4-flexure system.

The 3-Flexure system had demonstrated this stable behaviour both experimentally and in FEA models, but what was the mechanism for this behaviour? Testing hypotheses of why this behaviour occurred required an accurate understanding of the dynamics of the system as it displaced. This is where FEA modelling is invaluable because the deflection of every point in the system can be plotted in all three axes in incremental time steps.

The first test conducted was to check whether the asymmetry of the flexure profile had anything to do with the observed 3-flexure behaviour. The flexure geometry was therefore

[4] At 210 frames per second, ten oscillations occupied 913 frames. The ability to determine the frame in which the peak of an oscillation was reached could cause an error of a frame or two. Over a total of 913 frames, however, this error is too small to register on the graph displayed in figure 2.9.

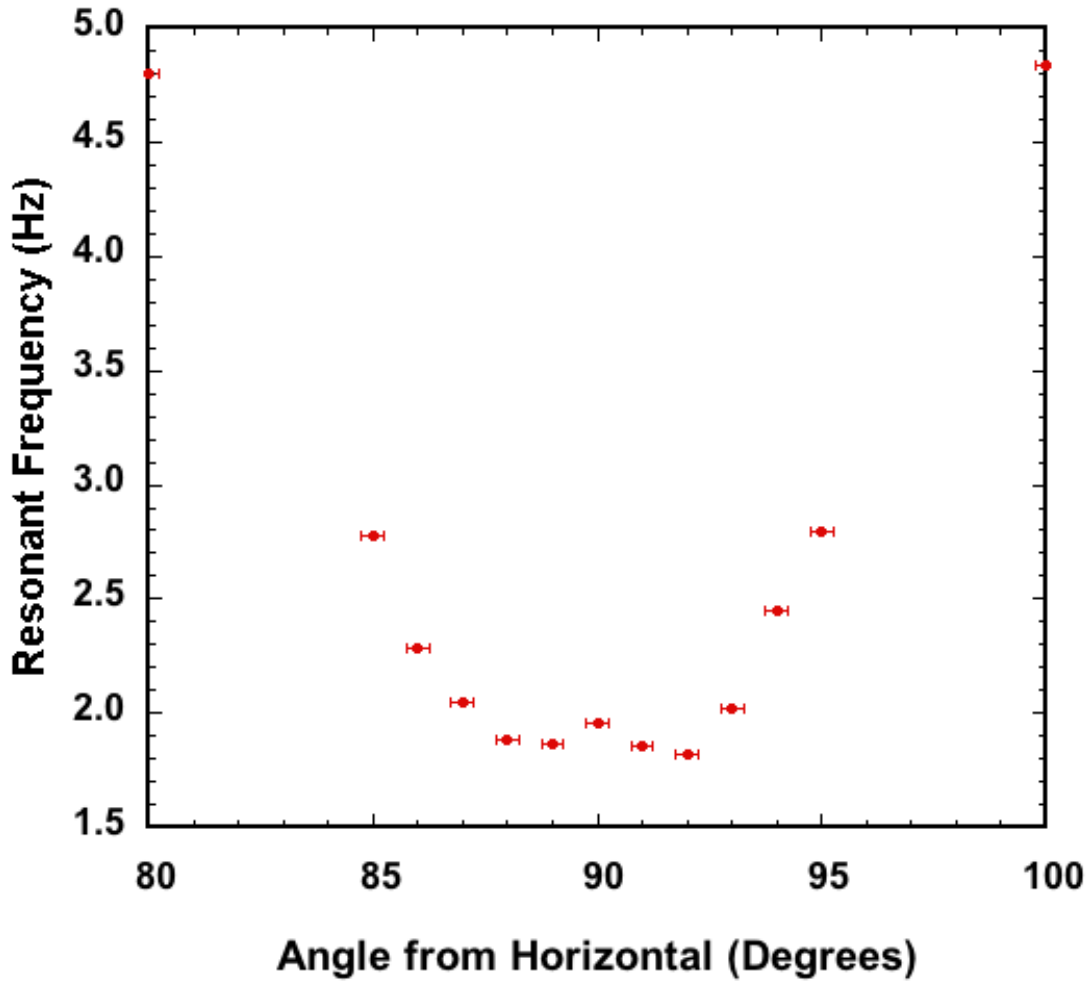

Fig. 2.9 An experimental series demonstrating the effect of increased gravitational loading on a three flexure system. As the device is tilted further towards the vertical, the resonant frequency drops, reaching a minimum at 88° of 1.85 Hz. At 90° the resonant frequency goes up to 2.3 Hz. Above 90° the trend is a mirror of that just below 90°.

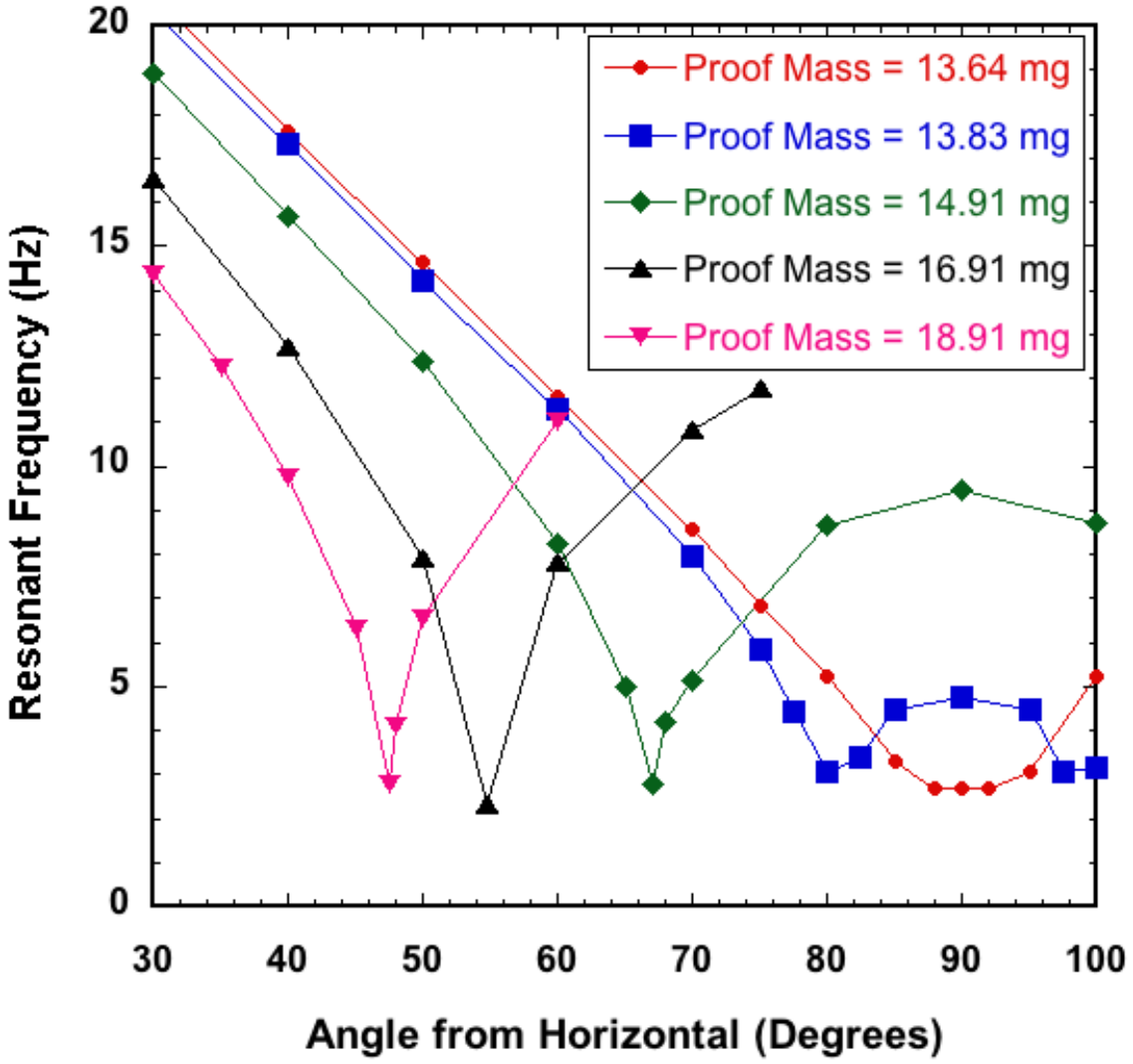

Fig. 2.10 A series of FEA models of 3-Flexure MEMS devices with varying mass. Unlike the 4-flexure system (Fig. 2.8) no instability was observed. Instead, the resonant frequency reached a minimum and then increased again with increasing tilt. The position of this minimum is shown to depend on the mass of the proof mass. All of the models used to populate this plot used flexures with rectangular profiles.

altered so that it was no longer trapezoidal, but rectangular. This meant that the only asymmetry in the FEA model was the absense of the fourth flexure. It was observed that regardless of whether the profile was rectangular or trapezoidal, the same trends occurred as shown in Fig. 2.10: a minimum was always observed.

The absense of the fourth flexure therefore had to be the reason for the observed stability. The anti-spring effect relies on the constraint of the motion along the red axis displayed in Fig. 2.4. It was therefore suspected that the 3-flexure system eventually moved away from this constraint because of its asymmetry, thus causing a minimum in the resonant frequency, rather than an instability.

Two FEA models were selected, one with four flexures and one with three. These were each picked because they had very similar resonant frequencies (9.58 Hz for the 4-Flexure system and 9.47 Hz for the 3-flexure system) when mounted vertically. Crucially, the three flexure system was selected because it was a model that had already passed through its frequency minimum (the same model used to produce the 90° data point in the green series of Fig. 2.10). This would allow the observation of what dynamics occur as the 3-flexure system passes through a resonance minimum.

The total vertical deformation of the proof masses were first calculated. It was observed that the 3-flexure system dropped 3.3 times more than the 4-flexure system (see red and green series in Fig. 2.11). Next, the tilt of the proof mass during its release was recorded both laterally and out of plane. Figure 2.4 demonstrates which dimentions are referred to as 'lateral' and 'out of plane'. The tilts were calculated by observing the motion of two vertex points, one at the top of the proof mass and one at the bottom (see blue dots in Fig. 2.4). For the 4-flexure system at full loading the proof mass had tilted out of plane by 0.0011°, the corresponding 3-flexure proof mass tilted out of plane by 0.0024° (2.2 times more). The lateral tilt, however, was much more significant. Whilst the 4-flexure proof mass only tilted laterally by $6.6\times10^{-4\circ}$ (blue series of Fig. 2.11 with a multiplication factor of 1000), the three flexure proof mass tilted by much more. Initially increasing to a maximum tilt of 1.88° (black series in Fig. 2.11), a sudden change in the direction of the tilt occured, with the angle ultimately settling at a tilt of 1.63° at full loading. This is a deflection 2451 times larger than that observed in the 4-flexure system at full loading. The location of the change in tilt direction also perfectly corresponds to the location at which the gradient of the vertical displacement lessens after a steep decent. The magnitude of the 3-flexure lateral tilt, and the fact that this tilt changes direction at the same loading as the steepening vertical deflection is recovered present clear evidence that it is the asymmetry of the 3-flexure system that breaks

the vertical constraint of the anti-spring as it deflects, thus ultimately stopping the anti-spring behaviour.

2.2.4 Triaxial Configuration

The tunability of the angle at which the lowest resonant frequency occurs is of interest since it could allow the development of a three-axis MEMS gravimeter. In such a device three tuned MEMS devices could be placed in the Galperin configuration [86] at an angle of $\theta = 54.7^\circ$ from the horizontal, and separated azimuthally from each other at an angle of 120° (see figure 2.12). The Galperin configuration was designed to allow three identical sensors to measure gravity (or seismic activity) in three dimensions. Different sensor geometries would be required if the sensors were simply mounted along x, y and z because the sensors in x and y would be perpendicular to the 1 g field, and the sensor in z would be parallel to it [87]. Having an oscillating system that can be tuned to operate at any angle is therefore beneficial. The red trend in Fig. 2.10 is an FEA plot of a MEMS device whose angle of minumum resonance has been tuned to 54.7° by altering the mass.

To test the theoretical efficacy of a device mounted at the Galperin angle ANSYS was used to model the effect on the device of a harmonic oscillation of acceleration with the same direction vector, magnitude and frequency as the Earth tides. The Earth tides are a useful predicable gravitational signal against which to test the sensitivity and stability of a new gravimeter [1]. It was observed that the displacement of each proof mass matched the expected magnitude given by $g_z \sin\theta$ in the vertical direction, and by $g_{x/y} \cos\theta$ in the horizontal plane. This modelling confirms that a triaxial device could be used to measure acceleration in three axes, given by equations 2.2, 2.3 and 2.4:

$$g_z = \frac{(g_1 + g_2 + g_3)\sin\theta}{3} \tag{2.2}$$

$$g_x = ((g_1 + g_2)\cos\alpha)\cos\theta - g_3\cos\theta \tag{2.3}$$

$$g_y = ((g_1 - g_2)\sin\alpha)\cos\theta \tag{2.4}$$

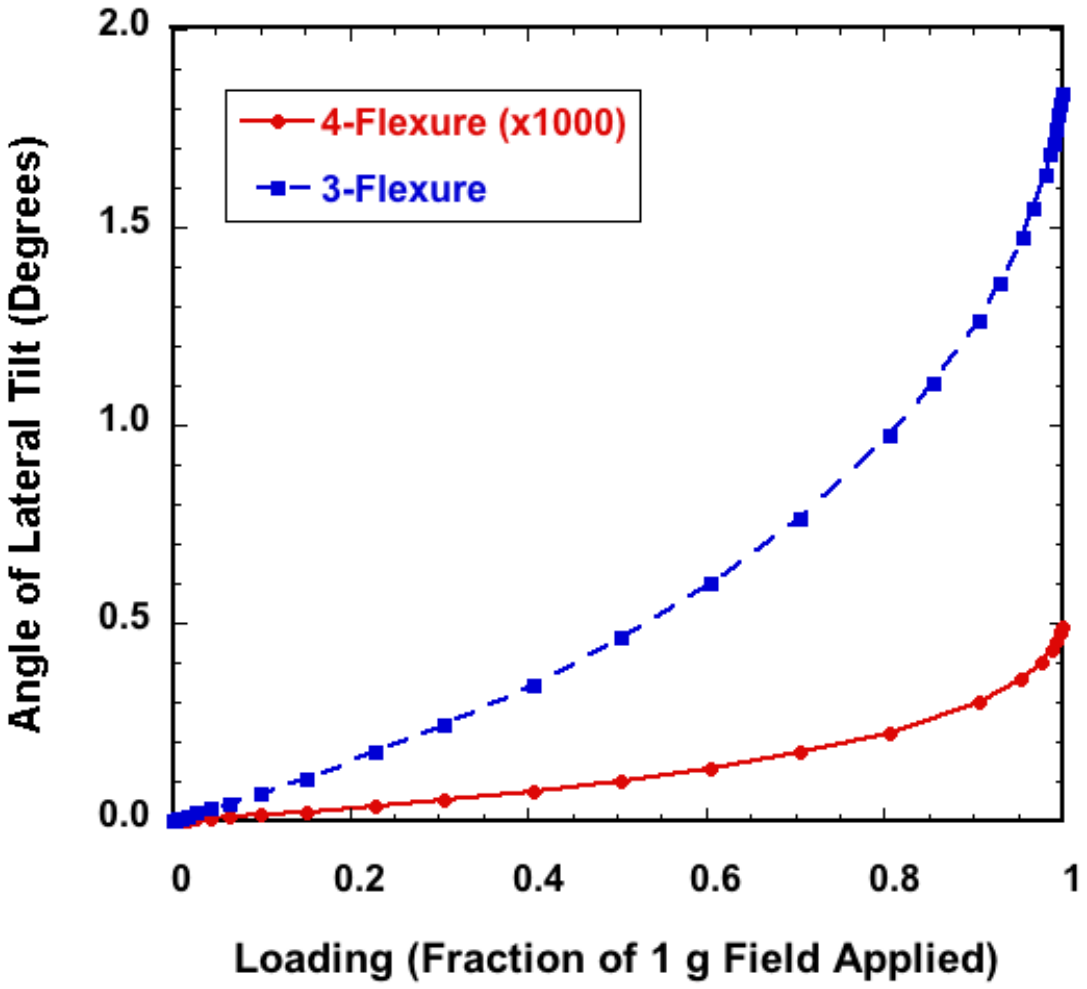

Fig. 2.11 The vertical displacement and the lateral (in-plane) tilt of two MEMS devices, one with three flexures and one with four. The x-axis shows the loading applied by the FEA model, at full scale the device is exposed to a force equivalent vertical force due to gravity on Earth. The 3-flexure system tilts 2451 times more than the 4-flexure system at full loading. It is this tilt and the sudden change in its direction that breaks the vertical constraint that is required for the anti-spring effect to continue and cause an instability.

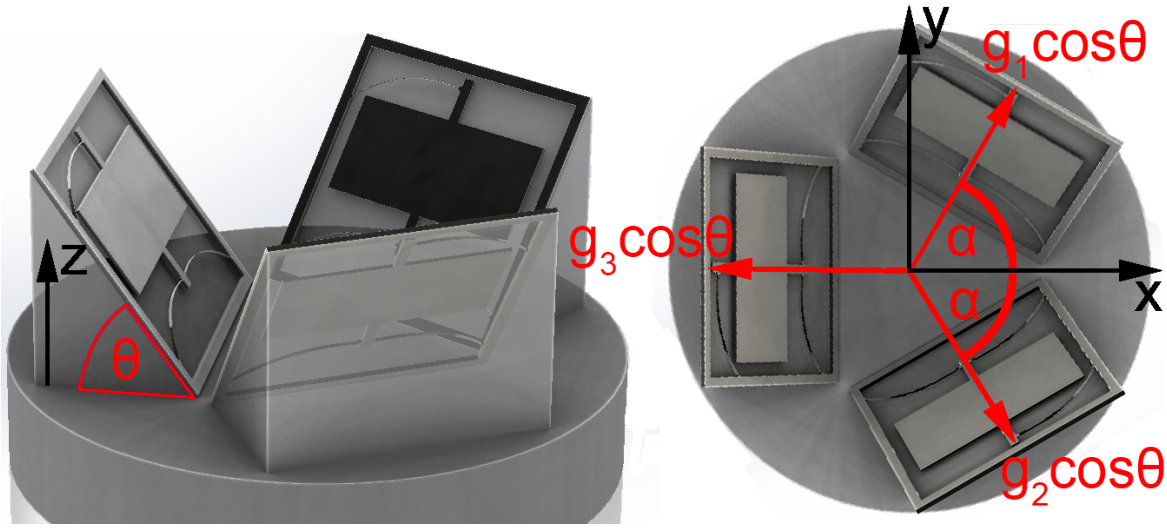

Fig. 2.12 A computer generated image of a three-axis MEMS gravimeter in a Galperin configuration [86].

2.3 Summary of the Geometrical Anti-Spring Design

Asymmetric geometrical anti-springs offer a novel method of achieving remarkably low resonant frequency oscillators. Unlike symmetrical geometrical anti-spring systems, asymmetric systems do not become unstable with increasing displacement because their motion is not constrained to the same level. Such low resonant frequency oscillators could be utilised in the accelerometer industry to achieve greater acceleration sensitivity, or as a means of passive vibration isolation down to very low frequencies in interferometric gravitational wave detectors. This three-flexure geometry achieves the most of the design specifications of any of the geometries considered: it has a resonant frequency of only 2.3 Hz; its motion is constrained to mostly one axis (with a ratio of 1:27 between the first and second modes of oscillation); and it can operate vertically to measure g_z. Since the angle at which the low resonant frequency occurs can be tuned, the design of this MEMS device could be used to create a triaxial MEMS gravimeter. The following chapter will focus upon the fabrication of these MEMS devices.

Chapter 3

MEMS Fabrication

The fabrication of the MEMS gravimeter was not a trivial process. Three years of development took place to ensure a reliable means of production of these devices. All of the MEMS fabrication was carried out in the James Watt Nanofabrication Centre (JWNC) at Glasgow University. This chapter contains a discussion of the optimisation of the various steps necessary to produce a free-standing device. The basic processing steps required to produce a MEMS device have been utilised for several decades. The intricacies of these processing steps, however, is always dependent on the structure being fabricated. It is inevitable, therefore, that very many person-hours are required to produce a working device. This was particularly the case for the development of the MEMS gravimeter. Whilst the JWNC has many years of nano-fabrication expertise, there has not been much development of MEMS devices, which require significantly deeper etches. This difference means that the method of masking the areas of silicon that are not to be etched also varies. Sections 3.1 and 3.2 outline the development of the masking and etching that was necessary to create this device. Several etches and masking processes that were developed for this work have now been adopted as recommended processes for other users of the clean room facility. Section 3.3. outlines the largest hurdle in creating the MEMS devices: namely, the process of making the samples free-standing. The JWNC did not have the tools that would normally be used for such a process, so an original means of sample release was developed to achieve this goal using the tools available. Again, this process has since been adopted by other users of the clean room. A short summary of the broad micro-fabrication processes is contained within the following paragraph, before sections 3.1 onwards detail the specific challenges that were overcome to produce the MEMS gravimeter samples.

Each device was constructed from single pieces of 220 μm thick silicon wafer with <100> a crystaline structure. The design of the MEMS device first needed to be transferred

onto the surface of the silicon. This was carried out using a process called photolithography. Photolithography involves spinning a liquid polymer layer – called 'resist' – onto the surface of the silicon. The spinning process involves placing the silicon sample on a vacuum chuck that can be rotated up to angular velocities of several thousand revolutions per minute. Resist is syringed onto the centre of the sample, and the rotation causes the resist to flatten into a layer of uniform thickness. The thickness of the layer depends on the initial viscosity of the resist, and the speed at which it is rotated on the vacuum chuck. This resist layer is then baked hard and exposed to an ultra-violet light source with a patterned plate in between. This plate is called a photolithography mask, and it is the means of transferring the design of the MEMS onto the resist[1]. The resist is then developed in a solution, and areas exposed to the ultra-violet light are washed away. Resist can either be 'positive' or 'negative'. Positive resists break down when exposed to ultraviolet light, and negative resists harden when exposed to ultraviolet light. The resist used for this process is positive. After development, the remaining resist is then used as a selective etch mask to protect the desired areas of the silicon whilst etching away the rest of the material using a deep reactive ion etch (DRIE). Alternatively, the resist can be used as a mask to pattern a layer of another material (say chrome or SiO_2) that is in turn used as a mask whilst etching the silicon. After the etch the MEMS device can be made free-standing. The details of the successes and failures of each of these steps, together with the final recipe developed to produce reproducible free standing structures, are discussed in the sections below.

3.1 Choice of Etch Mask

As mentioned above, an etch mask is used to protect some areas of the silicon wafer, while other areas are etched away with a DRIE process. Three different etch masks were investigated through the course of this project. Each of these masks needed to be robust enough to survive the harsh environment encountered during the DRIE process. The resiliance of a mask to survive long enough to protect silicon through an etch is characterised by the 'selectivity' ratio of the mask material and the silicon. A 1μm thick mask used for a silicon

[1]This statement begs the obvious question: 'then how was the photolithography mask produced?' The photolithography mask was produced by directly writing the desired pattern onto a chrome-on-glass plate using an electron-beam writer. Electron-beam writers can pattern down to sub-nm resolution but it is an expensive process to repeat. Copying the patten onto a photolithography mask provides a cheaper alternative because the mask is re-usable and the process is much quicker. Photolithography cannot be used for patterns with a feature size of much under 1 μm, but this was not the case for the design of our MEMS gravimeter. Copies of the photolithography mask are generally made from ferric oxide-on-glass plates, to avoid damaging the original chrome mask.

etch with a selectivity of 50:1 would be able to protect the silicon as it was etched down by 50 μm, until the mask would be etched away to nothing. The first mask considered was a single layer of resist, the second was a layer of chromium (patterned using resist), and the third was a combination of SiO_2 and resist.

3.1.1 Resist Masks

Resist masks (or 'soft masks') normally have a silicon etch selectivity of around 50:1, but this ratio varies depending on the tool used for the etch, and the etch recipe used. The process of creating a resist mask is outlined in figure 3.1.

After steps **a** to **f** in figure 3.1, SEM images of the resist were taken. These pictures revealed that after development, the resist edges were considerably sloped. This slope resulted in a thinning of the resist in the narrow flexures (as can be seen in figure 3.2a), which would provide little protection during the silicon etch process. It was therefore decided to conduct a series of experiments to test the effect of various parameters on the resist edge angle. This optimisation process was a laborious one in which the following parameters were tested:

- **Use of primer.** It was discovered that using Microposit MC 80/20 primer improved adhesion of the resist to the silicon. When applied to the surface of silicon methyl groups form and create a hydrophobic layer over the silicon, improving wetting and adhesion of the resist [88].

- **Method of baking (oven or hotplate).** Hotplate baking was selected over oven baking because the solvents were baked out from bottom to top, allowing an even bake. The oven bake resulted in a hard shell of resist on the surface through which the solvents were not able to escape, this resulted in softer resist underneath.

- **Length of resist bake.** It was discovered that to bake all of the resist evenly, a bake time of just over one minute per micron of resist was required.

- **Edge bead removal.** The removal of the edge bead with a scalpel allowed the photomask to make a closer contact with the resist, giving a sharper edge to the developed areas (a vacuum contact was also used to get the mask and resist in the closest proximity possible).

- **Exposure length.** Exposure lengths between 10 to 30 seconds were trialed, with an 18 second exposure giving the most vertical profile.

(a) Silicon wafer is solvent cleaned.

(b) AZ4562 photo-resist is spun onto the sample at 4000 rpm for 60 seconds, leaving a 7μm thick layer of resist with an 'edge bead'.

(c) The edge bead is removed using a scalpel and the sample is baked on a hotplate for 8 minutes at 100°C.

(d) The photo mask with the geometrical anti-spring pattern is positioned on the sample (ferric oxide side down).

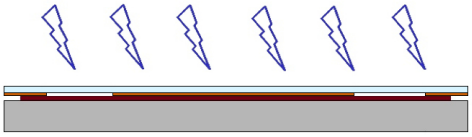

(e) The sample is exposed to UV light. Sections covered by mask are protected from this radiation.

(f) The sections of resist are cleared by developing in AZ400K developing solution.

(g) The sample is etched. Silicon covered with resist is protected during this process.

Fig. 3.1 The process of creating a resist mask using photolithography.

- **Delay times.** The most significant results were shown by increasing the delay times between process steps, as recommended by the resist manufacturer. After spinning, excess solvents were allowed to evaporate from the resist for a minimum of 20 minutes improved the results. Following the bake, a minimum time of 20 minutes was needed for the resist to rehydrate, to give a more even resist strength before exposure. Finally, after exposure (which involves nitrogen purging cycles during the vacuum contact) the sample has to be left for a minimum of 30 minutes to allow any nitrogen bubbles to escape. Leaving the samples for longer timescales than those listed above did not make any noticeable improvement to the resist profile verticality.

Other parameters (such as the use of multiple exposures, and variable developing times) were tested but discovered to have little or no effect on the resist edge slope. The improvement in resist angle can be seen in images 3.2b to 3.2d. After all of this parameter optimisation, a resist edge slope of 78° from the horizontal could be consistently realised. The final process for realising this optimum angle is outlined below.

The sample was cleaned in an ultra-sonic bath of acetone for 5 minutes, followed by isopropanol for 5 minutes, and then blown dry with a nitrogen gun. To ensure that the sample was completely dry, the sample was baked in a 180° oven for 5 minutes. The next stage of processing was to spin on the resist. Since the resist sometimes failed to adhere to the surface, an adhesion promotor was first applied to the surface. *MicroChemicals HDMS Primer* was syringed onto the surface of the sample, left for 30 seconds, and then spun at 4000 RPM for 5 seconds. To cure the primer, the sample was baked on a hotplate at 115°C for 1 minute. Once the adhesion promotor was cured *Microposit AZ-4562* resist was spun onto the sample at 4000 RPM for 1 minute, creating a 7 μm thick layer. The spinning process leaves what is called an 'edge bead' around the edge of the sample. This bead is much thicker than 7 μm and its presence would limit the proximity that a photolithography mask could be placed against the sample during exposure. The edge bead was therefore removed with a scalpel. The sample was left in air for 30 minutes to ensure that all of the solvent in the resist had fully evaporated, reducing the risk of bubble formation when the resist was baked. To cure the resist, the sample was baked on a hot plate for 8 minutes at 100°C. A hotplate was used rather than an oven because the hotplate heats the resist layer from the bottom upwards, forcing out any remaining solvent. An oven creates a hard film over the top of the resist, trapping remaining solvent and increasing the risk of bubble formation. After baking, the sample was placed in a *SUSS MircoTec MA6* mask aligner. This tool is used to manipulate the photolithography mask over the correct position of the sample, and then to expose the sample to g-line ultra-violet light (435.8 nm). The sample was exposed for 18 seconds. The

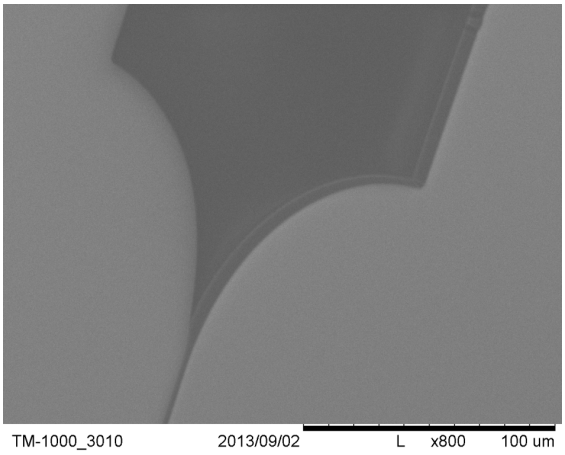

(a) Early resist test in which sloped sides left little resist over the springs to mask the silicon.

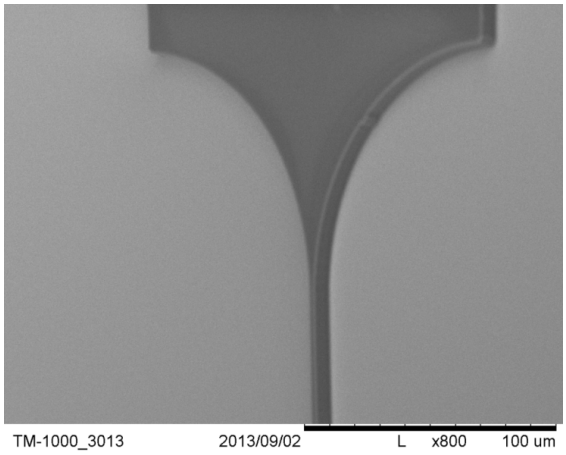

(b) The first resist test in which the profile was vertical enough to leave a horizontal surface on top of the resist over the spring.

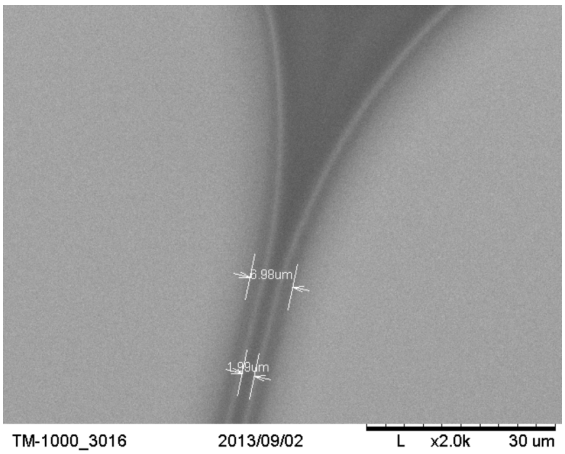

(c) The same test as in subfigure 3.2b from a different viewing angle.

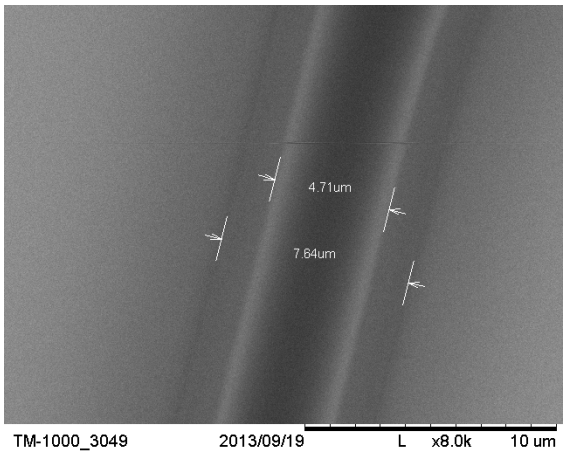

(d) Later test in which the best resist profile was achieved (with an angle of 78.4°).

Fig. 3.2 Four SEM images demonstrating the optimisation of the resist edge profile.

sample was developed by rinsing in a beaker of 1:4 solution of *Microposit MF-319 developer* and de-ionised water for around 3 minutes, and then rinsed in de-ionised water and blown dry with a nitrogen gun. The sample was then ready for a silicon etch.

This resist etch mask was used to successfully produce samples. The slope of the profile, however, meant that the etch would always be detrimentally affected. The edges of the resist mask would fail before fully etching to the centre, leaving areas of the silicon exposed that were not supposed to be. Since the the flexures were only 7 μm wide, the sloped resist walls had a particular impact here, where the effect of the slope could change the width of the flexure by as much as 2 μm.

The solution to this issue was to switch to a hard mask. Hard masks are generally made of oxide or metal and have much higher selectivities than soft masks, they can therefore be made much thinner. This means that a slope on the edge of the sample is not a problem.

3.1.2 Chrome Masks

The first hard mask tested was chromium. Chrome masks are often used in micro-fabrication because this metal adheres well to Silicon [89]. Chrome masks were used to produce most of the MEMS samples used to gather data during this project. The process of producing a chrome mask was quite similar to that outlined in figure 3.1. The silicon was first coated with a 200 nm layer of chrome and then cleaned in the same manner outlined above. The chrome then needed to be patterned so a resist mask of *Mircoposit S1818* resist was spun onto the surface at 4000 RPM for 30 seconds. This resist only produced a layer of 1.8 μm when spun at this speed. Adhesion was not a problem for this process so no dehydration bake or primer application was necessary. The *S1818* resist was baked at 85°C for 2 minutes and then placed in the mask aligner tool. The sample was exposed for only 5 seconds and then developed in neat *Microposit MF-319* developer for 70 seconds, followed by a 70 second rinse in de-ionised water. At this point the resist could be used as a mask to wet etch the chrome. The sample was dipped in a nitric acid chrome etchant for two minutes, disolving the areas of chrome not covered by the resist mask. Finally the resist mask was removed by agitating the sample in an ultrasonic bath: first for 5 minutes in acetone, and then for 5 minutes in isopropanol.

To all intents and purposes, chrome masks have an infinite selectivity. There was no chance of a chrome mask of this thickness being etched away during the silicon etch process. Chrome, however, did present some problems. The chrome mask induced an electric field that interacted with the charged ions that are used to etch the silicon (see section 3.2). This

effect caused an undercut of the mask of about 2.5 μm, reducing the total width of the flexure by 5 μm. This undercutting can be observed in figure 3.3. Although it was possible to increase the initial width of the chrome flexures on the mask, the undercut was still an unnecessary inconvenience.

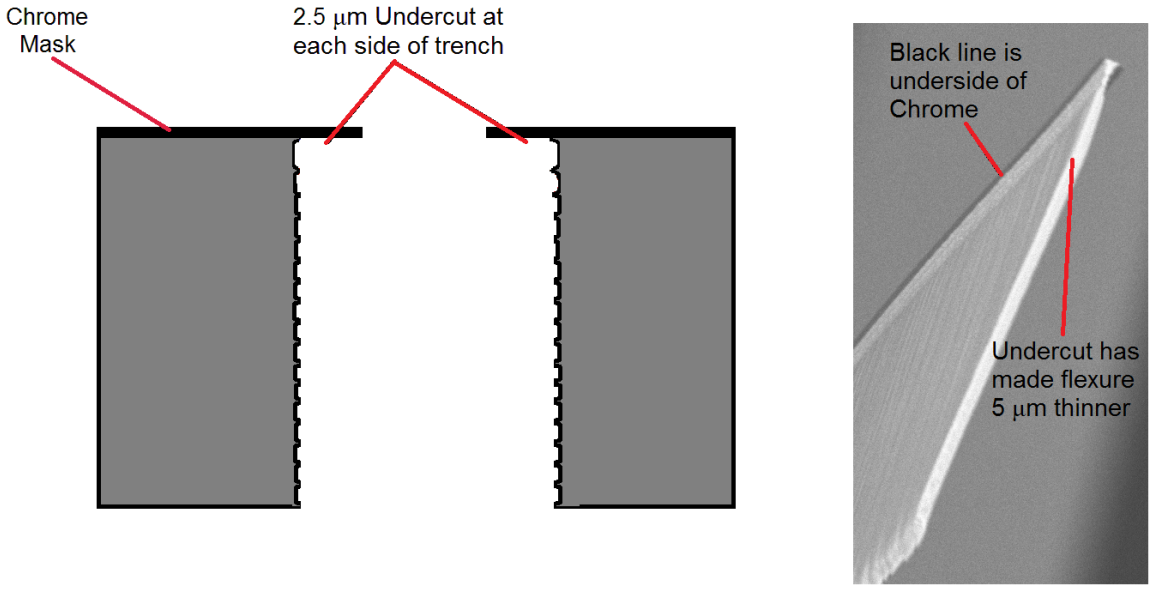

Fig. 3.3 The left hand cartoon in this figure demonstrates the undercut that was observed when using a chrome mask. The photo on the right is an SEM image of the profile of an etched flexure for which a crome mask was used. The undercut and the resulting thinning of the flexure are clearly visible.

3.1.3 SiO_2 Masks

The final etch mask tested was a combination of SiO_2 and resist. SiO_2 is classed as a hard mask but its selectivity lies between that of resist and metal masks. SiO_2 has the advantages of being widely used in industrial MEMS fabrication, and of not causing undercutting during the silicon etch process. The process of creating this mask is very similar to the creation of a chrome mask. Instead of depositing chrome in an evaporation tool, 2 μm of SiO_2 was deposited using a plasma enhanced chemical vapour deposition (PECVD) tool. Instead of *S1818* resist, *Microposit S1828* resist was spun onto the sample. The only difference between these two resists is that *S1818* creates a 1.8 μm layer, and *S1828* creates a 2.8 μm layer. After baking, the resist was exposed for the slightly longer time of 10 seconds, and developed using the same MF-319 development solution for the same length of time as used for *S1818*. The sample was then placed in a reactive ion etch (RIE) tool that would etch the SiO_2 areas

not covered by resist. This process took around 1 hour; an interferometer was used to trace the progress of the etch so that the run could be stopped when the SiO_2 had been etched to the full depth. Since SiO2 is not as hard as the chrome mask the resist was left on the surface of the SiO_2 to provide extra protection during the etch.

3.2 Silicon Etch Optimisation

So far the etching process of the silicon has not been touched upon. This is a process that also required optimisation. As viewed from above, the flexures were only 7 μm wide, but they needed to be etched to the full depth of the silicon wafer (220 μm) in order to make the sample free-standing. This high aspect ratio of the flexures meant that the device would only have one predominant mode of oscillation, with out-of-plane motion kept to a minimum (as discussed in chapter 2). The high aspect ratio is not achievable by etching with a liquid chemical. The liquid chemical etching process is known as 'wet etching'. Wet etching is achieved by exposing the silicon to a liquid such as potassium hydroxide (KOH), if <100> silicon is used (as is the case for this project), the KOH attacks the silicon along the <111> crystal plane [90]. This plane is is at an angle of 55.74° from the surface of the silicon so clearly wet etching cannot be used to achieve vertical etches. The samples were therefore etched using the Bosch Process. The Bosch Process [85] is a patented form of a deep reactive ion etch, and is capable of a highly uniform and directional (anisotropic) etching, making vertical side walls possible. The sample is first exposed to an isotropic etching plasma: Sulphur Hexaflouride (SF_6) is used to etch silicon. The SF_6 chemically etches the silicon isotropically. The gas in the chamber is then switched to produce a passivation layer on the surface of the sample (e.g Octafluorocyclobutane [C_4F_8]). This layer acts as a barrier that will stop the chemical etching of the substrate. Ions are then accelerated by a high RF current to physically etch the surface (see figure 3.4). This ion bombardment removes the passivation layer only in the horizontal plane, leaving the passivation layer intact on the side walls of the trench but leaving the bottom of the trench clear to be etched by the SF6. The process is then repeated multiple times. By tuning the length of time of the passivation and etching cycles, vertical sidewalls can be fabricated. A cartoon of this process can be observed in figure 3.5. The cyclical nature of the Bosch Process produces a scalloping of the sidewalls (see figure 3.6). Larger scallops are caused by longer etching cycles. The size of these scallops is therefore reduced by switching the etching and passivation plasmas at a higher rate.

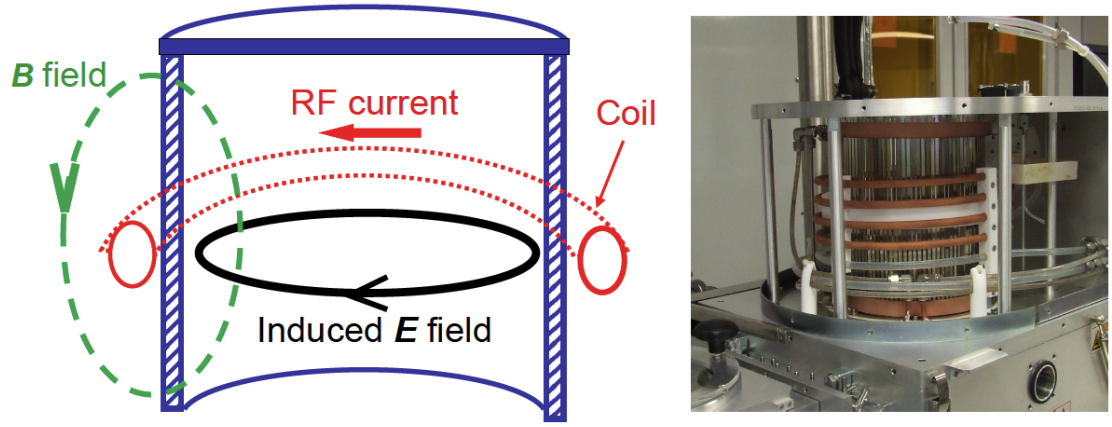

Fig. 3.4 Schematic and photo of the STS coils which generate the RF current and B field used to accelerate the ions (image courtesy of Haiping Zhou).

3.2.1 Large-Area Etching

The first etch trials were carried out on as *STS* inductively coupled plasma (ICP) tool. At this stage an optimised resist mask was being used, and the mask was designed to cover the flexures, proof mass and outer frame. This meant that all of the open areas of the design had to be completely etched away. An etch recipe was provisionally selected that had produced highly uniform vertical walls in the samples of other users of the tool. This etch recipe had an SF_6/C_4F_8 cycle time ratio of 11 s/7 s. The patterns used by these other users, however, were generally made up of trenches and did not include large open areas like this design. In early etch tests it became apparent that this recipe was giving the walls of the flexures a negative profile. A negative profile etch is one in which the side walls become steadily more under-cut as the depth increases (a positive profile is obviously the opposite to this) (see figure 3.7). Given the high aspect ratio of the flexures, they were quickly etched to zero width, and completely destroyed. Figure 3.8 shows SEM images of these initial tests in which the flexures were destroyed before the sample had been etched to a useful depth. Ideally, the samples would be anisotropically etched to several hundred microns because it would give the flexures an even higher aspect ratio, decreasing the out-of-plane motion of the proof mass.

In order to make the etch more vertical, the lengths of the etching and passivation cycle times were altered: decreasing the etching cycle time whilst decreasing the passivation cycle time. This made the profile less and less negative, but never completely vertical. The angle closest to vertical achieved by optimising this variable was 87.4° (see figure 3.9). This was achieved with an SF_6/C_4F_8 cycle time ratio of 9.5 s/9 s. The etch could potentially be

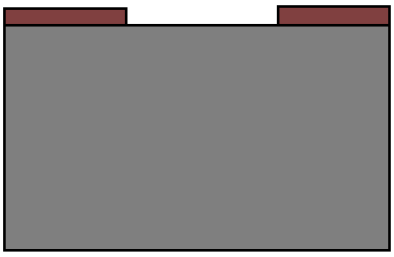

(a) The sample is placed in the chamber with an etch mask selectively protecting the silicon.

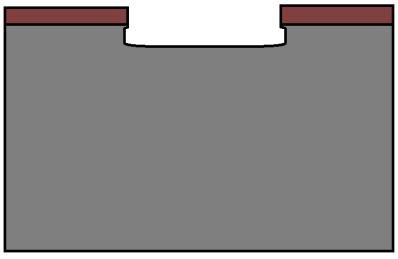

(b) SF_6 is used to isotropically etch a trench in the surface of the exposed silicon.

(c) A protective layer of C_4F_8 is deposited isotropically over the sample.

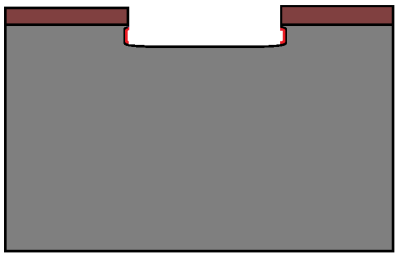

(d) A highly anisotropic ion bombardment removes the C_4F_8 from all non-vertical surfaces.

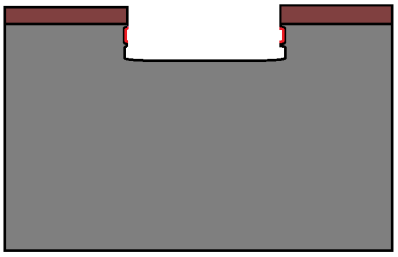

(e) SF_6 is again used to isotropically etch another trench in the surface of the exposed silicon.

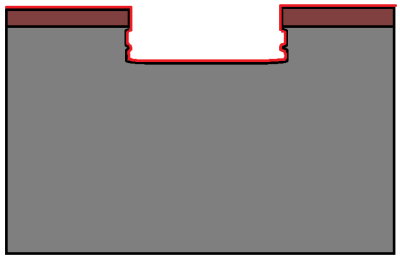

(f) A protective layer of C_4F_8 is again deposited isotropically over the sample.

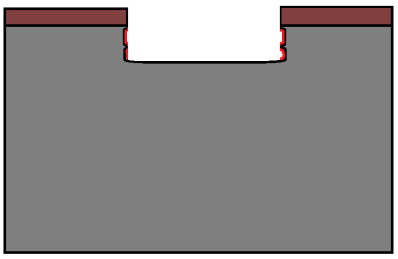

(g) A highly anisotropic ion bombardment again removes the C_4F_8 from all non-vertical surfaces.

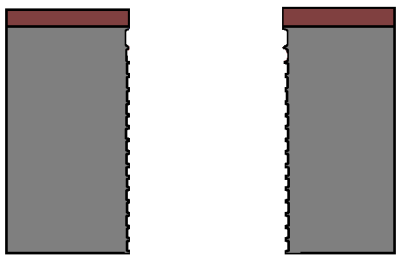

(h) This process is repeated until the sample has been etched to the desired depth.

Fig. 3.5 A sequence of images to demonstrate the Bosch Process. The silicon is etched vertically using a combination of chemical and physical etching via ion bombardment.

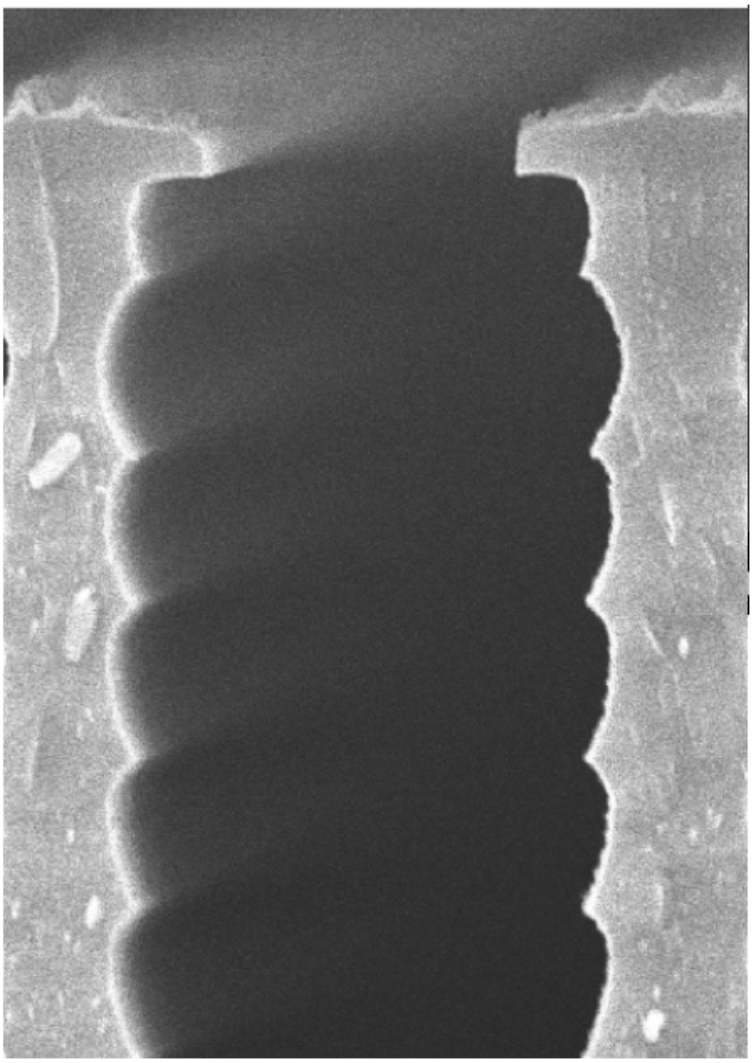

Fig. 3.6 An SEM image of the scalloping caused by the Bosch Process (image courtesy of Haiping Zhou).

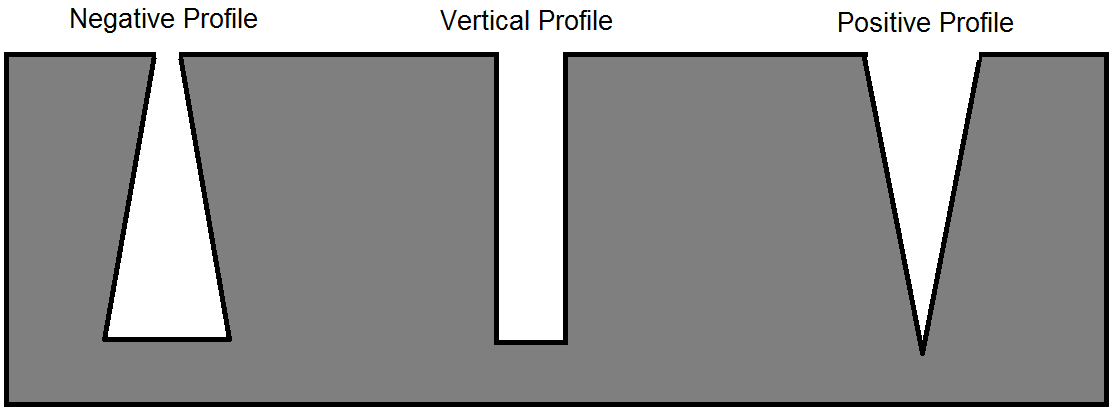

Fig. 3.7 A schematic diagram demonstrating the different kinds of etch profile that can result from a Bosch etch.

made more vertical than this, but increasing the passivation cycle time also has the effect of reducing the etch rate. This meant that the resist mask spent longer exposed to the etching plasma, and could therefore not survive the length of etch required to etch to the desired depth. The angle of 87.4° meant that the flexures had a triangular profile, tapering to zero width at a depth of around 150 microns. This etch profile set the limit for the depth of spring that could be realised with this etch process. To etch samples to a greater depth, this large area etch process was abandoned in favour of a 'halo etch'. Based on the work of previous users of the JWNC, it was expected that this halo etch would allow the silicon to be etched anisotropically to a greater depth. In anticipation of this level of anisotropy, samples of around 50% greater thickness (220 μm)were purchased to carry out the tests of this new process. Wafers of this thickness have continued to be used ever since.

3.2.2 Halo Etching

The *STS ICP* etch tool, used for the large-area etching described above, is capable of etch rates of 4-5 μm/minute. At this stage in the development of the MEMS device, a new tool was commissioned – the *PlasmaPro 100 Estrelas Deep Silicon Etch System* – that was capable of etch rates of up to 30 μm/minute. The etching of the samples was therefore switched over to this tool. Concurrently to this switch, two further changes to the process were made: instead of using a resist mask, a chrome mask was used; and instead of large-area etching a halo etch [91] was adopted. In a halo etch, instead of etching away all of the unwanted

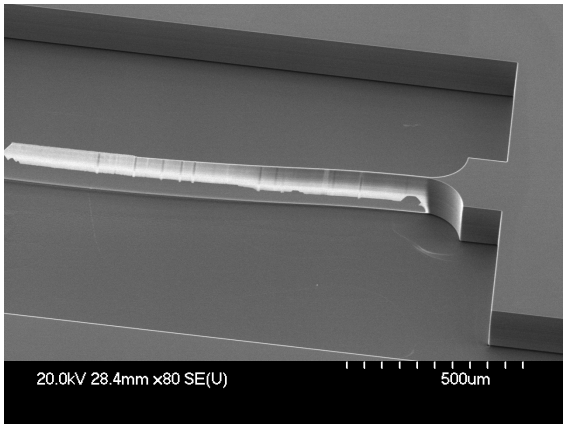

(a) A sample with an etch depth of 150μm. The springs are broken by the negative profile of the etch.

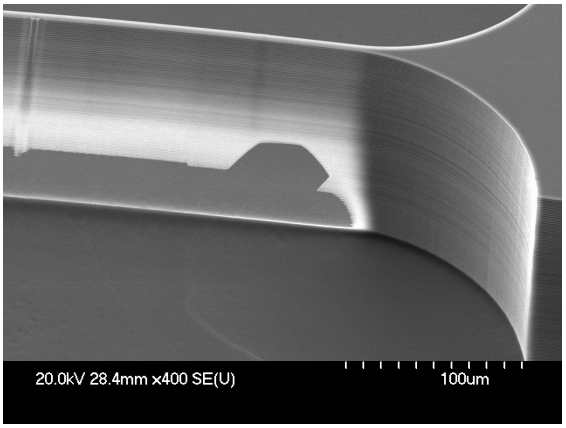

(b) A zoomed in image of the sample shown in figure 3.8a.

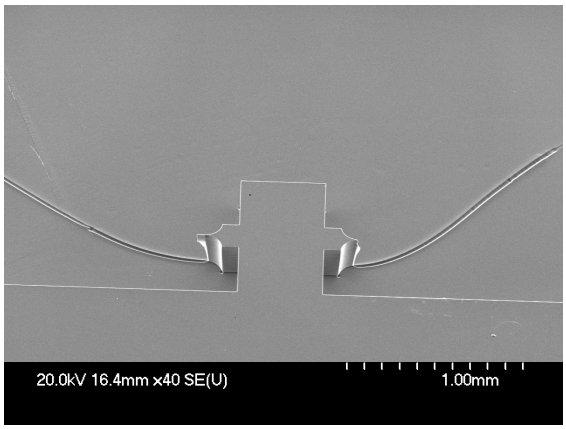

(c) A sample with an etch depth of 300μm, using the same recipe as that used for figure 3.8a. By this depth the flexures were completely obliterated.

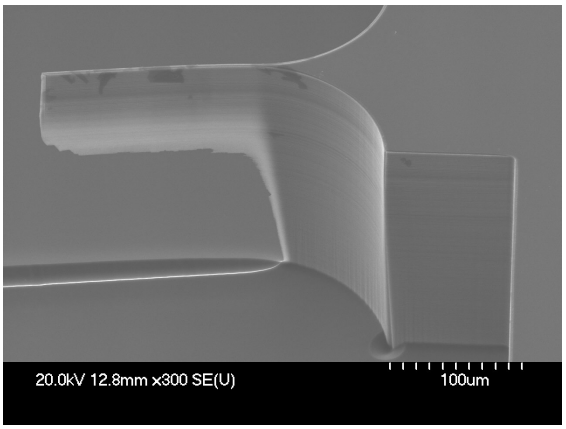

(d) A zoomed in image of the sample shown in figure 3.8c.

Fig. 3.8 Four SEM images of the undercutting of the flexures when unaltered etch recipes were used.

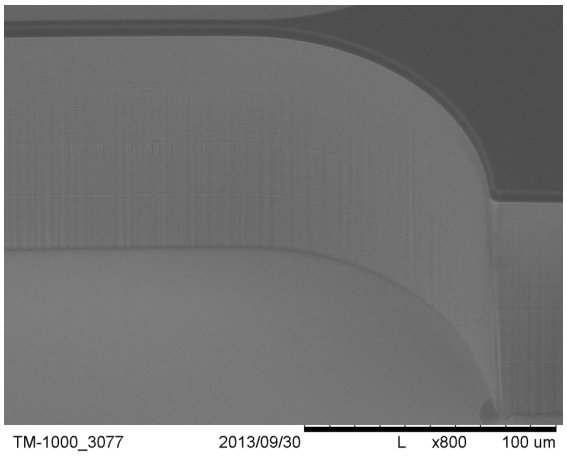

(a) This is the first etch test with an improved resist mask, here a depth of 135μm has been reached without a breach in the spring due to the negative etch profile.

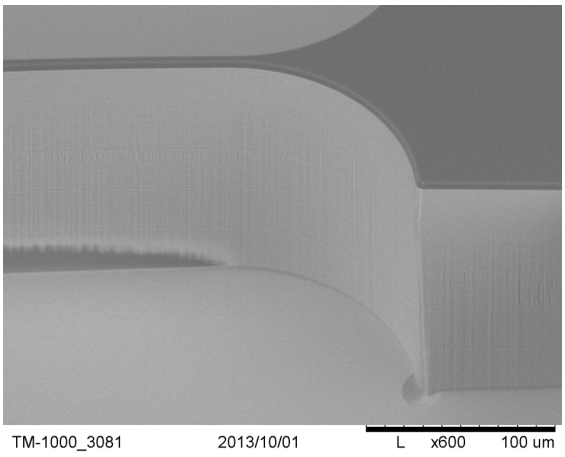

(b) This is the same sample as in subfigure 3.9a, it has been etched a further 38μm, resulting in a breach of the spring at a depth of about 150μm.

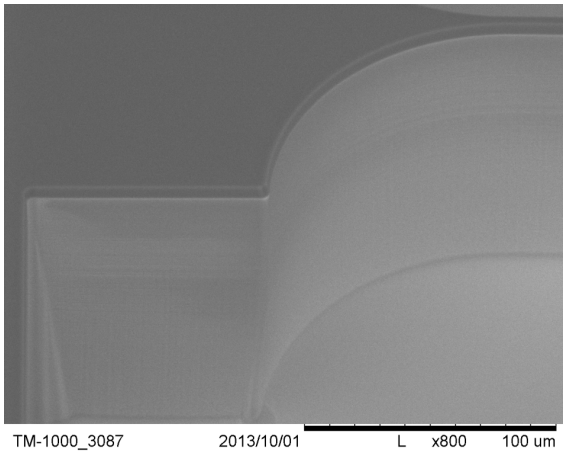

(c) This is the second etch test with an improved resist mask, here a depth of also 135μm has been reached without a breach in the spring due to the negative etch profile. This etch differs from that in the previous two sub figures in that it has a longer passivation cycle time.

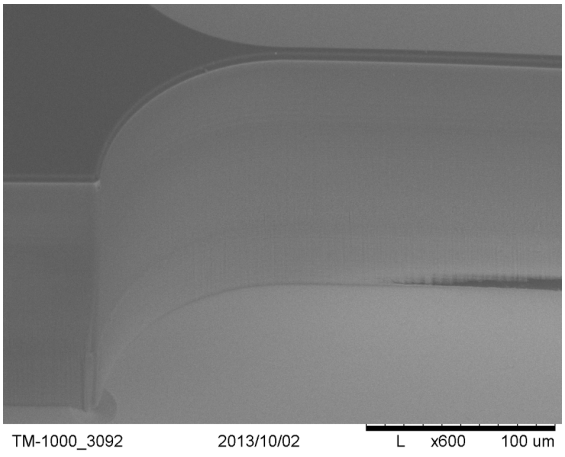

(d) This is the same sample as in subfigure 3.9c, it has been etched a further 38μm, resulting in a breach of the spring again at a depth of about 150μm.

Fig. 3.9 Four SEM images showing open-area Bosch etch optimisation tests. By altering the length of the passivation cycle, the profile of the etch could be altered. As the the passivation cycle length was increased, the etch become more anisotropic.

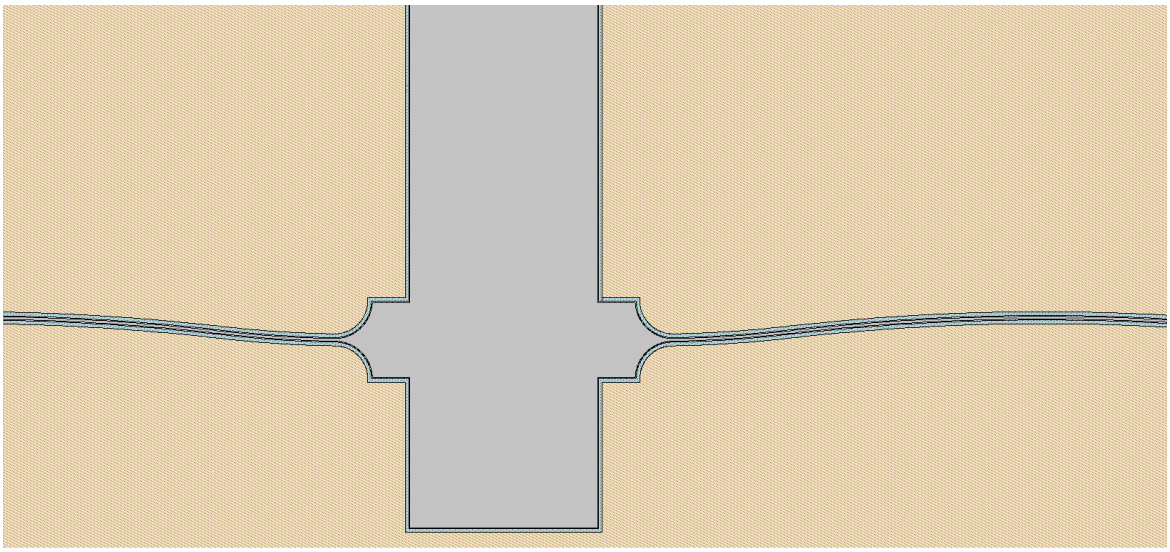

Fig. 3.10 A schematic diagram of the halo etch process. Instead of etching away all of the unwanted areas of silicon, trenches were etched around the pattern like a jigsaw. In this image the MEMS device is coloured grey, the beige areas are the unwanted pieces of silicon left behind after release, and the cyan region separating the two is the halo trench. By etching the same width of trench all around the sample (10 μm), the etch rate could be kept constant.

areas of silicon, 10 μm wide trenches[2] were used in an outline of the structure, to keep a constant etch rate and profile over all the etched areas. A schematic diagram of a halo mask can be seen in figure 3.10. The halo etch also solved a problem that had been encountered in the previous method of etching: open areas etched faster than more enclosed areas[3]. The halo etch also allowed a much more vertical etch compared to large-area etching, in which a negative profile was always found. Some SEM images of the halo etch tests can be observed in figure 3.11.

3.3 Release Mechanisms

Once the etch profile had been optimised, it was then necessary to make these structures free-standing. The release of samples to make them free-standing was one of the most difficult problems to solve in the project. This release is challenging because the samples

[2]Given the undercutting observed when using the chrome mask, the 10 μm masked trenches widened to 15 μm. The flexures also narrowed from 7 μm down to 2 μm. The mask had to be adjusted accordingly to widen the flexures to their designed width. The width of the flexures was increased to 12 μm, so that the resultant etched flexures would have a width of 7 μm.

[3]This difference in etch rate occurred because when the gas in the etch chamber is switched, the previous gas takes longer to clear from areas that are more enclosed.

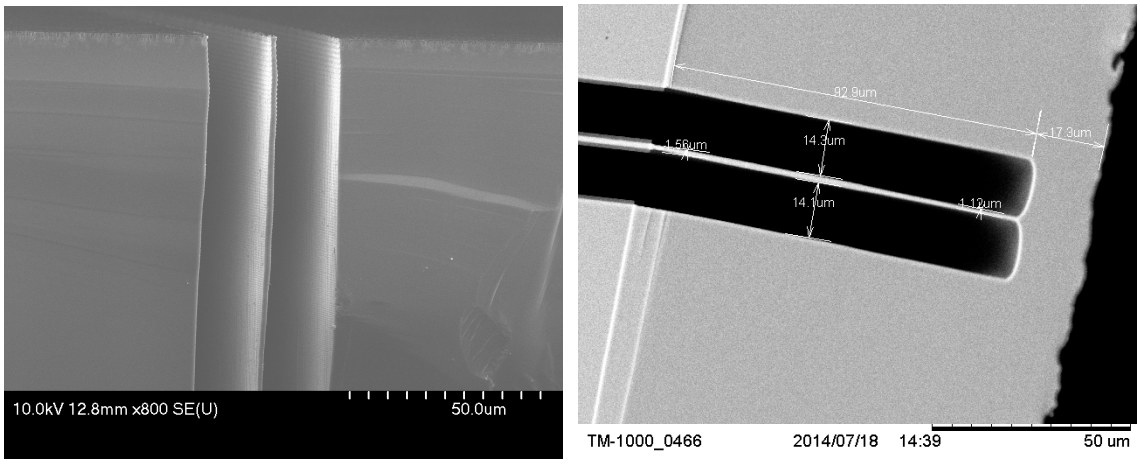

(a) A test of the halo etch process with the Estralas etch tool. Two 15 μm trenches can be seen on either side of a flexure.

(b) The same etch test as shown in figure 3.11a. From this angle the verticality of the halo etch can be observed. Here an etch angle of 89.9° has been achieved (compared to the 87.4° etch angle when using the open area etch process).

Fig. 3.11 Two SEM images demonstrating the halo etch trials with the Estralas etch tool.

have to be stuck down to a carrier wafer whilst being etched. They are stuck down with a thermally conducting material because the chamber heats up considerably during the etch, and the samples can only be cooled by conducting the heat away through the carrier wafer which is cryogenically cooled from below. Two main varieties of thermally conducting material are used in the JWNC: cool grease which is acetone soluble, and crystal bond – a wax which comes in both acetone and water soluble varieties. The challenge was to remove these delicate silicon structures from these very sticky materials. Figure 3.12 shows what the sample looked like after it had been large-area etched in the STS etch tool. The white material in this image is cool grease.

3.3.1 Wet Release Mechanisms

The most common means of releasing a sample from a carrier wafer is to place them in a chemical that will dissolve whatever compound is sticking them down. This is called a ‘wet’ release. The first release mechanisms that were tested were all wet. At first, all of the releases of the MEMS devices were carried out by dissolving the cool grease or wax in acetone. Although cool grease is acetone soluble, its ‘greasiness’ did not allow the structures to be removed without physical force which often broke them.

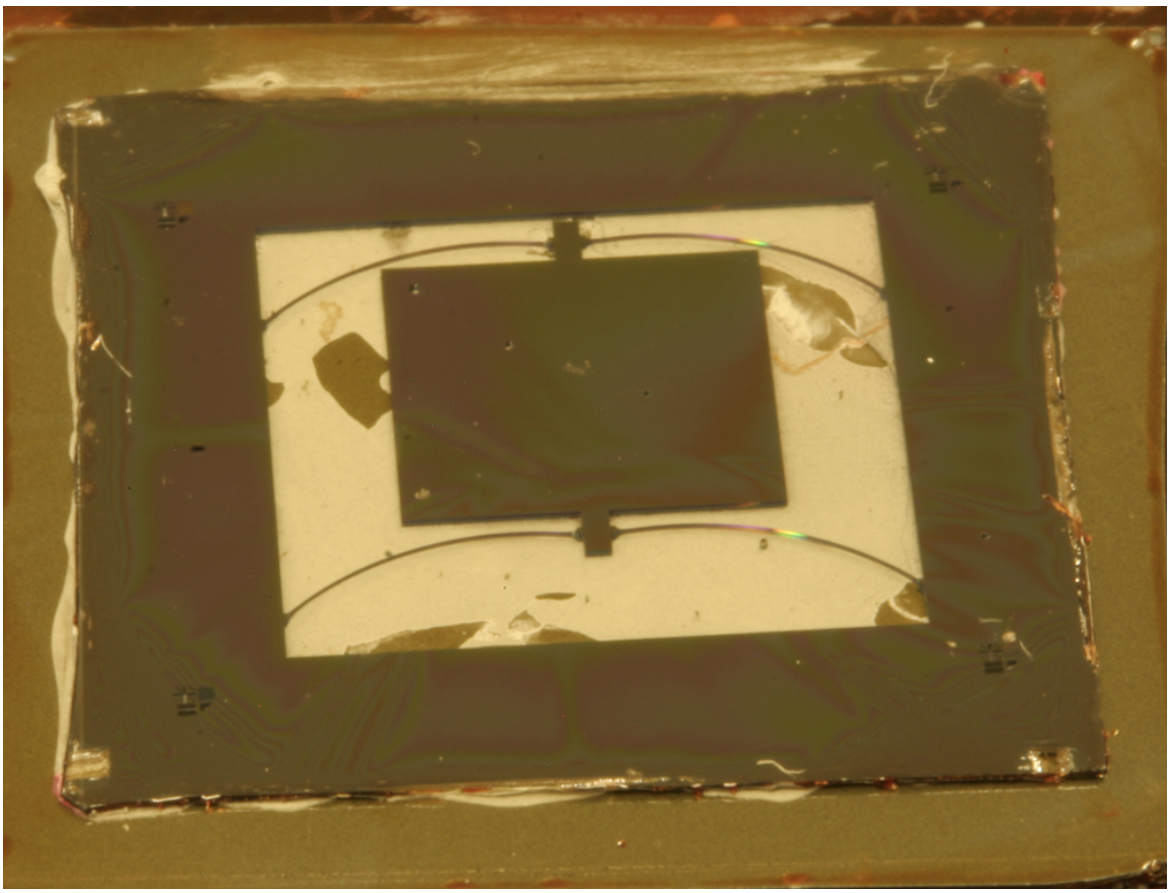

Fig. 3.12 A sample that has been etched with an ‘open-area’ etch process is stuck to the carrier wafer using cool grease. The proof mass in this sample is a square. As mentioned in chapter 2, the square pattern was swapped for an oblong design to avoid the proof mass touching the flexures as it was displaced.

There were some successful releases from cool grease using Piranha solution (sulphuric acid and hydrogen peroxide), but the bubbles resulting from the exothermic reaction made the process too risky as they could break the flexures. For this reason wax was seen as favourable compared to the grease. Samples stuck down with crystal bond wax were soaked in acetone overnight, and the samples generally floated off from the carrier with little or no agitation. Another release method was also trialled in which the wax or grease was separated from the silicon by a layer of aluminium. This aluminium could then be dissolved using a *Microposit MF319* developing solution. The advantage of this over the method described previously is that the thickness of deposited aluminium can be controlled to the nm level, therefore the release time can be predicted accurately. There were many successful means of releasing the MEMS from the carrier wafer using different solutions. This, however, was only the first step in making the samples free-standing. The second problem was how to remove the sample from the solution without breaking it. The surface tension of the liquid created stresses on the samples that were too large, and many breakages occurred whilst trying to remove the samples from liquid. Isopropanol was used instead of acetone at one stage since it has a lower surface tension (by 8%), but this did not make any noticeable difference to the number of breakages.

The obvious solution to this surface tension problem was to use a 'critical point dryer' (CPD). These tools replaced the liquid by a gas whilst avoiding crossing the liquid-gas phase boundary [92]. They do this by altering the temperature and pressure to take the liquid to the 'supercritical' region of the solution's phase diagram (see figure 3.13). In this region there is no distinction between liquid and gas, and therefore surface tension ceases to be an issue. The CPD available in the JWNC, however, was not designed to release samples from a carrier in this manner. This was therefore not a viable means of releasing the samples.

Several other means of removing the samples from the liquid were also tested. The first method attempted was to let the liquid evaporate, leaving the sample on the base of the beaker (see figure 3.14). This, however, left samples stuck to the base by resist residues, requiring more physical stresses to remove them, which – again – often broke the samples. Another method was tried in which the samples were lifted out of the liquid vertically so that the stresses on the flexures were minimised. This process found some success, but it was too reliant on the steady hands of the user. The most successful (and repeatable) liquid release process involved the use of a supporting structure for the MEMS to be placed on whilst in the liquid. This structure held the MEMS whilst the liquid evaporated, but had very little surface area for the MEMS to stick to once it had dried out – much like a sieve. All of these

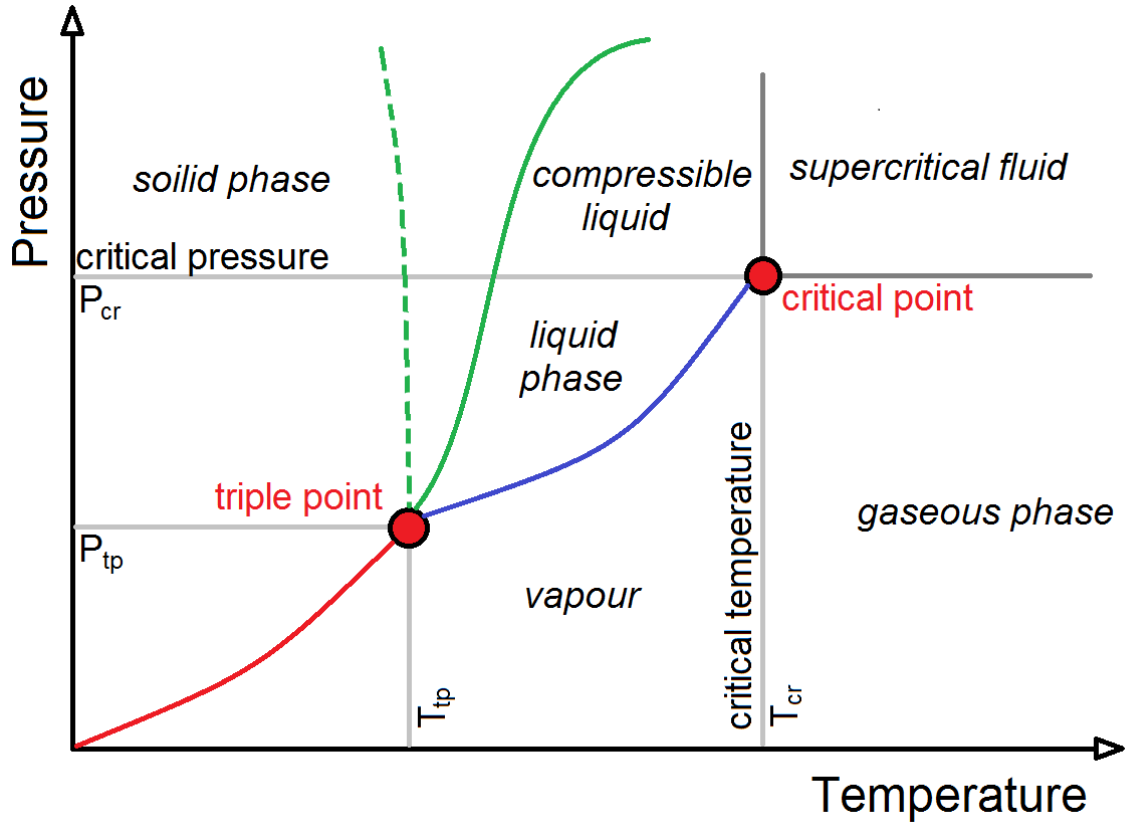

Fig. 3.13 A graph demonstrating the location of the critical point on the phase diagram of a liquid. At this point this there is no distinction between liquid and gas.

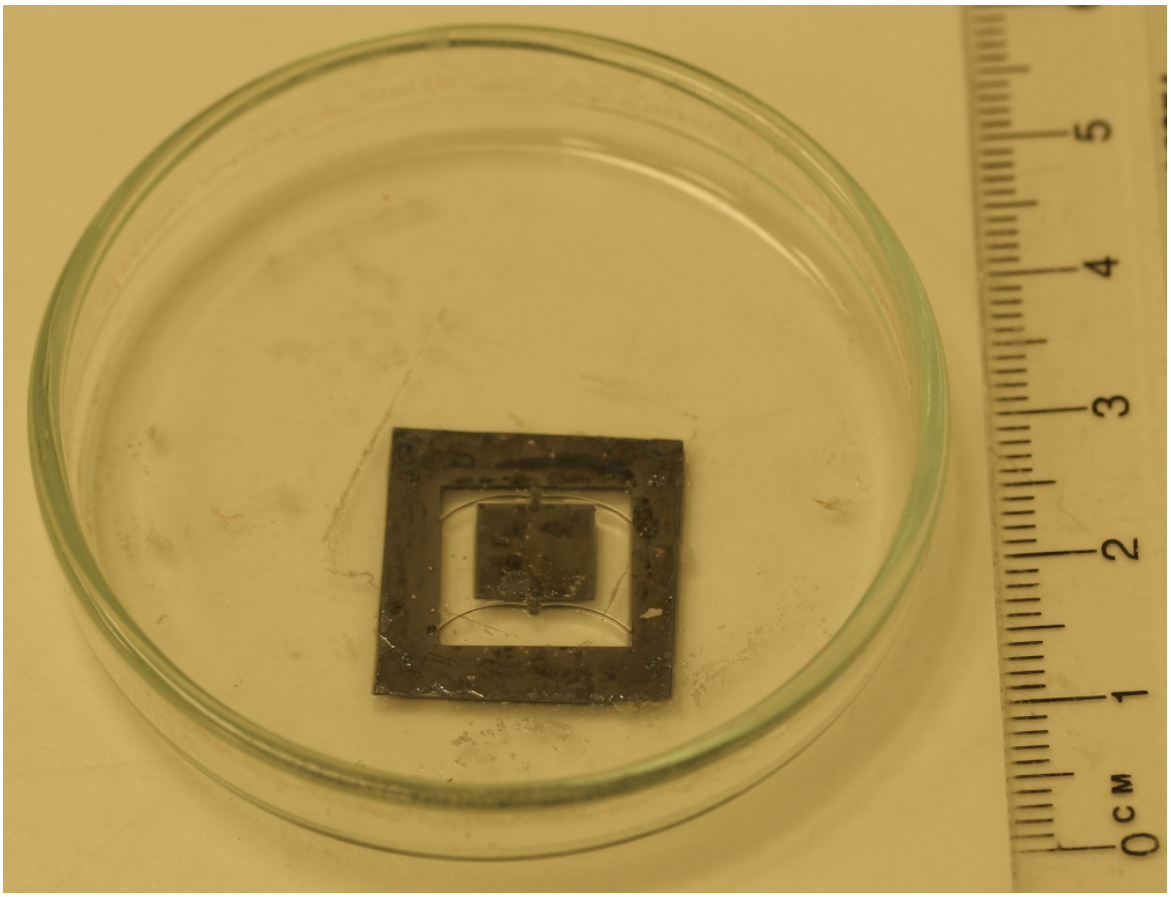

Fig. 3.14 The first attempt at a liquid release, the sample remained intact during the evaporation but one flexure was broken because the sample became stuck to the base once dry.

processes, however, involved careful manipulation by the hands of the experimenter and therefore did not lend themselves to repetition in an industrial setting.

In MEMS foundries, samples are normally released using a hydroflouric (HF) acid vapour. HF vapour etches oxides such as SiO_2 but does not etch silicon. Structures are therefore generally made from an SOI (silicon-on-insulator) wafer. These wafers have a layer of oxide underneath a silicon substrate. After a structure is etched from the silicon, the sample is exposed to the HF vapour, the oxide is removed, and the samples becomes free-standing without the need for a wet etch. An HF vapour release tool was not available in the JWNC at the time of this process development, so this was not an option for the MEMS gravimeter. Some features of this method, however, were borrowed to develop a bespoke means of releasing the samples that did not involve liquids.

3.3.2 Dry Release Mechanism

The switch away from wet releases also occurred at the same time as the halo etch was adopted. Although an HF tool was not available, other tools were that could etch oxide layers using a plasma. The idea was struck upon to deposit a thin layer of SiO_2 on the bottom of the sample before it was stuck down to the carrier wafer. This layer would act as a support for the mechanical silicon structure that could be etched away once the sample was removed from the carrier wafer. This method was tested: a sample was etched and the carrier then placed on a hot plate to melt the crystal bond. The sample was then pushed laterally to minimise the stress on the SiO_2 support layer. The SiO_2 layer, however, was too susceptible to cracking as the sample was pushed off the carrier. To strengthen the support layer it was decided to spin on a 7 μm layer of *AZ4562* resist onto the SiO_2 support layer. This double layer was sufficient to support the silicon structure as the samples were pushed off the carrier.

The next stage of the release was to remove the resist and crystal bond from the bottom of the sample. The sample was turned upside down and placed (but not stuck) onto a piece of blank silicon and placed in an *Oxford Instruments BP80* plasma ashing tool. Both crystal bond and resist can be removed using an O_2 plasma ash. The cyrstal bond, however, was very slow to etch and the ash was taking a considerable number of hours to etch down to the SiO_2 layer. To make the crystal bond layer thinner a new means of applying this bonding compound was required. Previously a stick of crystal bond had been smeared onto the carrier wafer whilst it was heated to the melting point of the wax. There was no way of controlling the thickness of this smear. Instead, crystal bond was ground into a powder, and dissolved in acetone. This solution was then spun onto the carrier wafer, creating a layer of only a few microns thick. Now, the crystal bond was thin enough – post-etch – to be stripped off with an O_2 ash. The only layer now supporting the MEMS structure was the 2 μm of SiO_2. The sample was therefore placed in a *Plasmafab 80 plus* RIE etch tool that was capable of etching SiO_2 but not silicon. Using a combination of CHF_3 and Argon, the SiO_2 was etched away completely. The sample was now dry, free-standing and sitting on a piece of blank silicon, but also remaining were the unwanted areas of silicon that were not etched during the halo etch.

To separate the sample from the unwanted bits of silicon, a vacuum chuck was designed. This chuck had suction holes drilled in areas that would attach only to the MEMS proof mass and frame, but not the unwanted lumps of silicon (see figure 3.15). The chuck was attached to a micrometer stage, allowing it to be lowered onto the sample. The vacuum pump could then be turned on and the sample lifted clear. The vacuum pump used was a *Windrush FV-10* that could apply a variable vacuum pressure from -4 kPa to -14 kPa. A photo of a free

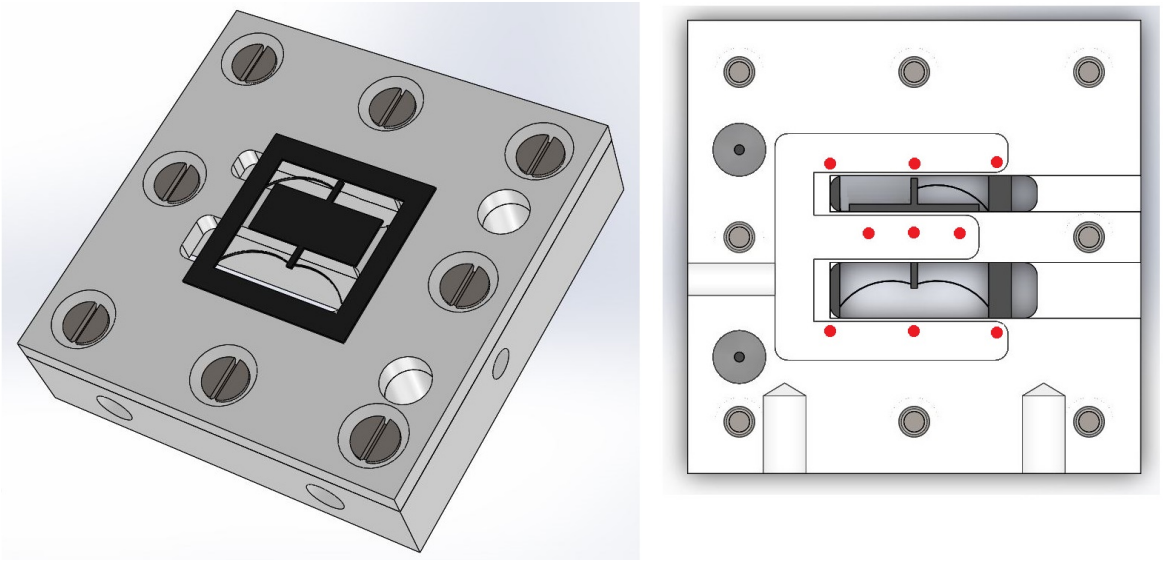

Fig. 3.15 The vacuum chuck designed to pick up the sample. Suction holes (coloured red in the diagram) hold onto the proof mass and the outer frame. The chuck can then be lifted with a micrometer stage, leaving behind the unwanted pieces of silicon.

standing MEMS device is displayed in figure 3.16, and an SEM of another device is shown in figure 3.17.

3.4 Summary: The Final Etch Recipe

The final etch recipe is outlined here for completeness. The MEMS device was fabricated from a single chip of 220 μm thick silicon. Both the top and bottom of the sample was coated with 2 μm of PECVD SiO_2. A 2.8 μm layer of *Microposit S1828* resist was then spun onto the top surface of the silicon. The MEMS device pattern was then created in this layer of resist using a photolithography process. The mask was a 'halo' design [91] i.e. instead of etching away all of the unwanted areas of silicon, trenches were used in an outline of the structure, to keep a constant etch rate and profile over all etched areas. The halo width that was eventually settled upon was 20 μm. The photoresist pattern was then used as a mask to dry etch the SiO_2 using a *Plasmafab 80 plus* RIE etch tool, thus etching the MEMS device pattern into the SiO_2. A 7 μm layer of *AZ-4562* photoresist was then spun onto the back of the sample to be used later as an additional mechanical support layer.

The sample was fixed to a carrier wafer using a thin, spun-on layer of *Crystalbond 509* in solution with acetone. To ensure a good thermal contact the sample was weighted and left on the hotplate at 88° C (just above the melting point of *Crystalbond*) for 5 minutes.

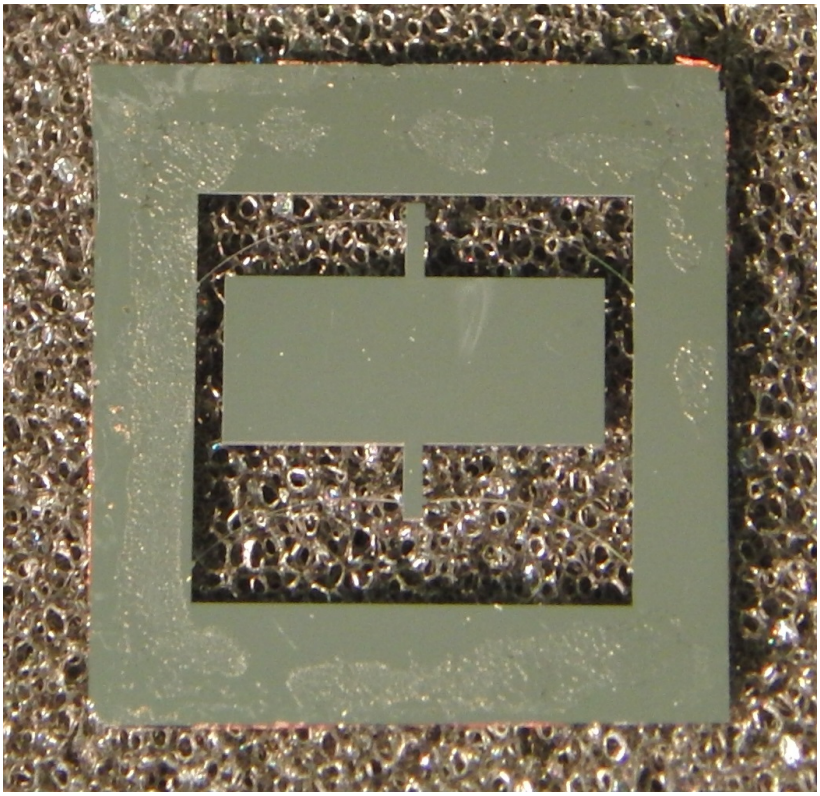

Fig. 3.16 A photograph of a MEMS device that has been released by etching away the SiO_2 support layer.

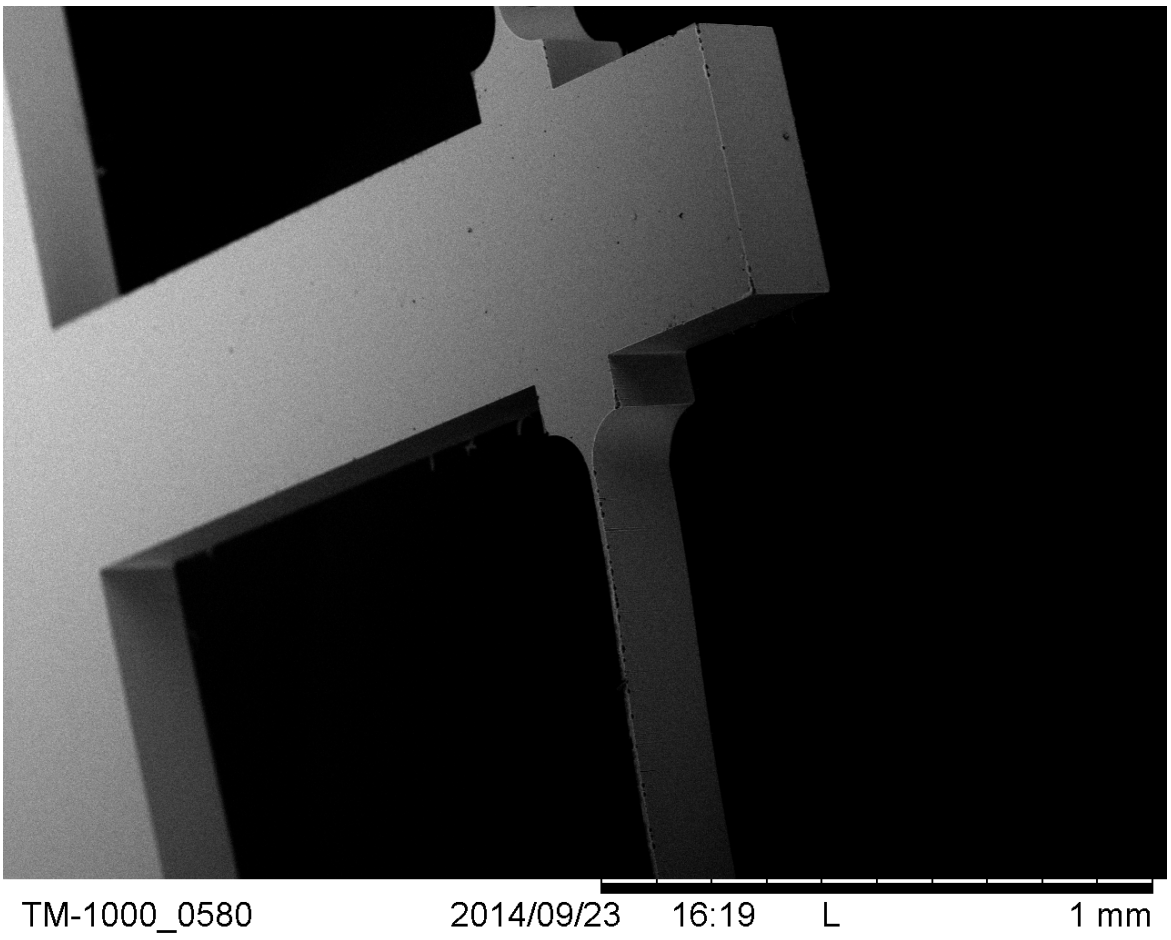

Fig. 3.17 An SEM of a MEMS device that has been released by etching away a SiO_2 support layer.

The sample was next placed in an *Oxford Instruments PlasmaPro 100 Estrelas Deep Silicon Etch System*, and Bosch etched [85] for 90 minutes using an SF_6, C_4F_8 process optimised for highly anisotropic trenches. This etch was the same depth as the silicon and stopped when it reached the SiO_2 back layer. The *PlasmaPro 100 Estrelas Deep Silicon Etch System* allows control of the gas flow enabling processes to be tuned with negative and positive defined etch profiles. The spring profiles are vertical to within 0.5°.

To remove the sample from the carrier wafer it was heated to 88° C for 5 minutes, and then pushed laterally off the - now fluid - *Crystalbond*. The SiO_2 and *AZ-4562* layers enabled this to be done without damaging the MEMS device structure. The sample was then turned upside down and placed (not affixed) to a blank piece of silicon. The residual *Crystalbond* and photoresist were removed from the bottom of the sample using an O_2 plasma ash. The sample was exposed to a CHF_3/Ar etchant plasma until all of the SiO_2 was removed, making the sample free standing. The sample could then be picked up using a specially designed vacuum chuck.

*

The rate of success of fabricating these MEMS devices has increased steadily. The stage during which most samples were broken was the release from the carrier wafer. Since the release has been conducted using a dry process, and the vacuum chuck has been adopted, this has become a much less risky endeavour. At present the yield will be somewhere above 70% but equipment down-time has limited the number of samples that could be made. Once the samples are made in bulk it is expected that this percentage will get very close to 100%. There is no reason why this process could not be scaled to produce many samples at the same time. A photomask could be created that made tens of samples on a single wafer, this could then be etched and the samples lifted using a larger vacuum chuck that could align with the outside of the wafer. Mass production is an issue for the future. At this stage, once a sample had been produced, a sensor was required to measure the displacement of the proof mass as it moved under the influence of gravitational anomalies. The design optimisation of this sensor is the topic of the following chapter.

Chapter 4

Position Sensor Construction

The MEMS gravimeter would not be of use without a means of measuring the displacement of the proof mass. From equation 1.3, it can be observed that in order to maximise the sensitivity to gravitational acceleration, g, not only must the ratio of k/m be minimised, but the sensitivity to displacement, x, must also be as accurate as possible. For example, a device with a resonant frequency of 1 Hz would require a displacement sensitivity of 2.5 nm/$\sqrt{\text{Hz}}$ in order to reach an acceleration sensitivity of 10 ng/$\sqrt{\text{Hz}}$, since:

$$x = \frac{g}{(2\pi f_0)^2} \tag{4.1}$$

where f_0 is the resonant frequency of the device. Furthermore, the geometry of the MEMS – discussed in chapter 2 – also places constraints on the design of the optical sensor. There is a large initial displacement of the proof mass when it is oriented vertically due to the anti-spring effect. This displacement is of the order 0.8 mm (the absolute value varies depending on the thickness of the flexures). Any sensor must be non-contact and operate with a large dynamic range. The expected level of the seismic noise that would influence the system led to the target of having a displacement sensor with a linear range of at least 50 μm. Optical sensing was selected over capacitive sensing because it can provide high sensitivity without introducing parasitic forces due to stray electromagnetic fields [93].

In this chapter an early design for a diffractive optical sensor will first be discussed. Since this design was abandoned at an early stage, the majority of the chapter will consist of a discussion of the displacement sensor that was ultimately used to monitor the MEMS gravimeter – an optical shadow sensor. The basic design of the optical shadow sensor will be outlined, along with its associated readout circuitry. This will be followed by a discussion of the noise sources of the readout electronics. Along with seismic noise, it was these electrical

noise sources that would limit the ultimate sensitivity of the sensor. Since gravimetric measurements sometimes need to be carried out over periods of days, weeks or months: it is important that the displacement sensor maintains its noise floor over the same time scales. Some details of the steps that were taken to mitigate against sources of drift in the displacement sensor are therefore discussed. This chapter will conclude with a discussion of the experimentally observed performance of the device.

4.1 Diffractive Sensor

The first design of displacement sensor considered was one based upon the diffraction of light [94, 95]. It consisted of a laser beam that was shone through a single slit, producing a sinc function intensity pattern at a grating. By moving the grating laterally across this pattern, the change in the resulting intensity pattern would allow the grating movement to be measured. It was thought that the grating could be mounted upon the MEMS proof mass. Figure 4.1 is a demonstration of this sensor design, using data obtained using the *Wavetrace* [96] package for *Labview*. Although achieving a reasonable signal-to-noise ratio of around 1 nm/$\sqrt{Hz}$ (depending on the spacing of the gratings), this design had significant drawbacks. Firstly, with a maximum linear response range of only $\sim$2 μm, the design would not have enabled measurement of the expected maximum displacements of the proof mass. Secondly, gratings would have had to be fabricated with a high tolerance - a lengthy and expensive process. Thirdly, micrometer level precision would have been required in setting up the sensor for it to get even close to its possible detection accuracy. Given the large initial displacement of the proof mass, this would be difficult to achieve. On the basis of these factors it was decided that this was an infeasible design to use for this purpose.

4.2 Optical Shadow Sensor and Readout Circuitry

The second displacement sensor considered was an optical shadow sensor. Optical shadow sensors have been used as displacement sensors in the Advanced LIGO gravitational wave detectors [97, 98]. These sensors achieve sensitivities of 3×10^{-10} m/$\sqrt{\text{Hz}}$ over a linear range of 600 μm (see figure 4.2). The basic design of a shadow sensor consists of a light source and a photodiode. The light source is shone onto the photodiode, creating a photocurrent. If an object is placed in the light beam, it will cast a shadow onto the photodiode. As the object is moved, the shadow will cause the photocurrent to change. This

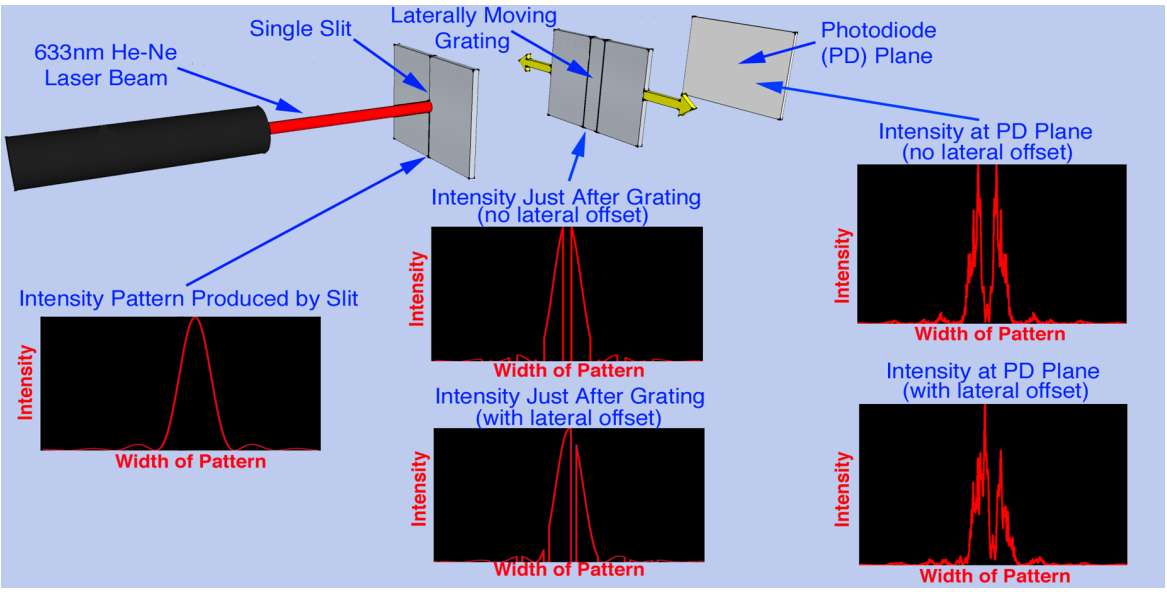

Fig. 4.1 A schematic diagram of a diffractive optical motion sensor and intensity graphs to explain its operation.

change – if the system is properly calibrated – can be used as a measure of the object's motion.

Given the level of sensitivity realised by the optical shadow sensors in Advanced LIGO, the decision was made to construct a sensor along similar lines for the MEMS gravimeter. Firstly, a structure was required on which to mount the components. A 'C' shaped structure was made from fused silica[1], which held a 635 nm (red) LED that was pointed towards a pair of 5 mm $\times$ 10 mm planar silicon photodiodes. For the purposes of testing the shadow sensor, a piece of silicon was affixed centrally over the two photodiodes using epoxy resin. This piece of silicon (or 'flag') would ultimately be replaced with a MEMS proof mass.

The red LED signal was modulated using an *HP 33120A* square wave signal generator in order to increase the low frequency performance (this will be discussed in more detail later in this chapter). The Advanced LIGO detector, in contrast, operated with DC light intensity. It was modulated at a frequency of 107 Hz with a 50:50 duty cycle. A resistor was wired in series with the LED. A resistor was required because LEDs (like all diodes) do not behave according to Ohm's Law (R = V/I). Instead, their resistance changes according to a non-linear I-V curve [99]. LEDs require a certain forward voltage to turn on, but there is also a voltage above which the resistance of the LED falls off sharply. If the voltage becomes too high, enough current can be drawn to 'blow' the LED. It is therefore important to select

[1]The choice of this material will be discussed later in this chapter.

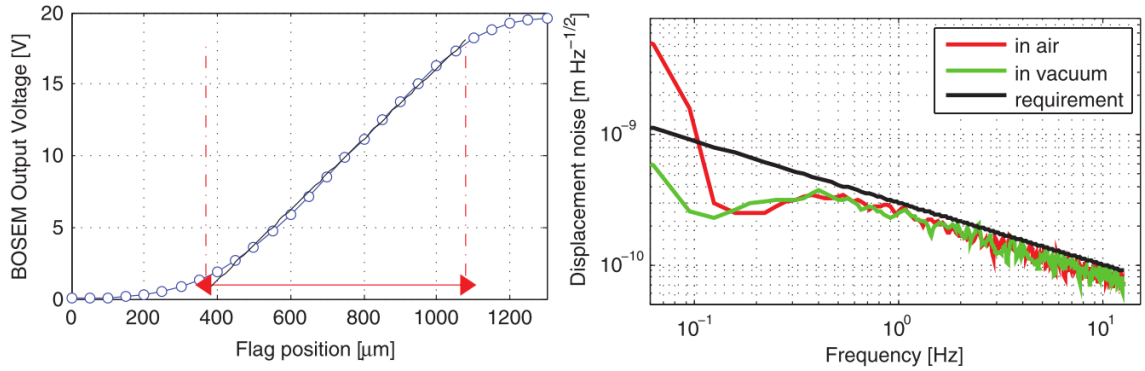

Fig. 4.2 This figure is taken from a paper by Carbone et al [97], showing the performance of the optical shadow sensor developed for the Advanced LIGO gravitational wave detector. The plot to the left demonstrates the 600 μm linear range of the sensor. The plot to the right shows the noise performance of the device. The black line is the required performance for the gravitational wave detector. The red and green lines show the noise performance of the shadow sensor in air and vacuum respectively. At 1 Hz the device has a sensitivity of 3×10^{-10} m/$\sqrt{\text{Hz}}$.

a resistor that keeps the LED at the optimum position on its I-V curve. This is called the characteristic current. The optimum resistor value, R, can be calculated by [99]:

$$R = \frac{V_s - V_f}{I} \tag{4.2}$$

where V_s is the supply voltage, V_f is the forward voltage drop, and I_f is the LED forward current. The values of both V_f and I_f are specific to the particular LED and can be found in the product datasheet (*Thorlabs LED631E* epoxy-encased LED) [100]. A high precision, temperature stable, 1 kΩ resistor was used for this purpose. This resistor was glued onto the fused silica structure (which was temperature controlled), to avoid any further risks of temperature induced resistance variations.

The two photodiodes were wired differentially [101, 102] (as seen in figure 4.4). This is a standard configuration for light balancing circuits. In this configuration the anode of one photodiode was wired to the cathode of the other, and vice versa. In other words, the photodiodes were connected in reverse parallel. One of the wire pairs was connected to ground, and the other was used as the output[2]. This meant that if both photodiodes were evenly illuminated by the LED the output signal would be zero. Crucially, with a low or zero output signal, the amplification of the output signal could be increased, improving the overall

[2]The photodiodes were operated in photovoltaic mode (i.e. no reverse bias was applied). This meant that there was zero dark current [103].

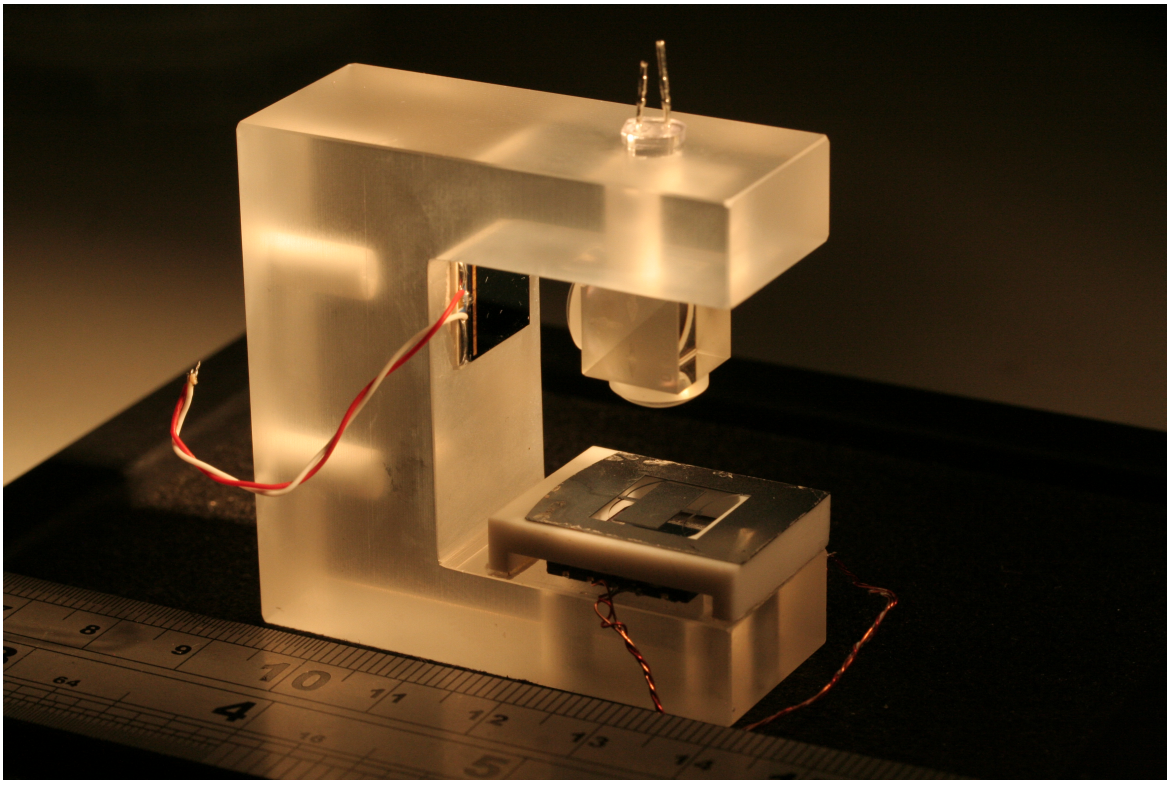

Fig. 4.3 A photograph of the shadow sensor. An LED shines onto a split photodiode with the MEMS device mounted in between. As the shadow cast by the proof mass moves over the photodiodes, the resultant change in photocurrent can be used as a measure of the displacement. The components are mounted on a fused silica structure, with a beam splitter and second photodiode to monitor any fluctuations in the intensity of the LED.

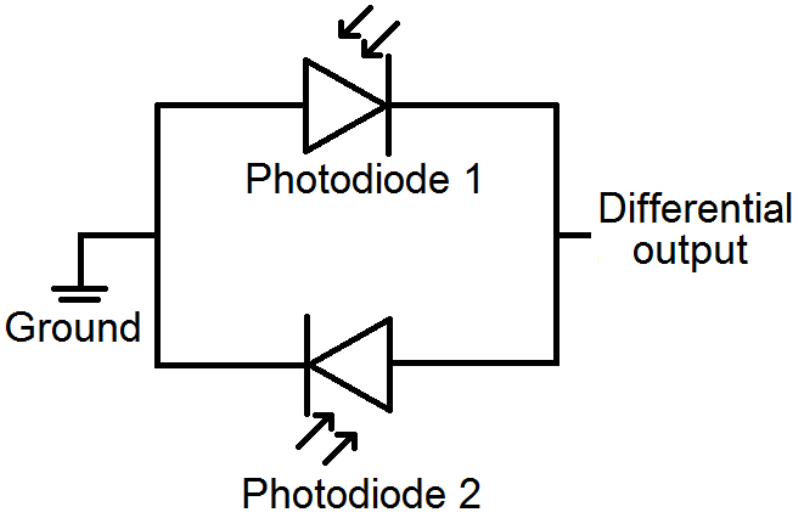

Fig. 4.4 The circuit diagram for the differential configuration [101, 102] of the photodiodes in the shadow sensor. Two planar silicon photodiodes are wired in reverse parallel. If both are evenly illuminated then the output signal is zero.

noise performance of the amplification circuitry[3]. A diagram of this amplification circuitry can be observed in figure 4.5. Each component of this circuit diagram is discussed in turn below.

The output photocurrent of the differentially configured photodiodes was then passed through an *SRS SR570* current-to-voltage (transimpedance) amplifier. This converted the photocurrent into a voltage, and amplified the signal by a factor of one million (1 μA/V)[4].

After the signal was amplified by the transimpedance amplifier it was passed through a *Femto LIA-MV-200*) analogue lock-in amplifier[5]. This used the reference from the signal

[3]This is the case when the noise floor is limited by the amplification circuitry.

[4]The *SRS SR570* also allowed a band-pass filter to be implemented. A band-pass was used between 3 Hz and 1 kHz. This was carried out to reduce the noise outside of the modulation frequency. A reduction in noise was useful in the event that one wanted to observe the signal on an oscilloscope before it was demodulated with the lock-in amplifier. The band-pass filter was not of importance for any reasons other than this because the lock-in amplifier rejected signals outside of the 107 Hz modulation frequency.

[5]Initially, a digital lock-in amplifier (an *SRS 830*) had been used instead of the *Femto*. The full scale of the *SRS 830* could be varied from 1 V down to 1 nV. The scale could therefore be changed so that the output was not influenced by digitisation noise. This would have been sufficient if one wanted to observe mV variations in a signal that was mV in size, or nV variations in a signal that was nV in size. This, however, was not the case for the output of the split photodiode. Since it was challenging to perfectly centre the MEMS proof mass over the two sides of the photodiode, a small positive current was always present in the output of the photodiodes. This meant that the voltage entering the lock-in could be hundreds of mV, but the scale of the variations that needed to be observed were at the nV level. Digitisation noise therefore became a problem; the digital lock-in output was clearly made up of discrete steps (when running on full scale the digitisation noise in the output was 0.3 mV). To avoid this problem, the *SRS 830* was replaced with an analogue lock-in amplifier – the (*Femto LIA-MV-200*) – that would not suffer from digitisation noise.

generator to de-modulate the signal, converting the signal from AC to DC. As will be discussed later in this chapter, the utilisation of the lock-in amplification technique helped to reduce drift in the signal. The lock-in amplifier was set to amplify the signal by a factor of 1000 and take readings with a time constant of 3 s.

Once the signal had been demodulated it was passed through an *SRS SR560* preamplifier. This was included to act as a low pass filter for signals below 0.03 Hz. Such a filter was deemed necessary to rid the signal of any aliasing effects. Aliasing is a phenomenon that can occur whenever signals are sampled [104]. Signals of different frequencies can become aliases of one another and therefore indistinguishable. The low-pass filter would also be beneficial at a later stage once the MEMS device had been placed in the sensor and was free to oscillate. It was expected that the signal from the MEMS device would include significant levels of seismic noise. Most of this seismic noise would lie above the 0.03 Hz low-pass frequency [60] and therefore be filtered from the signal.

In order to record the output signal with a computer, the analogue signal needed to be digitised. The signal was digitised using a 16 bit, 12 dB/octave *National Instruments M Series 6229* analogue-to-digital converter (ADC). The output from the ADC was then recorded by a computer with a 24 s time constant.

4.3 Shadow Sensor Voltage Output

4.3.1 Signal Propagation

The theoretical output voltage of the circuit in figure 4.5 can be calculated as follows.

The photocurrent produced by each photodiode is a function of its illuminated area. As can be seen in figure 4.6, when the flag is centered each photodiode (PD_A and PD_B) has an illuminated area of $W \times L$. If the flag moves towards PD_B by a distance of x, then the photocurrents of PD_A and PD_B will be given by:

$$I_{PDA} = RP_d(W+x)L \quad \text{A} \tag{4.3}$$

$$I_{PDB} = RP_d(W-x)L \quad \text{A} \tag{4.4}$$

where R is the responsivity of the photodiode, and P_d is the power density:

$$P_d = \frac{P}{\pi R_s^2} \quad \text{W/m}^2 \tag{4.5}$$

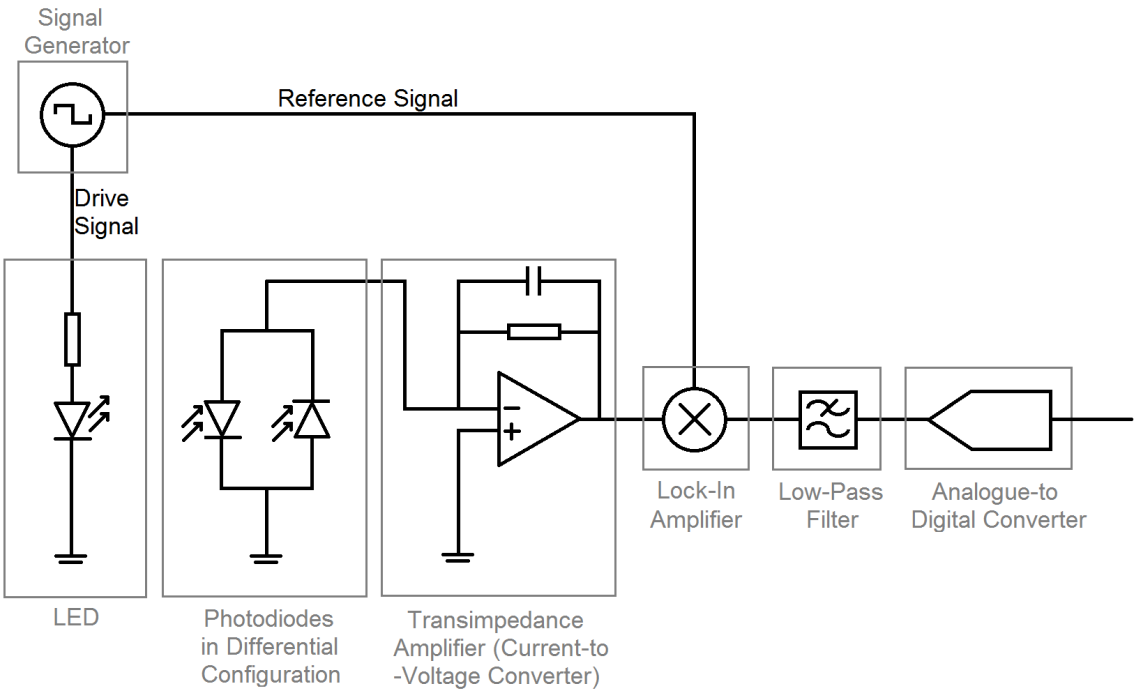

Fig. 4.5 The circuit diagram of the optical sensor readout. A modulated 635 nm (red) LED was shone onto a pair of photodiodes in a differential configuration. The MEMS was mounted so as to cast a shadow on the photodiodes. If the MEMS proof mass was perfectly centered then the output signal from the photodiodes was zero. If the MEMS proof mass moved off-centre then the output signal became non-zero and could be amplified. The resultant output current was first passed through a transimpedance amplifier that converted the signal into a voltage and amplified it by a factor of 10^6. The output voltage of the amplifier was then de-modulated with an analogue lock-in amplifier (with a further gain of $1000\times$), low passed, and finally digitised using an analogue-to-digital converter (ADC).

where P is the emitted power of the LED, and R_s is the radius of the LED spot. This assumes an even illumination over the entire spot. Even illumination could have been achieved by mounting a diffusing plate (say, a sample of frosted glass) over the LED exit pupil.

Since the two photodiodes are configured differentially, the total output current is given by the difference between I_{PDA} and I_{PDB}. The total voltage output of the entire system is therefore given by the total output current multiplied by the gain of the amplification electronics:

$$V_{\text{out}} = G_{\text{SR570}} G_{\text{LIA}} (I_{PDA} - I_{PDB}) \quad \text{V} \tag{4.6}$$

where G_{SR570} is the gain of the *SRS SR570* transimpedance amplifier (10^6), and G_{LIA} is the gain of the *Femto LIA-MV-200* lock-in amplifier (10^3).

4.4 Potential Sources of Noise in Readout Circuitry

In the next section the theoretical noise performance of the readout circuitry will be outlined. Before this, however, a brief background is given on different sources of electronic noise.

4.4.1 Johnson-Nyquist Noise

Johnson-Nyquist noise [105, 106] is a form of noise that is found in all electrical components. It is white in nature and is caused by the thermal fluctuations of charge carriers in a conductor [107]. It gets larger with both increasing circuit resistance and increasing temperature and its amplitude spectral density is given (in units of $\text{V}/\sqrt{\text{Hz}}$) by:

$$v = \sqrt{4 k_B T R} \tag{4.7}$$

where k_B is the Boltzmann constant, T is the temperature, and R is the resistance of the component. The RMS noise is found my multiplying through by the square root of the frequency bandwidth, Δf. The RMS noise can therefore be reduced by decreasing the bandwidth of the measurement. This can be achieved by applying filters that cut the detection window to a finite size. For example, this was implemented in the shadow sensor readout circuitry by introducing a band-pass filter to the signal using the *SRS SR570*.

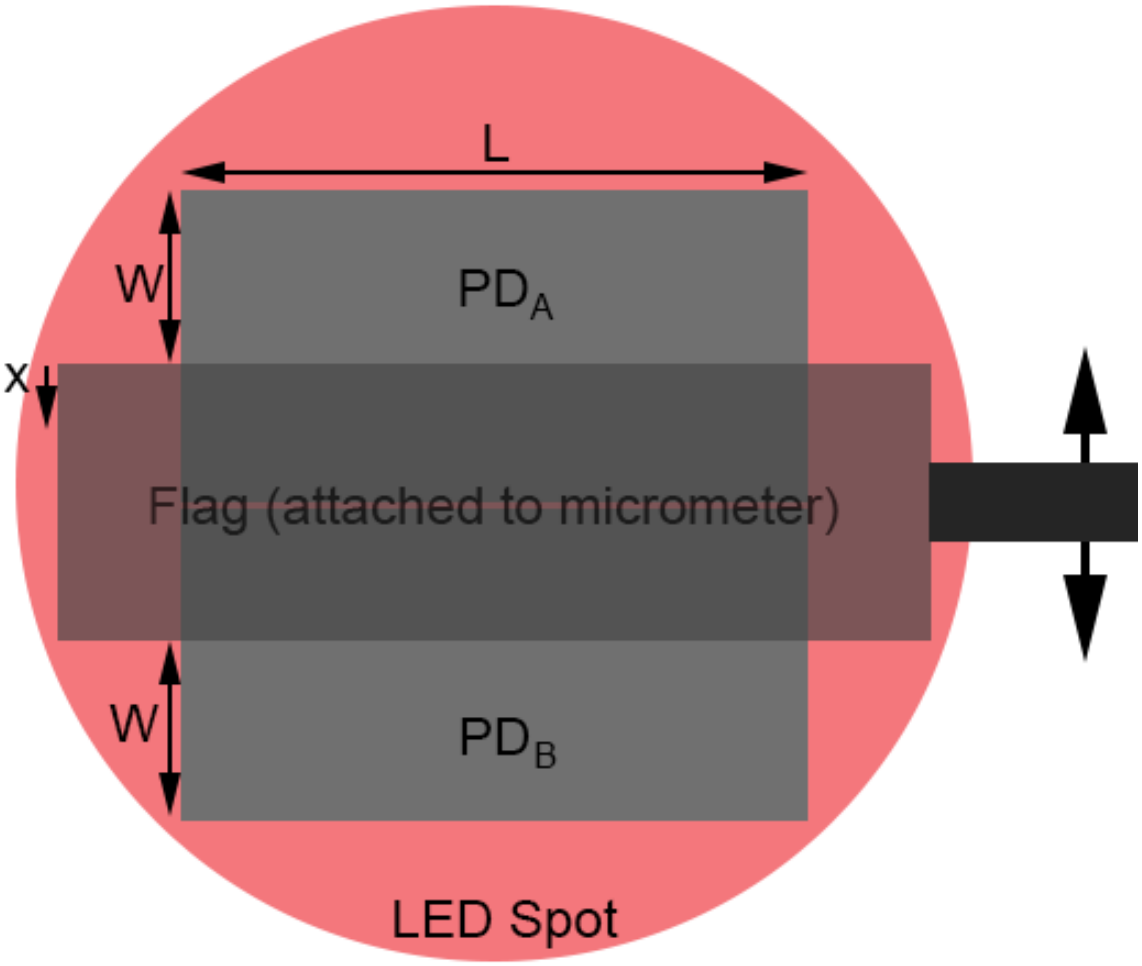

Fig. 4.6 A schematic diagram of the means by which a signal is produced from the split photodiodes. Two differentially wired photodiodes (PD_A and PD_B) are shown illuminated by a red LED spot. Over the photodiodes a flag is placed (made translucent in this image to show what lies beneath). This flag casts a partial shadow over both photodiodes. Each photodiode therefore has an illuminated area of length, L, and width, W, when each are evenly covered by the flag. The flag is attached to a micrometer stage that can move the flag over the two photodiodes. This displacement has a magnitude of x.

4.4.2 Shot Noise

Another fundamental source of noise is due to the discrete photon behaviour of light – Shot noise. As individual photons hit the photodiode, then the standard deviation of the signal is governed by Poisson statistics [108]. This means that for N photons that hit the photodiode, the standard deviation will be given by $\sqrt{N}$. Therefore the lower the intensity of the incident light (i.e. small N), the lower the signal-to-noise ratio becomes. Shot noise creates noise in a conductor through which a current is flowing. The amplitude spectral density of this current noise is given (in units of A/$\sqrt{\text{Hz}}$) by:

$$\sigma_{is} = \sqrt{2qI_s} \tag{4.8}$$

where q is the charge of a photoelectron, and I_s is the photocurrent. Again, the RMS noise is found my multiplying through by the square root of the frequency bandwidth, Δf. Given the nature of shot noise, it is obvious that the best way to mitigate against its effect is to turn up the intensity of the light. For the shadow sensor, the light intensity was therefore made as large as possible without the resulting output saturating the readout electronics.

4.4.3 Bias Current Noise

A final source of noise in the system will be the noise caused by the input bias of the current-to-voltage amplifier. An ideal amplifier would have infinite input impedance, and it would draw no current. Such an ideal system, however, is not practically possible and so real amplifiers will always have a bias current (a current difference between the two inputs). The level of this bias current is intrinsic to the amplifier and is caused by shot noise within the amplifier transistors. The amplitude spectral density of this noise source therefore has the same form as equation 4.8. It is given (in units of A/$\sqrt{\text{Hz}}$) by:

$$\sigma_{ib} = \sqrt{2qI_b} \tag{4.9}$$

where q is the charge of a photoelectron, and I_b is the bias current. Once again, the RMS noise is found my multiplying through by the square root of the frequency bandwidth, Δf. The quality of the amplifier determines the size of the bias current. Given the quality of modern amplifiers, this noise source will be significantly smaller than either Johnson-Nyquist noise or Shot noise.

4.5 Error Budget of the Readout Circuitry

The propagation of noise through the amplification circuit can be calculated as follows.

First consider the noise that arose from the photodiodes and the *SRS SR570* transimpedance amplifier. Each photodiode had a Shot noise level given by equation 4.8. Given an estimated emitted power level of 40 μWatts for the LED; a beam spot size of 10 mm; a photodiode responsivity of 0.4 A/W; a photodiode length, L, of 10 mm; and a photodiode illuminated width, W, of 2 mm: the shot noise level for each photodiode was found to be $\sigma_{isPD} = 6.01\times10^{-13}$ A/$\sqrt{\text{Hz}}$.

The *SRS SR570* transimpedance amplifier had a Johnson-Nyquist noise level given by equation 4.7 and a bias current noise given by equation 4.9. These two sources of noise in the transimpedance amplifier can be combined to give a total input current noise. This total input current noise was 6.00×10^{-13} A/$\sqrt{\text{Hz}}$ at a sampling frequency of 100 Hz (found in the data sheet of the *SRS SR570* [109]). The noise sources from the photodiodes and the amplifier sum in quadrature (see equation 4.10). Each term has been multiplied by the gain of the amplifier to provide the total voltage noise of the photodiodes and transimpedance amplifier, V_{N1}.

$$V_{N1} = \sqrt{(\sigma_{isPDA}G_{\text{SR570}})^2 + (\sigma_{isPDB}G_{\text{SR570}})^2 + (\sigma_{SR570}G_{\text{SR570}})^2} \quad \text{V}/\sqrt{\text{Hz}} \tag{4.10}$$

where σ_{isPDA} is the shot noise of PD_A, σ_{isPDB} is the shot noise of PD_B, G_{SR570} is the gain of the *SRS SR570* transimpedance amplifier, and σ_{SR570} is the input current noise of the *SRS SR570*. Using equation 4.10, the cumulative voltage noise at this stage was found to be 1.04×10^{-6} V/$\sqrt{\text{Hz}}$.

After the signal had passed through the transimpedance amplifier, it was demodulated by the *Femto LIA-MV-200* lock-in amplifier and amplified by a further factor of 1000. The lock-in also has its own voltage input noise of 1.2×10^{-8} V/$\sqrt{\text{Hz}}$ (found in the data sheet of the *Femto LIA-MV-200* [110]), which can be summed in quadrature with the noise already propagated through the circuit:

$$V_{N2} = G_{\text{LIA}}\sqrt{V_{N1}^2 + V_{LIA}^2} \quad \text{V}/\sqrt{\text{Hz}} \tag{4.11}$$

where V_N2 is the total voltage noise after the lock-in amplifier, G_LIA is the gain of the lock-in amplifier, and V_{LIA} is the input voltage noise of the lock-in amplifier. The input

voltage noise had little effect on the propagated noise floor, V_N2 was therefore calculated to be 1.04×10^{-3} V/$\sqrt{\text{Hz}}$.

Finally, the analogue signal was passed through a band-pass filter (an *SRS SR560*). This did not apply any further amplification but it did inject a small amount of noise: V_{560} = 1.2×10^{-8} V/$\sqrt{\text{Hz}}$ at a 100 Hz sampling frequency. This noise was therefore summed in quadrature with the noise propagated from the lock-in amplifier, giving a total voltage noise level for the amplification circuit:

$$V_{NTot} = \sqrt{V_{N2}^2 + V_{560}^2} \quad \text{V}/\sqrt{\text{Hz}} \tag{4.12}$$

The input voltage noise of the *SRS SR560* also had little effect on the total propagated noise. The total noise, V_{NTot}, for the amplification circuit was found to be 1.04×10^{-3} V/$\sqrt{\text{Hz}}$. Clearly, the dominant noise sources were the Shot noise in the photodiodes, and the input current noise of the *SRS SR570* transimpedance amplifier. As will be seen in the final section of this chapter, this value aligned closely with the experimentally determined result. Any discrepancies between the theoretical and experimentally observed noise floors, however, could be explained by estimations made during the above calculation. It was assumed that the LED spot was of even power density, yet this was not the case since a diffuser had not been used. The active area of the photodiodes was also an estimation: it is likely that it was smaller than estimated because electrodes occupied part of the active area. Finally, none of the datasheet values for the *SRS SR570*, the *Femto LIA-MV-200*, and the *SRS SR560* were experimentally verified.

4.6 Shadow Sensor Drift Mitigation Methods

All of the long term variations that reduced the stability of this sensor were in some manner caused by temperature variations. Long-term stability was therefore achieved by reducing the impact of temperature variations on the system. This was done in three ways: by utilising the lock-in amplification technique, by using less temperature sensitive materials or components (passive control), or by using feedback mechanisms to maintain the temperature of the system (active control).

4.6.1 Lock-in Amplification

'Pink' or '1/f' noise is a source of noise that is found ubiquitously in electronics. It describes a rise in noise at low frequencies (proportional to the inverse of the sampling frequency –

hence the name) that is observed in the spectral density plots of all electrical components. The source is not down to one specific physical phenomenon, but due to the fact that at low frequencies components tend to drift, causing a variation in their output. To avoid 1/f noise, the best solution is to sample at high frequencies. Since the aim of this project is to observe slowly varying gravitational signals, 1/f noise would be a major problem. To avoid this, a lock-in amplifier was used. A lock-in amplifier works by taking a signal that is initially swamped in noise, this signal is then multiplied by a modulated reference signal of known frequency, phase and amplitude [111]. A frequency is selected that is beyond the 1/f noise in the frequency spectrum. The signal is then band-passed so that only signals with the reference frequency are measured. This allows the original signal to be measured with a significantly higher SNR than it originally had. The original signal is given by:

$$S = V_s \sin(\omega_s t + \phi_s) \tag{4.13}$$

where V_s is tkhe voltage amplitude of the signal, t is the time and ϕ_s is the phase of the signal. An equivalent expression also describes the reference signal:

$$R = V_R \sin(\omega_r t + \phi_r) \tag{4.14}$$

Multiplying these signals together gives the following expression:

$$V_{psd} = V_s V_r \sin(\omega_s t + \phi_s) \sin(\omega_r t + \phi_r) \tag{4.15}$$

or:

$$V_{psd} = \frac{1}{2} V_s V_r \cos[(\omega_s - \omega_r)t + \phi_s - \phi_r] - \cos[(\omega_s + \omega_r)t + \phi_s + \phi_r] \tag{4.16}$$

The band-pass filter then removes any signal frequencies that are not equal to the reference frequency. So for this situation where $\omega_s = \omega_r$, V_{psd} becomes:

$$V_{psd} = \frac{1}{2} V_s V_r \cos(\phi_s - \phi_r) \tag{4.17}$$

As discussed above, a *Femto LIA-MV-200*) analogue lock-in amplifier was used to carry out this process.

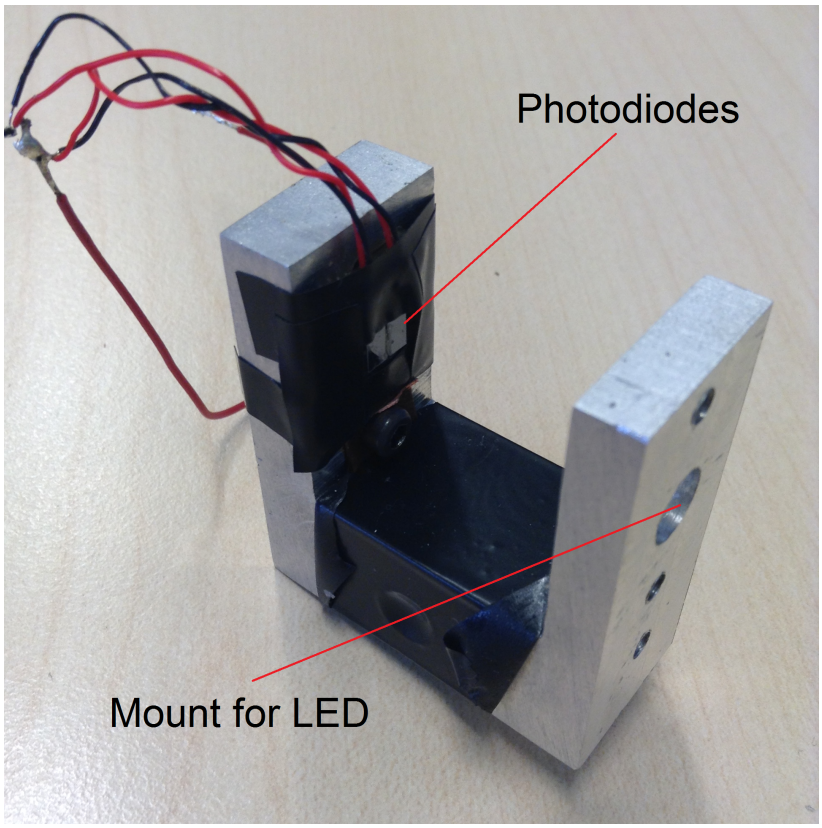

Fig. 4.7 A photograph of the first mount that was constructed for the optical shadow sensor components, it is made from aluminium. This structure was ultimately replaced by one made from fused silica because it has a better thermal stability than aluminium.

4.6.2 Passive Control

The first means of passive control was the selection of the material to build the structure upon which the electrical components would be mounted. A prototype 'C' structure was made from aluminium (see figure 4.7). This was used to demonstrate the high dynamic range of the sensor, but it was never intended for use with a MEMS device. This is because aluminium has a high thermal expansion coefficient, α, of 2.4×10^{-5} K^{-1} at room temperature. If it were used for measuring the displacement of a MEMS device where nm stability was imperative, the temperature would need to be held impractically stable to avoid thermal fluctuations of the aluminium being confused with motion of the proof mass. When designing the structure to support a MEMS device, a material with a lower thermal expansion coefficient was selected – fused silica ($\alpha = 4.1 \times 10^{-7}$ K^{-1}) [112]. The 'C' structure made from fused silica can be observed in figure 4.3.

Another means of ensuring that the system required a lower level of active control was to run the sensor in vacuum. The entire shadow sensor was placed in a vacuum tank and pumped down to a pressure of $\leq 10^{-5}$ mTorr. This took the chamber into the molecular flow regime - where the size of the vacuum tank is smaller than the mean free path of the gas molecules [113]. This meant that less radiative heat transfer could occur between the outside of the tank and the shadow sensor inside compared to keeping the sensor at atmospheric pressure (the viscous flow regime). The isolation was not perfect, however, so some temperature control still had to be implemented. This control will be discussed in subsection 4.6.3.

It was also possible that the LED could vary with temperature [114, 115]. With varying temperature the intensity of emission could change, the peak wavelength could change, or the width of the emission peak could change. It was therefore decided to monitor the LED intensity directly. A 1 cm^2 beam splitter was hydroxy-catalysis bonded [116] to the shadow sensor at the exit pupil of the LED hole (see figure 4.3). This sent half of the LED light to the split photodiode, and the other half to a reference photodiode that could be used to monitor the intensity of the LED. It was found that intensity variations did not occur at a level that would affect the readings of the system once a MEMS device was in place.

The responsivity of the photodiodes could also have caused instabilities in the shadow sensor output. Silicon photodiodes have a responsivity that varies with the wavelength of light incident upon them. This responsivity curve rises to a peak at around 950 nm and then falls off. LEDs were used in this system with an emission wavelength of 635 nm (a wavelength where the responsivity of a silicon photodiode is sloped with a gradient of around 50 μA/W/nm). This meant that any changes in the LED wavelength would change the output of the photodiodes. One way of countering this would be to use an LED that emitted at 950 nm – the turning point of the photodiode responsivity – where the responsivity gradient goes through zero. This alteration has not been carried out at the time of writing.

4.6.3 Active Control

As much passive isolation was included as possible, but temperatures within the system still needed to be controlled. Several control loops were implemented to keep the sensor at a constant temperature. Once a MEMS device was in place, the primary control loop would maintain the temperature of the MEMS device directly. As well as this, another loop controlled the temperature of a copper thermal shield that encased the entire shadow sensor (Fig. 4.8). Another controlled the temperature of the LED, and a final one the temperature of the plate upon which the shadow sensor sat. The control loops used to maintain the

temperature of the system were proportional integral derivative (PID) control mechanisms, written in *Labview*. Temperatures were monitored using a four-terminal measurement of small platinum resistors, via two *Keithley 2000* digital mulitmeters. A four-terminal measurement eradicates contact resistance by driving the thermometer with a current and measuring the voltage across it. This removes the temperature sensitivity of external wires. Low temperature coefficient *Manganin* wires were used for these connections to minimise parasitic thermal conduction. Wire wound resistors were used as the heating mechanism to feedback into the system. The output signal to the heaters was sent via a *National Instruments (USB 6211)* card, and the heaters were powered with non-inverting amplifiers with a capability to power up to 100 mA. All circuitry and instrumentation used to amplify and measure the output signal, and to measure and control the system temperature, were selected for their high thermal stability.

The three legs upon which the plate sits in figure 4.8 were also designed as a feedback mechanism. These were all made from piezo actuators so their height could be altered by applying a voltage. If tilt (caused by the thermal variations of the floor) had caused a change in the output signal of the gravimeter then these legs could be used as part of another control loop to maintain a level platform. As will be discussed in the next chapter, this was not required.

4.7 Shadow Sensor Experimental Performance

To find out the what displacement sensitivity the sensor was achieving, a calibration was carried out. The silicon 'flag' – that had previously be affixed over the photodiodes – was detached and placed on a micrometer stage. The micrometer was then used to position the flag over the split photodiode. The flag was scanned over the photodiodes in increments of 200 μm. Several steps were made on either side of the zero point of the sensor. The output voltage was recorded as these steps were made. After scanning one way, the direction was reversed and the flag was scanned back to the starting point. This was done to ensure that there was no hysteresis effects from the micrometer stage. The data from each of the steps in both directions was averaged and plotted against displacement. This graph can be observed in figure 4.9. The uncertainty for each measurement of displacement was ± 5 μm (half of the smallest division on the micrometer). Since two measurements at each location, the error bars in figure 4.9 are ± 7.1 μm (the quadrature sum of the two displacement uncertainties). Error bars have not been plotted in the y-axis because the uncertainty in the voltage measurement was at the mV scale. For the duration of this calibration, the amplification of the sensor was reduced by a factor of 100. This was in order to reduce the error caused by the positioning of

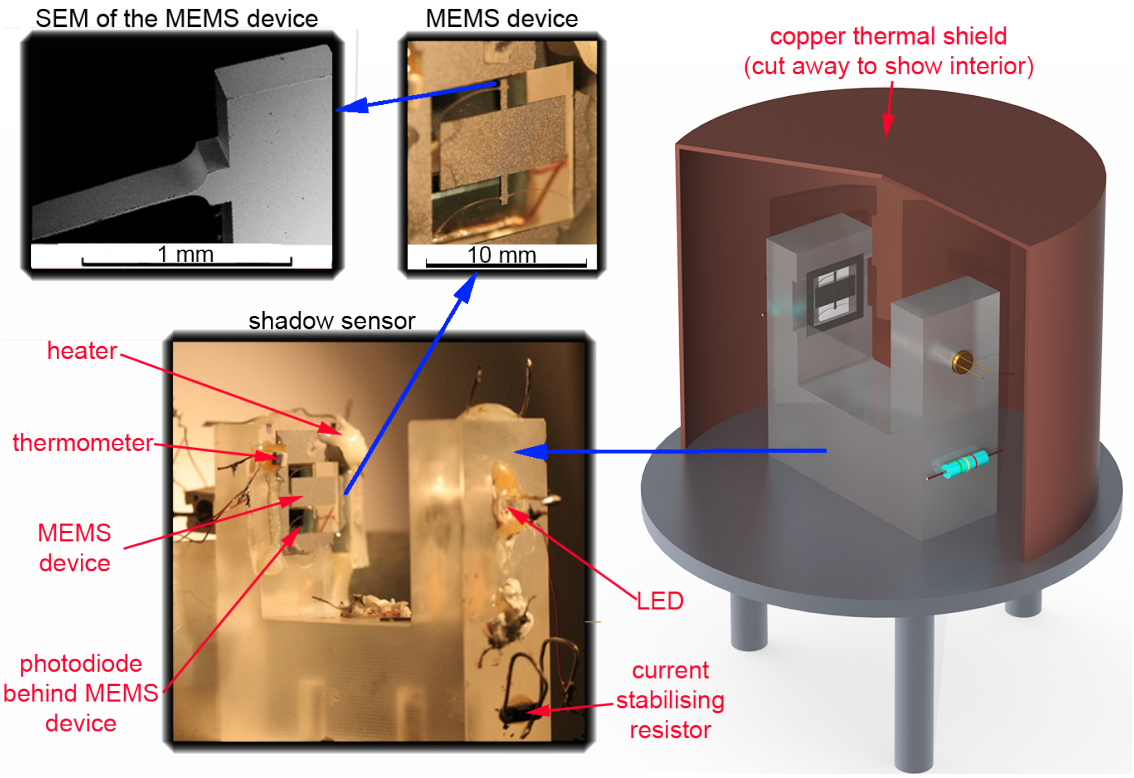

Fig. 4.8 A schematic of how the MEMS device would later be incorporated within the shadow sensor and how both or these were thermally controlled. Both sit on an aluminium plate and are encased in a copper thermal shield. Both the MEMS device and the shield are thermally controlled, as well as the LED and the plate. At the top left is a photograph and scanning electron microscope (SEM) image of the MEMS device. At the bottom left is a photograph of the MEMS device mounted on the optical shadow sensor with epoxy glue holding the heater and thermometer in place. The inside of shield was painted black to reduce the effect of stray reflections from the reflective metal surface. These reflections has the potential to vary with temperature.

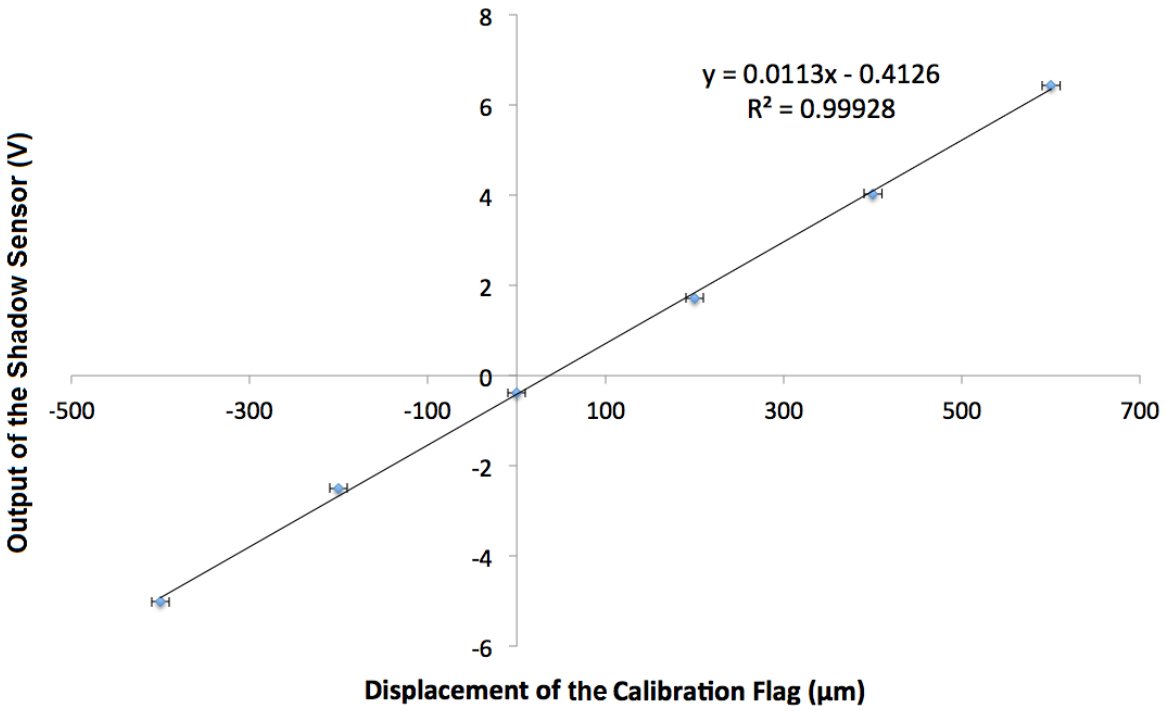

Fig. 4.9 The motion sensor curve of the shadow sensor. The measurements were made by moving a flag over the split photodiodes using a micrometer stage. The measurement was carried out with the circuit amplification reduced by a factor of 100 (to reduce the impact of the displacement error). This curve demonstrated that the shadow sensor had a sensitivity of 11.3 kV/m. Therefore, once the amplification was re-set to its original level, this sensitivity became 1.13 MV/m.

the flag by the micrometer. Had the sensor been at full amplification, the x-axis error bars would have been comparatively much larger.

Accounting for the reduction in sensitivity while the calibration was carried out, this motion sensor curve indicates that the sensor had a sensitivity of 1.13 MV/m. It also shows that this sensitivity was maintained over a linear range of at least 1 mm (although at the higher sensitivity the readout circuitry would saturate if 1 mm displacements occurred).

Once the calibration had been carried out, the noise performance could be assessed in terms of displacement. With the stationary flag re-affixed over the centre of the photodiodes, a time series was taken with a sampling frequency of 0.03 Hz. At this sampling frequency, an RMS noise level of measured of 0.8 mV. This value only marginally differs from the theoretical noise floor (1.04 mV). The discrepancy can easily be explained by the sources of uncertainty in the theoretical calculation (non-even illumination, incorrect estimation of active area etc.). Using the calibration of 1.13 MV/m, the experimental noise level was converted into units of displacement. A noise floor of 0.7 nm was the result. For a MEMS

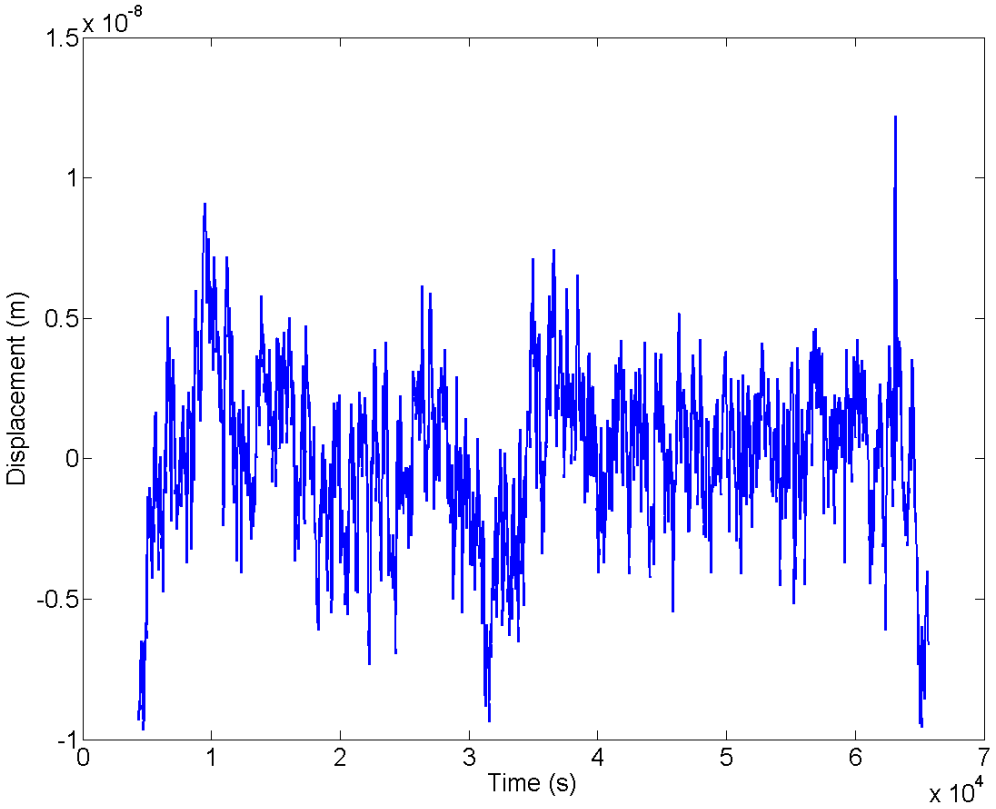

Fig. 4.10 A time series plot of the shadow sensor output. This data was recorded over a 12 hour period with a time constant of 44 seconds. The y-axis has been converted from units of voltage into units of displacement using the calibration of 1.13MV/m.

device with a resonant frequency of 2.3 Hz, this would create an acceleration noise floor of $\sim$10 μGal.

To assess the the drift characteristics of the sensor, the output of the sensor was recorded for a period of 12 hours. This data can be observed in figure 4.10. The data appeared fairly stable over this time-scale. To test this observation an amplitude spectral density was plotted (see figure 4.11). It can be observed from figure 4.11 that there is evidence of 1/f noise in this data. This plot shows that the sensor has excellent noise performance at low frequencies, operating down to a frequency three orders of magnitude below the sensor of Carbone et al. [97](see figure 4.2).

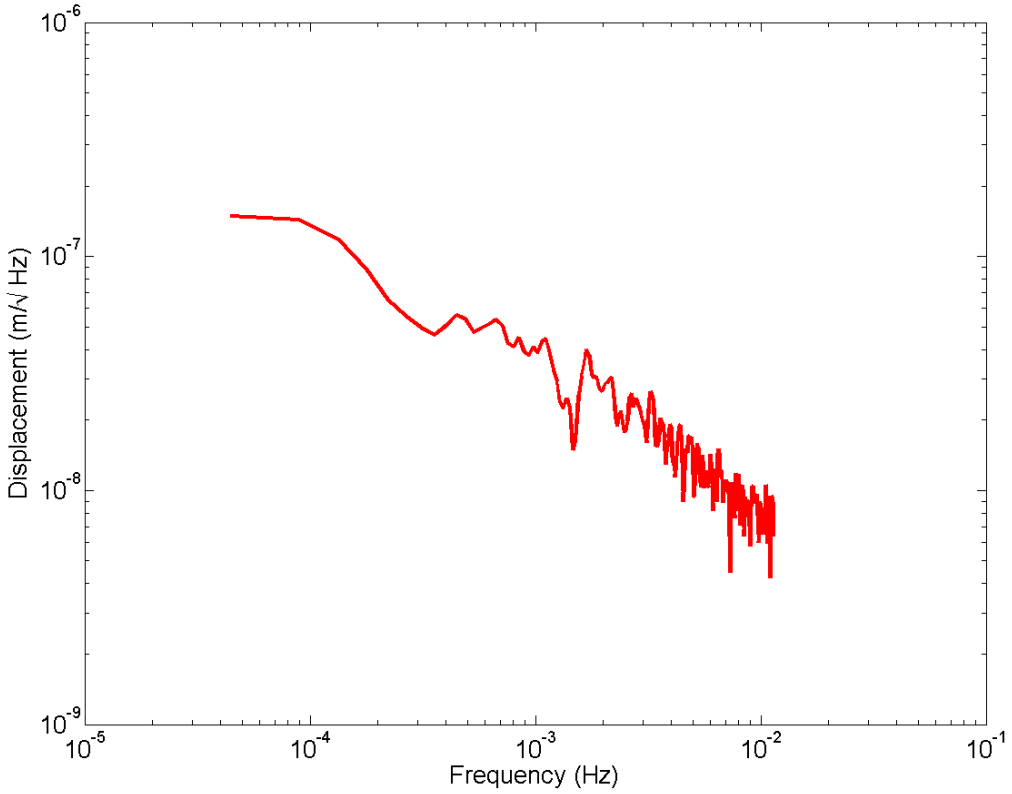

Fig. 4.11 An amplitude spectral density plot of the shadow sensor output. This data was recorded over a 12 hour period with a time constant of 44 seconds. The y-axis has been converted from units of voltage into units of displacement using the calibration of 1.13MV/m.

4.8 Summary: Shadow Sensor Performance

To summarise, the shadow sensor has a a dynamic range of at least 1 mm and a readout noise floor of 0.8 mV at the sampling frequency of 0.03 Hz. Given the calibration, this means the sensor has a displacement sensitivity of under 1 nm. If a 2 Hz device were placed in this sensor then it was expected that the acceleration noise floor would be $\sim$10 μGal. The next chapter will include a discussion of what happened when a MEMS device was placed in the shadow sensor.

Chapter 5

Measurement of the Earth Tides

In December 2014, an effort was made to produce a four-flexure MEMS device so that the apparatus could be run over the Christmas holidays. At this point it was expected that the best design for the MEMS device would be a four-flexure system. Given problems with the MEMS release mechanism that were being experienced at this time, the only device that was produced in time for the holidays was one with a broken upper flexure. Since this device was the only one available, it was placed in the optical sensor for investigation. Knowing the resonant frequency, and the sensitivity of the shadow sensor, it was possible to calculate the maximum achievable sensitivity of the device using equation 4.1. It was thus estimated that the sensitivity of the device to acceleration would lie around 50 μGal/$\sqrt{\text{Hz}}$. If the device was able to measure accelerations down to this level, whilst maintaining stability over long time scales of days to weeks, a measurement of the Earth tides would be possible (see chapter 1). At this stage it was not known how the device would respond to seismic noise, or changes in temperature. Ultimately it turned out that the Earth tides were measured over the Christmas 2014 holidays, and onwards throughout the start of 2015. This measurement was not straightforward, however, and this chapter covers the details of how it was achieved.

5.1 Mounting the MEMS Device

The first stage of the experiment was to mount the MEMS device onto the shadow sensor. Soft wax was used to do this, so that the sample could later be removed or moved around. Crucially, the proof mass needed to cast a shadow that covered half of one photodiode and have of the other. As discussed in chapter 4, this would mean that the output signal would be zero (due to the differential configuration of the photodiodes) until the device was moved by a changing acceleration. For operation the device needed to be mounted vertically within the

shadow sensor, so that the sensitive axis was also vertical. Mounting the sample vertically with the wax would have led to the risk of breakage while the wax was fluid, so the device was stuck down whilst horizontal then rotated to a vertical position. The process of zeroing was then carried out iteratively by heating the wax sufficiently to enable tiny motions of the device, without making the wax fully fluid. During this time the output signal was observed on the computer monitor until the signal got as close to zero as possible.

5.2 Potential Causes of Noise

With the introduction of the MEMS device to the system, it was inevitable that new sources of noise would arise. These could either affect the stability of the device or the noise level. Some potential sources of noise/instability are discussed below. Of these sources, some turned out to be important to the sensitivity of the device, and others less so.

5.2.1 Thermal Noise

The fundamental noise floor for the performance – assuming no seismic noise or readout noise – will be limited by the thermal fluctuations within the material itself due to the non-zero temperature of the body. The behaviour of this noise is described by the Fluctuation-Dissipation Theorem [117]. Fluctuation-Dissipation Theorem tells us that the displacement noise of a harmonic oscillator (in the form of a power spectral density) is given by equation 5.1 [118] (assuming that losses are due to structural damping[1]):

$$G_x(f) = \frac{4k_BT}{m\omega} \frac{\omega_0^2 \phi(\omega)}{\left[(\omega^2 - \omega_0^2)^2 + \omega_0^4 \phi^2(\omega)\right]} \, m^2/\text{Hz} \tag{5.1}$$

where k_B is the Boltzmann constant, T is the temperature of the body, m is the mass of the oscillator, ω is the angular frequency of oscillation, ω_0 is the angular resonant frequency and $\phi(\omega)$ characterises the frequency dependence of the dissipation of energy (known as the 'loss angle'). The acceleration of the oscillator (assuming a Hooke's Law behaviour) is given by:

$$\ddot{z} = \frac{k}{m} z \tag{5.2}$$

[1]For structural damping is it assumed that ϕ is constant. This is a good model for losses in an oscillating system for which the inherent quality factor of the material, Q, dominates the damping of the system. The alternative model is viscous damping, for which it is assumed that ϕ is frequency dependent (proportional to ω). This is a good model for an oscillating system damped mainly by air or magnetic resistance.

To find the displacement noise associated with thermal fluctuations in the low frequency regime, we can therefore equate equations 5.1 and 5.2 and rearrange for z:

$$\ddot{z} = \frac{zk}{m} = \frac{k}{m}\sqrt{G_x(f)} = \frac{k}{m}\sqrt{\frac{4k_BT}{m\omega}\frac{\omega_0^2\phi(\omega)}{\left[(\omega^2-\omega_0^2)^2+\omega_0^4\phi^2(\omega)\right]}} \tag{5.3}$$

Since our device is allowed to resonate at its natural frequency, the largest amplitude oscillations occur at this frequency. Equation 5.3 can therefore be simplified by considering the situation where $\omega_0 = \omega$. The loss angle, $\phi(\omega)$, is given by $\omega/\omega_0 Q$ (where Q is the quality factor of the oscillator), which can also be simplified to: $\phi(\omega) = 1/Q$. Equation 5.3 therefore becomes:

$$\ddot{z} = \frac{k}{m}\sqrt{\frac{4k_BTQ}{m\omega_0^3}} \tag{5.4}$$

For an oscillating system, the quality factor, Q, is given by:

$$Q = \pi f_0 \tau \tag{5.5}$$

where f_0 is the resonant frequency, and τ is the relaxation time of the ring down [119]. An experiment was conducted to measure the relaxation time of the device. The device was placed under vacuum, and the resonance excited by tapping the side of the vacuum tank. The relaxation time was then measured as the time taken for the oscillation amplitude to decrease by a factor of $1/e$ (where e is Euler's number). Once the relaxation time was measured, it was used to calculate Q using equation 5.5. Q is also a function of resonant frequency, and the resonant frequency of the device changed depending on its angle away from horizontal (as discussed in chapter 2). Q was therefore calculated for the device from horizontal to vertical, giving a range of values (as seen in figure 5.1. Graph 5.1 shows the trend that one would anticipate from equation 5.5: Q is directly proportional to resonant frequency. This behaviour is due to the fact that in geometrical anti-springs – as the resonant frequency is lowered – the restoring force becomes comparable to internal friction [120].

The quality factor of the device when vertical was calculated to be $\sim$80 (given a resonant frequency of 2.3 Hz, and a relaxation time of $\sim$11 s). Taking this value for Q, the displacement noise that could be expected from thermal fluctuations within the silicon would be of order $\sim 2.6\times10^{-11}$ m (using equation 5.4). This equates to a theoretical thermal noise floor of 5.1 μGal/$\sqrt{Hz}$. It is clear that this will not be the noise limit of the sensor, given the current optical readout noise of $\sim 10\mu$Gal/$\sqrt{\text{Hz}}$.

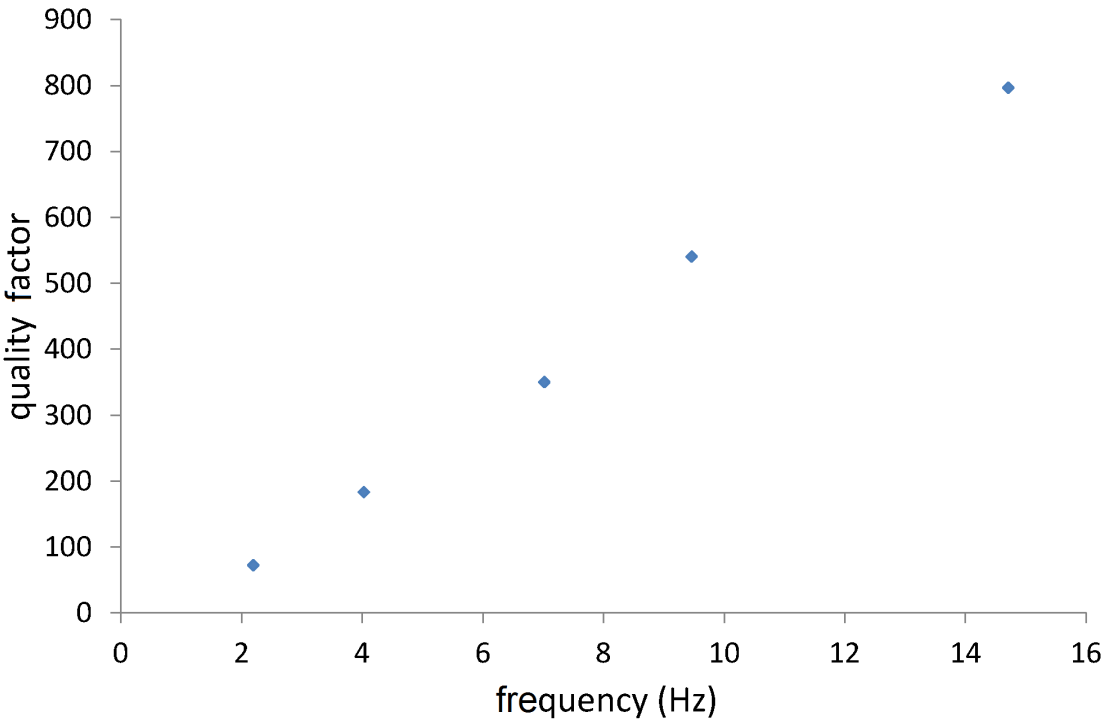

Fig. 5.1 This graph demonstrates a trend of decreasing quality factor, Q, with decreasing frequency for the MEMS device under vacuum. Q was calculated using equation 5.5. At low frequencies the internal friction of the material becomes the dominant loss mechanism [120].

5.2.2 Sensitivity to Temperature Instability

Observation of the Earth tides required stable operation over several days. The main contributor to parasitic motion of the proof mass is the varying temperature of the system. Unlike the noise caused by seismic motion, temperature fluctuations can not be assumed to be random, and they therefore need to be limited as much as possible since a varying temperature could easily occur with a similar frequency to the tide signal. The effect of temperature fluctuations can be limited either passively or actively. As discussed in the previous chapter, fused silica was used to construct the shadow sensor 'C' because of its low room temperature thermal expansion coefficient (4.1×10^{-7} K^{-1}) [112]. Silicon has a significantly larger thermal expansion coefficient (2.6×10^{-6} K^{-1}) [121], but silicon was used to make the MEMS because it is a standard fabrication material in the semiconductor industry, it has high mechanical strength, and its thermal properties are well characterised.

To estimate how temperatures would affect the MEMS device, a simplified analytical solution to the system was investigated. Instead of a curved cantilever, a straight beam was considered of length, L, thickness, t, and width, w. The beam was considered to be rigidly held at one end and free to move at the other, and made of a material with a Young's Modulus, E. If a force, F was then applied to the free end of the beam then Euler-Bernoulli Beam Theory [122] says that the bending moment, M, of the beam is given by:

$$M = EI\frac{d^2y}{dx^2} \tag{5.6}$$

where I is the moment of inertia of the system and d^2y/dx^2 is the slope of the beam. Assuming that the beam bends from one point, then the bending moment magnitude, M, can also be written as:

$$M = F(L-x) \tag{5.7}$$

Equating equations 5.6 and 5.7 and rearranging for d^2y/dx^2 gives:

$$\frac{d^2y}{dx^2} = \frac{F}{EI}(L-x) \tag{5.8}$$

where both $dy/dx = 0$ and $y = 0$ when $x = 0$. Integrating equation 5.8 with respect to x yields:

$$\frac{dy}{dx} = \frac{F}{EI}\left(Lx - \frac{x^2}{2}\right) \tag{5.9}$$

Integrating again gives:

$$y = \frac{F}{EI}\left(\frac{Lx^2}{2} - \frac{x^3}{6}\right) = \frac{F}{EI}\left(\frac{L^3}{2} - \frac{L^3}{6}\right) \tag{5.10}$$

By substituting x for L, the vertical deflection of the end of the beam is given by:

$$y = \frac{F}{EI}\left(\frac{L^3}{3}\right) \tag{5.11}$$

By substituting Hooke's Law ($F = ky$) – and rearranging for k – we can show:

$$k = \frac{3EI}{L^3} \tag{5.12}$$

The moment of inertia, I, for a beam with a rectangular profile is:

$$I = \frac{wt^3}{12} \tag{5.13}$$

The expression for the spring constant of a rectangular cantilever, k, therefore simplifies to:

$$k = \frac{Ewt^3}{4L^3} \tag{5.14}$$

The variation of the spring constant can be put into the form of a partial differential equation:

$$\left(\frac{\delta k}{k}\right)^2 = \left(\frac{\delta E}{E}\right)^2 + \left(\frac{\delta w}{w}\right)^2 + \left(3\frac{\delta t}{t}\right)^2 + \left(3\frac{\delta L}{L}\right)^2 \tag{5.15}$$

This can be rearranged for $\delta k/k$:

$$\frac{\delta k}{k} = \sqrt{\left(\frac{\delta E}{E}\right)^2 + \left(\frac{\delta w}{w}\right)^2 + \left(3\frac{\delta t}{t}\right)^2 + \left(3\frac{\delta L}{L}\right)^2} \tag{5.16}$$

The reason for putting equation 5.16 in this form was to asses how a change in temperature would affect the spring constant of the cantilever. Specifically, whether the spring constant would be affected more by the change in dimensions of the cantilever, or by the change in the Young's Modulus. Since $\delta L/L = \delta w/w = \delta t/t = \alpha\delta T$ (where α is the thermal diffusivity of the material), equation 5.16 can be written as:

$$\frac{\delta k}{k} = \sqrt{\left(\frac{\delta E}{E}\right)^2 + (19\alpha\delta T)^2} \tag{5.17}$$

By looking at the result of equation 5.17 if a 1 mK δT is applied, it can be observed that the Young's Modulus term is the dominant mechanism by which temperature fluctuations change the spring constant [123, 124]. Based on these calculations, it can be assumed that a change in temperature of 1 mK will result in a variation of k, $1/k\ dk/dT$, of 7.88×10^{-6} K^{-1}. This change in k would in turn give an uncertainty in the gravity reading of $\sim$25 μGal. Temperature variation of the MEMS device is therefore a major source of noise and instability in the system. In section 5.3 it will be demonstrated that the observed dependency of the output of the MEMS device to temperature was 15 μGal/mK.

Despite controlling the temperature of the MEMS to within 1 mK, the device did not always stay stable. Ultimately it was realised that the room temperature and the output of the gravimeter were correlated. It was assumed that this was due to a temperature sensitive electronic component outside of the vacuum tank since the system was so well temperature controlled inside the tank. Care had been taken to buy or build electronic components/equipment that had very good thermal stability, but it was reasoned that something within the room was temperature sensitive. There were a number of potential sources of this sensitivity, as figure 5.2 illustrates.

To determine which piece of equipment was temperature sensitive each piece of instrumentation in turn was heated with a heat-gun and the output monitored. This method, however, was not very successful since it was very hard to isolate which bit of equipment was heating up given the poor directionality of the heat gun. The heat gun also had the effect of quickly heating up the entire room, triggering the additional temperature coupling. Instead of the heat gun, a box was constructed using insulating foam. Each of the pieces of electronic equipment were placed in the box one by one. Generally these devices produced a reasonable amount of heat themselves, so by containing them within the box they naturally heated up but without injecting heat into the room as a whole.

No temperature dependence was found until the temperature of the Femto lock-in amplifier was investigated. A heating cycle was carried out by placing the Femto in the foam box for 10000 s, giving a temperature rise, and then removing it from the box to let it cool. All the while the voltage output was monitored. Both the gravimeter voltage output, and the Femto temperature are plotted in figure 5.3. The red series is the Femto temperature and the blue series is the voltage output. This test suggested that the voltage output of the MEMS gravimeter could be dependent on the Femto temperature since both sets of data appeared to change sign at the same time. To further investigate this potential correlation, the time differentials of both series were plotted. This graph is displayed in figure 5.4. The blue series is the time differential of the MEMS gravimeter voltage output, and the red series is the time

Fig. 5.2 There were a great number of electronic instruments that could have been the cause of the temperature sensitivity.

differential of the Femto temperature. Each of these time differentials was calculated by dividing the change in signal (either voltage, ΔV, or temperature ΔT,), by the corresponding change in time, Δt:

$$\text{Time differential of voltage} = \frac{\Delta V}{\Delta t} \tag{5.18}$$

$$\text{Time differential of temperature} = \frac{\Delta T}{\Delta t} \tag{5.19}$$

Since there was a level of noise in both time series, the time differential of each was calculated over 50 data points (corresponding to 6600 s). This running average allowed the global variations in gradient to be observed, rather than those resulting from short term noise. It can be observed from figure 5.4 that the rate of change of the two series are correlated. This gives further evidence that there is a causality between the change in Femto temperature and the output of the gravimeter. To estimate the rough magnitude of this dependency, figure 5.3 was consulted. A temperature change of 5°C resulted in a voltage variation of 5 mV. Given the calibration of the sensor at the time, this equated to a variation in the gravity measurement of around 250 μGal/°C. Since the output variation for a temperature change of 1°C was of the same order as the magnitude of the Earth tides, it was important to take steps to mitigate against this effect. The Femto lock-in was therefore left in the box to passively isolate it from room temperature variations, and it was also actively controlled with another PID loop. This was carried out by heating the casing of the Femto using a power resistor – an example of unipolar control [125].

5.2.3 Tilt

Before running the experiment, it was thought likely that tilt could cause parasitic motion of the MEMS device. Tilt could occur as the floor distorted with changing temperature. To mitigate against this risk, a stage was fabricated upon which the MEMS shadow sensor could sit. This stage consisted of an aluminium plate mounted on three piezo legs. The plate – which can be seen in figure 5.5 – was designed to be held firmly by the legs, without being over-constrained. For this reason the the points at which the legs made contact with the plate were machined into radial grooves. If it were necessary, this stage could have been run via another PID control loop, to keep the MEMS device level.

After the MEMS device was mounted and data was taken, the level of the system was measured using an electrolytic bubble level. No correlation was observed between the output

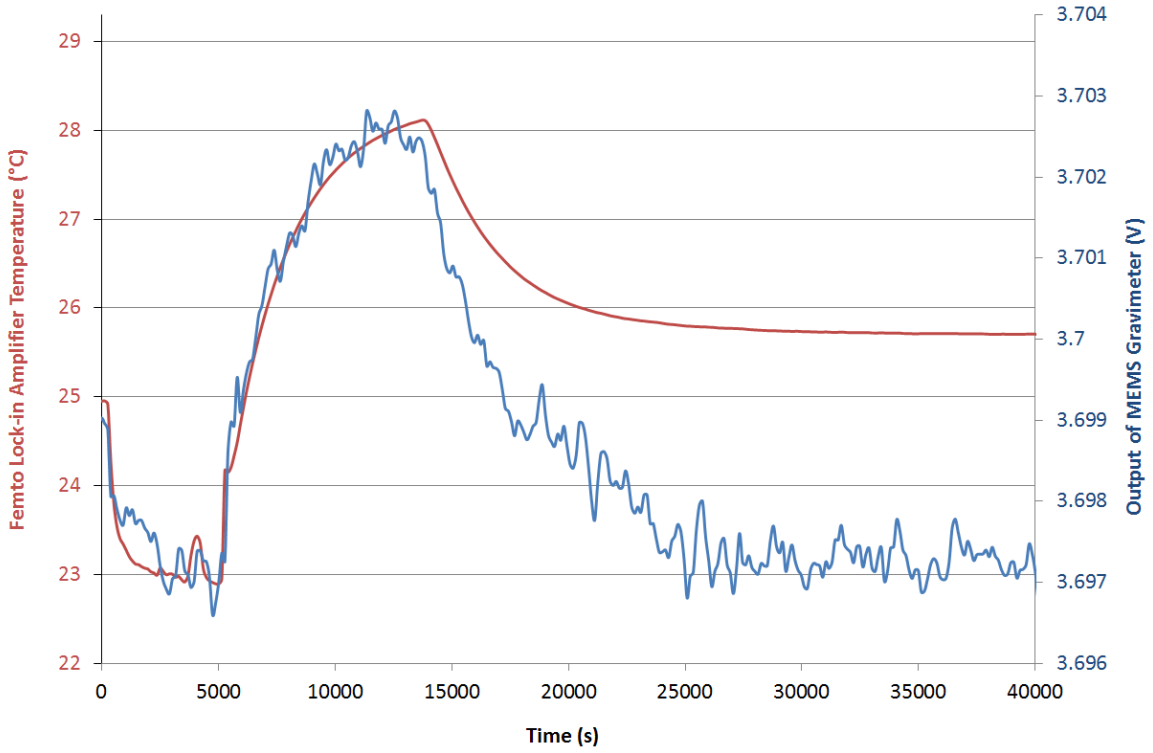

Fig. 5.3 A dual axis graph containing both the temperature of the Femto lock-in amplifier (red series) and the voltage output of the MEMS gravimeter (blue series). The data was acquired by placing the Femto in a foam box – allowing it to heat up – and then removing it from the box to let it cool down. The point at which the Femto was placed in the box can be seen at the 5000 s mark on the graph's horizontal axis, and the point at which it was removed can be observed at about 15000 s. The gravimeter voltage output was recorded concurrently to this heating cycle. It can be observed that the voltage output appears to be rise at the same time as the Femto started heating, and that it appears to drop when the Femto started cooling. This suggested that the voltage output could be dependent on the Femto temperature.

Fig. 5.4 A graph of the time differentials of the two series displayed in figure 5.3. The red series is the rate of change of the Femto temperature, $\Delta T/\Delta t$, and the blue series is the rate of change of the MEMS gravimeter voltage output, $\Delta V/\Delta t$. It can be observed that these two series are correlated – suggesting that output of the gravimeter is causally related to the temperature of the lock-in amplifier.

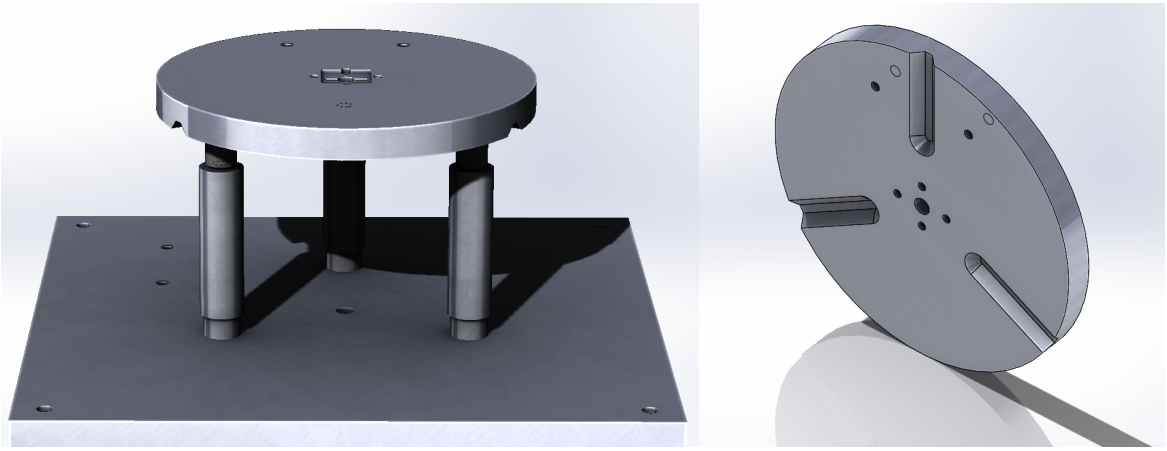

Fig. 5.5 Figure 5.5 is a computer generated image of the plate of the piezo stage which was fabricated to control the level of the MEMS in the situation that the tilt of the floor caused parasitic motion of the MEMS proof mass. The full stage can be seen in figure 4.8. Ultimately this stage was not needed because the tilt did not effect the device at a level that was larger than other sources of instability.

of the gravimeter, and the tilt that was measured by the bubble level. For this reason, it was concluded that there was no need to run the piezo stage to stabilise the the stage.

Although tilt did not have an effect on the tide measurement, experiments were conducted to investigate at what point tilt would become an issue. Figure 5.7 presents two plots of an experiment used to asses the effect of tilt on our device. Inside the vacuum tank, the MEMS device was mounted vertically and aligned with the tilt sensor. The y-axis of the tilt sensor was aligned with the plane of the MEMS device, with the x-axis perpendicular to this (see Fig. 5.6). Figure 5.7b demonstrates the correlation between the output of the sensor in μGal and the tilt of the x-axis in arc seconds. Figure 5.7a demonstrates the corresponding change in the output of the device for the y-axis tilt.

Initial visual inspection lead to the conclusion that the correlation between the gravimeter output and the y-axis tilt, was greater than that between the gravimeter output and the x-axis tilt. There were, however, common features in the data that were shared between both the y-axis and x-axis tilt (e.g. the minimum at 70 seconds, the minimum at 320 seconds, and the minimum at 680 seconds). These common features occurred because it was a challenge to induce a tilt solely in one axis at a time. Since the vacuum tank was attached to the ground via a three-legged mount, applying a force designed to induce a tilt in one of the axes would invariably have a measurable effect on the other.

To assess the level of tilt sensitivity for each axis, something more rigorous than a visual inspection was required. A regression function was used in *MATLAB*[2] to ascertain the level of dependency that the gravimeter output had on each of the axes. Regression analysis is a method of investigating connections between independent and dependent variables of data sets [126]. It is a 'least squares' fit [127] for multiple parameters. Using this function it was possible to calculate a level of dependency of the gravimeter gravimeter output to tilts in the two axes in units of μGal/arcsec: a y-axis tilt sensitivity of 21.2 μGal/arcsec, and an x-axis tilt sensitivity of only 0.6 μGal/arcsec.

The y-axis variation was larger because the device has a mode of oscillation in which the proof mass tilts in-plane, pivoting about the upper cantilever flexure. The x-axis tilt sensitivity was low because in the vertical configuration, the spring was close to the minimum at which it regains a Hooke's Law response (see figure 5.8, for which the x-axis tilt variation was plotted against the resonant frequency [the acceleration sensitivity of the device is proportional to the square of the resonant frequency]). Ultimately the spring could be tuned to operate with even less tilt dependency in this axis if it were positioned to operate at one of its minima. Alternatively the flexures could be made marginally thicker to shift the minimum in resonant

[2]This data analysis technique will be discussed in greater detail in the following section.

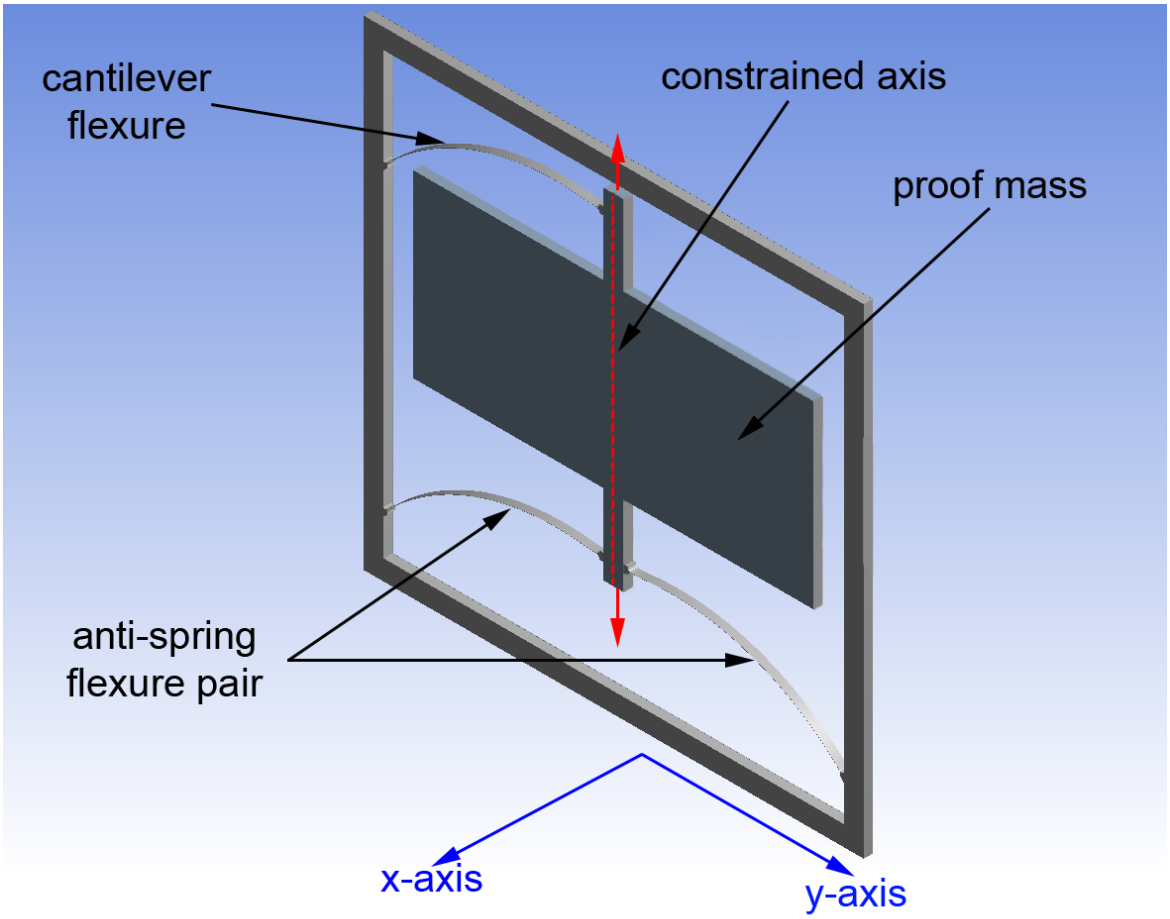

Fig. 5.6 A figure demonstrating the design of the MEMS gravimeter (as also shown in the right hand image of figure 2.4). The central proof mass is suspended from three flexures: an anti-spring pair at the bottom and a curved cantilever at the top. The anti-spring pair constrain the motion of the proof mass along the red axis. The frequency is lowered by this constraint until the cantilever pushes the motion off-axis, stabilising the MEMS device at a lower frequency. The x-axis and y-axis annotations in this figure correspond to the axes referred to in figure 5.7.

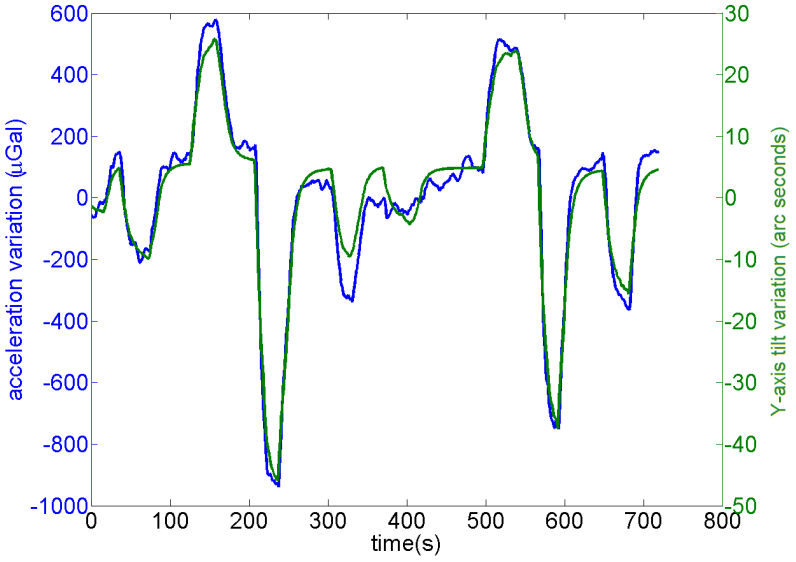

(a)

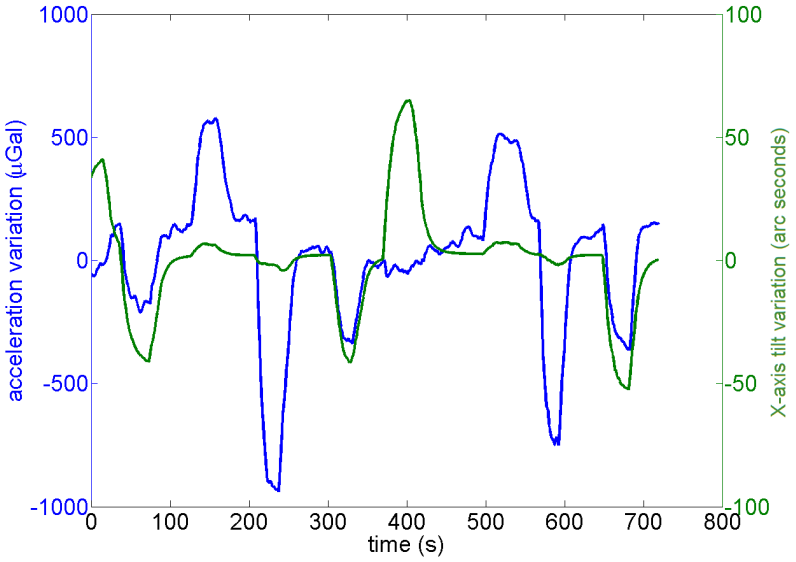

(b)

Fig. 5.7 Figure 5.7a demonstrates the variation in output of the MEMS device with the y-axis (in-plane) tilt of the sensor. Figure 5.7b shows the same for the x-axis (out of plane) tilt. There is a y-axis tilt sensitivity of 21.2 μGal/arc second, but in the x-axis the tilt sensitivity is only 0.6 μGal/arc second.

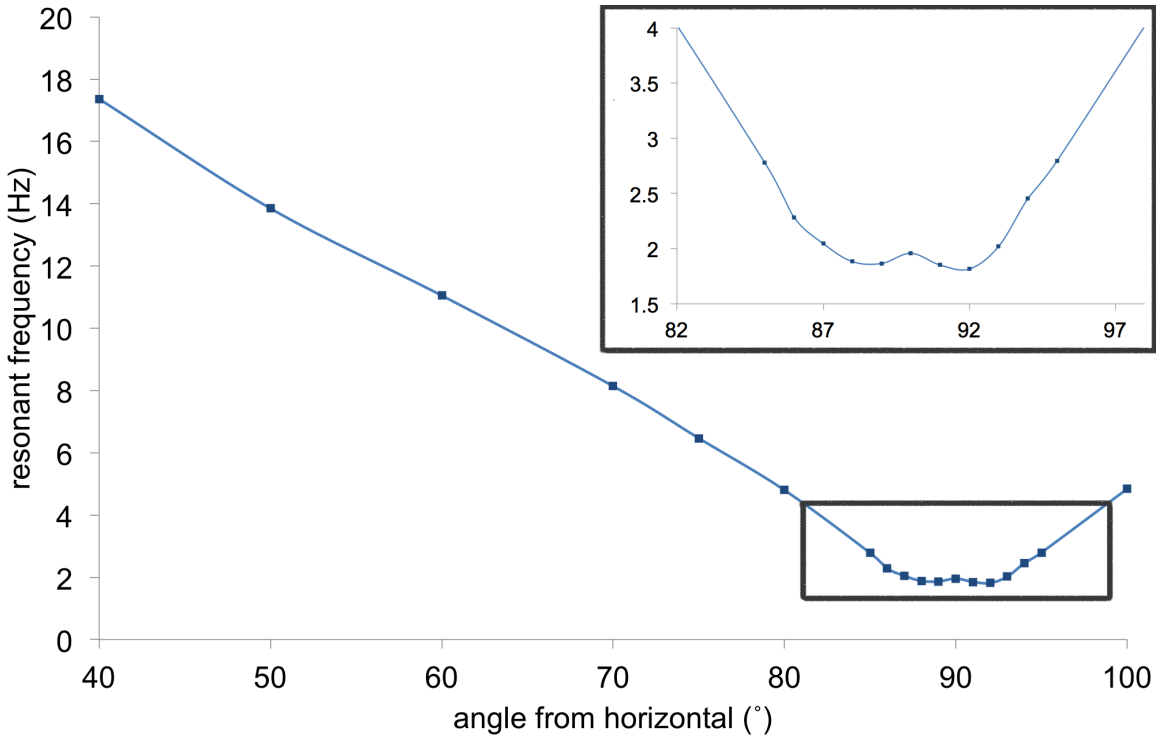

Fig. 5.8 This figure is an adaptation of figure 2.9, using the same data. The resonant frequency decreases as the MEMS device gets closer to vertical due to the geometrical anti-spring effect. At 88° and and 92° there are minima in the plot. At this point the frequency is constant with tilt and the system displays a Hooke's law behaviour. The resonant frequency of a symmetric anti-spring would reach an instability here. This figure also demonstrates that whilst the instrument is operated at 90° the resonant frequency is 2.3 Hz, it can be lowered to 1.8 - 1.9 Hz by tilting to operate at one of the minima.

frequency to 90°, this was not carried out because the device did not show sufficient tilt sensitivity to cause concern.

When vertical, the device would need to be levelled with an accuracy limited by the y-axis sensitivity (i.e. less than 2 arc seconds to maintain the current sensitivity) to make repeatable measurements in different locations. This accuracy of levelling is achievable with a simple surveyor's bubble level.

5.2.4 Buoyancy

When the device was placed into the vacuum tank and pumped down, there was always a large initial displacement of the MEMS device of around 20 μm. It was conjectured that this could be due to the relative change in buoyancy force incident on the proof mass between the system in air and the system under vacuum. A calculation was therefore carried out to

investigate whether this buoyancy effect could indeed be the cause of the observed initial displacement. From Newton's Second Law, the buoyancy force is given by:

$$F_B = mg = \rho V g \tag{5.20}$$

where ρ is the density of the gas in the vacuum tank, and V is the volume of gas displaced by the proof mass. The change in displacement of the MEMS proof mass as the system is pumped from atmospheric pressure to vacuum is given by:

$$\Delta z = \frac{F_{atm.}}{k} - \frac{F_{vac.}}{k} = \frac{V g(\rho_{atm.} - \rho_{vac.})}{k} \tag{5.21}$$

The pressure of the system under vacuum was measured to be 0.227 Pa, equating to a density of 2.744×10^{-6} kg/m^3 (atmospheric pressure, $P_{air} = 1.4$ kg/m^3). Δx was therefore found to be 27 μm. This aligned with the deflection that was observed experimentally, which was approximately 20 μm. The volume of the proof mass is 9.9×10^{-9} m^3.

Whilst looking for the cause of the temperature coupling that ultimately turned out to be a temperature sensitivity of the Femto lock-in amplifier, it was considered whether the pressure could be the cause. If the vacuum changed pressure with changing temperature, then there could be a change in buoyancy that could move the MEMS.

$$\rho = \frac{P}{RT} \tag{5.22}$$

where P is the pressure, R is the specific gas constant, and T is the temperature. A change of 1°C would cause a density variation of order 1×10^{-8} kg/m^3, leading to a change in displacement of order 1×10^{-12}m. It was clear that this could not be the mechanism that caused the temperature coupling between the room temperature and the output of the gravimeter.

5.3 Regression

From December 2014 the system was left in continuous operation whilst the servo control was optimised. Although all of the most temperature sensitive components were controlled using PID loops[3], the data did still not initially look like the tidal signal. The blue series in figure 5.9 is a plot of the output of the shadow sensor (converted into units of μGal) over a period of 6 days in March 2015. The solid red line is a theoretical plot of the Earth tides as should be observed at our location (55.8719° N, 4.2875° W), and was plotted using

[3]For the data displayed in figure 5.9 the shield temperature, the LED temperature, and the MEMS temperature were all actively controlled. It was not known at this stage that the lock-in amplifier had a temperature sensitivity.

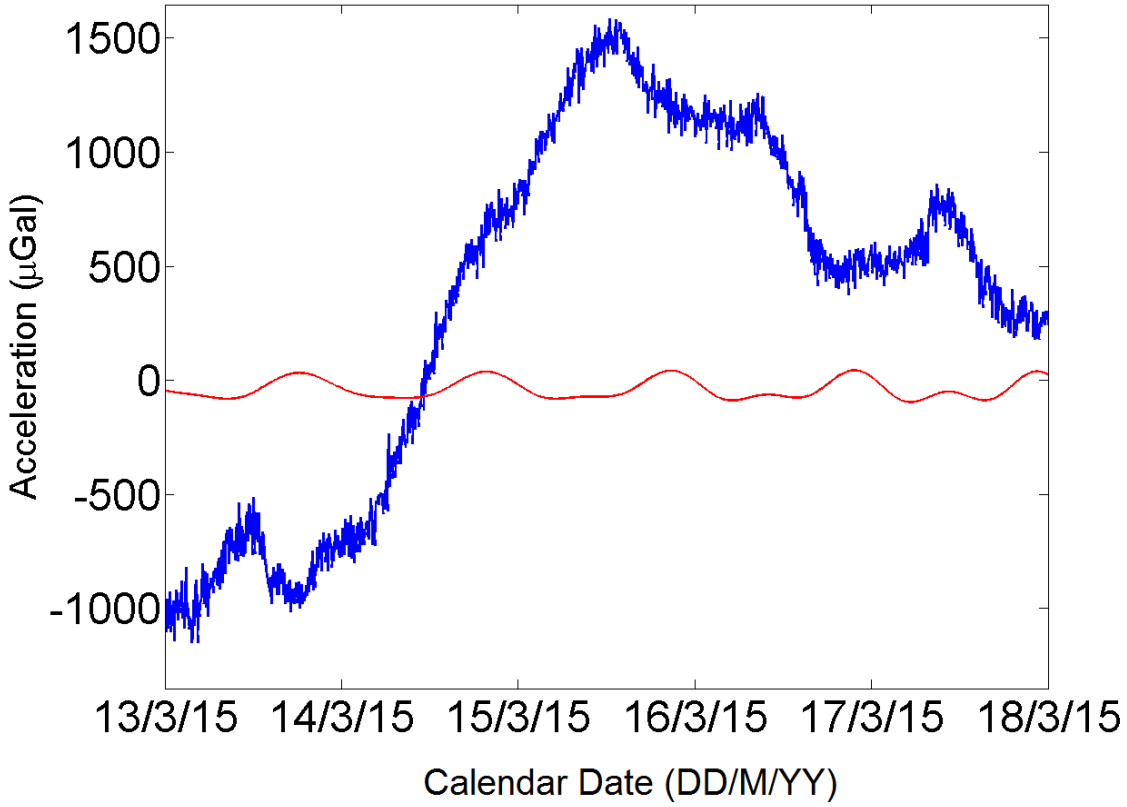

Fig. 5.9 The blue series is the raw output of the shadow sensor. The red series is the expected Earth tide variation over this period in Glasgow. It is clear that in order to observe the tides, post-processing of the data was required. The two series have a correlation coefficient, R of only -0.04.

TSOFT [30]. An ocean loading correction is also included in this theoretical plot to account for the effect of nearby tidal waters pressing on the Earth's crust, although the effect is at the level of only 5% for our laboratory. As displayed in figure 1.4, this tidal signal has a peak-to-peak magnitude of around 200 μGal. The experimental data was clearly varying too much compared to the tidal signal. In fact, from this plot it looks very unlikely that the tidal signal could be observed. The correlation coefficient, R, between these two series was calculated using *Matlab's 'corrcoeff'* function. It was found that the correlation coefficient was -0.04, indicating that there was a very small anti-correlation between the theoretical tide data and the MEMS gravimeter output.

It was thought that temperature variations in the system were still affecting the output of the sensor. All of the measured temperature variations for this period were therefore plotted. These can be observed in figure 5.10.

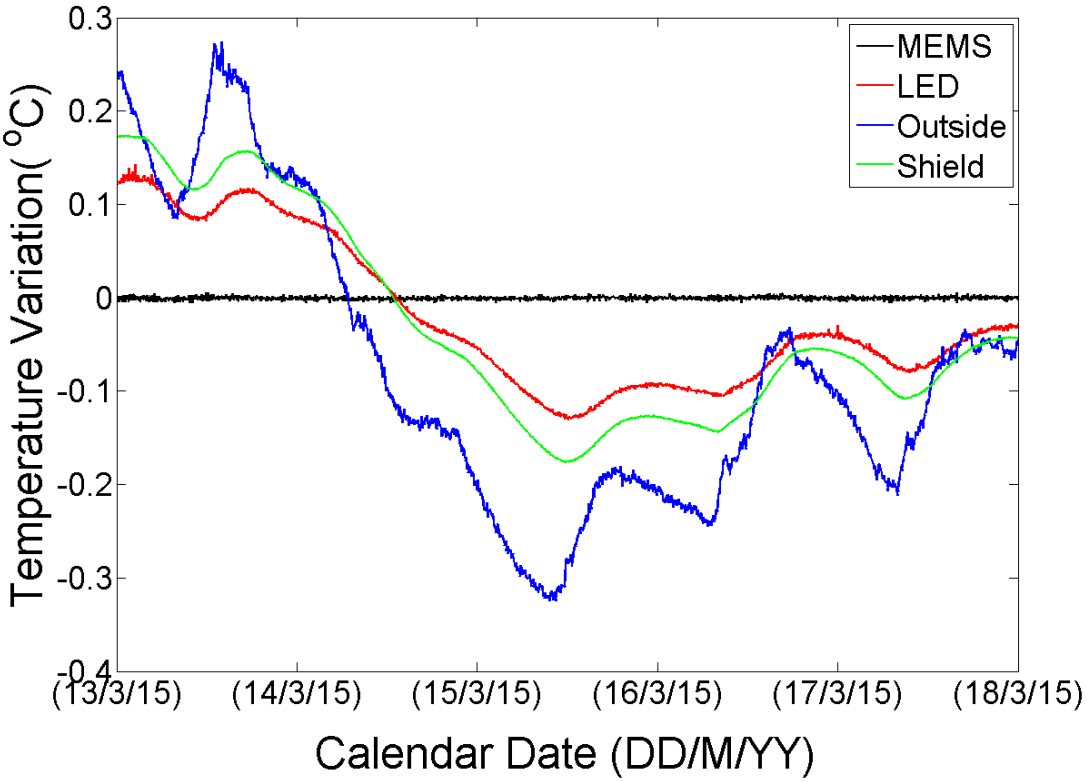

Fig. 5.10 This plot displays the temperature variations of the MEMS device, the LED, the outside (room) temperature, and the shield temperature over the same 6 day period of figure 5.9. A regression analysis was performed to assess in what way the temperatures independently affected the output of the gravimeter.

A visual inspection of figures 5.9 and 5.10 suggested that there was an anti-correlation between the variation of the device output and the red, green and blue temperature series. To test this hypothesis in a more rigorous manner, any potential dependencies between the temperatures and the MEMS device output needed to be computationally checked. The method used to conduct this check was a multiple regression.

Multiple regression is a tool often used in econometrics to identify how a dependent variable depends on more than one independent variable [128]:

$$Y = \beta_1 + \beta_2 X_2 + \beta_3 X_3 + ... + \beta_n X_n \tag{5.23}$$

where Y is the dependent variable, the $X_{2...n}$ terms are the independent variables (up to a number n), β_1 is the Y-intercept or offset term, and the terms $\beta_{1...n}$ are the partial regression coefficients. A partial regression coefficient can be defined as follows: *"β_n measures the change in the mean value of Y, per unit change in X_n, holding the values of $X_{3...n}$ constant" [128].* In other words it gives the net effect of the independent varable, X_n, on the mean value of Y. The purpose of a multiple regression is to determine the values of the regression coefficients. The larger the value of β_n, the larger the effect of X_n on Y.

This methodology can be applied to the MEMS gravimeter. The dependent variable Y is the MEMS output, and the independent variables are the linear drift of the time series (X_2), and the temperature measurements: the MEMS temperature (X_3), the LED temperature (X_4), the outside temperature (X_5), and the shield temperature (X_6). The values of the regression coefficients ($\beta_{2...6}$) will therefore demonstrate the net effect of the independent variables on the MEMS output, and β_1 will be a measure of any Y offset in the data. Once all of these values are known, the dependencies can be corrected for in the data. For this data set, the multiple regression equation 5.25 will take the form:

$$Y_{\text{regression}} = \beta_1 + \beta_2 X_{2(\text{drift})} + \beta_3 X_{3(\text{MEMS temp})} + \beta_4 X_{4(\text{LED temp})} + \beta_5 X_{5(\text{outside temp})} + \beta_6 X_{6(\text{shield temp})} \tag{5.24}$$

A regression was carried out in two ways. Firstly, the *Mregg* function was used within *Matlab* (see Appendix C for full code). *Mregg* calculated values for all of the β terms, but it did not provide any means of identifying the level of confidence to which the terms had been calculated. For the purpose of confidence estimation the econometric analysis software

package *EViews* was used. As well as providing values for all of the β terms[4], *Eviews* also calculated the standard error of each regression coefficient, given by:

$$\text{Standard Error (se)} = \sqrt{\frac{\sigma^2}{n-1}} \tag{5.25}$$

where σ is the standard deviation and n is the number of measurements in independent variable time series (in this case, all of the independent variables consisted of 2917 data points). The standard error was used to calculate two confidence levels for the regression coefficients (95% and 99%). These confidence intervals were calculated using [128]:

$$\hat{\beta} - t_{\alpha/2} se(\hat{\beta}) \leq \beta \leq \hat{\beta} + t_{\alpha/2} se(\hat{\beta}) \tag{5.26}$$

where $\hat{\beta}$ is the calculated value for the regression coefficient, $t_{\alpha/2}$ is the student t-value, $se(\hat{\beta})$ is the standard error of the measured regression coefficient, and β is the true regression coefficient. The student t-value, $t_{\alpha/2}$ can be read from a standard Student's t distribution table [129]. Its value depends on the number of independent variables, the number of measurements in the time series, and the desired confidence interval. Since all of the series used in this experiment contained several thousand data points each, the t-values are close to those given for time series of infinite data points. For the 95% confidence interval the t-value is 1.96 and for the 99% confidence interval the t-value is 2.58. For the 95% confidence interval, equation 5.26 states that if 100 measurements were made, the true value for β would be contained within the upper and lower bounds 95 times out of 100. For the 99% confidence interval this would be the case 99 times out of 100. This means that an uncertainty for the regression coefficient can be written in the form:

$$\beta \text{ error} = \pm t_{\alpha/2} se(\hat{\beta}) \tag{5.27}$$

The results of the multiple regression are displayed in table 5.1.

The temperature with the largest influence on the output of the MEMS device was the MEMS temperature (see table 5.1). This was unsurprising since it had already been estimated that a 1 mK change would cause an uncertainty of $\sim$25 μGal. In descending order of impact on the gravimeter output the MEMS temperature was followed by the shield temperature, the outside room temperature, and then the LED temperature. To observe the magnitude of the

[4] *Eviews* and *Mregg* both produced very similar values for the coefficients. All of the coefficients lay within 3 significant figures of each other with the exception of that for the LED temperature, which differed between both software packages after the first decimal point. As will be noted in the following analysis, however, the LED temperature had both the smallest coefficient, and the largest error on the said coefficient.

Table 5.1 The results of the multiple linear regression. This analysis technique was used to identify the net effect of each of multiple independent variables on the output of the MEMS device. The net effect of each independent parameter on the output is given by the regression coefficients. A positive coefficient implies that a rise in the independent variable will also increase the dependent variable, whilst the antithisis is the case for negative coefficients. The coefficients are displayed in units of dependency (i.e. *dependent variable unit/independent variable unit*). The standard error of each regression coefficient is also displayed, as are two confidence intervals.

Variable	Regression Coefficient, β	Standard Error	Confidence Interval (95%)	99% Confidence Interval (99%)
Offset	752.9 μGal	4.60	$\pm$9.03	$\pm$11.86
Drift	-111.0 μGal/day	0.68	$\pm$1.33	$\pm$1.75
MEMS Temperature	-14841.9 μGal/°C	581.6	$\pm$1139.9	$\pm$1498.2
LED Temperature	286.6 μGal/°C	620.4	$\pm$1216.0	$\pm$1598.1
Outside Temperature	641.5 μGal/°C	26.1	$\pm$51.2	$\pm$67.3
Shield Temperature	-9305.8 μGal/°C	482.5	$\pm$945.7	$\pm$1242.9

regression coefficients displayed in table 5.1, each coefficient was multiplied by its respective time-series. Plots of the resulting series are displayed in two figures. Figure 5.11 shows the drift and offset time series, whilst 5.12 demonstrates the extent to which each temperature variation affected the MEMS device output.

It can be observed in figure 5.12 that although the MEMS temperature has the largest regression coefficient, it is the shield that has the highest impact on the distortion of the output data. This is because these temperatures varied far more than the MEMS device did. The linear drift was under 111 μGal per day once the system had been left evacuated for over a week. This drift term is thought to be due to stress in the silicon flexures. Like all mechanical systems, application of stress leads to anelasticity which causes creep and drift over long timescales [130]. The MEMS device also showed a polynomial drift which decayed away approximately one week after evacuating the apparatus. The polynomial drift was likely due to adsorbed water on the surface layer of silicon, and could have been mitigated against by baking out the system before evacuation. Figure 5.13 demonstrates this initial polynomial drift. Floor tilt and power variation of the LED were also monitored, but neither had any discernible effect on the signal and were therefore not included in the regression analysis.

Now that the regression coefficients had been calculated, it was possible to re-express the original data (figure 5.9) with the dependencies taken into account. $Y_{\text{regression}}$ (from equation 5.24) was subtracted from the original MEMS output time series, giving a corrected output:

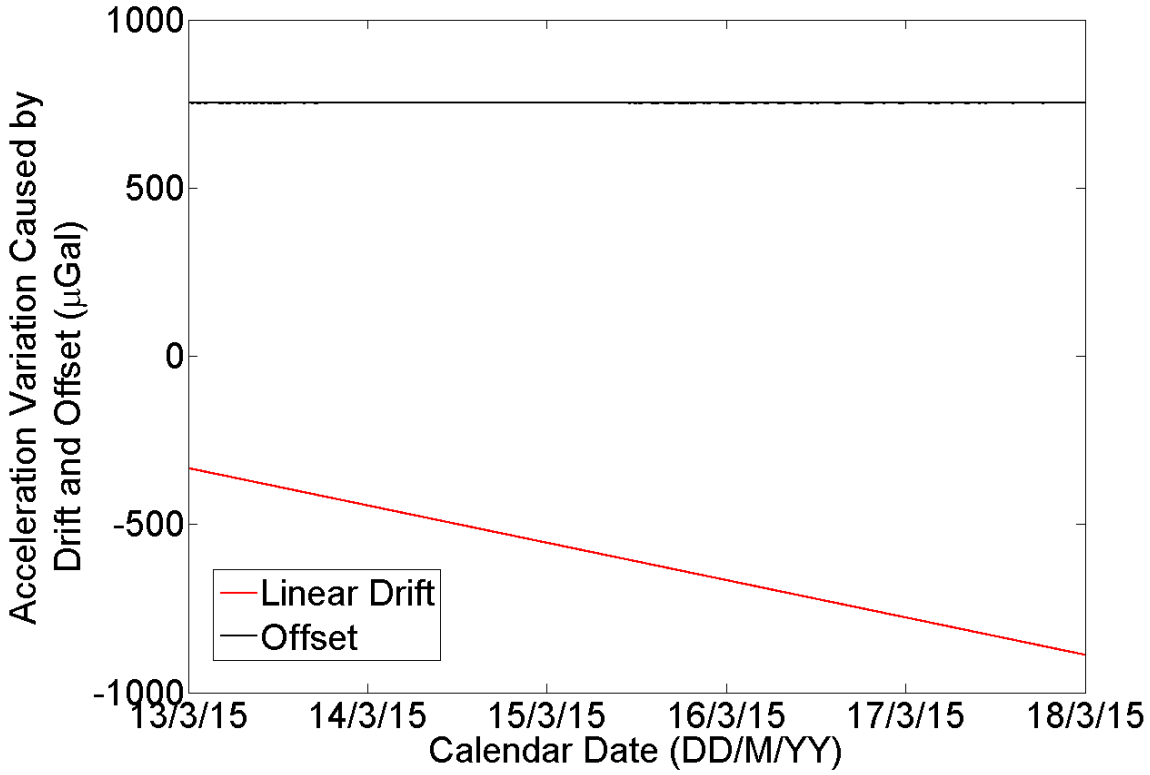

Fig. 5.11 A plot of the offset and drift regression coefficients. The offset series is the β_1 value from equation 5.24, for which the numerical value is displayed in table 5.1. The drift term is the result of the β_2 value from equation 5.24.

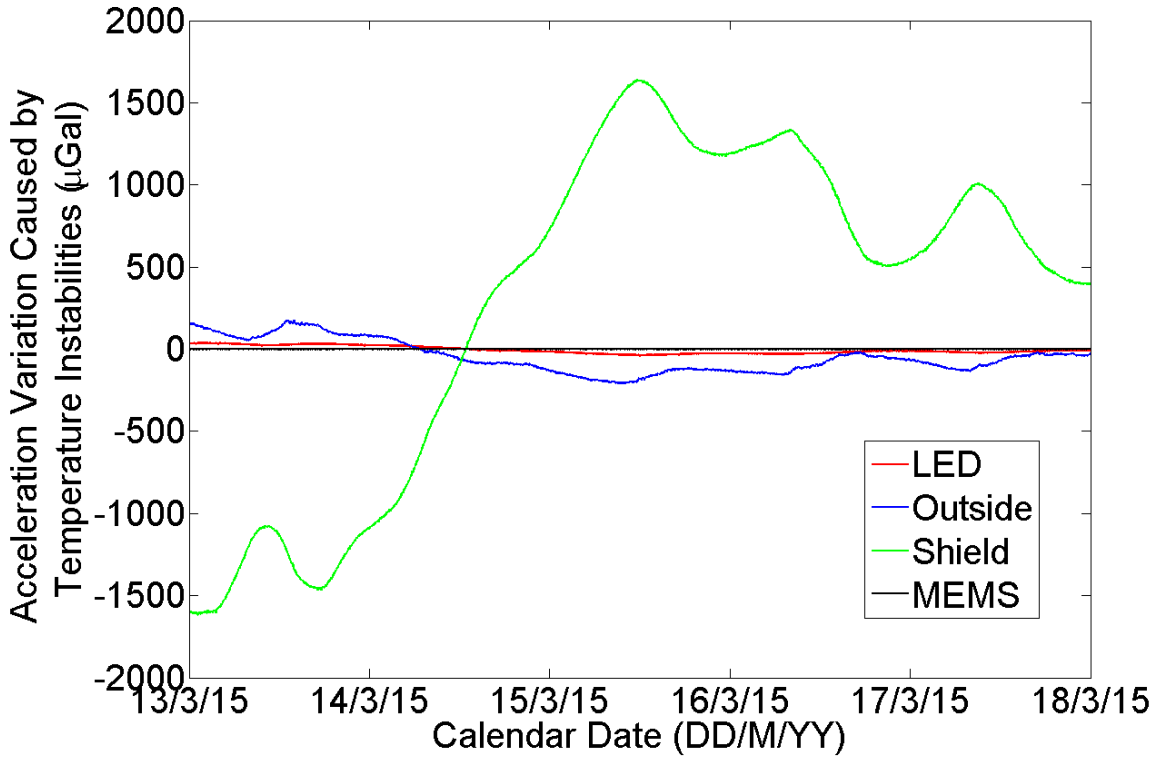

Fig. 5.12 Each of the series in this plot is the product of the temperature regression coefficients from table 5.1 multiplied by the original temperature series displayed in figure 5.10. This is a visual representation of which temperatures had the greatest effect on the MEMS output. It can be observed that variations in the shield temperature altered the MEMS output the most, despite having a smaller regression coefficient than the MEMS temperature. This is due to the fact that the MEMS temperature was controlled more precisely than the shield temperature.

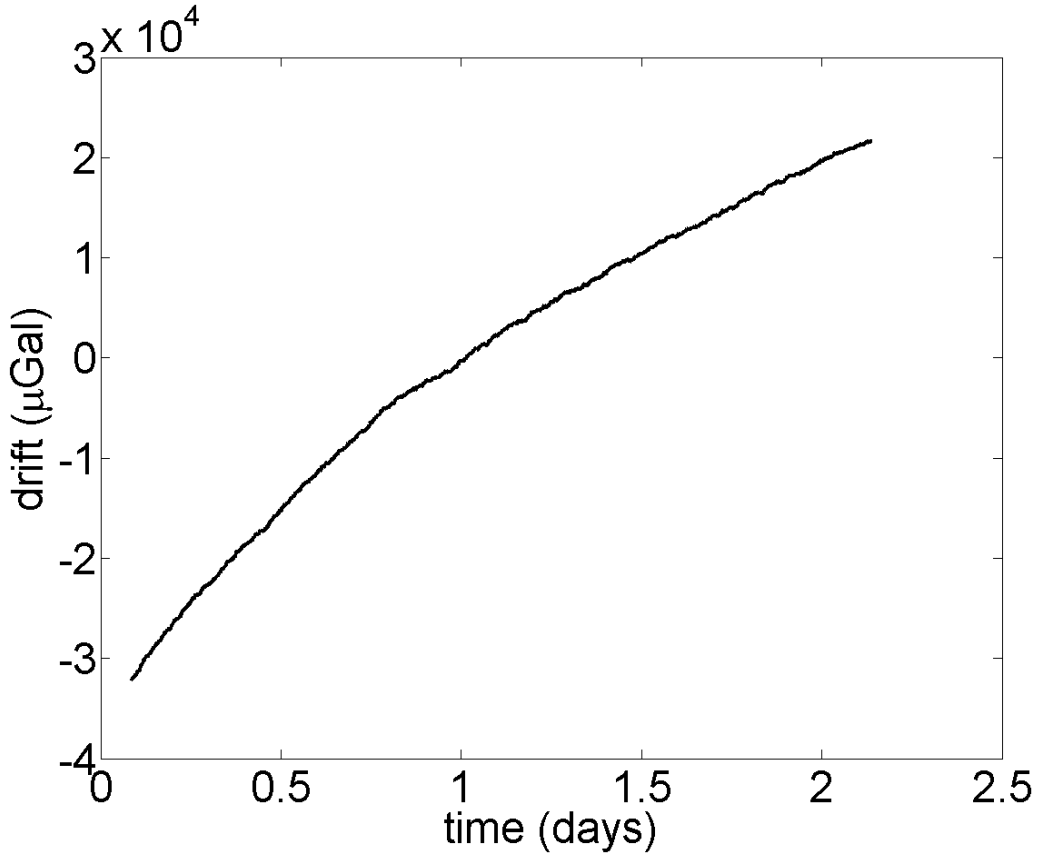

Fig. 5.13 This plot demonstrates the drift in the data shortly after the vacuum pump has been turned on. A polynomial component to the drift is clearly visible. Once the vacuum system has settled, however, the drift becomes linear as demonstrated in figure 5.19c.

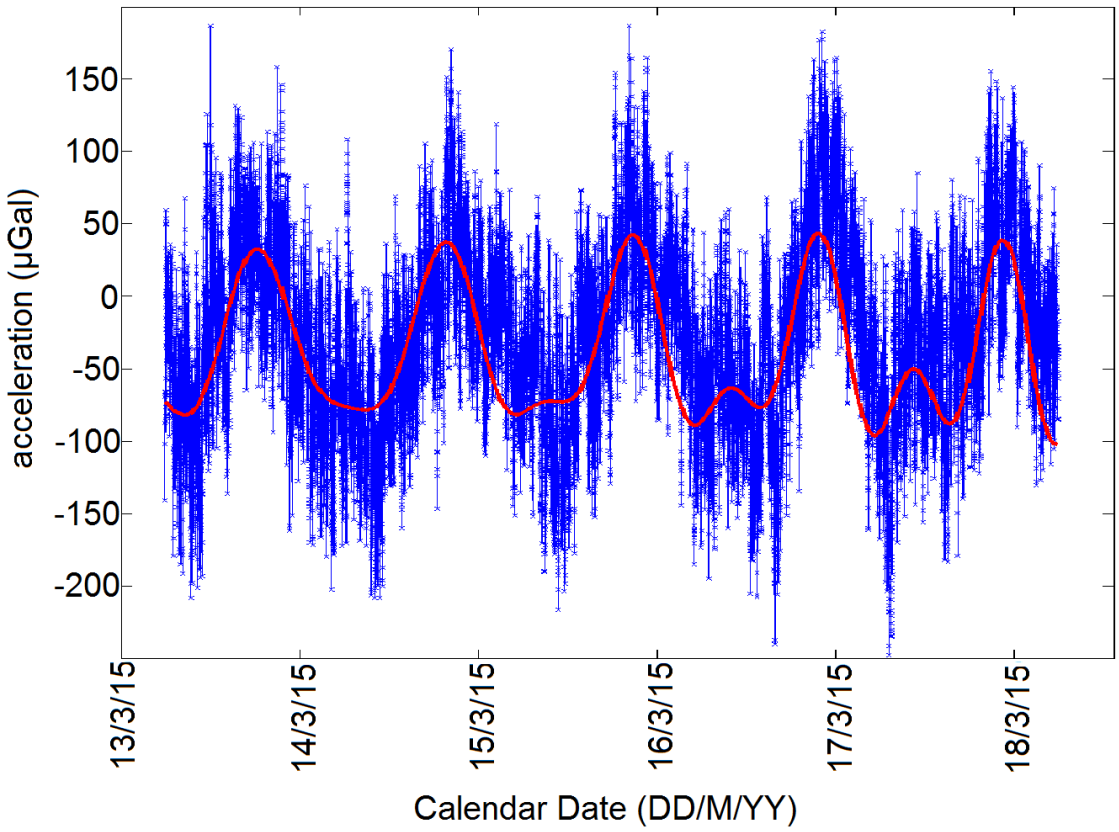

Fig. 5.14 The measurements of the Earth tides obtained from the MEMS device after regression. The red series is a theoretical plot calculated with *TSOFT*, including an ocean loading correction. The blue series is the experimental data with a sampling time of 30 seconds.

$$Y_{\text{corrected}} = Y_{\text{original}} - Y_{\text{regression}} \tag{5.28}$$

The resulting series was then subtracted from the original data. This produced a new series for which temperature variations, drift and offset were all accounted for[5]. This series is plotted in blue in figure 5.14, alongside the theoretical prediction of what the Earth tide should look like in red (using the same data as used for figure 5.9).

[5]It is worth noting here that the Femto Lock-in temperature sensitivity is incorporated within the outside temperature regression coefficient. This is because at the time of measurement, it was not known that the the outside temperature sensitivity was caused by the Femto.

5.4 Averaging

After a visual inspection of figure 5.14, it was noted that there was a correlation in both phase and amplitude between the experimental data and the theoretical tide signal. This suggested that the Earth tides had been observed. There was, however, more analysis that could be carried out to both improve the data, and provide evidence that the Earth tides had been observed. It was thought that a lot of the noise in this data came from the effect of the seismic noise because the vacuum tank was bolted to the concrete floor of the laboratory and no isolation was included. The most obvious means of reducing noise with Poisson behaviour is to average the data. The data was first averaged with a time constant of 10 minutes, and then with an extreme time constant of 240 minutes. The plots of these two averages are displayed in figures 5.15a and 5.15b respectively.

A series of graphs is also displayed in figure 5.16. Each of these also includes a theoretical Earth tide signal in red, and a regressed MEMS output in blue. Each graph, however, has been regressed with the exclusion of one dependent parameter: shield temperature, outside temperature, LED temperature, MEMS temperature, Offset, and drift. Otherwise, the regression analysis used to produce each of these plots is identical to that used in the production of figure 5.15b.

5.5 Correlation Coefficient

The correlation coefficient, R, between the averaged theoretical and experimental tide data was again calculated using *Matlab's 'corrcoeff'* function. For the plot presented in figure 5.15b, an R value of 0.86 was produced. This suggests that it was extremely likely that a measurement of the Earth tides had been made. To check the level of significance of our experimental data, however, it was compared to the correlation of the noise alone. 10,000 random permutations of the data set were created and the correlation coefficient was calculated for each with respect to the theoretical data. This set of R values were plotted as a histogram (see figure 5.17). This histogram had a distribution with a mean value of zero and a standard deviation of 0.008. Since the R value from the un-randomised data is 0.86, this number would appear in the histogram at a distance of 114 σ away from the mean at zero. This suggested that the correlation between the experimental tide data and the theoretical tide data was real to an extremely high degree of confidence.

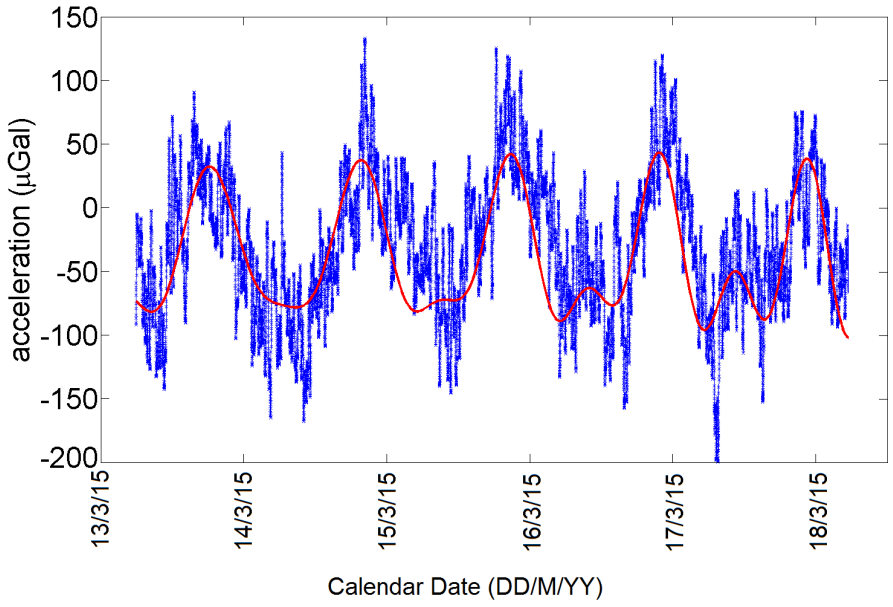

(a)

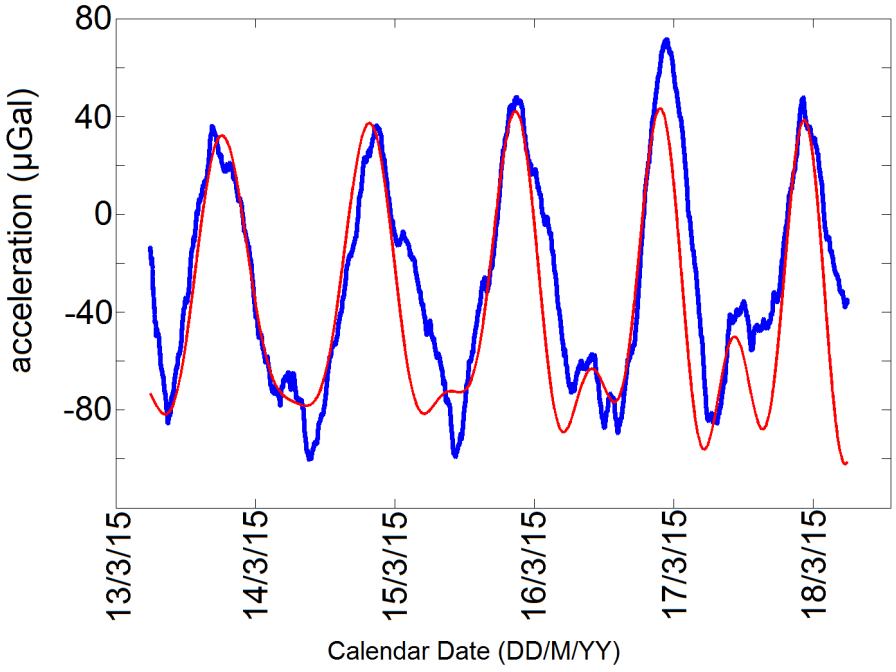

(b)

Fig. 5.15 The effect of averaging on the measurement of the Earth tides. Figure 5.15a shows the data with a 10 minute filtering time. Figure 5.15b shows the data when it has been averaged with a time constant of 240 minutes. The red lines are theoretical plots calculated by *TSOFT*, including an ocean loading correction.

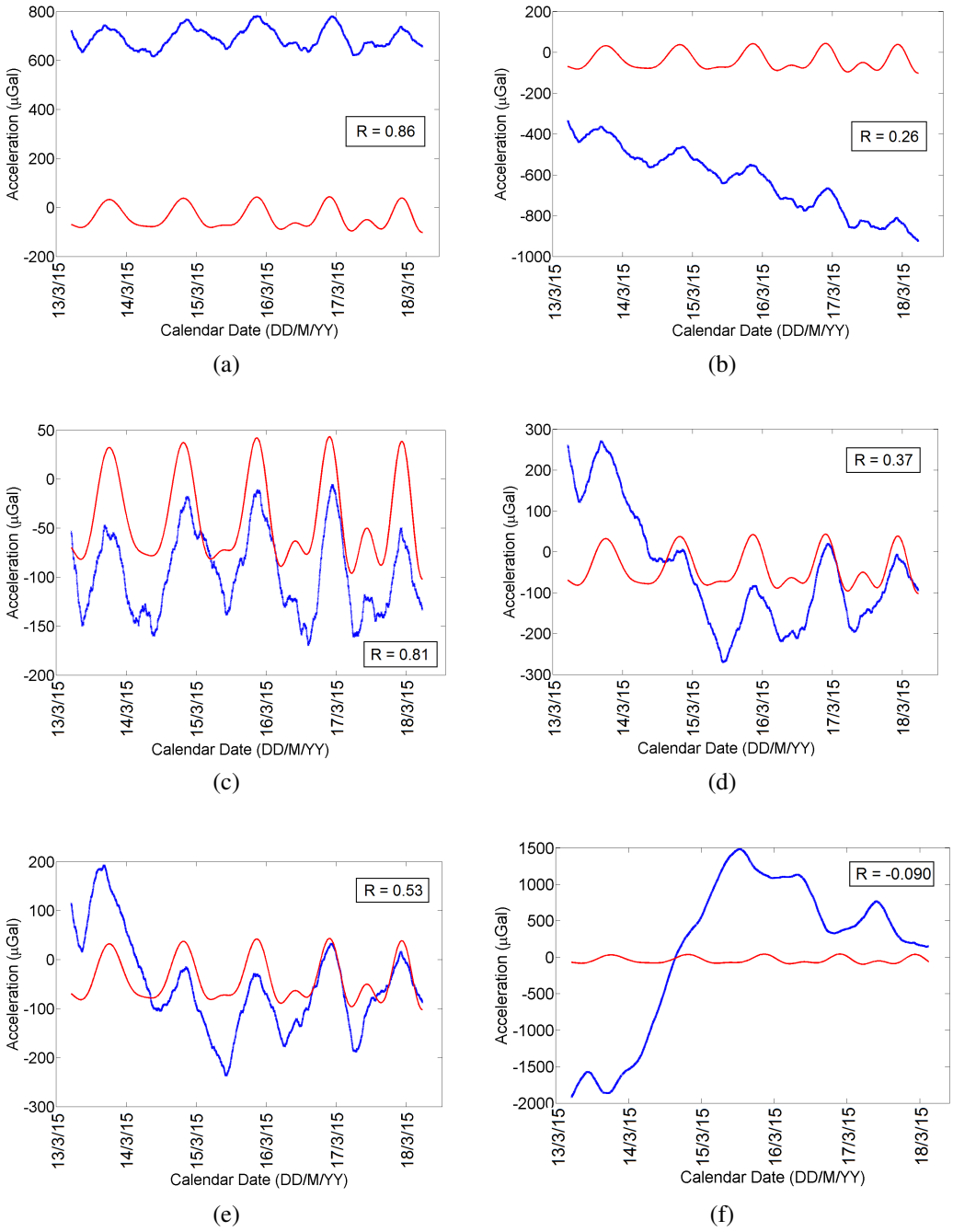

Fig. 5.16 A series of plots demonstrating the effect of not including different series upon which the MEMS output depends. In all of the graphs, the red series is the theoretical Earth tide signal, and the blue series is the regressed output of the MEMS gravimeter. The resultant correlation coefficient, R, between the two series is also included in a legend in each plot. The data in each subplot was obtained using equation 5.28. In each subplot, however, a different regression coefficient has been excluded from the $Y_{\text{regression}}$ term. The offset term (β_1) has been excluded from subplot 5.16a; the linear drift term ($\beta_2 X_{2(\text{drift})}$) has been excluded from subplot 5.16b; the MEMS temperature term ($\beta_3 X_{3(\text{MEMS temp})}$) has been excluded from subplot 5.16c; the LED temperature term ($\beta_4 X_{4(\text{MEMS temp})}$) has been excluded from subplot 5.16d; the outside temperature term ($\beta_5 X_{5(\text{outside temp})}$) has been excluded from subplot 5.16e; and the shield temperature term ($\beta_6 X_{6(\text{shield temp})}$) has been excluded from subplot 5.16f.

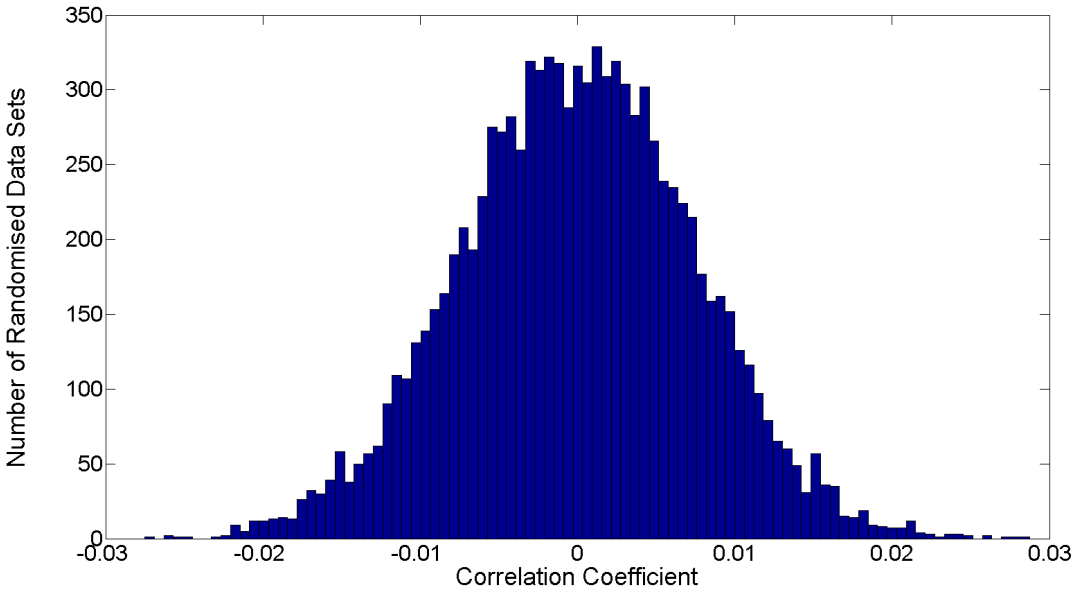

Fig. 5.17 A histogram of the correlation coefficients between the theoretical Earth tide signal and 10,000 randomised permutations of the experimental Earth tide data (see figure 5.15b). The histogram is divided into 100 bins. The peak of this histogram is centered at 0, indicating that on average there is no correlation between the randomised data and the theoretical Earth tide data. The histogram has a standard deviation, σ, of 0.08 (calculated at the full width at half maximum (FWHM) of the bell curve). The correlation coefficient for the unrandomised data set was 0.86, a value 114 multiples of σ away from the mean of the histogram.

5.6 Frequency Spectra

Figure 5.18 is a plot of the RMS acceleration sensitivity of the device over its full spectral range. This plot is comprised of two different data series. The Red series is the data that was used to plot the Earth tides in figure 5.14. Since this data was recorded over long time-scales, the sampling rate was reduced to 0.03 Hz to minimise the size of the data files. This sampling rate, however, means that no information was recorded above 0.03 Hz. Another series was therefore recorded with a sampling rate of around 10 Hz. This allowed higher frequency end of the spectrum to be observed. This data is presented in blue in figure 5.18.

In figure 5.18 the tide signal can be observed at 1×10^{-5} Hz. The peak at 10^{-3} Hz is an artefact of the temperature servo. Between 0.1 Hz and 0.2 Hz the micro-seismic peak can be recognised, its presence indicates that the device is also a sensitive seismometer. Past observations – made from Scotland in February to March 2000 – of the microseismic peak[131] confirm the validity of our observation. At 2.3 Hz the primary resonant mode of the MEMS device generates a large peak due to excitation from seismic noise. This plot was used to calculate the sensitivity of the MEMS device. To find a sensitivity in μGal/$\sqrt{\text{Hz}}$, it is just necessary to read off the acceleration sensitivity at the point where the data crosses 1 Hz on the horizontal axis. It was believed that the value of 40 μGal/$\sqrt{\text{Hz}}$ is an overestimate of the true sensitivity of the device because at 1 Hz the influence of both the primary resonance of the device and the micro-seismic peak are significant. At the LIGO Livingston Observatory, the magnitude of ground motion on a noisy day at 2 Hz can be expected to be around 20 n$m/sqrt$Hz [132]. This limitation, however, is not a cause for concern when it comes to the measurement of slowly varying signals such as the Earth tides. Given the seismic noise is random in nature, it can be averaged away to observe long-term gravitational signals.

5.7 Allan Variation

To further investigate the stability of the device, the Allan deviation of the data was assessed. Allan deviation is a technique used to measure the variation over the full frequency range of a signal by averaging over increasingly shorter time intervals [133]. Allan deviation and Allan variance are analysis techniques originally used to assess the stability of clocks [134]. The Allan deviation is the square root of the Allan variance:

$$\sigma_y(\tau) = \sqrt{\sigma_y^2(\tau)} \tag{5.29}$$

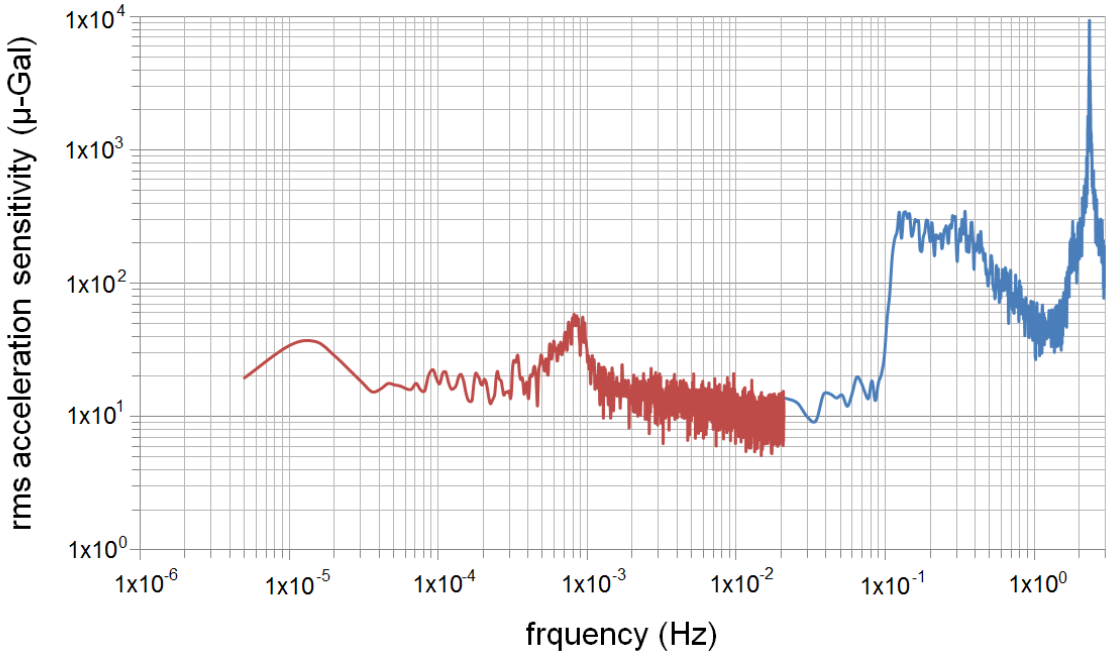

(a)

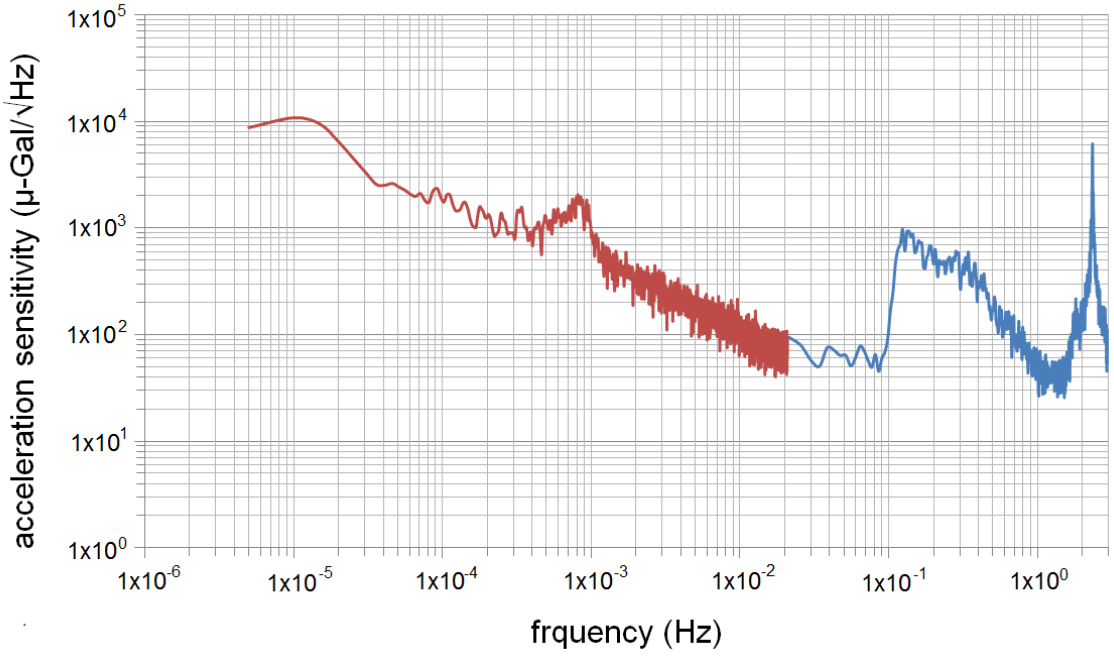

(b)

Fig. 5.18 Figure 5.18a demonstrates the RMS acceleration sensitivity of the MEMS device in μGal. The tide signal can be observed at 10^{-5} Hz; the peak at 2×10^{-3} Hz is the artefact of the temperature servo discussed earlier; the microseismic peak can be observed 0.1 Hz and 0.2 Hz; and the 2.3 Hz resonant frequency can be observed to the right of the plot. The plot is a composite of two data series because the temporal resolution required to record the higher frequency data would not be possible to maintain at lower frequencies. Figure 5.18b is the same plot in units of μGal/$\sqrt{\text{Hz}}$.

where the Allan variance is itself given by [133]:

$$\sigma_y^2(\tau) = \frac{1}{2}\langle (y_{n+1} - y_n)^2 \rangle \tag{5.30}$$

where $\sigma_y^2(\tau)$ is the variance of a series of y values, τ is the length of the time interval, and the angled brackets represent the average value of the term enclosed within them. This term $(y_{n+1} - y_n)$ is the finite difference of the measurements made of y, where n is the n^{th} measurement of y [135]. The factor of 1/2 is included so that if the data set is white in form, the Allan variance will be equal to the classical variance (where the classical variance is the standard deviation of a distribution squared [136]). Equation 5.30 is often simplified to:

$$\sigma_y^2(\tau) = \frac{1}{2}\langle (\Delta y)^2 \rangle \tag{5.31}$$

where the finite difference term is replaced by Δy.

In other words, to calculate the Allan deviation of a time series the data is broken into increasingly smaller time increments; the standard deviations of the data contained within these increments are then calculated. The Allan deviation is the standard deviation between these standard deviation values themselves. As mentioned above, if the noise of the data is perfectly 'white', the Allan deviation will be the same as the standard deviation. If the noise is 'non-white', however, the standard deviation sometimes does not converge whereas Allan deviation always will. This is useful when one wants to analyse data that has long term drift (i.e. 1/f noise). It can therefore be used to assess the stability of a data set. If the Allan deviation were plotted for a time series that was purely white, it would show a greater level of Allan deviation in the short time intervals than the long time intervals. If the same plot was created for a time series that contained 1/f noise the Allan deviation would rise in the long time intervals.

Figure 5.19 consists of eight subplots demonstrating the allan deviance of the MEMS device. Figure 5.19a shows the full-noise tide data without a linear drift correction. Figure 5.19c shows the same data but with the tide signal removed. Figure 5.19e shows the same data again but with a linear drift correction. Figures 5.19b, 5.19d, 5.19f and 5.19h show the Allan deviation for the data in figures 5.19a, 5.19c, 5.19e and 5.19g respectively.

The data analysed in figure 5.19 spans a frequency range from 10^{-5} Hz to 0.03 Hz (the sampling frequency of this data set). The Allan deviation for the high frequency series (see figure 5.18) is polluted by the presence of two large signals: the resonant frequency of the device, and the microseismic peak [137, 131]. This deviation plot is not a useful measure of the noise of the device and has therefore not been included in figure 5.19. Figures 5.19b and

5.19d demonstrate the linear drift that the device experiences. Figures 5.19b, 5.19d and 5.19f also demonstrate a small peak at 500 s that is an artefact of the temperature servo. The broad peak that is only visible on the rising edge of Fig. 5.19b is the tide signal.

5.8 Calibration Stability

As discussed in the previous chapter, to convert the raw voltage output of the device into a unit of acceleration, a calibration factor was required in units of volts per μGal. This calibration factor was essentially a metric of the sensitivity of the shadow sensor to the motion of the MEMS proof mass. If it were to change over time then the amplitude of the gravimeter output would also change. A change in the calibration could have occurred for many reasons, including mechanical hysteresis of the MEMS device, the MEMS device moving relative to the sensor, or the individual components of the sensor moving relative to each other. Although six days was the longest set of data in which the device maintained a stability good enough to continuously measure the Earth tides, the Earth tides were measured using the same device in intervals spanning several months. Over this time it was entirely possible that the device could have drifted enough to change the calibration factor. To assess whether this was the case two short Earth tide measurements – separated by nearly four months – were plotted using the same regression analysis, and crucially using the same calibration factor (see figure 5.20). If the calibration factor had drifted significantly over time, then this would have appeared as a change in amplitude of the experimental data (compared to the theoretical data) between the two subplots in figure 5.20. No such change could be visually observed between the two subplots.

To check how a change in calibration factor would alter the appearance of the plots, the calibration factor was varied in small increments. It was found that a 5% change in the calibration factor caused in the output made the amplitudes of the experimental and theoretical series noticeably different. Changes smaller than 5% were not possible to resolve visually. It can be therefore assumed that if the calibration factor changed, it did so by no more than 5% over 4 months. During this time period, the vacuum tank was vented and evacuated several times. These manoeuvres made the MEMS proof mass oscillate to an extremely large amplitude; to the extend that the proof mass would bounce off the top and bottom of its frame. Despite all of this violent motion, the calibration factor seemed to remain stable, demonstrating that the mechanical stability of the device is sufficient. Such a mechanical stability is an important feature of a device that could eventually be used in the field.

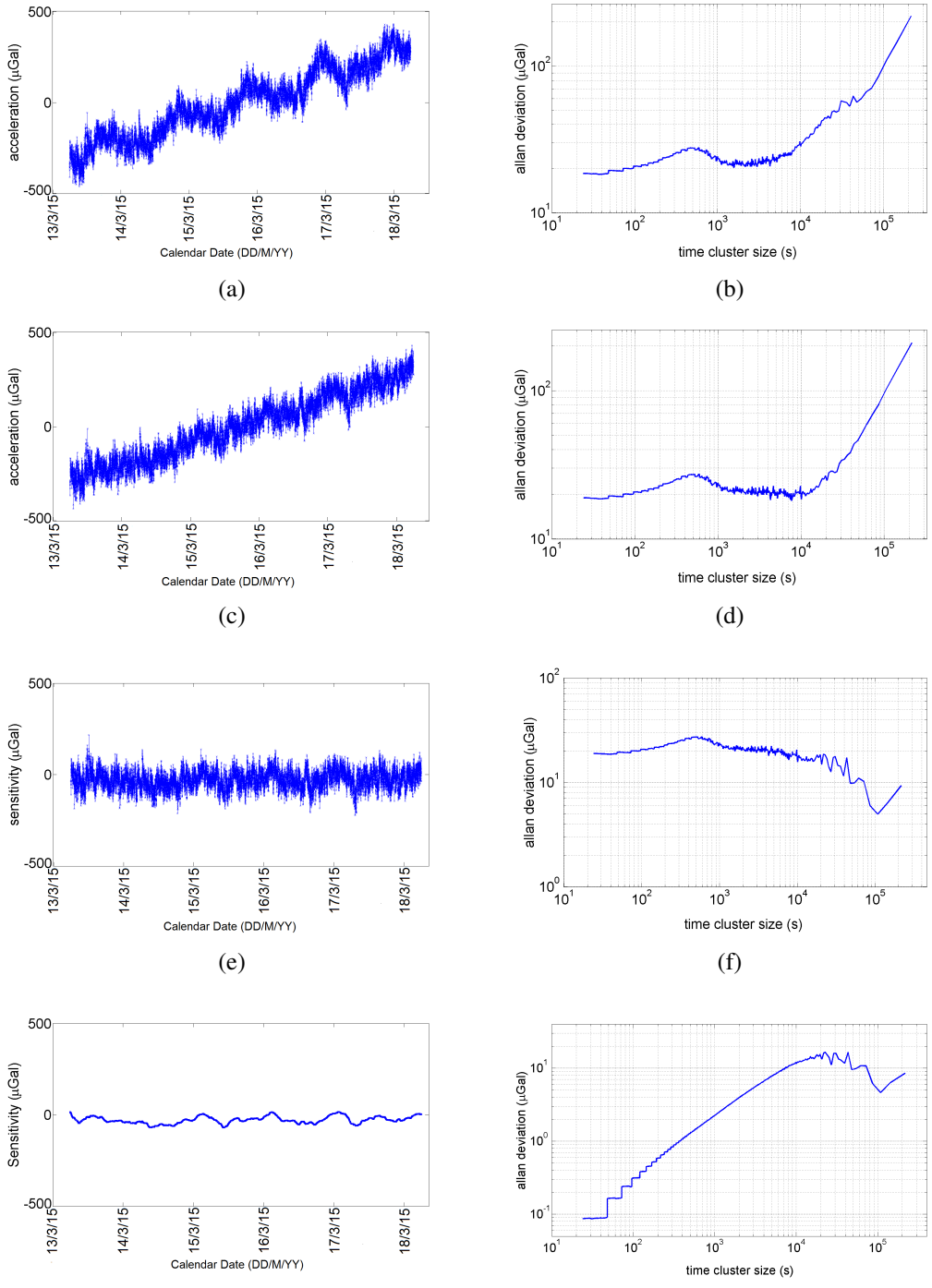

Fig. 5.19 **5.19a** is a full noise time series of the tide measurement. **5.19b** is the Allan Deviation of the series in **5.19a**. **5.19c** is a full noise time series of the tide measurement with the tide signal removed via a regression against the theoretical data from *TSOFT*. **5.19d** is the Allan Deviation of the series in **5.19c**. **5.19e** is a time series of the tide measurement with the tides removed and the linear drift corrected, **5.19f** is the corresponding Allan deviation plot. **5.19g** is the same data as **5.19e** but with a 4 hour filter added. **5.19h** is the Allan deviation plot of this filtered data.

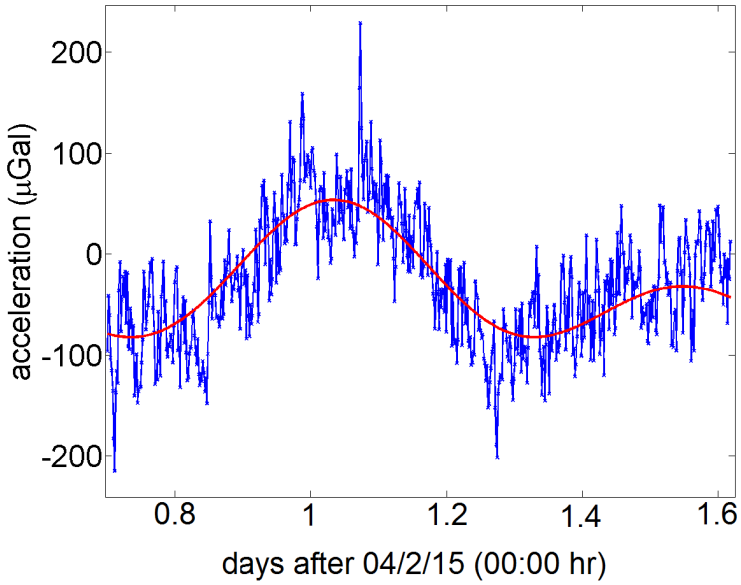

(a)

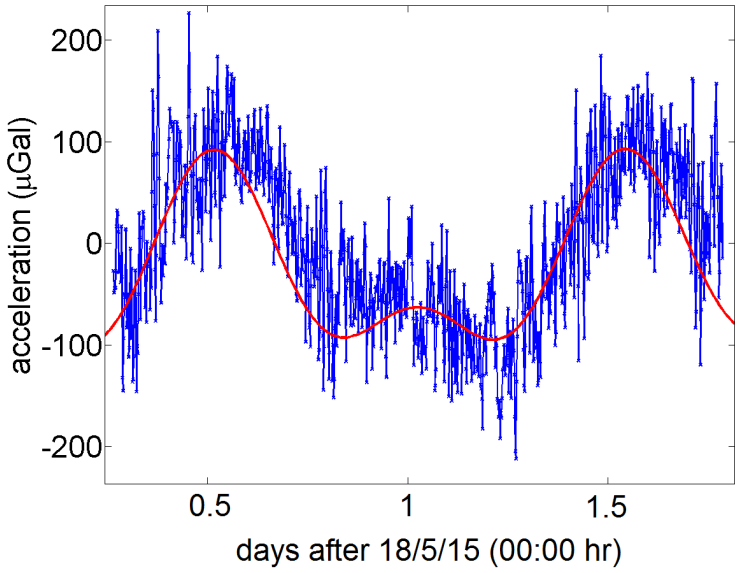

(b)

Fig. 5.20 Figures **5.20a** and **5.20b** are two data sets separated by approximately 4 months, with no filtering employed. During this period the vacuum chamber was evacuated and vented several times, despite this the calibration factor of the device has not changed by more than 5%.

5.9 Summary of The Earth Tide Measurement

A measurement of the Earth tides is a major stepping stone in the development of the MEMS gravimeter. It proves that the device has the prerequisite sensitivity (40 μGal/$\sqrt{\text{Hz}}$) and stability (down to 10^{-6} Hz) to be a useful gravity measuring device for many commercial applications. What has not been demonstrated is its ability to be used in the field. The system described in this thesis is large and requires a mains power supply. A field prototype is now under development, the construction of which will be discussed in the second half of the following chapter.

Chapter 6

Conclusions and Plans for Future Work

6.1 Summary and Conclusions

In the course of this PhD project, a MEMS gravimeter has been developed. Arguably this is the first MEMS device that can be called a gravimeter. It is certainly the first such instrument that is capable of measuring the Earth tides. The device has an unprecedented stability down to 10^{-6} Hz, and a sensitivity of 40 μGal/$\sqrt{\text{Hz}}$. To put the sensitivity of the device into context, 40 $\mu Gal/\sqrt{Hz}$ is sufficient in 1 second to detect a tunnel with a cross-sectional area of 2 m^2 and length of 4 m at a depth of 2 m; it could be used to find oil reservoirs of 50 m $\times$ 50 m $\times$ 50 m (with a density contrast of 50%) at a depth of 150 m; a change of 45 μGal was a 'clear precursor' to a volcanic eruption in the Canary Islands in 2011 [54]. Our device would also have the sensitivity to see this signal. It is accepted that intrusion of new magma into a reservoir precedes volcanic eruptions [26]; continuous micro gravity measurements around volcanoes are a useful tool in monitoring such events [55]. The ratio of ground deformation to change in gravity can be used to monitor magma chambers at depths of several km [56].

The MEMS device has been designed to have a resonant frequency of under 4 Hz. To achieve such low frequencies a geometric anti-spring system [82, 83] was chosen. With increasing displacement, anti-springs get softer and their resonant frequency gets lower. An asymmetric geometrical anti-spring was ultimately selected, consisting of a pair of anti-spring flexures supporting the lower portion of the proof mass, and a single flexure supporting the top. The three flexure system maintains an anti-spring behaviour as the gravitational loading increases (when the device is tilted from horizontal to vertical). Due to the asymmetry of the design, however, a small level of y-axis (in-plane) tilting occurs. This tilt pulls the system off its constrained axis. When the system reaches its equilibrium, it regains a Hooke's Law behaviour. This creates a device which is stable but at a much lower frequency than

traditional MEMS devices. A resonant frequency of 2.3 Hz is the lowest resonant frequency of any reported MEMS device to date. The angle at which the lowest resonant frequency occurs can also be tuned. This feature means that three devices could be mounted in a triaxial configuration, allowing sensitivity to gravity variations in all three dimensions.

The MEMS device was fabricated from a single chip of 200 μm thick <100> silicon. The device was etched using a 'halo' design [91] i.e. instead of etching away all of the unwanted areas of silicon, trenches of constant width were used in an outline of the structure. A uniform trench width meant that the etch rate was uniform over the whole patten. The halo was 20 μm wide. The Bosch process allows control of the gas flow enabling processes to be tuned with negative and positive defined etch profiles. The spring profiles achieved here were vertical to within 0.5°. After the sample was etched, a bespoke vacuum chuck was used to pick up the sample.

Once the sample was free-standing, it was placed vertically in a mount that could be used to measure the displacement of the proof mass as changes in g occurred. The proof mass motion was measured using an optical shadow sensor [97]. Here a light emitting diode (LED) illuminates a photodiode with the MEMS device mounted in between. Motion of the proof mass modulated the shadow, generating a change in the current output of the photodiode. This shadow sensor achieved a high sensitivity (equating to an acceleration noise floor of $\leq$10 μGal at the sampling frequency of 0.03 Hz), whilst allowing a large dynamic range of up to 50 μm.

The temperature of the system had to be carefully controlled to maintain the stability of the device. The dominant mechanism by which temperature variations affected the gravity measurement was the change in Young's Modulus, Y, of the flexures [123, 124]. This in turn altered the spring constant of the flexures, resulting in a variation of the spring constant of the flexures, k, 1/k dk/dT, of 7.88×10^{-6} K^{-1}. Servo control loops were thus implemented to maintain the temperature of the system to within 1 mK. A 1 mK change in temperature would give an uncertainty in the gravity reading of $\sim$25 μGal. The primary control loop maintained the temperature of the MEMS device directly, the second controlled the temperature of a copper thermal shield that encased the entire shadow sensor (Fig. 4.8). The MEMS device was placed inside a vacuum system. This was bolted to the floor without an external seismic isolation table, which would be a large and expensive addition.

From December 2014 the system was left in continuous operation whilst the servo control was optimised. Figure 1.4 demonstrates a data run of five days between the 13/03/15 to the 18/03/15 in which gravitational acceleration is plotted against time. The solid red line is a theoretical plot of the Earth tides as should be observed at the laboratory location

(55.8719° N, 4.2875° W), and was plotted using *TSOFT* [30]. An ocean loading correction was also included in this theoretical plot to account for the effect of nearby tidal waters pressing on the Earth's crust, although the effect is at the level of 5% for the laboratory. There is a strong correlation coefficient, R, of 0.86 between the experimental data and the theory plot. The correlation indicated that this is the first measurement of Earth tides demonstrated by a MEMS device, a landmark result for MEMS gravimetry. This measurement provided a natural calibration for the gravimeter, the results of which allow us to determine that the present sensitivity of the device is 40 μGal/$\sqrt{\text{Hz}}$. A stability test was performed of the calibration factor for the device by monitoring the tides at two intervals approximately 3 months apart. The calibration remained constant to better than 5 % (Fig. 5.20).

The noise floor of the device is limited by seismic noise. A theoretical thermal noise floor of under 0.5 μGal/$\sqrt{\text{Hz}}$ can be calculated, assuming that losses are due to structural damping [117]. This calculation is based upon a measurement of the quality factor, Q, of the device under vacuum of $\sim$80 (the relaxation time of the MEMS device is $\sim$11 s). It was observed that the Q reduced as the resonant frequency was lowered (Fig. 5.1), resulting from the fact that in geometrical anti-springs the reduction of resonant frequency resuts in the restoring force becoming comparable to internal friction [120].

The obvious question to ask at this point was: 'how does this gravimeter compare to other similar MEMS devices?'. Although mobile phone accelerometers are not very sensitive, some MEMS devices have been developed that reach sensitivities much better than the 0.23 mGal/$\sqrt{\text{Hz}}$ of the iPhone MEMS device [43]. For example: a device developed by Krishnamoothy et. al. [68] has a sensitivity of 17 μGal/$\sqrt{\text{Hz}}$; the *SERCEL QuietSieis* [66] has a sensitivity of 15 μGal/$\sqrt{\text{Hz}}$; and a microseismometer developed by Pike et. al. [65] has a sensitivity of under 1 μGal/$\sqrt{\text{Hz}}$. These devices, however, only operate as seismometers and do not demonstrate the stability to be classed as gravimeters, which are capable of monitoring low frequency gravimetric signals such as the Earth tides (around 10 μHz). Figure 6.1 is an adaption of figure 1.14, now including the data from this device – the red series in this plot. The data used to create this plot of this device performance is the same data used in figure 5.19e. This is data for which the linear drift and the Earth tide signal has been removed. A signal that has not been removed from the the data in figure 6.1 is the microseismic peak [131]. This could have been removed by monitoring the seismic background with a reference seismometer, as was done for the Pike microseismometer (magenta series) [65]. Since the low frequency output of the device was of interest, a reference seismometer was not used. Instead a simple average of the data was carried out to remove this signal.

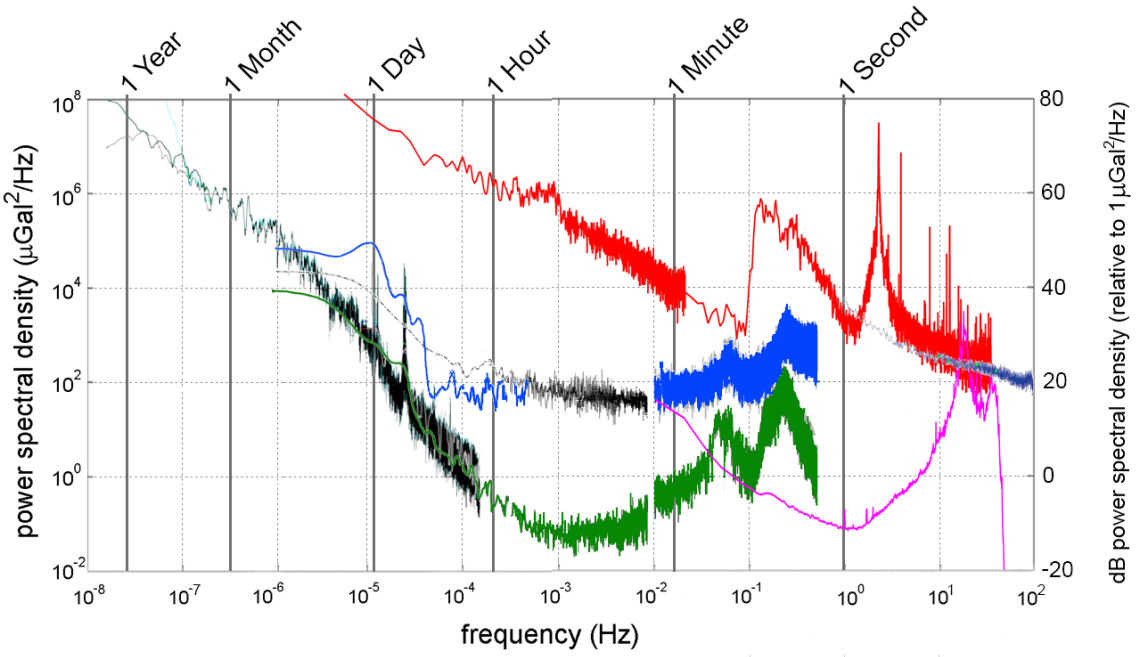

Fig. 6.1 The red series – plotted using the data from 5.19g – is the MEMS gravimeter, demonstrating its sensitivity down to the tidal frequency regime. The filtering time means that the sensitivity rolls off above 10^{-4} Hz. The black series is the *Scintrex CG5*, the blue series is the *Micro-g Lacoste gPhone-054*, the green series is the *SG-C026 superconducting gravimeter*. The data from these three series are taken from a figure by Riccardi et. al. [67] (©Bureau International des Poids et Mesures. Reproduced by permission of IOP Publishing. All rights reserved.). The magenta series is the microseismometer by Pike et. al. [65].

This MEMS device, capable of measuring the Earth tides, represents a significant step forward in the field – it is not just an accelerometer, but a gravimeter. Made from a single silicon chip the size of a postage stamp, this sensor has the lowest reported resonant frequency of any linearly oscillating MEMS device (1.85 Hz), is within an order of magnitude of the best acceleration sensitivity of any MEMS device (40 μGal/$\sqrt{\text{Hz}}$), and has the best reported stability of any MEMS device. This prototype will enable the development of a new density contrast imaging technology applicable in many industrial, defence, civil, and environmental applications. It has the potential to be inexpensive, mass-produced and lightweight which opens up new markets: it could be flown in drones by oil and gas exploration companies, limiting the need for dangerous low altitude aeroplane flights; it could be used to locate subterranean tunnels; it could be used by building contractors to find underground utilities. Networks of sensors could be operated in unsafe areas for monitoring natural and man-made hazards; for example, on volcanoes or unstable slopes to improve the spatial and temporal resolution of subsurface density changes. This will allow improved hazard forecasting and the reduction of occupational risk to monitoring personnel [56, 57].

6.2 Plans for Continuing and Future Work

There are many plans for the continuation of the development of the MEMS gravimeter. Some of these plans are long term i.e. the production of a commercially packaged triaxial MEMS gravimeter, and others are much more imminent. Below is a rough outline of the plans for the device, ordered in the chronological sequence in which they are expected to be implemented.

6.2.1 On-Chip Thermal Control

As discussed in chapter 5, the temperature of the MEMS needs to be controlled to 1 mK. At present wire-wound resistors are used as heating elements, and small platinum resistors are used to measure the temperature. These resistors have to be glued onto the surface of the silicon after fabrication of the device. In the coming months, all of these separate heaters and thermometers will be replaced by on-chip versions that will be fabricated at the same time as the MEMS device (see figure 6.2). The thermometers will be made from thin films of palladium, and the heaters from thin films of Ni-Chrome. The on-chip thermometers will send state information to the PID controller, which will feed back to the system via on-chip resistive heaters. Temperature measurements will be made with a four-terminal

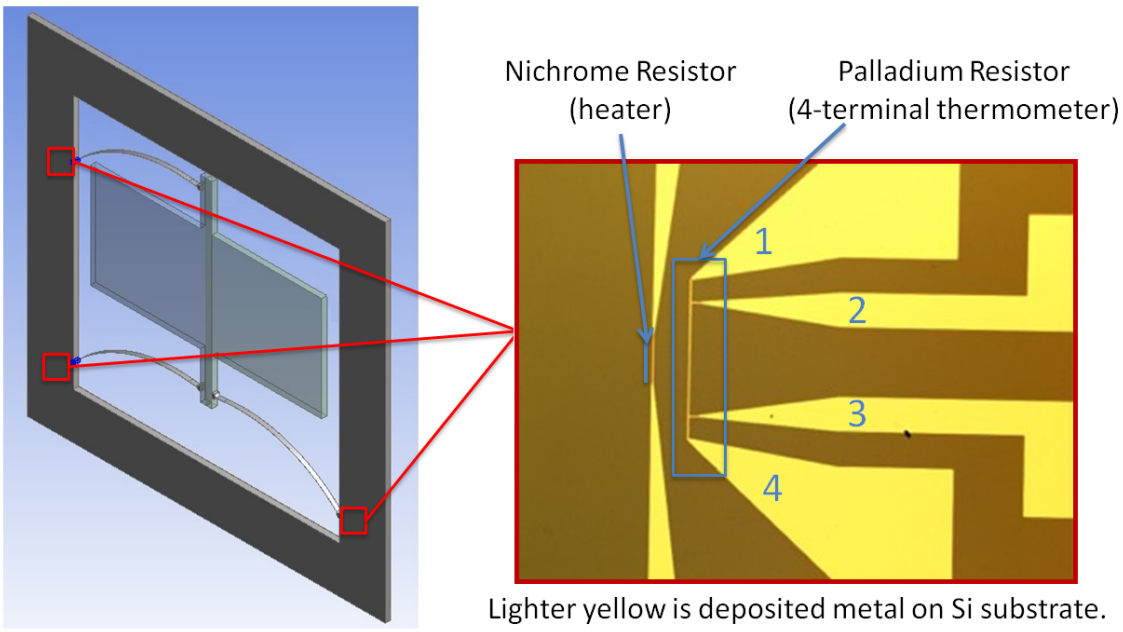

Fig. 6.2 The locations of the on-chip thermometers and heaters. To make a four-terminal measurement of the temperature current will be driven between terminals 1 and 4, and the voltage will be measured between terminals 2 and 3.

sensor. Four-terminal measurement eradicates the effect of contact resistance. Current is driven between two probes of the thermometer (probes 1 and 4 in figure 6.2), and the voltage is measured between two other probes (points 2 and 3 in figure 6.2). This means that the temperature sensitivity of external wires will not affect the measurement.

6.2.2 Optical Readout

The optical sensor is currently the size-limiting feature of the gravimeter. There will therefore be a focus on the miniaturisation of this sensor. There are two main ways in which this miniaturisation will be approached. The first method is to simply make the shadow sensor smaller. Figure 6.3 shows the size difference between the original shadow sensor and another that has been recently fabricated. This new 'C' structure is only 2.6 cm $\times$ 2.6 cm $\times$ 1.5 cm, but another design is also being developed that will see the structure shrink to a cuboid with sides of 2 cm $\times$ 2 cm $\times$ 1 cm.

The second means of shrinking the optical sensor would be to go for a completely new design altogether. Ideally this new design would be completely 'on-chip' so that it could be fabricated at the same time as the MEMS device, considerably reducing the building costs. The first design that is being considered is a silicon photonic waveguide Michelson

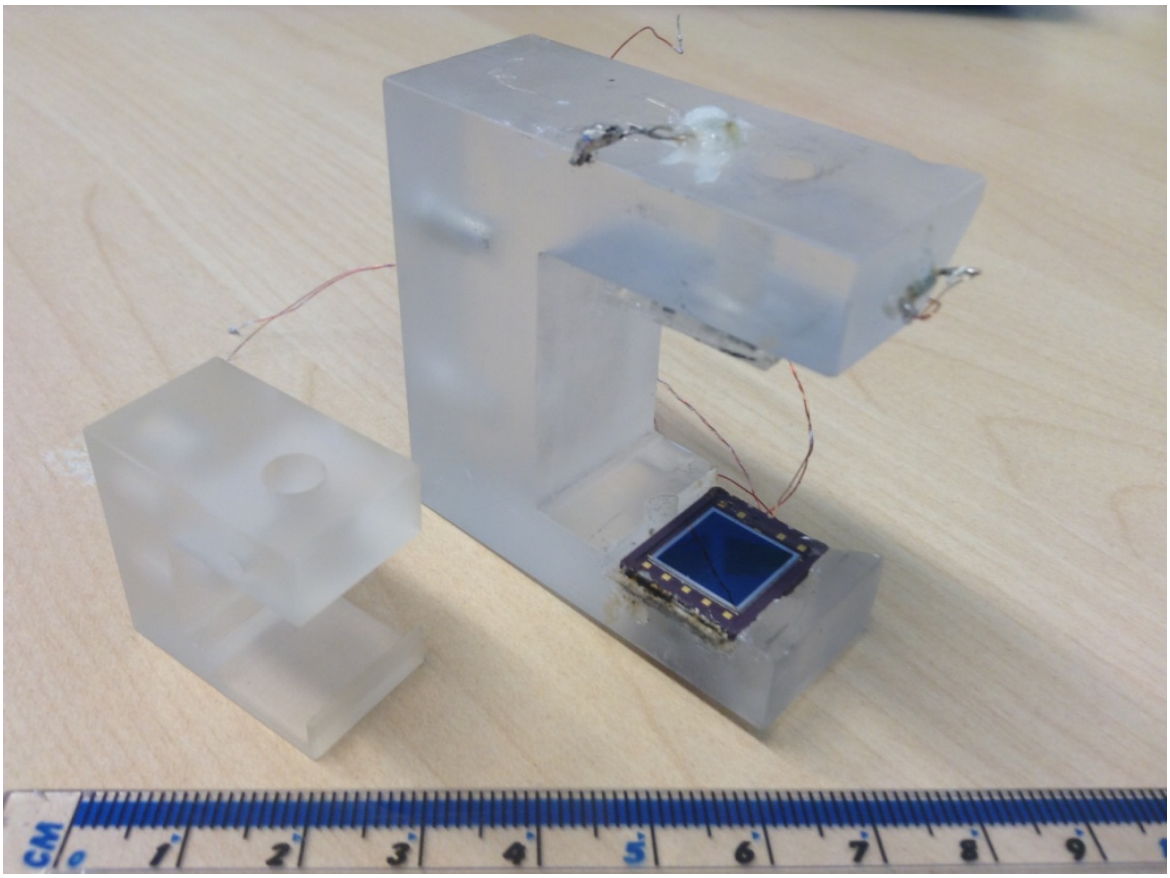

Fig. 6.3 A new miniaturised shadow sensor is now only 2.6 cm $\times$ 2.6 cm $\times$ 1.5 cm. It is positioned next to the original shadow sensor that is 5 cm $\times$ 5 cm $\times$ 2 cm. Fabrication of an even smaller device with dimensions of 2 cm $\times$ 2 cm $\times$ 1 cm is currently underway.

interferometer. Silicon photonic waveguides are a means of carrying optical signals over the surface of a semiconductor device [138]. Waveguides can be designed to carry single of multiple modes of light. Generally lasers with wavelengths of 1550 nm are used to send light along the waveguides. Devices requiring waveguides are made from silicon-on-insulator (SOI) material. These wafers consist of a silicon substrate layer, a thin layer of insulator (e.g. SiO_2), and then another thin layer of silicon. Mechanical structures can be fabricated in the substrate layer, whilst waveguides can be fabricated in the upper layer of silicon on top. The waveguides are therefore separated from the substrate silicon, so that light modes do not couple into the substrate. Mirrors and beam splitters – the basic components of a Michelson Interferometer [139] – are both possible to construct using silicon waveguides [140, 141].

Silicon waveguides have been used as accurate displacement sensors [142], but this process has required light coupling between waveguides spaced less than 500 nm apart [143]. Since the coupling is evanescent, sensitivity drops of dramatically as the separation is increased. Spacing two waveguides this close together on the geometry would not have been possible due to the large initial displacement of the proof mass. A Michelson Interferometer is envisaged where 1550 nm light could be split between two waveguide arms: one would run along the frame of the MEMS device and end at a stationary Bragg mirror, and the other would exit the frame, travel through free-space and reflect from a Bragg mirror on the side of the proof mass.

Since the diffraction of loss of a waveguide decreases as the waveguide gets bigger, it is also being considered whether a Michelson Interferometer could be made from fibre optics instead of silicon waveguides [144]. These can be made larger than silicon waveguides and the diffraction losses are therefore less severe. Trenches could be etched into the surface of the MEMS device frame, and optical fibres could be placed within the trenches. Optical fibres with ball tips would be used because they can focus the light exiting the fibre to further reduce diffraction loss. A composite image of this potential design is displayed in figure 6.4. Drawings of the fibres have been superimposed upon an SEM image of trenches and beam splitter (which have been constructed by Antonio Samarelli as an initial test of the design).

A even simpler design was also considered for a fibre optic sensor. Instead of creating an interferometer with two arms and a beam splitter, a single arm was considered. A fibre could be pointed at the moving MEMS proof mass. Light would be reflected back from the proof mass, but another internal reflection would occur from the end of the fibre itself. The interference of these two waves could be used as an interferometric readout. Since this measurement isn't differential (unlike a Michelson configuration), changes in intensity could not be rejected. The simplicity of this design, however, make it appealing.

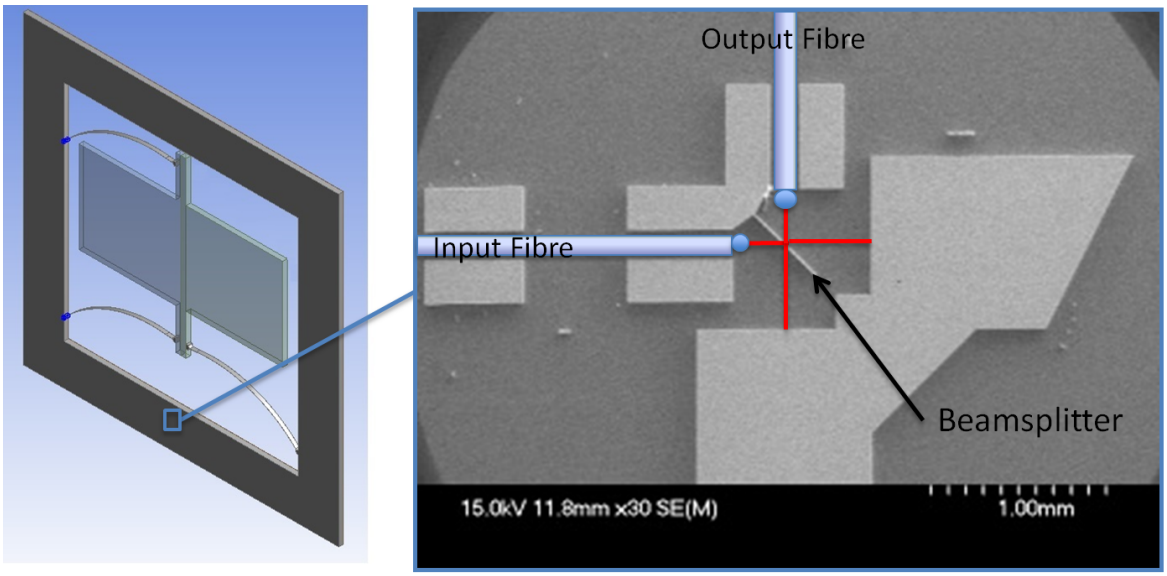

Fig. 6.4 The design of a fibre-optic Michelson interferometer that could be etched into the side of the MEMS device frame.

6.2.3 Field Tests and Demonstrators

Figure 5.2 shows how large the vacuum system was that enclosed the experiment. The tank was this large simply because the system was available, not because it was specifically selected for this work. A small cube-shaped vacuum enclosure has been purchased to house the MEMS device for a field prototype MEMS gravimeter. This cube is shown in figure 6.5, a pen is also included in the image for scale. This cube is still over-sized but it will alow hands-on alterations while the prototype is optimised. Two layers of thermal shielding will be incorporated within the cube for maintaining the temperature of the device. The cube will be evacuated using a getter pump, which does not require a power supply.

As also displayed in figure 5.2, the electrical equipment required to conduct the experiments discussed in chapter 5 was extensive: lock-in amplifiers, multimeters, power supplies, signal generators and a computer took up two whole 19" racks. Obviously, in this state there was no chance that the system could be transportable, which is the ultimate aim of the project. A significant effort has therefore been put into the development of a printed circuitry board (PCB), that could incorporate the functionality of all of the above instruments. It needed to modulate the LED, readout the photodiode output with a lock-in technique, control several temperatures with a PID system, and record all of the data. A freelance electronic engineer has been commissioned to design and build this PCB in collaboration with this team. The design centres around a dsPIC microcontroller that will replace the computer in the current

system. This will run the PID control of the temperatures, modulate the LED, and read in the output via a software-based lock-in amplifier. Opamps are included to amplify the signal and several digital-analogue converters (DACs) are present for the input and output of both digital and analogue signals. All of the data will be saved on an SD card. Additionally, a GPS chip has been mounted for measuring the position of the gravimeter surveys. The position of the gravimeter (particularly the height above sea-level) is important to know because this will have a significant effect on the gravity reading via the impact of the Free-Air Effect. The board is in the early stages of testing but it looks like it will achieve all of the required functionality. An image of the first version of the PCB is shown alongside the vacuum cube in figure 6.5.

Once the field demonstrator is fully constructed in the coming months, several tests will be carried out to assess its performance outside of the laboratory. The first of these tests will be to place the gravimeter in a lift within the building. Since a rise in altitude of 1 m will create a Free-Air anomaly equivalent to a tide signal, this test will provide a useful gravitational signal that can be replicated with periods of a more practical length that the Earth tides. The lift is also a moving platform for which vibrations will be more significant. The second test that will be carried out is a time lapse gravity survey of a hydroelectric power station. The Cruachan is a dammed loch in Scotland (see figure 6.6) that is used as a pumped-storage hydro electric power station. The water level therefore changes by a significant amount on a daily basis, providing a corresponding change in the local gravitational acceleration. Measuring the g change that would result from the changing water level in the dam will be an appropriate proxy for a the monitoring of a draining oil reservoir, or the progress of a carbon dioxide sequestration project. The third test is to take measurements of gravity over a grid or line, to observe known faults or other gravity anomaly causing geological features. An arrangement is in place with a collaborating geophysics company – *Bridgeporth Geophysics* – to borrow a commercial gravimeter and operatate it sumultaneously to all of the proposed field tests. This will provide a side-by-side comparison for the MEMS gravimeter.

6.2.4 Modelling and Fabrication of a Triaxial Device

There are some questions resulting from the final section of chapter 2 that also ought to be addressed. If a triaxial MEMS gravimeter were constructed, how would it perform? Since all three sensor chips will have a sensitivity to g_z, the measured value will be taken as the average of these three systems. It is thought that this feature will provide some level of

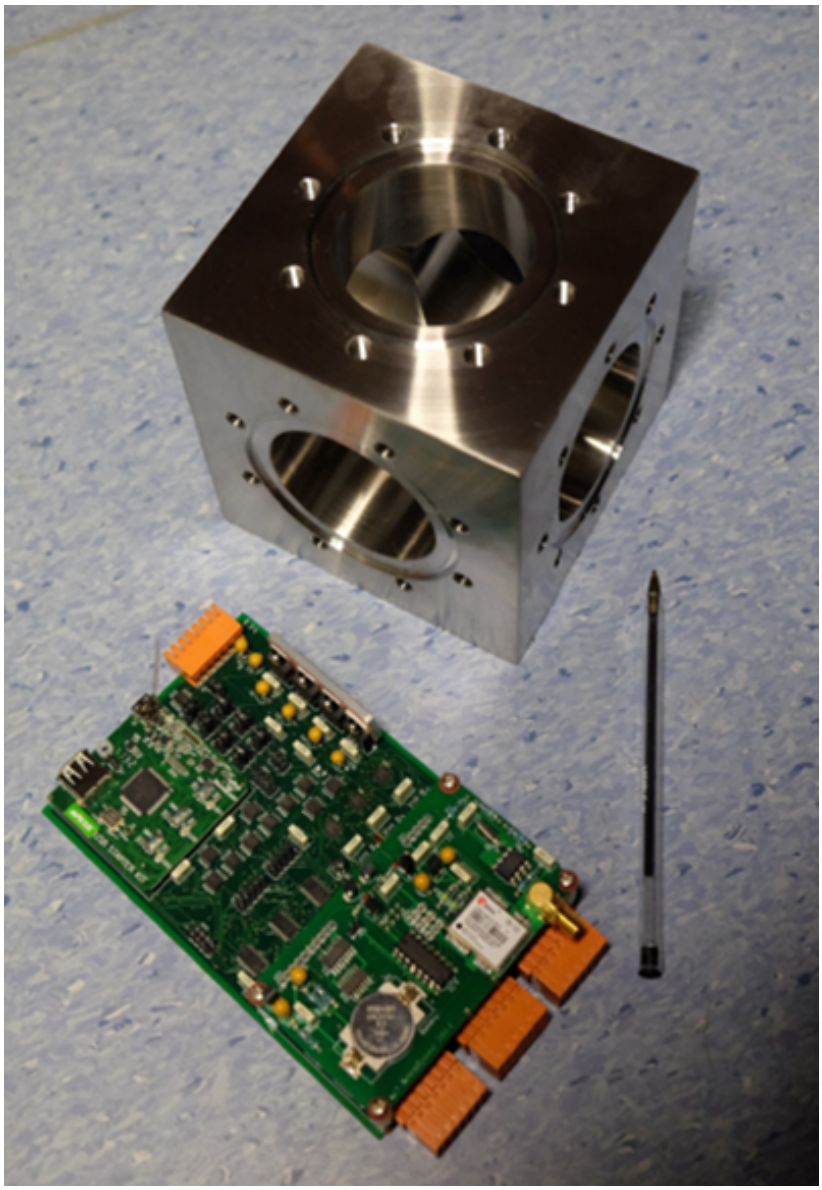

Fig. 6.5 The new vacuum chamber and electronics board of a MEMS gravimeter for field deployment.

Fig. 6.6 The Cruachan pumped storage hydro-electric dam. This dam will be used to conduct a time-lapse gravity survey as the water level rises and falls.

insensitivity to tilting of the platform upon which all three sensors sit, because as one sensor's output decreases due to a tilt, the others will increase; thus cancelling out the effect. This assumption, however, relies upon the linearity of the spring response. Since the springs upon which the proof masses are mounted are non-linear, there may be no tilt insensitivity, the the effect may only be reduced slightly. A series of ANSYS tests will provide an answer to this question.

Whatever the answer to this question, a triaxial MEMS gravimeter is a future target, and tilt will need to be monitored and corrected for to some extent. Initial tests are therefore being conducted into placing silicon photonic Sagnac interferometers [145, 146] onto the surface of the MEMS devices. These could be used to to monitor tilt via the interference caused by two counter-propagating waves around a waveguide ring.

6.2.5 Feedback Control

The gravimeter presently operates open loop by measuring the physical displacement of the MEMS proof mass. At some stage in the future it may be of interest to run the device in feedback mode. Here the device would be held in a stationary position by capacitive actuation. Instead of measuring g via the displacement of the proof mass, it could be measured by the relative force required to keep the device stationary. Feedback operation could help make the device more robust, since large deflections that cause the proof mass to hit the side of the frame would be less likely to occur. Actuation on MEMS devices is most often carried out with capacitive transducers [147, 148].

6.2.6 Different Sensing Platforms

The first (and easiest) aim of the ongoing project is to create a device that will operate on the ground, at first with single axis sensitivity but later evolving into a triaxial system. At a later stage, however, different sensing platforms could be investigated from which to conduct gravity surveys. One such platform that is already used commercially is the aeroplane. Gravimetry is regularly carried out from planes because large areas can be surveyed in a relatively short time frame by flying the sensors in a grid pattern over an area of interest. For such surveys, the gravimeters are either positioned on a gyro-stabilised platform to remove unwanted vibrations and tilts, or strapped down with the tilts and vibrations removed via the use of some other reference instrument. A simulated airbourne gravity survey was carried out by *Bridgeporth Geophysics* using the noise characteristics of the device in the lab. It was found that the acceleration noise caused by the limitations of the plane's GPS system

was more significant than the noise level of the MEMS gravimeter. Although this result is promising, it cannot be taken as proof that the device would work in a real-life recreation of this survey since the noise characteristics were based upon measurements taken in a seismically quiet lab. It is hoped, however, that such a recreation will be conducted once the field prototype has been developed further.

At an even later stage it will be of interest to test the possibility of conducting gravity surveys with the MEMS device mounted on a drone. Drone surveys would not place a pilot at risk as aeroplane surveys do, and they could also be conducted much more cheaply. The resolution also has the potential to be much greater since drones could fly in tighter grids and closer to the ground. Multiple drones could also fly in formation to conduct a survey simultaneously. No gravimeter has hitherto been mounted on a drone platform because they are too heavy (and since drones have only recently become so cheaply available). Drones are, however, much more susceptible to being buffeted by the wind when compared to planes. Much care would therefore have to be taken to mitigate for the effect of the extra parasitic acceleration that would inevitably occur.

6.2.7 Commercial Development

If the field prototype tests are successful, it is likely that some focus will turn to developing a commercial device. Such a device would initially be single axis, and intended for use in ground-based surveys. The device would be packaged in a much smaller vacuum system that the cube in figure 6.5. Discussions are underway with potential partners for the development of this commercial packaging. There are also many potential end-users of MEMS gravimeters that have expressed an interest in the work. The design of the MEMS gravimeter has been protected via an application for a patent that is now in the public domain [149].

References

[1] R.P. Middlemiss, A Samarelli, D.J. Paul, S. Rowan, J. Hough, and G.D. Hammond. Measurement of the Earth tides with a MEMS gravimeter. *Nature*, 535:614–617, 2016.

[2] I. Newton. *Philosophiae Naturalis Principia Mathematica*. The Royal Society, London, 1st edition, 1687.

[3] M. Denny. The pendulum clock: a venerable dynamical system. *European Journal of Physics*, 23:449–458, 2002.

[4] R. Schüler, G. Harnisch, H. Fischer, and R. Frey. Absolute schweremessungen mit reversionspendeln in Potsdam 1968-1969. *Veröffentlichungen des Zentralinstituts für Physik der Erde*, 10:193 p., 1971.

[5] E. Hytönen. Absolute gravity measurement with long wire pendulum. *Publications of the Finnish Geodetic Institute*, 75:142 p., 1973.

[6] P.N. Agaletzkij, K.N. Egorov, and A.I. Martsinjak. results of absolute determinations of the acceleration due to gravity by three independent methoids in the point of VNIM (Lenningrad). *Bulletin Geodesique*, 51:82–90, 1959.

[7] J.F.W. Herschel. *A Treatise on Astronomy*. Longman, London, 1st edition, 1833.

[8] O.H. Truman. "Gravity Meter", US Patent Number: US1988527 A, 1935.

[9] S.T.V. Thyssen and A. Schleusener. Ein neuer schweremesser. *Öl und Kohle*, pages 382–384, 1934.

[10] W.A. Prothero and J.M. Goodkind. A superconducting gravimeter. *Review of Scientific Instruments*, 39(9):1257, 1968.

[11] J.M. Goodkind. The superconducting gravimeter. *Review of Scientific Instruments*, 70(11):4131–4152, 1999.

[12] Z. Jiang, V. Pálinkáš, O. Francis, P. Jousset, J. Mäkinen, S. Merlet, M. Becker, A. Coulomb, K.U. Kessler-Schulz, H.R. Schulz, Ch. Rothleitner, L. Tisserand, and D. Lequin. Relative gravity measurement campaign during the 8th international comparison of absolute gravimeters (2009). *Metrologia*, 49(1):95–107, 2012.

[13] M. Lederer. Accuracy of the relative gravity measurement. *Acta Geodynamica et Geomaterialia*, 6(3):383–390, 2009.

[14] A. Guillet. Measure precise de l'acceleration g de la chute des corps dans le vide. *Comptes Rendus Academie Des Science Paris*, 207:614–616, 1938.

[15] C. Volet. L'intensité de la pesanteur déterminée par l'observation de la chute d'un corps. *Comptes Rendus Academie Des Science Paris*, 222:373–375, 1946.

[16] M. Van Camp. Uncertainty of absolute gravity measurements. *Journal of Geophysical Research: Solid Earth*, 110(B5):B05406, 2005.

[17] M. Kasevich and S. Chu. Measurement of the gravitational acceleration of an atom with a light-pulse atom interferometer. *Applied Physics B Photophysics and Laser Chemistry*, 54(5):321–332, 1992.

[18] S. Merlet, Q. Bodart, and N. Malossi. Comparison between two mobile absolute gravimeters: optical versus atomic interferometers. *Metrologia*, 47(4):L9–L11, 2010.

[19] M. de Angelis, A. Bertoldi, L. Cacciapuoti, A. Giorgini, G. Lamporesi, M. Prevedelli, G. Saccorotti, F. Sorrentino, and G.M. Tino. Precision gravimetry with atomic sensors. *Measurement Science and Technology*, 20(2):022001, 2008.

[20] J. S. Kissel. Calibrating and improving the sensitivity of the LIGO detectors. *Louisiana State University PhD Thesis*, 2010.

[21] W. Torge. *Gravimetry*. de Gruyter, Berlin and New York, 1st edition, 1989.

[22] W. Torge and J. Müller. *Geodesy*. de Gruyter, Berlin and Boston, 4th edition, 2012.

[23] H.O. Seigel. A guide to high precision gravimeter surveys. *Scrintex Ltd. Technical Report*, (905), 1995.

[24] B. Hofmann-Wellenhof and H. Moritz. *Physical Geodesy*. Springer Science & Business Media, Austria, 2nd edition, 2006.

[25] H. Alnes, O. Eiken, and T. Stenvold. Monitoring gas production and CO2 injection at the Sleipner field using time-lapse gravimetry. *Geophysics*, 73(6):WA155–WA161, 2008.

[26] K. Mogi. Relations between the eruptions of various volcanoes and the deformations of the ground surfaces around them. *Bulletin of the Earthquake Research Institute*, 36:99–134, 1958.

[27] W.E. Farrell. Earth tides, ocean tides and tidal loading. *Philosophical Transactions of the Royal Society A*, 274:253–259, 1973.

[28] J.B. Merriam. Atmospheric pressure and gravity. *Geophysics Journal International*, 109:488–500, 1991.

[29] A. Lambert and C. Beaumont. Nano variations in gravity due to seasonal groundwater movements - implications for the gravitational detection of tectonic movements. *Journal of Geophysical Research*, 82(2):297–306, 1977.

[30] M. Van Camp and P. Vauterin. Tsoft: graphical and interactive software for the analysis of time series and Earth tides. *Computational Geoscience*, 31(5):631–640, 2005.

[31] B. Shutz. *A First Course in General Relativity*. Cambridge University Press, Cambridge, 2nd edition, 2009.

[32] R. E. Bell, R. Anderson, and L. Pratson. Gravity gradiometry resurfaces. *The Leading Edge*, 16(1):55–59, 1997.

[33] R.J. Blakely. *Potential Theory in Gravity and Magnetic Applications*. Cambridge University Press, Cambridge, illustrate edition, 1995.

[34] a H Saad. Understanding gravity gradients — a tutorial. *The Leading Edge*, 25(8):942–949, 2006.

[35] J. M. Lumley, J. P. White, G. Barnes, D Huang, and H. J. Paik. A superconducting gravity gradiometer tool for exploration. *Airborne Gravity 2004 - Abstracts from the ASEG-PESA Airborne Gravity 2004 Workshop: Geoscience Australia Record 2004/18*, pages 21–39, 2004.

[36] C. A. (Bell Geospace) Murphy. The Air-FTG airborne gravity gradiometer system. *Airborne Gravity 2004 - Abstracts from the ASEG-PESA Airborne Gravity 2004 Workshop: Geoscience Australia Record 2004/18*, pages 7–14, 2004.

[37] S. Middelhoek. Celebration of the tenth transducers conference: The past, present and future of transducer research and development. *Sensors and Actuators A*, 82(1):2–23, 2000.

[38] K.D. Wise. Integrated sensors, MEMS, and microsystems: reflections on a fantastic voyage. *Sensors and Actuators A*, 136(1):39–50, 2007.

[39] I. Amato. Fomenting a revolution, in miniature. *Science*, 282(5388):402–405, 1998.

[40] Sandia National Laboratories News Release. New five-level layering process pioneered by Sandia promises more reliable, complex micromachines. *URL: http://www.sandia.gov/media/NewsRel/NR1999/layer.htm (Date accessed: 04/01/16)*, 2004.

[41] L.M. Roylance and J.B. Angell. A batch-fabricated silicon accelerometer. *IEEE Transactions on Electron Devices*, 26(12):1911–1917, 1979.

[42] H.V. Allen, S.C. Terry, and D.W. De Bruin. Accelerometer systems with built-in testing. *Sensors and Actuators: A. Physical*, 21(1-3):381–386, 1990.

[43] A. D'Alessandro and G. D'Anna. Suitability of low-cost three-axis MEMS accelerometers in strong-motion seismology: tests on the LIS331DLH (iPhone) accelerometer. *Bulletin of the Seismological Society of America*, 103(5):2906–2913, 2013.

[44] B. J. (Sandia National Laboratories) Merchant. MEMS applications in seismology. In *Seismic Instrumentation Technology Symposium*, 2009.

[45] Required Specifications. Market Opportunities for Advanced MEMS Accelerometers and Overview of Actual Capabilities I1. (figure 2):78–82, 2000.

[46] M.S Hons and R.R Stewart. Could MEMS-based accelerometers be used for gravity surveys. Technical report, 2008.

[47] Tim Niebauer. Private communication, 2014.

[48] H Rim and Y Li. Advantages of borehole vector gravity in density imaging. *Geophysics*, 80(1):G1–G13, 2015.

[49] A.C. Watts, V.G. Ambrosia, and E.A. Hinkley. Unmanned aircraft systems in remote sensing and scientific research: Classification and considerations of use. *Remote Sensing*, 4(6):1671–1692, 2012.

[50] P. Bauer-Gottwein, L. Christiansen, and D.A.N. Rosbjerg. Informing hydrological models with ground-based time-lapse relative gravimetry: potential and limitations. In *GRACE, Remote Sensing and Ground-based Methods in Multi-Scale Hydrology (Proceedings of Symposium J-H01)*, pages 187–194, 2011.

[51] D.K. Butler. Microgravimetric and gravity gradient techniques for detection of subsurface cavities. *Geophysics*, 49(7):1084 – 1096, 1984.

[52] A.J. Romaides, J.C. Battis, R.W. Sands, A. Zorn, D.O. Benson, and D.J. DiFrancesco. A comparison of gravimetric techniques for measuring subsurface void signals. *Journal of Physics D: Applied Physics*, 34(3):433–443, 2001.

[53] B. Kirkendall, Y. Li, and D. Oldenburg. Imaging cargo containers using gravity gradiometry. *IEEE Transactions on Geoscience and Remote Sensing*, 45(6):1786–1797, 2007.

[54] S.S-M. Aparicio, J.A. Sampedro, F.G. Montesinos, and J. Molist. Volcanic signatures in time gravity variations during the volcanic unrest on El Hierro (Canary Islands). *Journal of Geophysical Research: Solid Earth*, 119(6):5033–5051, 2014.

[55] M. Battaglia, J. Gottsmann, D. Carbone, and J. Fernandez. 4D volcano gravimetry. *Geophysics*, 73(6):WA3–WA18, 2008.

[56] H. Rymer, G. Williams-Jones, and M. Keynes. Gravity and deformation measurements. *Geophysical Research Letters*, 27(16):2389–2392, 2000.

[57] P.J. Baxter and A. Gresham. Deaths and injuries in the eruption of Galeras volcano, Colombia, 14 January 1993. *Journal of Volcanology and Geothermal Research*, 77(1-4):325–338, 1997.

[58] M.S. Hons and R.R. Stewart. Transfer functions of geophones and accelerometers and their effects on frequency content and wavelets. *CREWES Research Report*, 18(1), 2006.

[59] W. Lowrie. *Fundamentals of Geophysics*. Cambridge University Press, Cambridge, 1st edition, 1997.

[60] C. L. Liner. *Elements of Seismic Dispersion: A Somewhat Practical Guide to Frequency-dependent Phenomena*. Society of Exploration Geophysicists, 1st edition, 2012.

[61] D. Mougenot. Pushing toward the low frequencies. *World Oil*, September:25–28, 2005.

[62] S. Rosat, M. Calvo, J. Hinderer, U. Riccardi, J. Arnoso, and W. Zürn. Comparison of the performances of different spring and superconducting gravimeters and STS-2 seismometer at the Gravimetric Observatory of Strasbourg, France. *Studia Geophysica et Geodaetica*, 59(1):58–82, 2014.

[63] H. Kumagai, T. Ohminato, M. Nakano, M. Ooi, A. Kubo, H. Inoue, and J. Oikawa. Very-long-period seismic signals and caldera formation at Miyake Island, Japan. *Science*, 293(5530):687–690, 2001.

[64] Z. Jiang, V. Pálinkáš, O. Francis, S. Merlet, H. Baumann, M. Becker, P. Jousset, J. Mäkinen, H. R. Schulz, K. U. Kessler-Schulz, S. Svitlov, A. Coulomb, L. Tisserand, H. Hu, and Ch. Rothleitner. Accurate gravimetry at the BIPM Watt balance site. In *Earth on the Edge: Science for a Sustainable Panet, International Association of Geodesy Symposia*, pages 371–375, 2011.

[65] W.T. Pike, S. Calcutt, I.M. Standley, A.G. Mukherjee, J. Temple, T. Warren, C. Charalambous, H. Liu, A. Stott, and J.B. McClean. A silicon seismic package (SSP) for planetary geophysics. In *47th Lunar and Planetary Science Conference*, page 2081, 2016.

[66] J. Lainé and D. Mougenot. A high-sensitivity MEMS-based accelerometer. *The Leading Edge*, 33(11):1234–1242, 2014.

[67] U. Riccardi, S. Rosat, and J. Hinderer. Comparison of the Micro-g LaCoste gPhone-054 spring gravimeter and the GWR-C026 superconducting gravimeter in Strasbourg (France) using a 300-day time series. *Metrologia*, 48(1):28–39, 2011.

[68] U. Krishnamoorthy, R.H. Olsson, G.R. Bogart, M.S. Baker, D.W. Carr, T.P. Swiler, and P.J. Clews. In-plane MEMS-based nano-g accelerometer with sub-wavelength optical resonant sensor. *Sensors and Actuators A*, 145-146:283–290, 2008.

[69] J. C. McLaughlin and A. F. W. Willoughby. Fracture of silicon wafers. *Journal of Crystal Growth*, 85(1-2):83–90, 1987.

[70] A.V. Cumming, L. Cunningham, G.D. Hammond, K. Haughian, J. Hough, S. Kroker, I.W. Martin, R. Nawrodt, S. Rowan, C. Schwarz, and A.A. van Veggel. Silicon mirror suspensions for gravitational wave detectors. *Classical and Quantum Gravity*, 31(2):025017, 2014.

[71] T. M. Niebauer. "Double pendulum gravimeter and method of measuring gravity using the same", US patent number: US9291742 B2, 2016.

[72] D. J. R. Aliod, T. M. Niebauer, and H. Siegol. "Method and apparatus for measurements of gravity in small diameter boreholes", US patent publication number: US 2008/0295594 A1, 2008.

[73] G. Cagnoli, H. Armandula, C. A. Cantley, D. R. M. Crooks, and A. Cumming. Silica suspension and coating developments for Advanced LIGO. *Journal of Physics: Conference Series*, 32:386–392, 2006.

[74] A. M. Fitzgerald, R. H. Dauskardt, and T. W. Kenny. Fracture toughness and crack growth phenomena of plasma-etched single crystal silicon. *Sensors and Actuators, A: Physical*, 83(1):194–199, 2000.

[75] D. A. Porter. *Die Separation Strength for Deep Reactive Ion Etched Wafers*. PhD thesis, 2010.

[76] A. M. Fitzgerald. MEMS structural reliability and DRIE: how are they related? *A M Fitzgerald-Tegal Collaboration Technical Report*, 2010.

[77] M. Tariq Jan, N. Hisham Bin Hamid, M. H. Md Khir, K. Ashraf, and M. Shoaib. Reliability and fatigue analysis in cantilever-based MEMS devices operating in harsh environments. *Journal of Quality and Reliability Engineering*, 2014, 2014.

[78] J. Winterflood, T. Barber, and D.G. Blair. Using Euler buckling springs for vibration isolation. *Classical and Quantum Gravity*, 19(October):1639–1645, 2002.

[79] J. Winterflood, T.A. Barber, and D.G. Blair. Mathematical analysis of an Euler spring vibration isolator. *Physics Letters A*, 300(July):131–139, 2002.

[80] J. Winterflood and D.G. Blair. A long-period vertical vibration isolator for gravitational wave detection. *Physics Letters A*, 243(June):1–6, 1998.

[81] R.A. Ibrahim. Recent advances in nonlinear passive vibration isolators. *Journal of Sound and Vibration*, 314:371–452, 2008.

[82] A. Bertolini, G. Cella, R. Desalvo, and V. Sannibale. Seismic noise filters, vertical resonance frequency reduction with geometric anti-springs : a feasibility study. *Nuclear Instruments and Methods in Physics Research A*, 435(3):475–483, 1999.

[83] G. Cella, R. DeSalvo, V. Sannibale, H. Tariq, N. Viboud, and A. Takamori. Seismic attenuation performance of the first prototype of a geometric anti-spring filter. *Nuclear Instruments and Methods in Physics Research A*, 487(3):652–660, 2002.

[84] F Acernese et. al. The advanced virgo detector. *Journal of Physics: Conference Series*, 610:012014, 2015.

[85] F. Laermer and A. Schilp. "Method of anisotropic etching of silicon", US patent number: 5,501,893, 1996.

[86] E.I. Galperin. Azimuthal method of seismic observations. *Gostoptechizdat, Moscow*, 80, 1955.

[87] B. S. Kirkpatrick and Melton B. M. The symmetrical triaxial seismometer - its design for application to long-period seismometry by. *Bulletin of the Seismological Society of America*, 60(3):717–739, 1970.

[88] MicroChemicals. HDMS datasheet webpage. *http://www.microchemicals.com/ products/adhesion_promotion/hmds.html (Date Accessed: 01/05/16)*, 2016.

[89] K.R. Williams, K. Gupta, and M. Wasilik. Etch rates for micromachining processing - part II. *Journal of Microelectromechanical Systems*, 12(6):761–778, 2003.

[90] N. Wilke, A. Mulcahy, S.R. Ye, and A. Morrissey. Process optimization and characterization of silicon microneedles fabricated by wet etch technology. *Microelectronics Journal*, 36(7):650–656, 2005.

[91] W.T Pike. Analysis of sidewall quality in through-wafer deep reactive-ion etching. *Microelectronic Engineering*, 73-74:340–345, 2004.

[92] I.H. Jafri, H. Busta, and S.T. Walsh. Critical point drying and cleaning for MEMS technology. *Symposium on Micromachining and Microfabrication (International Society for Optics and Photonics)*, pages (pp. 51–58), 1999.

[93] J. Fraden. *Handbook of Modern Sensors: Physics, Designs, and Applications*. Springer, New York, 5th edition, 2016.

[94] Shuangshuang Zhao, Juan Zhang, Changlun Hou, Jian Bai, and Guoguang Yang. Optical accelerometer based on grating interferometer with phase modulation technique. *Applied Optics*, 51(29):7005, 2012.

[95] Bianca E. Keeler, Gregory R. Bogart, and Dustin W. Carr. Laterally deformable optical NEMS grating transducers for inertial sensing applications. *Proceedings of SPIE*, 5592:306–312, 2005.

[96] J. Courtial. Wavetrace software package. *(University of Glasgow)*, 2012.

[97] L. Carbone, S.M. Aston, R.M. Cutler, A. Freise, J. Greenhalgh, J. Heefner, D. Hoyland, N.A. Lockerbie, D. Lodhia, N.A. Robertson, C.C. Speake, K.A. Strain, and A. Vecchio. Sensors and actuators for the Advanced LIGO mirror suspensions. *Classical and Quantum Gravity*, 29(11):115005, 2012.

[98] L. Carbone. Private communication. *ASR Group, University of Birmingham*, 2013.

[99] M. Dutta and M. A. Stroscio. *Advances in Semiconductor Lasers and Applications to Optoelectronics.* World Scientific Publishing Co. Pte. Ltd., Singapore, 1st edition, 2000.

[100] Datasheet for LED631E Ultra Bright Red LED. *Thorlabs Ltd.*, pages 1–10, 2009.

[101] N A Lockerbie and K V Tokmakov. A 'Violin-Mode' shadow sensor for interferometric gravitational wave detectors. *Measurement Science and Technology*, 25(12):125110, 2014.

[102] Hamamatsu Photonics. *Opto-semiconductor handbook*. Hamamatsu Photonics, Hamamatsu City, 1st edition, 2014.

[103] W. Jung. *Op Amp Applications Handbook*. Newnes, Oxford and Boston, 1st edition, 2005.

[104] D. Reay. *Digital Signal Processing and Applications with the OMAP-L138 eXperimeter*. Wiley, Hoboken, New Jersey, 1st edition, 2012.

[105] J.B. Johnson. Thermal agitation of electricity in conductors. *Physical Review*, 32(1):97–109, 1928.

[106] H. Nyquist. Thermal agitation of electric charge in conductors. *Physical Review*, 32(1):110–113, 1928.

[107] R. Mancini (Editor-in-Chief). *Op Amps For Everyone: Design Reference*. Newnes, Burlington, MA, 1st edition, 2003.

[108] B. Schiek, I. Rolfes, and H-J. Siweris. *Noise in High-Frequency Circuits and Oscillators*. Wiley-Interscience, Hoboken, New Jersey, 1st edition, 2006.

[109] Datasheet for Model SR570 Low-Noise Preamplifier. *Stanford Research Systems*, pages 1–54, 2005.

[110] Datasheet for Lock-In-Amplifier Module LIA-MV-L. *FEMTO Messtechnik GmbH*, pages 1–10.

[111] J.H. Scofield. Frequency-domain description of a lock-in amplifier. *American Journal of Physics*, 62(2):129, 1994.

[112] C.J. Bell, S. Reid, and J. Faller. Experimental results for nulling the effective thermal expansion coefficient of fused silica fibres under a static stress. *Classical and Quantum Gravity*, 31:065010, 2014.

[113] J. F. O'Hanlon. *A User's Guide to Vacuum Technology*. Wiley, Hoboken, New Jersey, 3rd edition, 2005.

[114] S. Muthu, F.J. Schuurmans, and M.D. Pashley. Red, green, and blue LED based white light generation: issues and control. *Conference Record of the 2002 IEEE Industry Applications Conference. 37th IAS Annual Meeting (Cat. No.02CH37344)*, 1:327–333, 2002.

[115] A. Kitai. *Principles of Solar Cells, LEDs and Diodes*. John Wiley and Sons, Ltd., Chichester, 1st edition, 2011.

[116] G. Dz-Hung. "Ultra Precision and Reliable Bonding Method", US Patent No. US 6284085 B1, 2001.

[117] H.B. Callen and T.A. Welton. Irreversibility and generalized noise. *Physical Review*, 83(1):34–40, 1951.

[118] K. Yamamoto. *Study of the Thermal Noise Caused By Inhomogeneously Distributed Loss*. PhD thesis, University of Tokyo, 2000.

[119] K. Craig. *Studies of the mechanical dissipation of thin films for mirrors in interferometric gravitational wave detectors*. PhD thesis, University of Glasgow, 2015.

[120] E.J. Chin, K.T. Lee, J. Winterflood, L. Ju, and D.G. Blair. Low frequency vertical geometric anti-spring vibration isolators. *Physics Letters A*, 336(2-3):97–105, 2005.

[121] H. Watanabe, N. Yamada, and M. Okaji. Linear thermal expansion coefficient of silicon from 293 to 1000 K. *International Journal of Thermophysics*, 25(1):221–236, 2004.

[122] O.A. Bauchau and J.I. Craig. Euler-Bernoulli beam theory. *Structural Analysis*, pages 173–221, 2009.

[123] M.A. Poggi, A.W. McFarland, J.S. Colton, and L.A. Bottomley. A method for calculating the spring constant of atomic force microscopy cantilevers with a nonrectangular cross section. *Analytical Chemistry*, 77(4):1192–1195, 2005.

[124] C.H. Cho. Characterization of Young's modulus of silicon versus temperature using a "beam deflection" method with a four-point bending fixture. *Current Applied Physics*, 9(2):538–545, 2009.

[125] K.J.H. Åström. *Advanced PID Control*. The Instrumentation, Systems, and Automation Society, North Carolina, 1st edition, 2006.

[126] J. B. Ramsey. Tests for specification errors in classical linear least-squares regression analysis. *Journal of the Royal Statistical Society Series B (Methodological)*, 31(2):350–371, 1969.

[127] A-M. Legendre. *Nouvelles méthodes pour la détermination des orbites des comètes*. Firmin Didot, Paris, 1st edition, 1805.

[128] D.N. Gujarati. *Basic Econometrics*. McGraw-Hill, New York, 4th edition, 2004.

[129] W. Mendenhall, R. J. Beaver, and B. M. Beaver. *Introduction to Probability and Statistics*. Brooks/Cole, Belmont, 13th edition, 2009.

[130] G. J. Lloyd and R. J. McElroy. On the anelastic contribution to creep. *Acta Metallurgica*, 22, 1974.

[131] H.H. Essen, F. Kruger, T. Dahm, and I. Grevemeyer. On the generation of secondary microseisms observed in northern and central Europe. *Journal of Geophysical Research*, 108(B10):2506–2520, 2003.

[132] A. Effler, R.M.S. Schofield, V.V. Frolov, G. Gonzalez, K. Kawabe, J.R. Smith, J. Birch, and R. McCarthy. Environmental influences on the LIGO gravitational wave detectors during the 6th science run. *Classical and Quantum Gravity*, 32(3):035017, 2015.

[133] D.W. Allan. Statistics of atomic frequency standards. In *Proceedings of the IEEE*, volume 54, pages 221–230, 1966.

[134] J.E. Gray and D.W. Allan. A Method for estimating the frequency stability of an individual oscillator. *28th Annual Symposium on Frequency Control*, pages 243–246, 1974.

[135] D. W. Allan, N. Ashby, and C. C. Hodge. The science of timekeeping. *Hewlett Packard application note 1289*, pages 1–88, 1997.

[136] R. L. Lyman. *An Introduction to Statistical Methods and Data Analysis*. Brooks/Cole, Boston, 6th edition, 2010.

[137] J. Peterson. Observations and modeling of seismic background noise. *U.S. Geological Survey. Open-File Report*, pages 93–322, 1993.

[138] V.R. Almeida, C.A. Barrios, R.R. Panepucci, and M. Lipson. All-optical control of light on a silicon chip. *Nature*, 431(October):1081–1084, 2004.

[139] A.A. Michelson and E.W. Moreley. On the relative motion of the Earth and the luminiferous ether. *American Journal of Science*, 36(203):333–345, 1887.

[140] J.H. Apfel. Phase retardance of periodic multilayer mirrors. *Applied optics*, 21(4):733–8, 1982.

[141] Y. Akihama and K. Hane. Single and multiple optical switches that use freestanding silicon nanowire waveguide couplers. *Light: Science & Applications*, 1(May):e16, 2012.

[142] W.H.P. Pernice, Mo. Li, and H.X. Tang. Broadband all-photonic transduction of nanocantilevers. *Nature nanotechnology*, 4(6):377–82, 2009.

[143] D. Haronian. Displacement sensing using geometrical modulation in reflection mode (GM-RM) of coupled optical waveguides. *Journal of Micromechanics and Microengineering*, 8(4):323–326, 1999.

[144] C. Sun. Multiplexing of fiber-optic acoustic sensors in a Michelson interferometer configuration. *Optics letters*, 28(12):1001–1003, 2003.

[145] G. Sagnac. L'ether lumineux demontre par l'effet du vent relatif d'ether dans un interferometre en rotation uniforme. *Comptes Rendus de l'Académie des Sciences*, 157:708–710, 1913.

[146] J. Scheuer and A. Yariv. Sagnac effect in coupled-resonator slow-light waveguide structures. *Physical Review Letters*, 96(5):1–4, 2006.

[147] V. Kemp. *Inertial MEMS Principles and Practice*. Cambridge University Press, Cambridge, 1st edition, 2011.

[148] Zhu Li, Wen Wu, Pan Zheng, Jin Liu, Ji Fan, and Liang Tu. Novel capacitive sensing system design of a microelectromechanical systems accelerometer for gravity measurement applications. *Micromachines*, 7(9):167, 2016.

[149] P. Campsie, G.D. Hammond, R.P. Middlemiss, D.J. Paul, and A. Samarelli. "Measurement of Acceleration", PCT Patent Application Number: PCT/EP2015/069572, Publication Number: WO2016030435 A1, 2016.

Appendix A

Commonly Used Gravity Units

The units used to quantify gravitational acceleration are various. In this thesis units of *Gal* (or more specifically μGal) will generally be used to quantify gravitational acceleration. This is not an S.I unit (1 Gal is equivalent to 1cms^{-2}), but it is widely used by the geophysics community. Another commonly used unit is 'g', where 1g = 9.81 ms^{-2}. Since acceleration sensitivity can be different at different frequencies, device sensitivity is most commonly quoted in units of acceleration/$\sqrt{Hz}$. In other words, this is the acceleration sensitivity in an integration time of 1 second.

The gravity gradient has components given in units of s^{-2}. Also used is the Eötvös. Tables A.1 and A.2 below show conversions between these different units.

Table A.1 Gravitational Acceleration Unit Conversions

Gal	SI	g
1000 Gal	10 m s^{-2}	1 g
100 Gal	1 m s^{-2}	10^{-1} g
10 Gal	10^{-1} m s^{-2}	10^{-2} g
1 Gal	10^{-2} m s^{-2}	10^{-3} g
10^{-1} Gal	10^{-3} m s^{-2}	10^{-4} g
10^{-2} Gal	10^{-4} m s^{-2}	10^{-5} g
10^{-3} Gal	10^{-5} m s^{-2}	10^{-6} g
10^{-4} Gal	10^{-6} m s^{-2}	10^{-7} g
10^{-5} Gal	10^{-7} m s^{-2}	10^{-8} g
10^{-6} Gal	10^{-8} m s^{-2}	10^{-9} g
10^{-7} Gal	10^{-9} m s^{-2}	10^{-10} g
10^{-8} Gal	10^{-10} m s^{-2}	10^{-11} g
10^{-9} Gal	10^{-11} m s^{-2}	10^{-12} g

Table A.2 Gravity Gradient Unit Conversions

Eötvös	SI	Gal
1 E	10^{-9} s^{-2}	0.1 μGal m^{-1}

Appendix B

ANSYS Finite Element Analysis Modelling

ANSYS is a finite element analysis (FEA) software. Finite element analysis modelling is a numerical process used to solve complex dynamic systems. It does so by breaking down the system into smaller and smaller elements, solving partial differential equations for each element to give an overall solution to the initial problem. The modelling was carried out on ANSYS WORKBENCH software versions 14 - 17. An FEA model was required because the complexity of the asymmetric geometrical anti-spring would have been incredibly challenging to model analytically. A brief synopsis of how the FEA results were found is included below.

Figure B.1 shows the project outline of the MEMS gravimeter FEA model. The model is created by opening a static structural analysis module. This module can be dragged from the bar on the left hand side of the screen and is the far left module in the main window. In the static structural module the basic model is created. Firstly, the geometry is drawn, this can be observed in figure B.2. In this module the engineering data is also defined i.e. the physical characteristics of the material – the material used, its young's modulus, it's crystal structure etc. Many materials are already saved in the system so these characteristics mostly do not need to be entered manually. As well as the engineering data, the magnitude and direction of the acceleration that the object is exposed to can also be defined. This can be used to simulate the effect of the gravitational acceleration at the Earth's surface. Finally, the 'mesh' of the model needs to be solved. The mesh defines the distribution and density of the elements. The denser the mesh, the more realistic the model but the longer it will take to solve. Different densities can be used for different areas of the model. For the case of the

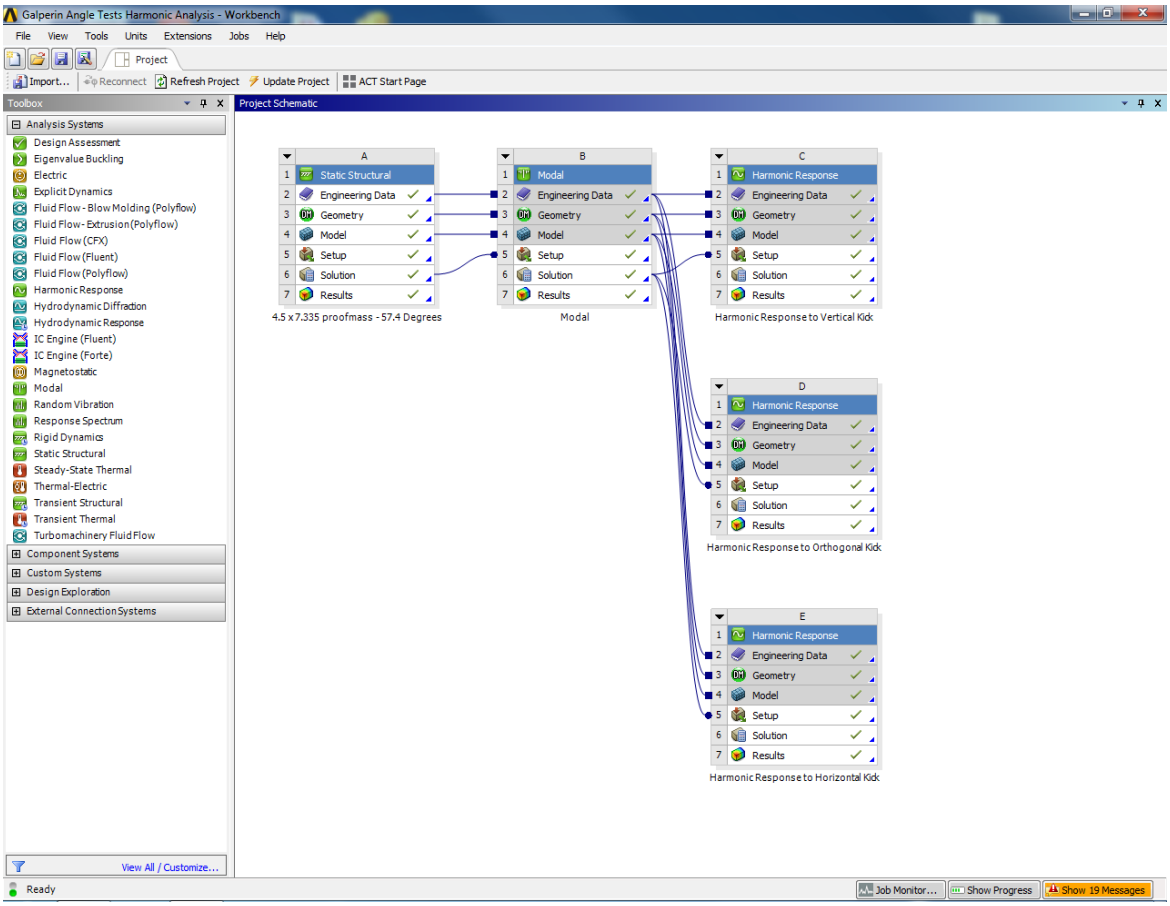

Fig. B.1 The project window of the ANSYS file in which the static structural, modal, and harmonic analysis modules can be selected.

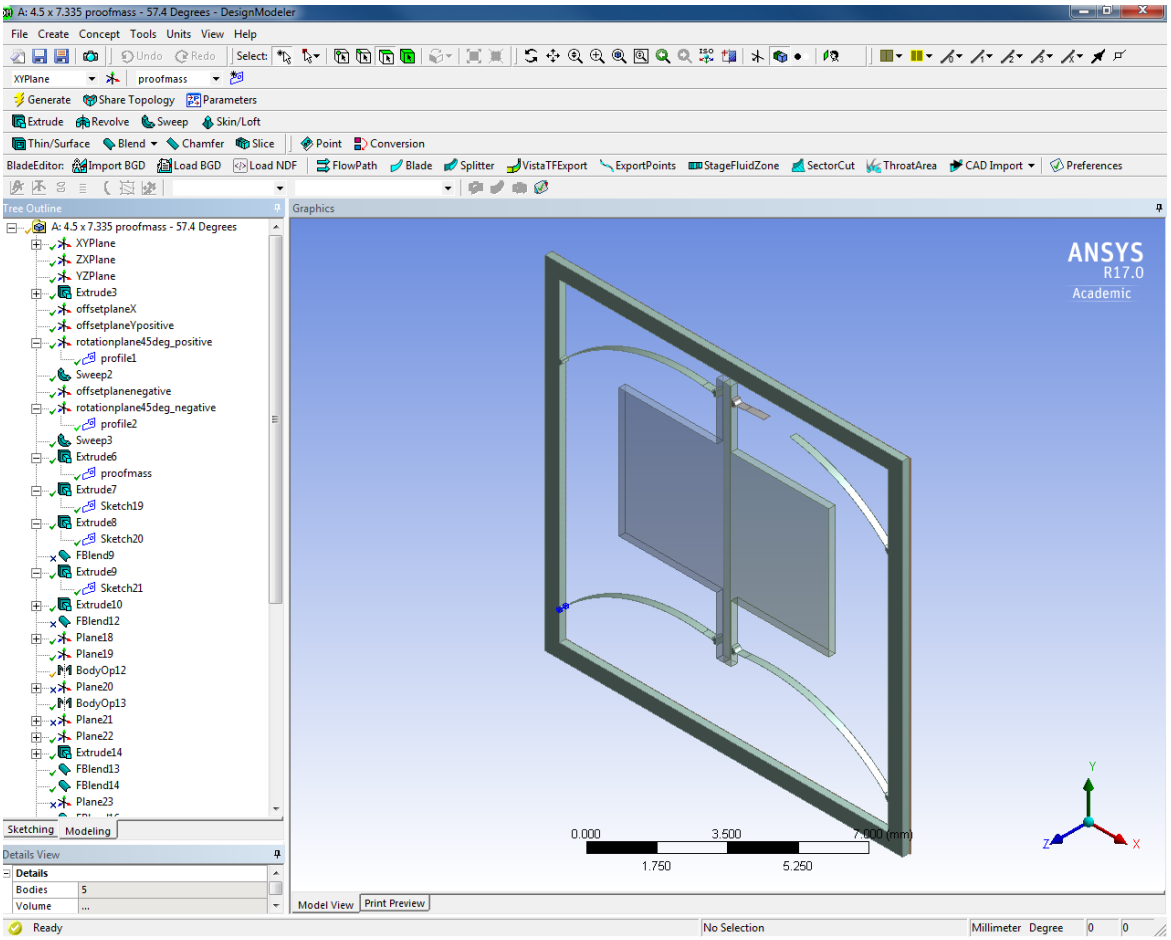

Fig. B.2 The static structural window in which the geometry of the design can be drawn.

MEMS gravimeter, it is much more important to have a dense mesh over the flexures than the proof mass or frame.

Once the static structural model has been configured, it can then be solved. The aim of the solution is to observe how the proof mass displaces when exposed to a uniform acceleration. In incremental time steps, ANSYS attempts to solve the boundary conditions of the partial differential equations for each element. If it succeeds, it steps forward and attempts to solve the equations for the next time increment. If it fails, it tries to solve again but with a smaller time increment. This process continues until the solution either fails to solve or reaches a time of 1 second. If the model has solved, then the x, y and z displacement for every element in the model is known.

The static structural model only gives information about the displacement of the elements. It does not give any information about the modes of oscillation of the system. For that, a modal analysis module needs to be dragged into the project outline window. This module

uses all of the information used to create the static structural model, and the results that the static structural model outputs. The modal model can then be used to observe the harmonics of the structure. For the MEMS gravimeter we are most concerned with the frequency of the first mode. This mode is oscillation of the proof mass along its sensitive access. There ins't a limit to the number of modes that can be calculated, although their significance decreases as the order of the mode increases. As can be observed in figure 2.6, only the first 6 modes were calculated for the MEMS gravimeter. To model the effect of the Earth tides on the MEMS device, a harmonic analysis needed to be incorporated into the model. A harmonic analysis module was therefore dragged into the project window. Here the acceleration could programmed to oscillate with the same period and magnitude as the Earth tides. Once this was implemented, the relative displacement of the MEMS could be measured as the acceleration changed.

Appendix C

MATLAB Code for Gravity Data Analysis

This appendix contains a copy of the MATLAB file that was used to process the data presented in chapter 5 of this thesis. The code is commented but a rough outline is as follows:

- It starts by reading in the three data files and interpolating the time series where necessary so that all data sets can be plotted on the same axis.
- It then plots the temperature variations for all of the recorded temperatures.
- A regression is then performed against chosen parameters to remove any correlated trends between these parameters and the experimental data.
- Figure 3 is a plot of the regression fit, followed by the data with this fit removed.
- Figure 4 plots the experimental data from the previous lower subplot, and also plots the theoretical tide data next to this.
- Figure 5 is a histogram of 10,000 randomised experimental data sets, this is used to calculated the significance of the correlation between theory and experimental data.
- Figure 6 is a plot of all of the regressed parameters.
- Figure 7 is the Allan deviation of the data.
- Figure 8 a plot of the power spectral density of the data.
- To get the full, unsmoothed data, 'down' must be set to 1, and 'NSG' set to 2. Other values of NSG remove various different correlations.

```
% read data
format long e
clear all

'****************************'

offcorr=0;
driftcorr=0;

% v1 Time
% v2 Plate
% v3 LED
% v4 MEMS
% v5 Shield
% v6 outside can
% v7 data
% v8 PD

% number of parameter to regress
% 1=T1,T2,T3,T4,off
% 2=T1,T2,T3,T4,off,lin
% 3=T1,T2,T3,T4,off,Tides
% 4=T1,T2,T3,T4,off,Tides,lin


Nreg=2;
Ns=1;

%smooth=1, no smooth=0
smth=1;

%Calibration Correction Factor: (the higher, the smaller the amplitude)
fac=1.3

% tide smoothing (always on) (average data) (600 for ten min sampling)
Nsg=1;

%resample data
down=10;

DOY=69;

download=datenum(2015,3,22,10,03,00)

tidedata=datenum(2015,3,10,00,00,00)

%download=datenum(2015,2,6,11,11,00)
%datenum(now);

% Read in data files
%fid1=fopen('overnight_temp_old.txt');
fid1=fopen('overnight_temp.txt');
variable1 = textscan(fid1,'%f32 %f32 %f32 %f32 %f32 %f32 %f32 %f32');
fclose(fid1);
```

```
Nstart=10100;
Nend=length(variable1{1})-11360;

fid2=fopen('Tidal_Correction_10Mar_15days.txt');
variable2 = textscan(fid2,'%f32 %f32 %f32:%f32:%f32 %f32 %f32 %f32');
fclose(fid2);
tide_t=(variable2{2}'+(variable2{3}'+(variable2{4}'/60))/24)-DOY;
tide_amp=variable2{8}';


cal=96500*fac

v1=variable1{1}';
v2=variable1{2}';
v3=variable1{3}';
v4=variable1{4}';
v5=variable1{5}';
v6=variable1{6}';
v7=variable1{7}';
v8=variable1{8}';


tau=0;

t_data=v1(Nstart:Nend);

% time of download
tinitial=double(datenum(download)-v1(length(v1))/86400);
starttime=datestr(tinitial);
tt_in=datevec(tinitial);

hh=tt_in(4);
mm=tt_in(5);
ss=tt_in(6);

prog_start=(hh+mm/60+ss/3600)/24

datastart=datestr(double(tinitial+v1(Nstart)/86400));
dat_in=datevec(datastart);

% date offset for tide plotting (value is integerised)
date_offset=floor(datenum(dat_in)-tidedata);


hh_data=dat_in(4);
mm_data=dat_in(5);
ss_data=dat_in(6);

data_start=(hh_data+mm_data/60+ss_data/3600)/24;

t_data=(t_data-t_data(1))/86400+data_start;
```

```
t_data=t_data+date_offset;

y_data=v7(Nstart+tau:Nend+tau);
y_data=(y_data-mean(y_data))./cal;

t_ds=downsample(t_data,down);

T1=v4(Nstart:Nend);
mean_T1=mean(T1);
T1=T1-mean_T1;

T2=v3(Nstart:Nend);
mean_T2=mean(T2);
T2=T2-mean_T2;

T3=v6(Nstart:Nend);
mean_T3=mean(T3);
T3=T3-mean_T3;

T4=v5(Nstart:Nend);
mean_T4=mean(T4);
T4=T4-mean_T4;

T5=v2(Nstart:Nend);
mean_T5=mean(T5);
T5=T5-mean_T5;

PD=v8(Nstart:Nend);
mean_PD=mean(PD);
PD=PD-mean_PD;

if smth==1
T1s=smooth(T1,Ns)';
T2s=smooth(T2,Ns)';
T3s=smooth(T3,Ns)';
T4s=smooth(T4,Ns)';
T5s=smooth(T5,Ns)';
PDs=smooth(PD,Ns)';

else
T1s=T1;
T2s=T2;
T3s=T3;
T4s=T4;
T5s=T5;
PDs=PD;

end
y_datas=y_data;

T1_ds=downsample(T1s,down);
T2_ds=downsample(T2s,down);
T3_ds=downsample(T3s,down);
T4_ds=downsample(T4s,down);
T5_ds=downsample(T5s,down);
```

```
PD_ds=downsample(PDs,down);
y_data_ds=downsample(y_datas,down);

figure(1)
plot(t_ds,T1_ds,'k')
hold on
plot(t_ds,T2_ds,'r')
hold on
plot(t_ds,T3_ds,'b')
hold on
plot(t_ds,T4_ds,'g')
%legend ('MEMS', 'Shield')
legend ('MEMS','LED', 'Outside', 'Shield')
    ylabel('Temperature Variation( ^oC)')
    xlabel('Calendar Date (DD/M/YY)')



% interpolate tide data

tsig=interp1(tide_t,tide_amp,t_ds);

%tsig=tsig(Nstart:Nend);
if smth==1
signal=smooth(tsig,Ns)';
else
signal=tsig;
end

signal_ds=downsample(signal,down);


ntot=length(y_data_ds);
refine=1e-5;

d_lambda=refine;

[row,col] = find(d_lambda);

% starting parameters

%offset
off1=0;
%drift1 (linear)
off2=0;
%drift1 (poly 2nd order)
off3=0;




%%%%%%%%%%%%%%%%%%%%%%%%%%%%%%%%%%%%%%%%%%%%%%%%%%%%%%%%%%%%%%%%%%%%%%%%%%%%%%%%
```

```
if Nreg==1
ampT1=0.01;
ampT2=0.01;
ampT3=0.01;
ampT4=0.01;

b=[off1 off2 ampT1 ampT2 ampT3 ampT4];

ntot
count=0;
for i=1:ntot
y(i)=off1+off2*t_ds(i)+ampT1*T1_ds(i)+ampT2*T2_ds(i)+ampT3*T3_ds(i)+ampT4*T4_
ds(i);
d_beta(i)=y_data_ds(i)-y(i);
df_d0(i)=1;
df_d1(i)=t_ds(i);
df_d2(i)=T1_ds(i);
df_d3(i)=T2_ds(i);
df_d4(i)=T3_ds(i);
df_d5(i)=T4_ds(i);
count=count+1;
end

al=['df_d0 :';'df_d1 :'; 'df_d2 :';'df_d3 :'; 'df_d4 :'; 'df_d5 :';];
Xd=[df_d0; df_d1; df_d2; df_d3; df_d4; df_d5; y_data_ds];
P=mregg(Xd,0,0,al);

%%%%%%%%%%%%%%%%%%%%%%%%%%%%%%%%%%%%%%%%%%%%%%%%%%%%%%%%%%%%%%%%%%%%%%%%%%%%

elseif Nreg==2
ampT1=0.01;
ampT2=0.01;
ampT3=0.01;
ampT4=0.01;

b=[off1 off2 ampT1 ampT2 ampT3 ampT4];

ntot
count=0;
for i=1:ntot
y(i)=off1+off2*t_ds(i)+ampT1*T1_ds(i)+ampT2*T2_ds(i)+ampT3*T3_ds(i)+ampT4*T4_
ds(i);
d_beta(i)=y_data_ds(i)-y(i);
df_d0(i)=1;
df_d1(i)=t_ds(i);
df_d2(i)=T1_ds(i);
df_d3(i)=T2_ds(i);
df_d4(i)=T3_ds(i);
df_d5(i)=T4_ds(i);
count=count+1;
end

al=['df_d0 :';'df_d1 :'; 'df_d2 :';'df_d3 :'; 'df_d4 :'; 'df_d5 :';];
Xd=[df_d0; df_d1; df_d2; df_d3; df_d4; df_d5; y_data_ds];
P=mregg(Xd,0,0,al);
```

```
%%%%%%%%%%%%%%%%%%%%%%%%%%%%%%%%%%%%%%%%%%%%%%%%%%%%%%%%%%%%%%%%%%%%%%%%%%%%%%%%

elseif Nreg==3
ampT1=0.01;
ampT2=0.01;
ampT3=0.01;
ampT4=0.01;
ampsignal=0.01

b=[off1 off2 ampT1 ampT2 ampT3 ampT4 ampsignal];

ntot
count=0;
for i=1:ntot
y(i)=off1+off2*t_ds(i)+ampT1*T1_ds(i)+ampT2*T2_ds(i)+ampT3*T3_ds(i)+ampT4*T4_
ds(i)+ampsignal*signal(i);
d_beta(i)=y_data_ds(i)-y(i);
df_d0(i)=1;
df_d1(i)=t_ds(i);
df_d2(i)=T1_ds(i);
df_d3(i)=T2_ds(i);
df_d4(i)=T3_ds(i);
df_d5(i)=T4_ds(i);
df_d6(i)=signal(i);
count=count+1;
end

al=['df_d0 :';'df_d1 :'; 'df_d2 :';'df_d3 :'; 'df_d4 :'; 'df_d5 :'; 'df_d6
:';];
Xd=[df_d0; df_d1; df_d2; df_d3; df_d4; df_d5; df_d6; y_data_ds];
P=mregg(Xd,0,0,al);
%%%%%%%%%%%%%%%%%%%%%%%%%%%%%%%%%%%%%%%%%%%%%%%%%%%%%%%%%%%%%%%%%%%%%%%%%%%%%%%%

elseif Nreg==4
ampT1=0.01;
ampT2=0.01;
ampT3=0.01;
ampT4=0.01;
ampsignal=0.01

b=[off1 off2 ampT1 ampT2 ampT3 ampT4 ampsignal];

ntot
count=0;
for i=1:ntot
y(i)=off1+off2*t_ds(i)+ampT1*T1_ds(i)+ampT2*T2_ds(i)+ampT3*T3_ds(i)+ampT4*T4_
ds(i)+ampsignal*signal(i);
d_beta(i)=y_data_ds(i)-y(i);
df_d0(i)=1;
df_d1(i)=t_ds(i);
df_d2(i)=T1_ds(i);
df_d3(i)=T2_ds(i);
df_d4(i)=T3_ds(i);
```

```
df_d5(i)=T4_ds(i);
df_d6(i)=signal(i);
count=count+1;
end

al=['df_d0 :';'df_d1 :'; 'df_d2 :';'df_d3 :'; 'df_d4 :'; 'df_d5 :'; 'df_d6
:';];
Xd=[df_d0; df_d1; df_d2; df_d3; df_d4; df_d5; df_d6; y_data_ds];
P=mregg(Xd,0,0,al);
%%%%%%%%%%%%%%%%%%%%%%%%%%%%%%%%%%%%%%%%%%%%%%%%%%%%%%%%%%%%%%%%%%%%%%%%

else
'wrong number'
end


initial=1;

S=sum(initial)^2;

u=ones(1,ntot);

if Nreg==1
y_fit=(P(1)+offcorr)+(P(2)+driftcorr).*t_ds+P(3).*T1_ds+P(4).*T2_ds+P(5).*T3_
ds+P(6).*T4_ds;

elseif Nreg==2
y_fit   =   (P(1)+offcorr)   +   (P(2)+driftcorr).*t_ds   +   P(3).*T1_ds   +
P(4).*T2_ds   +   P(5).*T3_ds   +   P(6).*T4_ds;

elseif Nreg==3
y_fit=(P(1)+offcorr)+(P(2)+driftcorr).*t_ds+P(3).*T1_ds+P(4).*T2_ds+P(5).*T3_
ds+P(6).*T4_ds+P(7).*signal;

elseif Nreg==4
y_fit=(P(1)+offcorr)+(P(2)+driftcorr).*t_ds+P(3).*T1_ds+P(4).*T2_ds+P(5).*T3_
ds+P(6).*T4_ds+P(7).*signal;

else
'wrong number'
end

yres_ds=y_data_ds-y_fit;

sum_square=sqrt(sum(yres_ds.^2)/(ntot-1))

figure(3)
subplot(2,1,1),plot(t_ds,y_fit,':r')
hold on
plot(t_ds,y_data_ds,'k')
hold on
subplot(2,1,2),plot(t_ds,yres_ds,':r')
title('Fit Data')
```

```
% Print P values:
P


% average data
ynew=smooth(yres_ds,Nsg)';

if Nreg==2
off=-30;
elseif Nreg==4
    off=-30
else
    off=0
end

ynew=(2*pi*2.31)^2.*ynew.*1e8+off;
Linear=P(2).*(2*pi*2.31)^2.*1e8;


Nstart2=50;
Nend2=length(ynew)-1419;
ynew=ynew(Nstart2:Nend2);
t_ds2=t_ds(Nstart2:Nend2);
signal2=signal(Nstart2:Nend2);

if Nreg==1
    ynew=(ynew-Linear.*t_ds2);
    off2=-mean(ynew);
    ynew=ynew+off2;
elseif Nreg==3
    ynew=(ynew-Linear.*t_ds2);
    off2=-mean(ynew);
    ynew=ynew+off2;
end



figure(4)
if Nreg==1
    plot(t_ds2,ynew,'x-')
    ylabel('Sensitivity (micro-Gal)')
    xlabel('Time (days)')
    title('Tide Data')
elseif Nreg==3
    plot(t_ds2,ynew,'x-')
    ylabel('Sensitivity (micro-Gal)')
    xlabel('Time (days)')
    title('Tide Data')
elseif Nreg==4
    plot(t_ds2,ynew,'x-')
    ylabel('Sensitivity (micro-Gal)')
    xlabel('Time (days)')
    title('Tide Data')
else
    plot(t_ds2,ynew,'x-')
```

```
    hold on
    plot(t_ds2,signal2,'r')
    ylabel('Acceleration (\muGal)')
    xlabel('Calendar Date')
end

if Nreg==2
Standard_Deviation=std(t_ds)
Corr=corrcoef(ynew,signal2);
Corr=Corr(2,1)

%Calculate Correlation Coefficient for i randomised data sets
%Calculate Correlation Coefficient:
for i=1:10000
   R=ynew(randperm(length(ynew)));
   Corr_rand=corrcoef(R,signal2);
   test(i)=Corr_rand(2,1);
end

%Plot histogram of randomised data sets
figure(5)
hist(test)
    ylabel('Acceleration (\muGal)')
    xlabel('Calendar Date')

%Calculate Sigma Value:
Sigma=Corr/std(test)

end
```

```
figure(6)
if Nreg==1
plot(t_ds,(P(1)+offcorr).*t_ds./t_ds)
hold on
plot(t_ds,(P(2)+driftcorr).*t_ds,'k')
hold on
plot(t_ds,P(3).*T1_ds,'b')
hold on
plot(t_ds,P(4).*T2_ds,'b')
hold on
plot(t_ds,P(5).*T3_ds,'k-')
hold on
plot(t_ds,P(6).*T4_ds,'y-')
legend ('Offset', 'Linear Drift','MEMS','LED','Outside','Shield')
title('Regressed Parameters')

elseif Nreg==2
plot(t_ds,(P(1)+offcorr).*t_ds./t_ds,'c')
hold on
plot(t_ds,(P(2)+driftcorr).*t_ds,'y')
hold on
```

```
plot(t_ds,P(3).*T1_ds,'k')
hold on
plot(t_ds,P(4).*T2_ds,'r')
hold on
plot(t_ds,P(5).*T3_ds,'b')
hold on
plot(t_ds,P(6).*T4_ds,'g')
legend ('Offset','Drift','MEMS','LED','Outside','Shield')
    ylabel('Temperature/Acceleration Correlation')
    xlabel('Calendar Date (DD/M/YY)')

elseif Nreg==3
plot(t_ds,(P(1)+offcorr).*t_ds./t_ds)
hold on
plot(t_ds,(P(2)+driftcorr).*t_ds,'k')
hold on
plot(t_ds,P(3).*T1_ds,'k')
hold on
plot(t_ds,P(4).*T2_ds,'k')
hold on
plot(t_ds,P(5).*T3_ds,'r')
hold on
plot(t_ds,P(6).*T4_ds,'b')
hold on
plot(t_ds,P(7).*t_ds,'g')
legend ('Offset', 'Linear Drift','MEMS','LED','Outside','Shield','Tides')
title('Regressed Parameters')

elseif Nreg==4
plot(t_ds,(P(1)+offcorr).*t_ds./t_ds)
hold on
plot(t_ds,P(2).*T1_ds,'b')
hold on
plot(t_ds,P(3).*T2_ds,'b')
hold on
plot(t_ds,P(4).*T3_ds,'k-')
hold on
plot(t_ds,P(5).*T4_ds,'y-')
hold on
plot(t_ds,P(6).*t_ds,'r')
legend ('Offset','MEMS','LED','Outside','Shield','Tides')
title('Regressed Parameters')

else
'wrong number'
end
'****************************'
```

```
% allan variance calculation

tsample=1;
N=length(ynew);
ydata=ynew;
t=t_ds2*86400;
allan_count=0;

% start with 2 clusters and end with N clusters

for K=2:N/5;

    % determine data points per cluster (N points split into K clusters)
    M=floor(N/K);

    % average of each cluster
    for j=1:K;
    avgcluster(j)=sum(ydata((j-1)*M+1:j*M))/M;
    end

    % perform allan variance
    allan_count=allan_count+1;
    sum_allan=0;
    for j=1:K-1

    %time cluster size
    tau(j)=((t(N)-t(1))/(j+1));
    sum_allan=(avgcluster(j+1)-avgcluster(j))^2+sum_allan;
    end
    K
    allan_variance(allan_count)=sum_allan/(2*(K-1));

    clearvars avgcluster
end

figure(7)
loglog(tau,allan_variance.^0.5)
%hold on

% Estimate sampling time and frequency
nsamp=length(t_ds);
ts=(t_ds(nsamp)-t_ds(1))/nsamp;
fs=1/ts/86400;

% Calculate the PSD
[Px,f]=pwelch(ynew,[],[],[],fs); %In units of uGal^2/Hz

% Calculate the ASD
asdx=(Px.^0.5).*(f.^0.5);


figure(8)
loglog(f,Px,'r')
title('Power Spectral Density')
```

```
% Fast Sampling Data for Higher Frequency Spectrum PSD

N=1
%fac2=1;
%cal=(160000/1.5)*fac2;

for i=1:N

filename=cat(2,'test',num2str(i),'.txt')

fid1=fopen(filename);
variable1 = textscan(fid1,'%f32 %f32');
fclose(fid1);

v1=variable1{1}';
v2=variable1{2}';

v2=v2-mean(v2);

t_temp(:,i)=v1;
y_temp(:,i)=((v2./cal).*(2*pi*2.31).^2).*1e8;

coeff=polyfit(t_temp,y_temp,1);

y_temp=y_temp-(coeff(1).*t_temp+coeff(2));

end

% average data

tval=0;
yval=0;

for i=1:N
tval=t_temp(:,i)+tval;
yval=y_temp(:,i)+yval;
end

t_data=tval/N;
y_data=yval/N;



tsample=1;
N=length(y_data);
ydata=y_data;
t=t_data
allan_count=0;
```

```
% start with 2 clusters and end with N clusters

for K=2:N/40

    % determine data points per cluster (N points split into K clusters)
    M=floor(N/K);

    % average of each cluster
    for j=1:K
    avgcluster(j)=sum(ydata((j-1)*M+1:j*M))/M;
    end

    % perform allan variance
    allan_count=allan_count+1;
    sum_allan=0;
    for j=1:K-1

    %time cluster size
    tau(j)=((t(N)-t(1))/(j+1));
    sum_allan=(avgcluster(j+1)-avgcluster(j))^2+sum_allan;
    end
    K
    allan_variance(allan_count)=sum_allan/(2*(K-1));

    clearvars avgcluster

end

%allan_variance
loglog(tau,allan_variance.^0.5)

figure(6)
plot(t_data,y_data);
```